applied sciences

Human Health Engineering Volume II

Edited by
Jean Marie Aerts

Printed Edition of the Special Issue Published in *Applied Sciences*

www.mdpi.com/journal/applsci

MDPI

Human Health Engineering Volume II

Human Health Engineering Volume II

Editor

Jean-Marie Aerts

MDPI • Basel • Beijing • Wuhan • Barcelona • Belgrade • Manchester • Tokyo • Cluj • Tianjin

Editor
Jean-Marie Aerts
KU Leuven
Belgium

Editorial Office
MDPI
St. Alban-Anlage 66
4052 Basel, Switzerland

This is a reprint of articles from the Special Issue published online in the open access journal *Applied Sciences* (ISSN 2076-3417) (available at: https://www.mdpi.com/journal/applsci/special_issues/Human_Health_Engineering_II).

For citation purposes, cite each article independently as indicated on the article page online and as indicated below:

LastName, A.A.; LastName, B.B.; LastName, C.C. Article Title. *Journal Name* **Year**, *Volume Number*, Page Range.

ISBN 978-3-0365-2311-8 (Hbk)
ISBN 978-3-0365-2312-5 (PDF)

Contents

About the Editor

Jean-Marie Aerts holds a Master of Science and a PhD degree in Bioengineering from the KU Leuven (former Catholic University of Leuven) in Belgium. Currently, he is leading the Measure, Model & Manage Bioresponses (M3-BIORES) Group of the Division Animal and Human Health Engineering (A2H) in the Department of Biosystems (BIOSYST) at KU Leuven. He is full professor and chairman of Leuven Health Technology Centre (L-HTC) and of the Department of Biosystems. His research focuses on data-based mechanistic modelling of biological systems as a basis for the development of human health engineering technology. Jean-Marie Aerts is an IEEE member and has been a visiting researcher at the Engineering Department of Lancaster University and at the Institute of Biomedical Engineering of the University of Oxford.

applied sciences

MDPI

Editorial

Special Issue on "Human Health Engineering Volume II"

Jean-Marie Aerts

KU Leuven, Department of Biosystems, Division Animal and Human Health Engineering, Measure, Model & Manage Bioresponses Group, Kasteelpark Arenberg 30, 3000 Leuven, Belgium; jean-marie.aerts@kuleuven.be

1. Referees for the Special Issue

A total of 23 manuscripts were received for our Special Issue (SI), of which 3 manuscripts were directly rejected without peer review. The remaining 20 articles were all strictly reviewed by no less than two reviewers in related fields. Finally, 12 of the manuscripts were recommended for acceptance and published in *Applied Sciences-Basel*. Referees from 16 different countries provided valuable suggestions for the manuscripts in our SI, the top five being the USA, Italy, UK, DE, and Spain. The names of these distinguished reviewers are listed in Table A1. We would like to thank all of these reviewers for their time and effort in reviewing the papers in our SI.

2. Main Content of the Special Issue

As explained by Aerts [1], we are standing on the shoulders of giants when looking to the development of the research field of Human Health Engineering, i.e., technology for monitoring the physical and/or mental health status of individuals in a variety of applications, as it evolved from seminal work of, among others, Walter Cannon [2], Norbert Wiener [3], and Ludwig von Bertalanffy [4]. For more detailed information on the background and history of the field of Human Health Engineering, the reader is referred to the editorial of Aerts [1] written for the first volume of the special issue on Human Health Engineering.

The 12 presented papers in this second volume are grouped according to their contributions to the main parts of the monitoring and control engineering scheme applied to human health applications, namely papers focusing on measuring/sensing of physiological variables [5–8], papers describing health monitoring applications [9–12], and finally, examples of control applications for human health [13–16]. As indicated by Aerts [1], it is envisioned that the field of human health engineering is complementary to the field of biomedical engineering as it not only contributes to developing technology for curing patients or supporting chronically ill people, but also covers applications on healthy humans (e.g., sports, sleep, and stress) and thus also focuses on disease prevention and optimizing human well-being more generally.

The first series of articles in this SI describes methods for (improved) measuring and/or sensing of health-related physiological signals. The work of Arciniega-Montiel et al. [5] contributes to developing methods for improving the measuring reliability of fetal monitors, used in the case of high-risk pregnancies, on the basis of probabilistic models. Al-Halhouli et al. [6] demonstrated the feasibility of using a wearable and stretchable inkjet-printed strain gauge sensor for estimating respiratory rate, which is a key vital sign variable in many medical and health applications. In their study, Alsayed et al. [7] developed an automated data acquisition system for measuring pinch and pulling forces in patients recovering from stroke. Nishio et al. [8] investigated a method for quantifying the functional decline in proprioceptors in patients with low back pain using vibrations with sweep frequencies covering the entire range of response frequencies of proprioceptors.

The second series of articles describes applications of human health monitoring. In their paper, Cheng et al. [9] described a method combining an electroencephalography

Citation: Aerts, J.-M. Special Issue on "Human Health Engineering Volume II". *Appl. Sci.* **2021**, *11*, 7844. https://doi.org/10.3390/app11177844

Received: 3 August 2021
Accepted: 23 August 2021
Published: 26 August 2021

image-based method with a convolutional neural network to predict drowsiness in drivers, which is a major cause of vehicle accidents. Yang et al. [10] developed a biometrics monitor allowing to verify individuals on the basis of an interval-based linear discriminant analysis algorithm applied to electrocardiogram signals. Visnovcova et al. [11] used linear and non-linear analyses of electrodermal activity signals for quantifying sympathetic dysregulation as a non-invasive potential biomarker for monitoring anorexia nervosa-linked cardiovascular risks. In the paper of Jin et al. [12], a system is described for monitoring gait in (elderly) people using toe-area activity as a predictor for stumbling risk.

Finally, the third series of articles in this SI discusses examples of control applications for human health management. Kaçar et al. [13] developed a prototype of a closed-loop controlled valveless piezoelectric insulin pump for keeping the blood glucose level of Type 1 diabetes mellitus patients within desired ranges. In their paper, Trappey et al. [14] developed a system for virtual reality-based exposure therapy for treating people suffering from driving phobia disorder using bioresponse measurements to optimise fear-based driving scenarios. Guttiérez et al. [15] reported about a serious game platform with haptic feedback and EMG monitoring developed for upper limb rehabilitation of spinal cord injury patients. Aprile et al. [16] demonstrated the feasibility of optimising the efficiency of a robot-assisted rehabilitation area for restoring upper limb function, allowing one physiotherapist to supervise four patients.

3. Conclusions

This SI presents recent contributions in the growing field of human health engineering. The contributions highlight research focusing on different aspects of the monitoring and control engineering scheme (sensors, sensing systems, monitoring approaches, and control algorithms) as applied to human health. Applications cover both healthy and (chronically) ill people and this is in relation to physical as well as mental processes.

The combination of ever growing possibilities in sensors and (wearable) sensing technology and powerful artificial intelligence tools is expected to further boost the field of human health engineering, which will become increasingly ubiquitous in our society and will increasingly assist people of all ages in living healthy, high quality, and productive lives.

Funding: This special issue frames within research funded by the European Union's Horizon 2020 Research and Innovation programme under the Marie Skłodowska-Curie grant number 645770.

Acknowledgments: We would like to sincerely thank our Section Managing Editor, Marin Ma (marin.ma@mdpi.com), for all the efforts she has made for this special issue in the past year.

Conflicts of Interest: The author declares no conflict of interest.

Appendix A

Table A1. Special Issue (SI) reviewer list.

Alessandro Nastro	Yun-Ju Lee	Wasim Ahmad
Joo Chuan Yeo	Mikail F. Lumentut	Oliver Pabst
Tareq Assaf	Mariya Aleksandrova	Juri Taborri
Shuang Song	Thanh Duc Nguyen	Chien-Chang Chen
Zhengguo Tan	Muhammad Nadeem	Fabio Stroppa
Jesús López Belmonte	Ghulam Hussain	Meytal Wilf
Simon Danner	Marco D'Alonzo	Astrid Gramstad
Lin Yao	Paul Farago	Andrea Viggiano
Isaac Macwan	Vahab Youssof Zadeh	Hyungju Kwon
Alfonso Javier Ibáñez-Vera	Yuvaraj Rajamanickam	Adam Gąska
		Zixuan Cang

References

1. Aerts, J.-M. Editorial—Special Issue on Human Health Engineering. *Appl. Sci.* **2020**, *10*, 564. [CrossRef]
2. Cannon, W.B. *The Wisdom of the Body*; Norton & Company Inc.: New York, NY, USA, 1932.
3. Wiener, N. *Cybernetics or Control and Communication in the Animal and the Machine*; MIT Press: Cambridge, MA, USA, 1948.
4. Von Bertalanffy, L. *General System Theory—Foundations, Development, Applications*; George Braziller Inc.: New York, NY, USA, 1968.
5. Arciniega-Montiel, S.; Ronquillo-Lomeli, G.; Salas-Zúñiga, R.; Salgado-Jiménez, T.; Barriga-Rodríguez, L. Compensation of measurement uncertainty in a remote fetal monitor. *Appl. Sci.* **2020**, *10*, 3274. [CrossRef]
6. Al-Halhouli, A.; Al-Ghussain, L.; El Bouri, S.; Habash, F.; Liu, H.; Zheng, D. Clinical evaluation of stretchable and wearable inkjet-printed strain gauge sensor for respiratory rate monitoring at different body positions. *Appl. Sci.* **2020**, *10*, 480. [CrossRef]
7. Alsayed, A.; Kamil, R.; Ramli, H.; As'arry, A. An automated data acquisition system for pinch grip assessment based on Fugl Meyer protocol: A feasibility study. *Appl. Sci.* **2020**, *10*, 3436. [CrossRef]
8. Nishio, R.; Ito, Y.; Morita, Y.; Ito, T.; Yamazaki, K.; Sakai, Y. Investigation of the functional decline in proprioceptors for low back pain using the sweep frequency method. *Appl. Sci.* **2020**, *9*, 4988. [CrossRef]
9. Cheng, E.J.; Young, K.-Y.; Lin, C.-T. Temporal EEG monitoring for drowsy driving prediction. *Appl. Sci.* **2020**, *9*, 5078. [CrossRef]
10. Yang, C.; Ku, G.W.; Lee, J.-G.; Lee, S.-H. Interval-based LDA algorithm for electrocardiograms for individual verification. *Appl. Sci.* **2020**, *10*, 6025. [CrossRef]
11. Visnovcova, Z.; Olexova, L.B.; Sekaninova, N.; Ondrejka, I.; Hrtanek, I.; Cesnekova, D.; Kelcikova, S.; Farsky, I.; Tonhajzerova, I. Spectral and nonlionear analysis of electrodermal activity in adolescent anorexia nervosa. *Appl. Sci.* **2020**, *10*, 4514. [CrossRef]
12. Jin, Y.; Shogenji, M.; Watanabe, T. Feature assessment of toe area activity during walking of elderly people with stumbling experiences through wearable clog-integrated plantar visualization system. *Appl. Sci.* **2020**, *10*, 1359. [CrossRef]
13. Kaçar, A.; Özer, M.B.; Taşcioğlu, Y. A novel artificial pancreas: Energy efficient valveless piezoelectric actuated closed-loop insulin pump for T1DM. *Appl. Sci.* **2020**, *10*, 5294. [CrossRef]
14. Trappey, A.; Trappey, C.V.; Chang, C.-M.; Kuo, R.R.T.; Lin, A.P.C.; Nieh, C.H. Virtual reality exposure therapy for driving phobia exposure: System design and development. *Appl. Sci.* **2020**, *10*, 4860. [CrossRef]
15. Guttiérez, Á.; Sepúlveda-Muñoz, D.; Gil-Agudo, Á.; de los Reyes Guzmán, A. Serious game platform with haptic feedback and EMG monitoring for upper limb rehabilitation and smoothness quantification on spinal cord injury patients. *Appl. Sci.* **2020**, *10*, 963. [CrossRef]
16. Aprile, I.; Pecchioli, C.; Loreti, S.; Cruciani, A.; Padua, L.; Germanotta, M. Improving the efficiency of robot-mediated rehabilitation by using a new organizational model: An observational feasibility study in an Italian rehabilitation center. *Appl. Sci.* **2020**, *9*, 5357. [CrossRef]

applied sciences

MDPI

Article

Compensation of Measurement Uncertainty in a Remote Fetal Monitor

Sadot Arciniega-Montiel [1], Guillermo Ronquillo-Lomeli [1,2,*], Roberto Salas-Zúñiga [3], Tomás Salgado-Jiménez [1] and Leonardo Barriga-Rodríguez [1]

[1] Department of Energy, Center for Engineering and Industrial Development, Santiago de Queretaro 76125, Mexico; sadot@cidesi.edu.mx (S.A.-M.); tsalgado@cidesi.edu.mx (T.S.-J.); lbarriga@cidesi.edu.mx (L.B.-R.)
[2] Faculty of Engineering, Autonomous University of Queretaro, Santiago de Queretaro 76010, Mexico
[3] Engineering and Technology Center, Santiago de Queretaro 76079, Mexico; roberto.salas.correo@gmail.com
* Correspondence: gronquillo@cidesi.edu.mx; Tel.: +52-442-211-9800

Received: 10 April 2020; Accepted: 2 May 2020; Published: 8 May 2020

Abstract: The perinatal mortality rate is very high throughout the world. A fetal monitor may be used remotely, and this would tackle the problem of continuous monitoring of high-risk pregnancies. There is evidence that current technology is of low reliability, and, therefore, of low precision to identify fetal health. In medical technological implementation, a safe, efficient, and reliable operation must be guaranteed, and the main problem is that remote fetal monitor gathers just a few samples, so the hypothesis of classical theory is not met. We are proposing an approach that improves the data's lack of reliability that accompanies the use of a remote fetal monitor. The method refers to how, by using the existing technologies and the initial experimental data, it is possible to apply probabilistic models that are truly representative of each application. This leads to the characterization of properties of the statistics used to generate a representative probabilistic model without the need to consider the hard suppositions. Results show that, for every case study, it was possible to improve estimations of measurement uncertainty. The proposed method is a useful tool to increase the reliability of medical technology, especially for pieces of equipment where a health care professional is not available.

Keywords: remote fetal monitor; measurement uncertainty; standard deviation; Monte-Carlo method (MMC); efficient estimator

1. Introduction

The perinatal mortality rate is very high throughout the world. According to the World Health Organization (WHO), it is estimated that 800 women die every day due to pregnancy or birth-related causes. From all pregnancies, four out of ten women are at high risk. There is no hospital infrastructure for the timely diagnosis of fetal distress due to overpopulation.

Continuous remote monitoring technology would provide a solution to solve some problems in high-risk pregnancies. Patients would no longer need to be at the hospital, and, from the comfort of their homes, would directly carry out and forward the studies prescribed by their physicians. The monitoring equipment could be configured for providing the corresponding studies directly by the patient without the need of a specialist. Patients may feel calm and reassured, knowing that their studies, once transmitted by the monitor, will be checked and assessed by a specialist.

Fetal monitoring technology faces reliability issues. When compared against intermittent auscultation, the use of technology reduces perinatal mortality [1–3]. However, some other studies from the 1970s and 1980s did not show similar results [4], and the contribution of technology to reduce perinatal mortality, as observed in the last decades, is still under discussion. On the other hand, the increase in rates of births via Caesarian section has become a matter of public interest in many countries, and there is a general belief that continuous monitoring during childbirth (CTG) has contributed to this.

CTG is subject to a poor observer interpretation, particularly while assessing variability and de-acceleration, in addition to the classification of tracing [5–7]. Diagnosis depends on the criteria used for tracing analysis [8], so objective guidelines are required to provide a practical approach.

It is necessary to have an approach that improves the data reliability produced by the remote fetal monitor to increase the diagnosis precision [9,10]. Fetal monitoring systems should yield reliable data, regardless of the conditions of use, such as location, installation, number of samples, etc., for the revision of fetal health and the prompt response of healthcare professionals.

In medical technology implementation, a safe and efficient operation must be guaranteed [11]. Attention is focused on the practical implementation of technology within a sanitary environment. The simple fact of having the necessary technology is not a whole solution. The processes of planning, evaluation, selection, and implementation of new technologies, all in concept and context, must be considered. This may imply a direct solution to specific assessments of sanitary technology. When developing new technology, guaranteeing precision and reliability for the chosen environment contributes to achieving safer results and sound medical attention.

Under these conditions, the main problem is to reassure the reliability of the data obtained by the remote fetal monitor, since health-care professionals would not be present, and there would be only a few samples of variables (heart rate (HR), uterine activity) that lead to the detection of anomalies. Therefore, the analysis of measurement uncertainty becomes necessary.

For reliable estimation of measurement uncertainty, it is necessary to guarantee some properties (distribution independence, a large sample size, and a normal distribution). Health-care professionals are not familiar with the measurement process carried out by remote fetal monitoring, and, in general, only have a few samples. This means it is not possible to verify the hypotheses required so that the evaluator may have the properties required by a good estimator. By means of a statistical approach, several works related to uncertainty estimation have been conducted, for cases where the hypothesis of classical theory is not verified.

A fetal monitor is a stochastic process that has few samples available. Therefore, it is very difficult to model by using conventional methods. Different approaches have been used when the hypothesis of the classical theory is not verified, including the Monte-Carlo method (MCM) [12], parametric and non-parametric theory formulation [13], adaptive estimators [14], spectrum-based estimation [15], stochastic gradient [16], and mean square error [17] estimators with Cramer–Rao type restriction and reliability estimation under measures degradation [18].

The MCM is a widely used tool for modeling stochastic systems since with a large enough sample, the probability that an estimator will deviate from the expected value can be as small as required. The MCM is used to get information related to estimator properties. The parameters of softening and form of estimating function are adjusted to modify the performance of maximum probability estimators. The MCM can be used for modeling unknown distribution functions. The parametric and non-parametric models are wide probability function estimation methods; theory formulation has been developed considering local asymptotic length and restrictions in sample size. Adaptive estimators that guarantee the consistency in finite samples for any distribution function are helpful in the fetal monitor application. The term adaptive integrates the concept that such estimators adapt to the sample using data to estimate a non-parametric density function. Adaptive estimators have been applied using the least-squares method with finite samples, reaching substantial increases in efficiency, but with hypotheses that are difficult to verify for applications with a few samples. The spectrum-based method is useful when the relationship between observations and parameter model is noisy, potentially non-linear, and not invertible. The stochastic gradient estimation is a numeric method that is stable and robust for fitting parameters and predicting standard errors well. Even though only the typical case, with some modifications, was considered, the hypothesis that let the Cramer–Rao type limit such estimators have been changed. The mean square error can be improved by implementing estimators with parametric restrictions that do not satisfy certain conditions. With a new definition of bias in restricted surroundings, a Cramer-Rao restriction type was determined for the pondered mean square

error estimators, for normal distribution only. Correlated perturbations were not considered. The reliability estimation for a system whose degradation measures are monotonous, can obtain the fault time distribution, and, therefore, system reliability.

The remote fetal monitor has a context application. The aim of this work is to obtain an integral maternal-fetal watch program, integrated by a technological platform that allows the timely detection of perturbations in baby heart rate, that enable us to remotely send information to an obstetric monitoring center for timely and reliable diagnosis of the patient.

When modeling a process, the most complicated component of the model is represented in probabilistic terms, and the hypotheses taken as valid in many situations are not met, and the results are not valid. This work presents a proposal of how, using the existing theory, with a deterministic model and the Monte-Carlo method [12], it is possible to apply probabilistic models that are genuinely representative of the application, and that characterize the statistics' properties used. In a specific application, the statistical properties of interest are generally mean, variance, extreme values, dependence on sample size, bias, etc. [13–17]. In general, only the mean and variance parameters are considered to obtain a probabilistic model because they characterize the uniform distributions that represent the worst-case scenario (total ignorance of the model) and the Gaussian distributions considered as typical or normal. However, to estimate these parameters, it is necessary to carry out a sampling to obtain more information about the system model. This additional information is not used in practice. This work proposes a new approach to include experimental data and to generate a representative probabilistic model without considering difficult suppositions. The suggested procedure is applied to a fetal monitor to correct the standard deviation estimation considering the noise type that occurs during the regular operation of the device.

2. Uncertainty Estimation Model

One of the main problems in metrology is the estimation of measurement uncertainty. According to [19], "estimated standard deviation associated to output, or measurement estimation is called combined standard deviation, and it is determined from the estimated standard deviation associated for each estimation of output, called standard uncertainty". In general, the process to be measured is ignored, and regularly, there are only just a few samples available. Measurements have defects that lead to an error in the result of such measurements. Although it is not possible to compensate for the random error in a measurement result, its effect can generally be reduced by increasing the number of observations until the expectations or expected value becomes zero.

Modeling of stochastic systems has been thoroughly studied, considering the hypothesis of the great numbers law. However, a measurement system is a stochastic system, with a limited or finite number of samples. The remote fetal monitor is a stochastic measurement system with a limited number of samples. Below an uncertainty estimation model for a measurement system with limited samples is presented.

A probability space $(\Omega, \mathcal{F}_0, P)$ for a random variable $X : \Omega \to \mathbb{R}^n$ where the conditional expectation $E\{(\cdot), \mathcal{F}_0\}$ concerning to sigma-algebra $\mathcal{F}_0 = \{\phi,\ \Omega\}$ [20] may be expressed as

$$E\{X|\mathcal{F}_0\} = E\{X\} \tag{1}$$

This means that the best estimation for the random variable, when there is no a priori knowledge of the process, is the mathematical expectation, and the associated standard uncertainty (u_c) may be obtained from the probability density function (PDF) of the random variable [21]. Therefore, the mean is proposed to estimate the following sample, and standard uncertainty is obtained from the standard deviation estimator.

Let A be the event where a device does not fail, the reliability is by definition $P(A)$ if the indicator function is considered χ_A,

$$\chi_A(\omega) = \begin{cases} 1, & \omega \in A \\ 0, & \omega \notin A \end{cases} \tag{2}$$

This means that the problem of calculating reliability is changed for the problem of estimating the expected value, for which the use of the Monte-Carlo method in this work is necessary.

In the estimation of the mathematical expectation, the equation regularly used is

$$\overline{X}_n = \frac{1}{n}\sum_{k=1}^{n} X_k, \tag{3}$$

being n the sample number.

In the normal case with independent samples, the mean estimator is optimal in the sense of the mean square error. In addition, the large number theorem is consistent for large samples, and its distribution is known by the central limit theorem [20], and is efficient [22].

In the general case, the estimator $\overline{X}_n$ is a random variable that depends on:

1. Sample size, n
2. Distribution, F_X
3. The degree of probabilistic dependence between samples, in addition to the fact that only linear or correlation dependence is considered $\rho_{X_i X_j}$.

To measure the quality of this, estimate the standard deviation is used (called uncertainty in the metrology area). This standard deviation is also estimated; this is done with S_n defined as

$$S_n := \sqrt{S_n^2}, \tag{4}$$

$$S_n^2 := \frac{1}{n-1}\sum_{k=1}^{n} (x_k - \overline{x}_n)^2, \tag{5}$$

for independent samples with the same distribution we get,

$$E\left\{S^2_{\overline{X}_n}\right\} = \frac{E\left\{S_X^2\right\}}{n} = \frac{\sigma_X^2}{n}. \tag{6}$$

So, the problem of determining the quality of the estimate focuses on determining σ_X. However, we must identify the restrictions in the estimation.

A widespread practice is to consider that if

$$\left\{S_n^2\right\} = \sigma^2, \tag{7}$$

then,

$$E\{S_n\} = \sigma. \tag{8}$$

Nonetheless, defining by z a random variable,

$$z(\omega) = 1,\ \forall\ \omega \in \Omega, \tag{9}$$

and applying Cauchy–Bunyakowskii–Schwartz inequality [20],

$$E\{S_n\} = E\{S_n z\} \leq \sqrt{E\left\{S_n^2\right\}E\{z^2\}} = \sqrt{E\left\{S_n^2\right\}}, \tag{10}$$

that is

$$E\{S_n\} \leq \sigma, \tag{11}$$

this inequality depends on all these three: sample size n, distribution function F_X, and correlation dependence $\rho_{X_i X_j}$.

For a sample, $X = (X_1, \cdots, X_N)$ corresponds a density function $f_X(X, \theta)$ for which the score $V(\theta)$ is defined

$$V(\theta) \equiv V_X(\theta) log f_X(X; \theta), \tag{12}$$

and the Fisher information matrix

$$I(\theta) E\left\{\left[\frac{\partial V(\theta)}{\partial \theta}\right]^2\right\}. \tag{13}$$

The Cramer–Rao theorem is fulfilled [20] where if $\hat{\theta}_n = \hat{\theta}(X_1, \ldots, X_n)$ is an unbiased estimator of θ^{∞} then

$$E_\theta\left\{\| \hat{\theta}_n - \theta \|^2\right\} \geq \frac{1}{nI(\theta)} \tag{14}$$

and also depend on sample size n, distribution F_X, and correlation dependence $\rho_{X_i X_j}$.

This means that in the case of the fetal monitor where there are few samples, it is possible to determine the boundaries for the reliability estimation and its uncertainty using the Monte-Carlo method.

3. Uncertainty Estimation Approach

This section describes a proposed approach to obtain a reliability estimator for heart rate measurement.

Reliability R, the probability that the measurement is correct, is a function of the measurement device, the perturbations represented by its distribution function and its correlation, in addition to the number of data used in the estimation.

To estimate the reliability and the uncertainty in the measurement, the following procedure is proposed:

1. System model: device model and perturbation model.
2. Distribution function estimation of the perturbations and correlation function.
3. Estimators properties analysis using the Monte-Carlo method.
4. Correction factors calculation to compensate estimators.
5. Confidence intervals for the R estimation.

3.1. System Model

In the block diagram of Figure 1, a system of single input u_k and single output y_k (SISO) is shown in simplified form. Noise ξ_k presence is assumed a priori, and, in this case, white noise properties are attributed, which is presented as additive noise r_k in the system output.

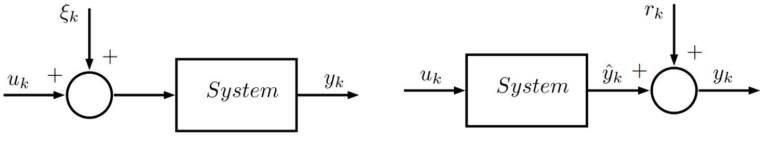

(**a**) (**b**)

Figure 1. Single-input and single-output (SISO) system: (**a**) With white noise to the input; (**b**) With additive noise to the output.

It is considered that an input–output data set of the system is available $(y_k,\ u_k; k = 1,\ 2, \cdots, n)$ where n is the measurement number taken from the input and output for modeling.

3.1.1. Device Model

To describe the dynamic behavior from a set of input and output measurements, an auto-regressive and exogenous (ARX) [23] (p. 81) linear model structure is assumed. A scheme for system modeling is shown in Figure 2.

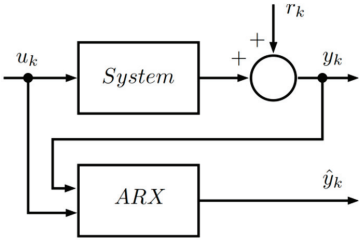

Figure 2. Scheme for linear system modeling based on auto-regressive and exogenous (ARX) structure.

The ARX structure model is

$$y_k = \phi_k^T \theta + \xi_k, \tag{15}$$

$\phi_k = [y_{k-1}, \cdots, y_{k-l}, u_k, \cdots, u_{k-l}]^T$ is the regression vector, $\theta = [a_1, \cdots, a_l, b_0, \cdots, b_l]^T$ is the parameter vector, while l is the system degree. Based on Equation (15), the relationship between the input and the output in a compact way can be written in the following vector form.

$$Y = \Phi\theta + \Xi, \tag{16}$$

where $Y = [y_1, y_2, \cdots, y_n]^T$, $\Phi = \left[\Phi_1^T, \Phi_2^T, \cdots, \Phi_n^T\right]^T$, and $\Xi = [\xi_1, \xi_2, \cdots, \xi_n]^T$.

With this information and applying the least-squares method [24] (pp. 17–27), a deterministic model is obtained which represents the fetal monitor dynamic, the solution is

$$\hat{\theta} = \left[\Phi^T\Phi\right]^{-1}\Phi^T Y. \tag{17}$$

Finally, the relationship between white noise ξ_k in the system input and additive noise r_k in the system output for the ARX model structure is

$$\mathrm{R}(z) = \frac{1}{1 - A(z)}\Xi(z), \tag{18}$$

where $A(z) = \hat{a}_1 z^{-1} + \cdots + \hat{a}_l z^{-l}$.

3.1.2. Perturbation Model

The probabilistic part is modeled by a stochastic process $\{\xi_k\}$, which must be strongly stationary, uncorrelated, with a cumulative distribution function (CDF) F_{Ξ_k}. These hypotheses are experimentally validated. The probabilistic model is used to determine the properties of the estimators used to determine the heart rate; considering that the noise ξ_k is naturally present and that it is transformed into r_k by the system during the route that the signal travels from the fetus heart through amniotic fluid, body fat, etc., to the fetal monitor output. Figure 3 shows a block diagram of the process for estimating the error distribution function F_{Ξ_k}.

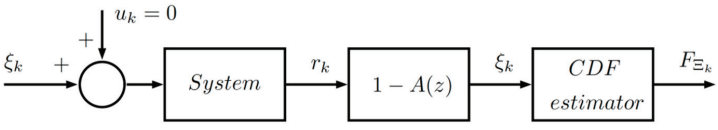

Figure 3. Estimation process of the error distribution function F_{Ξ_k}.

3.2. Distribution Function Estimation of the Perturbations and Correlation Function

For each patient, a stochastic model is determined, which describes the perturbation present in the fetal heart rate signal, which exists due to the individual anatomical characteristics of the patients, amniotic fluid, body fat, etc.

The stochastic model is obtained from data acquired by clinical studies using the patient's fetal heart rate monitor. Each clinical study (sample) is a set of measurements $(y_k,\ k = 1,\ 2, \cdots, n)$.

Using the data-normalized histogram, the probability density function (PDF) is estimated for n samples f_{Ξ_n}, numerically integrating and using some interpolator an estimator is obtained for the probability distribution function F_{Ξ_n} of the perturbations, which is used to build a ξ simulator required in the Monte-Carlo method. Each sample that is added improves the probability distribution function estimation, so that, the more samples available, the better the estimator.

To guarantee that the bias of the expectation estimate is zero, the correlation between the perturbation and the regression vector used in the least-squares model must be verified as zero. For this, a correlation degree estimate is made [20,22] that exists between the perturbations and the measured signal. The correlation is defined as follows

$$\rho_{XY}(k) := \frac{E\left\{X_{j+k}Y_j\right\}}{\sqrt{E\left\{X_{j+k}^2\right\}E\left\{Y_j^2\right\}}}, \tag{19}$$

where ρ_{XY} represents the correlation function between the random variables X and Y. This magnitude is estimated using

$$\hat{\rho}_{XY}(k) = \frac{\frac{1}{n}\sum_{j=1}^{n} X_{j+k}Y_j}{\sqrt{\frac{1}{n}\sum_{j=1}^{n} X_{j+k}^2 \frac{1}{n}\sum_{j=1}^{n} Y_j^2}}. \tag{20}$$

If there is a substantial correlation, a filter must be designed so that the perturbation behaves with white noise features.

3.3. Estimators Properties Analysis Using the Monte-Carlo Method

After obtaining the models of the system and the perturbations, it is necessary to estimate the value of the fetal heart rate. Simulated samples from the inverse distribution function $F_{\Xi_n}^{-1}$F_ (Ξ_n) were used for this estimation. To carry out this task, the sample mean $\overline{Y}_n$ and the sample deviation S_n were used. The mean is useful for determining the fetal heart rate value and the standard deviation for quantifying the quality of the estimate, known as uncertainty in the metrological area.

However, it should be noted that for these estimators to be used properly, it is necessary to determine their properties specifically for each patient. The most important property to determine is how the length of sample K impacts the distribution function.

On the other hand, the sample mean $\overline{Y}_n$ and the standard deviation S_n are in turn random variables that are characterized by their probability distribution function $F_{\overline{Y}_n}$ and F_{S_n}, respectively. These functions in classical theory can be approximated with large samples and hypotheses of probabilistic independence, which turned out to be difficult to verify in this application. To solve this mathematical problem, the Monte-Carlo method is proposed as a tool to determine these distribution

functions without the use of these hypotheses. The procedure is presented in Figure 4, where N is the number of samples used to simulate Ξ_k and K the number of samples to determine $F_{\overline{Y}_n}$ and F_{S_n}.

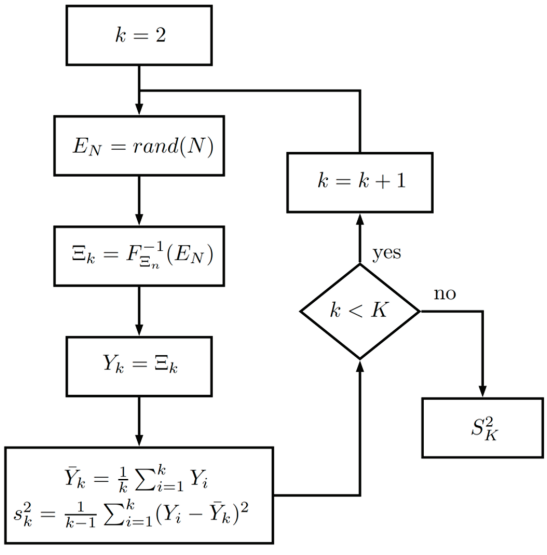

Figure 4. Simulation procedure with the Monte-Carlo method (MMC) to determine the variance s_k^2.

This procedure allows us to estimate the variance σ^2 because if K is large, the following is fulfilled

$$E\{Y\} = E\left\{\overline{Y}_K\right\}, \tag{21}$$

$$S_K^2 = \frac{1}{K-1}\sum_{i=1}^{K}[Y_i - E\{Y\}]^2, \tag{22}$$

$$\sigma^2 = E\left\{S_K^2\right\}. \tag{23}$$

3.4. Correction Factors Calculation to Compensate Estimators

This procedure removes the constraints that exist to achieve an adequate estimate of reliability and provides the factors that must be included to eliminate the estimators' bias. These factors are

1. Additive factor for $\overline{Y}_k$ $\left(\left[\Phi^T\Phi\right]^{-1}\Phi^T\Xi\right)$
2. Multiplicative factor for S_k (C_k)

In our case, the Φ and Ξ turned out to be uncorrelated, so this additive term is close to zero and was not considered in this study.

The multiplicative factor for S_k is obtained from the Cauchy–Bunyakowskii–Schwartz inequality described in Equation (10). In many cases where $E\{S_k\} < \sigma$, the question is how far is $E\{S_k\}$ from σ, so we will introduce a factor c_k that eliminates this bias, that is to say

$$E\{c_k S_k\} = \sigma \tag{24}$$

The new standard deviation estimator σ will be $c_k S_k$, this factor is estimated using the Monte-Carlo method and the relation

$$c_k = \frac{\sqrt{E\{(Y - E\{Y\})^2\}}}{\sqrt{\frac{1}{k-1}\sum_{i=1}^{k}\left(Y_i - \overline{Y}_k\right)^2}} = \frac{\sigma}{S_k}. \tag{25}$$

3.5. Confidence Intervals for the R Estimation

When clinical studies are performed on patients, new data are obtained, which must be analyzed to determine if they are correct. For carrying out this, confidence intervals are constructed on-line to ensure that the test is correct with a confidence level α.

The last sample's variations are analyzed. These variations are measured by standard deviation (s), which is calculated by means of the s_n estimator, considering the process defined by Y and the set of samples.

In a process defined by Y with N clinical studies set Y_n, $(n = 1,\ 2, \cdots, N)$, each clinical study has M samples $[Y_n]_m$, $(m = 1, 2, \cdots, M)$. The variations are measured by the standard deviation s_Y, which is estimated through the corrected s_n.

From a statistical point of view, a measurement is considered incorrect if it is an atypical value. The criteria to decide is built by considering the probability that the current measurement will fall outside a range defined by a standard deviation estimator, considering the necessary compensations for the used estimators.

Now, we will determine a criterion to eliminate measurements that, with a high probability, may be wrong, since values will be far from most of the measurements, known as atypical data.

To do so, the Chebyshev approximation [25] is used

$$P\left(\frac{\left|Y - \mu_Y\right|}{\sigma_Y} \geq k\right) \leq \frac{1}{k^2}, \tag{26}$$

$$P\left(\frac{\left|Y - \mu_Y\right|}{\sigma_Y} < k\right) \geq 1 - \frac{1}{k^2}, \tag{27}$$

where μ_Y and σ_Y are the mean and the standard deviation of the process, respectively.

If no further information is available but considering that new information is arriving every time a measurement is taken, the following statistics are considered

$$P\left(\frac{\left|Y - \mu_Y\right|}{c\, s_Y} < k\right) \geq 1 - \frac{1}{k^2}. \tag{28}$$

where c is a correction factor due to the finite number of samples, and to the law of standard deviation spread?

Since μ_Y, s_Y, and c are typically unknown, these parameters are replaced by their estimators $\overline{y}_n$, s_n, and c_n, respectively. Finally, the selection criterion is obtained

$$P\left(\frac{\left|Y_n - \overline{y}_n\right|}{c_n s_n} < k\right) \geq 1 - \frac{1}{k^2}, \tag{29}$$

which is equivalent to

$$\left(Y_n - \overline{y}_n\right)^2 < \beta s_n^2, \tag{30}$$

where $\beta = k^2 c_n^2$, and c_n is the correction factor that corresponds to the n^{th} clinical study.

Figure 5 shows the flowchart of the reliability estimation algorithm based on Chebyshev's inequality.

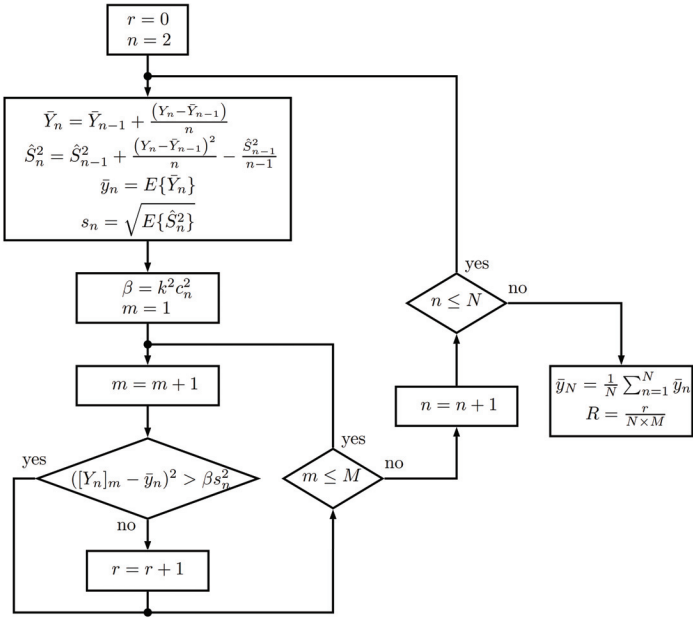

Figure 5. Reliability estimation algorithm.

3.6. Remote Fetal Monitoring Equipment

A fetal monitor was developed to provide a reliable remote monitoring of both mother and fetus during the pregnancy process. The fetal monitor has the capacity of recording fetal heart rate, uterine activity, and fetal movement. Its compact design allows the mother to use it herself. In addition, the fetal monitor allows the recording of studies, and features the capacity to send them directly to the obstetric monitoring center (OMC) to be evaluated by a specialist.

The purpose of this medical device is to provide monitoring of high-risk pregnancies, especially those in marginal areas, who cannot go to a clinical specialist periodically to reduce fetal distress, and, therefore, perinatal mortality in Mexico.

The fetal monitor is an embedded system, which includes a digital signal processor that allows for an adequate calculation to achieve higher precision in fetal heart rate reliability and signs of uterine activity. The algorithm developed included the proposed methodology of this work to guarantee the reliability of distance measurement. This instrument has enough hardware resources, such as remote connectivity by means of a mobile phone, through the general package radio service (GPRS), geo-referenced transmission, an alarm indicator for the patient, a speaker to listen to baby heartbeats, a flash memory to store studies and two Doppler ultrasound sensors, of 1.2 MHz in frequency, and 350 mW for output power, for the acquisition and processing of fetal monitoring variables. A block diagram with these functions is presented in Figure 6.

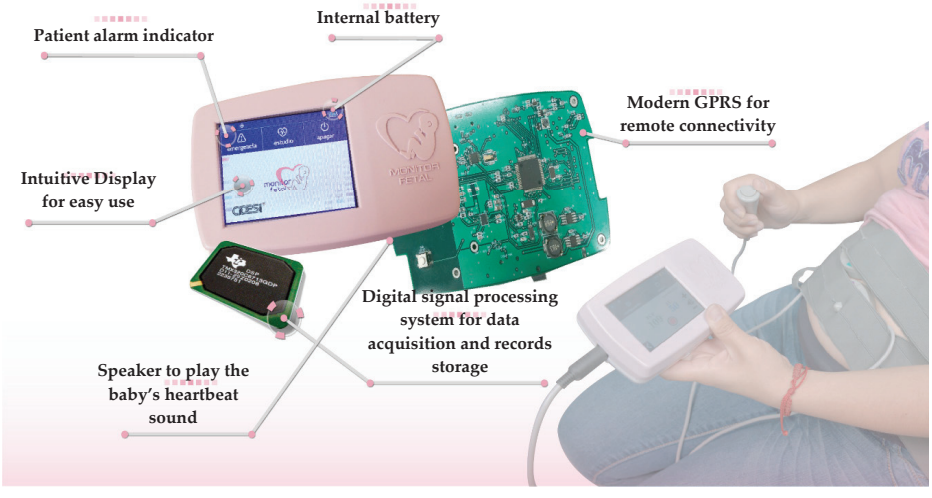

Figure 6. Scheme of the fetal monitor used for testing.

3.7. Experimental Clinical Studies

During experimental tests, several fetal monitoring instruments, in remote sites, were connected to patients and sent data signals to the OMC based at the Central Hospital. The patients were informed about their data usage and consented to publish their data for research purposes.

Data collected at OMC were primary signals without processing, that is, directly from the analog–digital converter of the instrument. For each test, a set of data with fetal heart rate and signs of uterine activity was stored. Table 1 shows the clinic studies in detail, to validate the proposed approach.

Table 1. Clinical Studies for approach validation.

Patient Name	Age (Year)	Studies Number	Place	Distance from OMC
Subject 1	37	42	Toliman	81.7 Km
Subject 2	41	45	Jalpan de Serra	187 Km
Subject 3	35	40	Querétaro	9.1 Km
Subject 4	26	43	Amealco de Bonfil	71.1 Km
Subject 5	43	32	Querétaro	9.4 Km
Subject 6	18	34	San Luis Potosí	215 Km
Subject 7	28	36	Querétaro	10.7 km
Subject 8	31	38	Querétaro	18.3 Km
Subject 9	19	43	Colima	576 Km
Subject 10	21	47	Querétaro	13.5 Km
Subject 11	39	51	Querétaro	30.4 Km
Subject 12	42	53	Querétaro	13.1 Km
Subject 13	29	54	El Marqués	7.1 Km
Subject 14	33	57	El Marqués	6.8 Km
Subject 15	36	58	Salamanca	89.7 Km
Subject 16	25	58	Puebla	329 Km
Subject 17	42	58	Guadalajara	378 Km
Subject 18	45	61	Querétaro	2.1 Km
Subject 19	38	75	Querétaro	17.4 Km

Experimental tests were conducted in the State of Querétaro. In the first stage, health care professionals of a Women and Child hospital in the city of Querétaro assessed patients. Patients were trained to handle the equipment at home, to step by step visualize data on the fetal monitor screen, and even to place two sensors on the abdominal region of the patient. One sensor measures the fetal heart rate, and the other measures the uterine activity of the patient. In the second stage, experimental tests for the fetal monitor were conducted with patients from remote sites. Data generated by each patient were sent to an OMC in the city of Querétaro. The locations of patients transmitting their records were in many different areas of the State of Queretaro, or in places nearby the State.

Distances from these sites to the OMC were 180 Km on average. Nineteen patients were evaluated, with around 40 studies for each patient. The number of measurements for each clinical study was 900, on average, to prove the approach proposed in this work, providing measurement reliability for fetal heart rate and uterine activity. Figure 7 shows some images of the sites where tests were conducted.

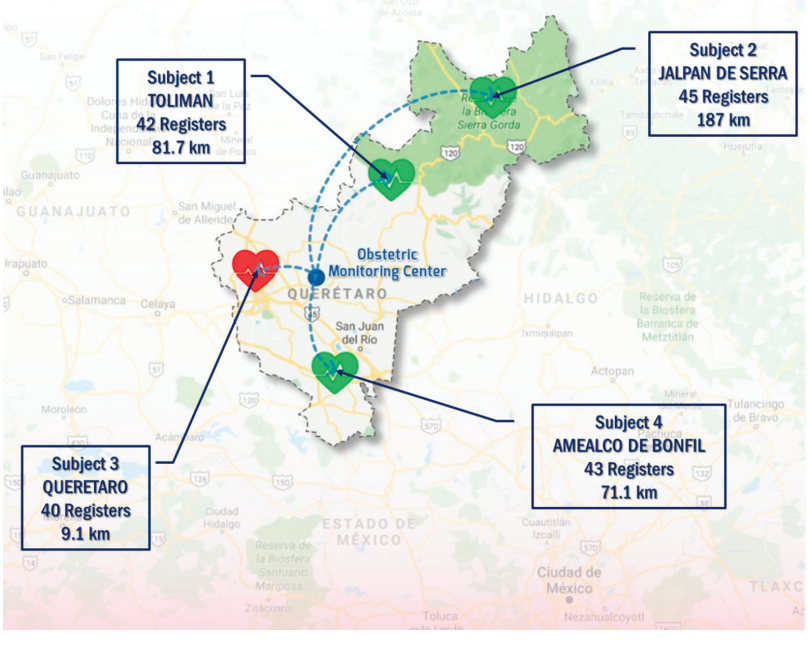

Figure 7. Map showing the location of the first four patients from Table 1.

Samples for each medical device were received and stored at OMC. The objective at this stage was to generate a database of unprocessed signals, containing bioelectrical perturbations, to implement and to validate the proposed methodology. Only fetal heart rate signals were processed.

4. Results and Discussion

Data from clinical studies carried out on 19 patients were used for system modeling and validating the proposed approach. The clinical study data was divided into two subsets, the first to model the system (data for modeling) and the second to validate the proposed approach (data for validation). The proposed approach was implemented in MATLAB® for building the model, calculating the compensated uncertainty, and evaluating the reliability.

4.1. Fetal Monitor Model

To obtain the dynamic model of the fetal monitor, a calibrated signal generator was used to generate an input signal u_k for obtaining an output y_k from the fetal monitor device used in this study. With these data and applying the least-squares method described in Section 3.1.1, a second-order linear deterministic model $l = 2$ was estimated, the ARX model parameters were $\hat{\theta} = [1.1381, -0.2829,\ 0.0985, -0447, 0.0907]$. The dynamic model response of the fetal monitor is shown in Figure 8.

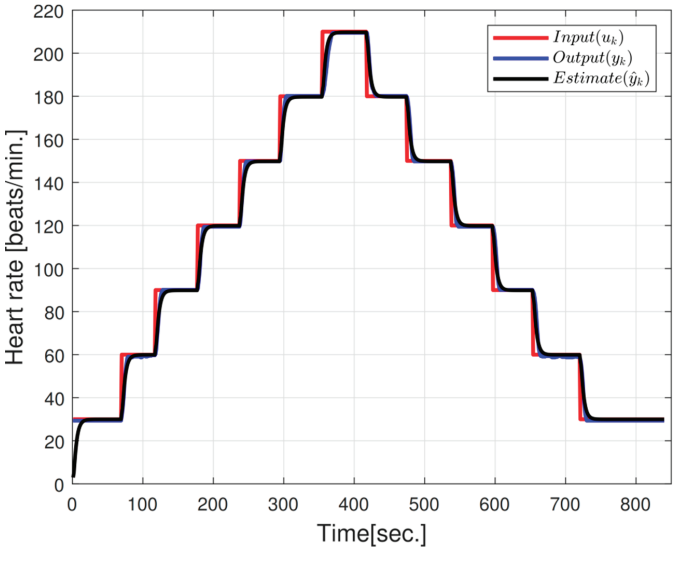

Figure 8. Fetal monitor model simulation results.

4.2. Stochastic Model

A probabilistic model for each patient was calculated from the experimental data set (data for modeling) acquired from clinical studies carried out on the 19 patients under study. From the fetal heart rate measurements, the perturbations ξ_k was obtained, using the dynamic model of the fetal monitor applying Equation (18), for each patient. Data for ten clinical studies per patient were used to obtain the probabilistic model. From perturbations histogram, estimations of probability density functions f_{Ξ_n} and distribution functions F_{Ξ_n} were obtained, finally a nonparametric model of the inverse function $F^{-1}_{\Xi_n}$ was available for each patient. The direct and inverse distribution functions were estimated by using a linear interpolation by parts [26]. Using the Monte-Carlo method with a large data number of the amount of $N = 10^5$ and $K = 10^3$, the probabilistic models $F^{-1}_{\Xi_n}$ were simulated applying the procedure described in Figure 4 and s^2_K was estimated to calculate the variance using $\sigma^2 = E\{s^2_K\}$. The probability distribution function models of the patients used in the simulation are shown in Figure 9, and Table 2 shows the estimated standard deviations and data number n used in the F_{Ξ_n} modeling.

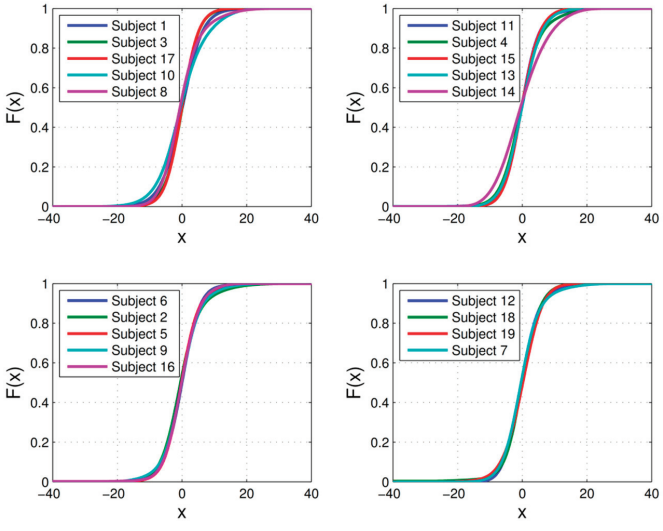

Figure 9. Modeled distribution functions of the patients.

Table 2. Estimated variance and data number used in stochastic modeling.

Patient Name	σ	n
Subject 1	7.75	12731
Subject 2	10.98	13821
Subject 3	12.77	9882
Subject 4	13.97	12062
Subject 5	9.19	13472
Subject 6	8.54	12778
Subject 7	10.52	13417
Subject 8	9.44	13125
Subject 9	11.13	12156
Subject 10	12.75	10243
Subject 11	8.64	13454
Subject 12	8.68	13357
Subject 13	9.61	13399
Subject 14	12.97	12410
Subject 15	6.88	13316
Subject 16	7.70	11677
Subject 17	7.49	13481
Subject 18	11.93	12010
Subject 19	8.07	14070

Finally, 100 variance correction coefficients were calculated for each patient, using the relationship defined in Equation (25).

4.3. Stochastic Model Validation

From the experimental data set (data for validation), the correction coefficients c_n(calculated during the modeling process) and the algorithm proposed in Figure 5, the corrected standard deviation and the expected fetal heart rate were estimated. For the validation process, $N = 5$ clinical studies with $M = 900$ samples per clinical study and β defined with $k = 1$ were considered to determine the minimum percentage of samples that fall within one standard deviation. Table 3 presents the results of

the modeled standard deviation σ, estimated s_n, and corrected $c_n s_n$, and the expected value and $\overline{y}_n$ with samples from five clinical studies for all patients.

Table 3. Expected Value and Standard Deviation Estimation of Fetal Heart Rate.

Patient Name	σ	$\overline{y}_5$	s_2	$c_2 s_2$	s_3	$c_3 s_3$	s_4	$c_4 s_4$	s_5	$c_5 s_5$
Subject 1	7.75	148.6	3.70	7.29	4.51	7.65	4.85	7.54	5.15	7.52
Subject 2	10.98	142.9	5.10	10.23	6.44	10.98	7.23	11.27	7.75	11.37
Subject 3	12.77	157.9	6.23	12.45	7.75	13.24	8.67	13.49	9.14	13.36
Subject 4	13.97	140.7	6.77	13.37	8.31	14.12	9.41	14.61	9.89	14.48
Subject 5	9.19	139.4	4.36	8.68	5.48	9.32	6.02	9.38	6.35	9.32
Subject 6	8.54	140.6	3.99	7.95	4.99	8.51	5.50	8.57	6.05	8.86
Subject 7	10.52	131.6	5.08	10.17	6.31	10.77	7.02	10.93	7.38	10.82
Subject 8	9.44	138.3	4.48	8.92	5.57	9.49	6.31	9.83	6.68	9.80
Subject 9	11.13	139.5	5.25	10.37	6.65	11.27	7.29	11.26	7.89	11.43
Subject 10	12.75	132.9	6.26	12.67	7.78	13.32	8.68	13.56	9.30	13.63
Subject 11	8.64	123.7	4.05	8.03	5.17	8.77	5.68	8.84	6.17	9.02
Subject 12	8.68	135.7	3.96	7.92	5.12	8.70	5.70	8.87	6.07	8.87
Subject 13	9.61	148.0	4.51	9.03	5.67	9.65	6.40	9.93	6.82	9.95
Subject 14	12.97	141.3	6.39	12.72	8.10	13.83	8.96	13.95	9.50	13.92
Subject 15	6.88	129.7	3.14	6.22	3.92	6.68	4.36	6.80	4.58	6.70
Subject 16	7.70	134.2	3.52	7.07	4.42	7.55	4.99	7.76	5.38	7.86
Subject 17	7.49	141.5	3.40	6.82	4.27	7.30	4.72	7.34	5.03	7.35
Subject 18	11.93	132.8	6.04	11.84	7.37	12.49	8.11	12.58	8.59	12.51
Subject 19	8.07	150.6	3.66	7.29	4.67	7.96	5.29	8.26	5.62	8.25

The algorithm in Figure 5, additionally, allows the evaluation of the reliability improvement using the corrected and uncorrected standard deviation (uncertainty). To verify the reliability behavior, the proposed algorithm was executed using two bands level: $\beta = k^2 c_n$ to obtain the corrected reliability value and $\beta = k^2$ to obtain the reliability value without correction. Figure 10 shows the results of the corrected and uncorrected reliability for two clinical studies $n = \sqrt{2}$, Figure 10a, and for five clinical studies $n = 5$, Figure 10b. The reliability increases when considering the corrected standard deviation (uncertainty).

In the case of total ignorance of the system, the Chebyshev inequality indicates that at least $1 - \frac{1}{k^2}$ of the sample, data must be within k standard deviations of the mean, for $k = \sqrt{2}$ for at least 50% of the data, see Figure 10. However, having the distribution function models allow us, in addition to estimating the compensated uncertainty, to know the number of measurements that were within $\sqrt{2}$ standard deviations, which was close to 90%.

The parameter estimator behavior in traditional models [12–14], was performed considering some theoretical distributions [3], and their behavior was evaluated considering finite samples. The problems that arose were that the distributions used were not representative of the applications considered in this work, and the estimator properties within finite time windows depended on the distributions. The method proposed in this work allows defining distributions in practical applications with few samples; that solve the problems presented in classical models.

Reliability determination with few samples could be useful due to the visual analysis of fetal heart rate tracings being subjective and inconsistent [5]. There is disagreement in the clinical decision in fetal heart rate (FHR) classification [7]. A simpler and more objective set of guidelines could provide better reliability [10]. Given the inherent limitations of electronic fetal monitoring technology and of the ability of human beings to characterize fetal heart rate parameters and patterns, the low-reliability degree may represent the best-case scenario of the visual fetal heart rate interpretation reliability [6].

In the international federation of gynecology and obstetrics (FIGO), national institute for health and care (NICE), and American college of obstetrics and gynecology (ACOG) guidelines [8], there are two fundamental parameters to determine normal, suspicious, and pathological patterns. The first is the heart rate baseline, and the other is variability. The method proposed in this work can be applied

directly to a correct estimate of the variability because it includes the specific distribution function of each patient. In the tests analyzed, differences of 10% were found in the estimate (n = 5). According to results, the baseline is not affected by the distribution.

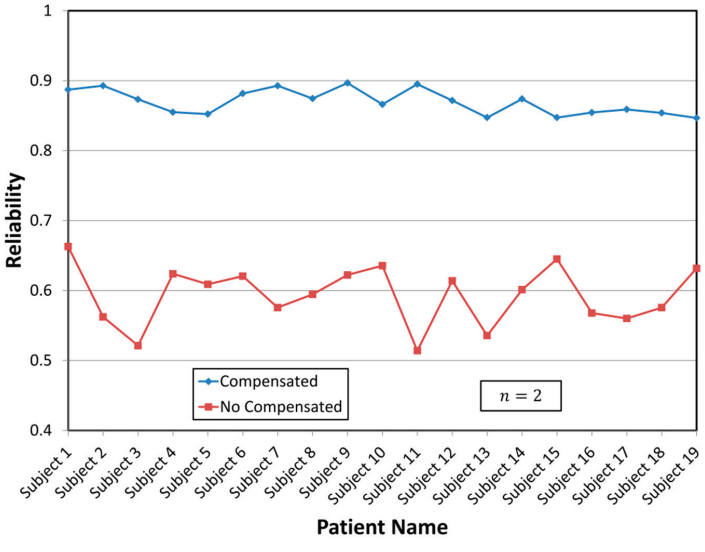

(**a**)

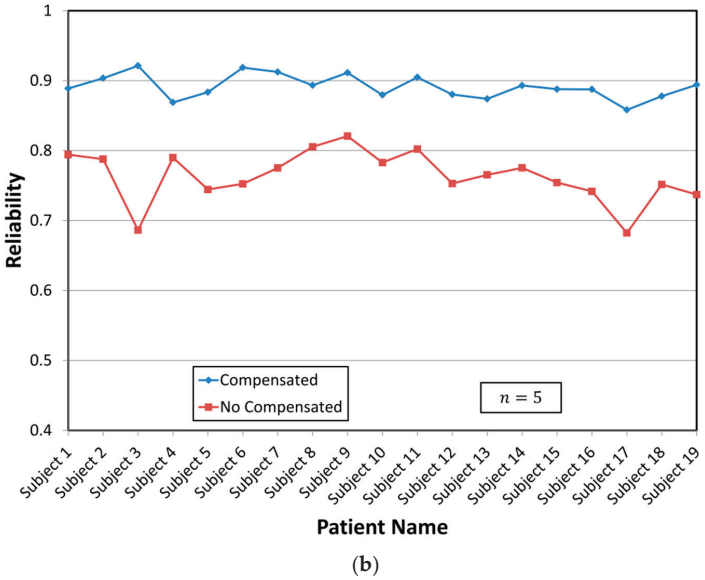

(**b**)

Figure 10. Corrected and uncorrected reliability (R) calculations; (**a**) with two clinical studies; (**b**) with five clinical studies.

5. Conclusions

Reliability has reached an important level for consideration at the beginning of product design, specifically for medical applications, which have been favored by including, as a quality criterion, the reliability level of the device.

Effect analysis of the distribution function and sample lengths in the typical estimators' calculation, mean, and standard deviation were presented. Specific distribution estimates of each patient were used; this procedure suggests a natural way to integrate the additional information obtained in each study. Several studies carried out on patients verified that the real distributions were far from the theoretical distributions that are usually used to determine the estimators' properties. Furthermore, these distributions were used to determine the factors necessary to obtain an unbiased estimator of uncertainty. This information was used to implement a simple algorithm that improves reliability estimation. With the available calculation tool, it is possible to obtain specific information that allows improving the estimators' behavior used in decision making without assuming hypotheses that are difficult to verify in daily applications. Applying classical theory without verifying that hypotheses are met may lead to incorrect results. However, it was demonstrated that these might be corrected by using compensation factors.

Considering how fast available electronic systems for the integration of medical devices change, the way reliability is assessed, restrictions imposed by classical estimation theory, and computer resources, the developed methodology attempts to be the spearhead of a series of works that would lead to a more accurate estimation of reliability.

Author Contributions: Conceptualization, S.A.-M. and R.S.-Z.; methodology, G.R.-L. and S.A.-M.; software, L.B.-R.; validation, G.R.-L., S.A.-M. and R.S.-Z.; formal analysis, R.S.-Z.; investigation, T.S.-J.; resources, S.A.-M.; data curation, R.S.-Z. and L.B.-R.; writing—original draft preparation, G.R.-L.; writing—review and editing, S.A.-M. and T.S.-J.; visualization, G.R.-L.; supervision, T.S.-J.; project administration, S.A.-M.; funding acquisition, S.A.-M. All authors have read and agreed to the published version of the manuscript.

Funding: This work was supported by the FOMIX, Queretaro State Mexico mixed foundation (Grant: QRO-2010-C02-149261).

Acknowledgments: Authors acknowledge Carlos Arturo Rebolledo Fernandez and Julio Cesar Ramirez Arguello for supporting the project logistic.

Conflicts of Interest: The authors declare no conflict of interest.

References

1. Parer, J. Fetal heart-rate monitoring. *Lancet* **1979**, *314*, 632–633. [CrossRef]
2. Yeh, S.-Y.; Diaz, F.; Paul, R.H. Ten-year experience of intrapartum fetal monitoring in Los Angeles County/University of Southern California Medical Center. *Am. J. Obstet. Gynecol.* **1982**, *143*, 496–500. [CrossRef]
3. Vintzileos, A.M.; Antsaklis, A.; Varvarigos, I.; Papas, C.; Sofatzis, I.; Montgomery, J.T. A randomized trial of intrapartum electronic fetal heart rate monitoring versus intermittent auscultation. *Obstet. Gynecol.* **1993**, *81*, 899–907. [PubMed]
4. Alfirevic, Z.; Devane, D.; Gyte, G.M.; Cuthbert, A. Continuous cardiotocography (CTG) as a form of electronic fetal monitoring (EFM) for fetal assessment during labour. *Cochrane Database Syst. Rev.* **2017**. [CrossRef] [PubMed]
5. Ayres-de-Campos, D.; Bernardes, J.; Costa-Pereira, A.; Pereira-Leite, L. Inconsistencies in classification by experts of cardiotocograms and subsequent clinical decision. *Bjog An. Int. J. Obs. Gynaecol.* **1999**, *106*, 1307–1310. [CrossRef] [PubMed]
6. Blackwell, S.C.; Grobman, W.A.; Antoniewicz, L.; Hutchinson, M.; Gyamfi Bannerman, C. Interobserver and intraobserver reliability of the NICHD 3-Tier Fetal Heart Rate Interpretation System. *Am. J. Obstet. Gynecol.* **2011**, *205*, 378. [CrossRef] [PubMed]
7. Chauhan, S.P.; Klauser, C.K.; Woodring, T.C.; Sanderson, M.; Magann, E.F.; Morrison, J.C. Intrapartum nonreassuring fetal heart rate tracing and prediction of adverse outcomes: Interobserver variability. *Am. J. Obs. Gynecol.* **2008**, *199*, 623.e1–623.e5. [CrossRef] [PubMed]

8. Santo, S.; Ayres-de-Campos, D.; Costa-Santos, C.; Schnettler, W.; Ugwumadu, A.; Da Graça, L.M. Agreement and accuracy using the FIGO, ACOG and NICE cardiotocography interpretation guidelines. *Acta Obs. Gynecol. Scand.* **2017**, *96*, 166–175. [CrossRef] [PubMed]
9. Dawes, G.S.; Rosevear, S.K.; Pello, L.C.; Moulden, M.; Redman, C.W.G. Computerized analysis of episodic changes in fetal heart rate variation in early labor. *Am. J. Obs. Gynecol.* **1991**, *165*, 618–624. [CrossRef]
10. Bernardes, J.; Moura, C.; Marques de Sa, J.P.; Pereira Leite, L. The Porto system for automated cardiotocographic signal analysis. *J. Perinat. Med.* **1991**, *19*, 61–65. [CrossRef] [PubMed]
11. Mytton, O.T.; Velazquez, A.; Banken, R.; Mathew, J.L.; Ikonen, T.S.; Taylor, K.; Painter, F.; Jean-Baptiste, R.; Poon, A.; Ruelas, E. Introducing new technology safely. *Qual. Saf. Heal. Care* **2010**, *19*, i9–i14. [CrossRef] [PubMed]
12. Hsieh, D.A.; Manski, C.F. Monte Carlo Evidence on Adaptive Maximum Likelihood Estimation of a Regression. *Ann. Stat.* **1987**, *15*, 541–551. [CrossRef]
13. Spokoiny, V. Parametric estimation. *Finite Sample Theory Ann. Stat.* **2012**, *40*, 2877–2909. [CrossRef]
14. Steigerwald, D.G. On the finite sample behavior of adaptive estimators. *J. Econ.* **1992**, *54*, 371–400. [CrossRef]
15. Yi, X.; Wang, Z.; Caramanis, C.; Liu, H. Optimal linear estimation under unknown nonlinear transform. In *Advances in Neural Information Processing Systems*; Cornell Univ: Ithaca, NY, USA, 2015.
16. Toulis, P.; Airoldi, E.M. Asymptotic and finite-sample properties of estimators based on stochastic gradients. *Ann. Stat.* **2017**, *45*, 1694–1727. [CrossRef]
17. Nitzan, E.; Routtenberg, T.; Tabrikian, J. Cramér-Rao bound for constrained parameter estimation using Lehmann-unbiasedness. *IEEE Trans. Signal Process* **2019**, *67*, 753–768. [CrossRef]
18. Siju, K.C.; Kumar, M. Bayesian estimation of reliability using time-to-failure distribution of parametric degradation models. *J. Stat. Comput. Simul.* **2018**, *88*, 1717–1748. [CrossRef]
19. *Evaluation of Measurement Data—Guide to the Expression of Uncertainty in Measurement, Joint Committee for Guides in Metrology 100*, 1st ed.; 2008; Available online: https://www.bipm.org/utils/common/documents/jcgm/JCGM_100_2008_E.pdf (accessed on 8 May 2020).
20. Shiryaev, A.N. *Probability*; Springer: New York, NY, USA, 1996; Volume 95. [CrossRef]
21. Lira, I.; Taylor, J.R. Evaluating the Measurement Uncertainty: Fundamentals and Practical Guidance. *Am. J. Phys.* **2003**, *71*, 93–94. [CrossRef]
22. Cramer, H. *Mathematical Methods of Statistics*; Princeton University Press: Princeton, NJ, USA, 1999; Volume 34. [CrossRef]
23. Ljung, L. *System Identification: Theory for the User*, 2nd ed.; Preniice Hall: Upper Saddle River, NJ, USA, 1999.
24. Ikonen, E.; Najim, K. *Advanced Process Identification and Control*; CRC Press: Hoboken, NJ, USA, 2001. [CrossRef]
25. Amidan, B.G.; Ferryman, T.A.; Cooley, S.K. Data outlier detection using the Chebyshev theorem. In Proceedings of the, Big Sky, MT, USA, 5–12 March 2005. [CrossRef]
26. Quarteroni, A.; Saleri, F.; Gervasio, P. *Scientific Computing with MATLAB and Octave*; Springer: Berlin/Heidelberg, Germany, 2014; Volume 2. [CrossRef]

applied sciences

MDPI

Article

Clinical Evaluation of Stretchable and Wearable Inkjet-Printed Strain Gauge Sensor for Respiratory Rate Monitoring at Different Body Postures

Ala'aldeen Al-Halhouli [1,2,3,*], Loiy Al-Ghussain [1,4], Saleem El Bouri [1], Fuad Habash [1], Haipeng Liu [5,6] and Dingchang Zheng [6]

1 Mechatronics Engineering Department/NanoLab, School of Applied Technical Sciences, German Jordanian University, P.O. Box 35247, Amman 11180, Jordan; loiy.al-ghussain@uky.edu (L.A.-G.); saleem.bouri@hotmail.com (S.E.B.); f.habash@gju.edu.jo (F.H.)
2 Institute of Microtechnology, Technische Universität Braunschweig, 38124 Braunschweig, Germany
3 Faculty of Engineering, Middle East University, Amman 11831, Jordan
4 Mechanical Engineering Department, University of Kentucky, Lexington, KY 40506, USA
5 Medical Device and Technology Research Laboratory, School of Allied Health, Faculty of Health, Education, Medicine and Social Care, Anglia Ruskin University, Chelmsford CM1 1SQ, UK; haipeng.liu@anglia.ac.uk
6 Research Centre of Intelligent Healthcare, Faculty of Health and Life Science, Coventry University, Coventry CV1 5FB, UK; dingchang.zheng@coventry.ac.uk
* Correspondence: alaaldeen.alhalhouli@gju.edu.jo

Received: 21 November 2019; Accepted: 11 December 2019; Published: 9 January 2020

Abstract: Respiratory rate (RR) is a vital sign with continuous, convenient, and accurate measurement which is difficult and still under investigation. The present study investigates and evaluates a stretchable and wearable inkjet-printed strain gauge sensor (IJP) to estimate the RR continuously by detecting the respiratory volume change in the chest area. As the volume change could cause different strain changes at different body postures, this study aims to investigate the accuracy of the IJP RR sensor at selected postures. The evaluation was performed twice on 15 healthy male subjects (mean ± SD of age: 24 ± 1.22 years). The RR was simultaneously measured in breaths per minute (BPM) by the IJP RR sensor and a reference RR sensor (e-Health nasal thermal sensor) at each of the five body postures namely standing, sitting at 90°, Flower's position at 45°, supine, and right lateral recumbent. There was no significant difference in measured RR between IJP and reference sensors, between two trials, or between different body postures (all $p > 0.05$). Body posture did not have any significant effect on the difference of RR measurements between IJP and the reference sensors (difference <0.01 BPM for each measurement in both trials). The IJP sensor could accurately measure the RR at different body postures, which makes it a promising, simple, and user-friendly option for clinical and daily uses.

Keywords: inkjet printing; respiratory rate; strain gauge; stretchable and wearable sensors; silver nanoparticles; clinical evaluation; body posture

1. Introduction

Clinically, respiratory rate (RR), defined as the times of breath per minute (BPM), is a vital sign whose abnormality could indicate various pathological conditions in cardiorespiratory system [1,2]. Compared with other vital signs such as heart rate and blood pressure, RR is more accurate in screening unstable patients [1,3,4]. Therefore, RR monitoring has been used in detecting sleep apnea, cardiac arrest, and sudden infant death syndrome [3,5]. Especially, compared with discrete RR measurement, continuous RR monitoring could detect RR abnormalities with more than 10 times of accuracy [2].

However, despite the clinical significance of RR, continuous, convenient, and accurate RR monitoring is still difficult. It was reported in [2] that the RR was the least documented vital sign even when the patients suffered from respiratory issues. Manual RR counting is widely used in clinical examination [3] but is not accurate [2]. Other traditional techniques of clinical RR monitoring include spirometry, pneumotachograph, and capnography [1,4,6]. These techniques could accurately measure RR, but are cumbersome, difficult to manipulate, or mask-based [4].

To achieve continuous and convenient RR monitoring, some new techniques have been developed [7–10]. Some researchers extract RR from other physiological signals such as photoplethysmogram and electrocardiogram [11]. Other studies derived respiration signals using non-contact techniques such as C-band sensing [12] and dual smartphone cameras [4]. Some researchers tried distant (less than 10 m) RR detecting based on Wi-Fi, radar, or thermal imaging [11]. Compared with these techniques, wearable and stretchable sensors could independently measure RR without limiting the daily activities of the users. Additionally, the stretchable and wearable sensors could achieve highly accurate RR measurement at a low cost [13].

For a wearable RR sensor, the high accuracy at different body postures could enable its application in various clinical and daily situations. Several studies [3,12,14] have investigated the accuracy of RR monitoring devices at different body postures (sitting, standing and supine and side). For instance, Huang et al. [3] embedded arrays of load sensors in an e-textile bed sheet to measure RR from the full body pressure distribution on the sheet. The sensor was tested on 14 human subjects in prone, side and supine postures during sleep. The results showed that RR measurement was more accurate in prone and supine postures compared with side posture. The authors deduced that this difference was due to the amplitude of respiratory movement which is more prominent in thoracic and abdominal areas than on both sides. Zhu et al. [14] developed a fiber bragg grating (FBG) sensor mat with three FBG arrays under the pillow, below upper chest, and below lower chest. The sensor was tested on 12 human subjects while lying in prone and side postures. For each of the three sensors, the mean error of RR measurement was lower than one BPM with standard deviation (STD) within ±0.25 BPM, compared with the reference RR measured by a polysomnography belt sensor. Guan et al. [12] developed a wireless system to measure RR based on C-band sensing. In prone, sitting, and standing postures, the error of RR detection was within 7%, 6.2% and 5.5% compared with a reference RR sensor. The author suggested that standing posture have the largest influence on the quality of C-band RR detection. Nam et al. [4] used dual cameras on a smartphone to measured RR by reflectance imaging on the chest and the abdomen, with average median error of 1.43% and 1.62%.

The majority of existing studies on the effect of body posture on RR detection accuracy were based on non-stretchable [15–17] or non-wearable RR sensors [3,12,14], with a lack of related study based on stretchable RR sensors. Compared with traditional RR sensors, stretchable RR sensors are in direct contact with body surface, and are therefore, more likely to be influenced by body posture. Considering the increasing amount of stretchable RR sensors and the possibility of application in different scenarios, there is an urgent need to investigate the effect of body posture on the accuracy of stretchable RR sensors.

The aim of this paper is to investigate the effect of different body postures (standing, sitting at 90°, Flower's position at 45°, supine and right lateral recumbent) on the accuracy of a new stretchable and wearable inkjet-printed RR sensor.

2. Methods

2.1. Physiological Measurements

2.1.1. Subjects

Fifteen healthy male subjects (mean ± SD of age: 24 ± 1.22 years) without any known cardiovascular or respiratory diseases participated in this study with written informed consent. The protocol adhered

to the tenets of the Declaration of Helsinki. Before the experiment, the procedure was explained in detail to each subject.

2.1.2. Sensors

Inkjet printing (IJP) is a promising technology in the fabrication of stretchable and wearable sensors. Compared with other fabrication techniques, IJP has less sophisticated process and lower cost [18–21]. The IJP RR sensor was fabricated on polydimethylsiloxane (PDMS) substrate using conductive silver nanoparticle ink, as shown in Figure 1a which was presented in [22]. During respiration, the sensor acted as a variable resistance whose value increased during inhalation and decreased during exhalation, due to the volume change in the ribcage or the abdomen. The change in resistance was obtained by a Wheatstone bridge circuit with three fixed resistances, amplified by an instrumentational amplifier, and finally fed into an Arduino microcontroller to derive RR.

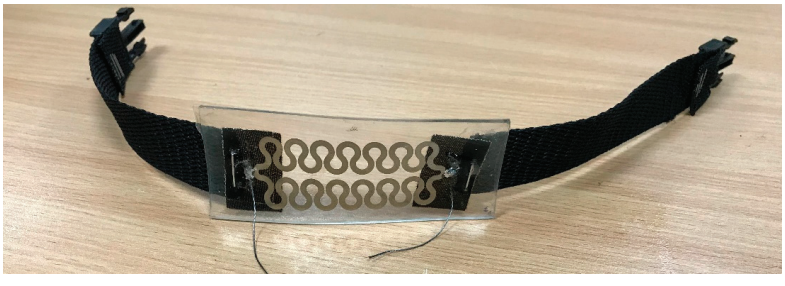

(**a**)

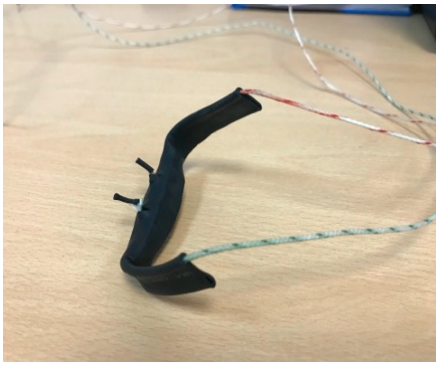

(**b**)

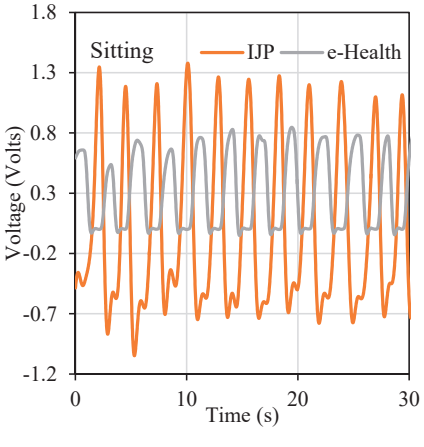

(**c**)

Figure 1. (**a**) The Inkjet printing (IJP) respiration rate (RR) sensor. (**b**) The reference e-Health RR sensor. (**c**) The derived respiratory signals in 30s.

The reference RR value was measured by a thermal nasal e-Health sensor (e-Health AirFlow sensor, Cooking Hacks), shown in Figure 1b, which has been validated previously in the literature [23,24]. The e-Health sensor detects the thermal changes in airflow during inhalation and exhalation. Due to the difference in working principle between IJP and reference RR sensors, their respiratory signals fluctuated in opposite directions with a phase shift, as shown in Figure 1c.

2.1.3. Measurement Procedure

During the measurement, the IJP sensor was mounted at the xiphoid process using adjustable fabric belt with e-Health sensor mounted at the nostril as shown in Figure 2. The IJP sensor was tested at five different body postures in randomized order: sitting at 90°, 45° Fowler's position, standing, supine, and right lateral recumbent, as shown in Figure 3. In the lateral recumbent, Flower's position and supine, the test subjects had their heads resting on a pillow. Only the right lateral recumbent was included without the left one, because the bilateral respiratory movements have been proved to be similar [25]. At each posture, the test was repeated twice in order to investigate the repeatability. The RR recording lasted for one minute in each trial, with a 60 s break between the two trials. The test subjects were asked not to move during the test and to breathe normally.

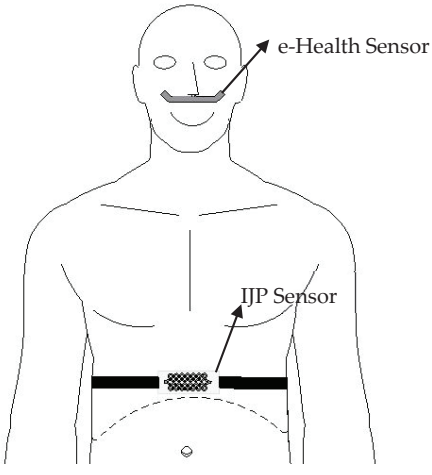

Figure 2. Mounting the IJP sensor at the xiphoid process using adjustable belt and the e-Health sensor at nostril.

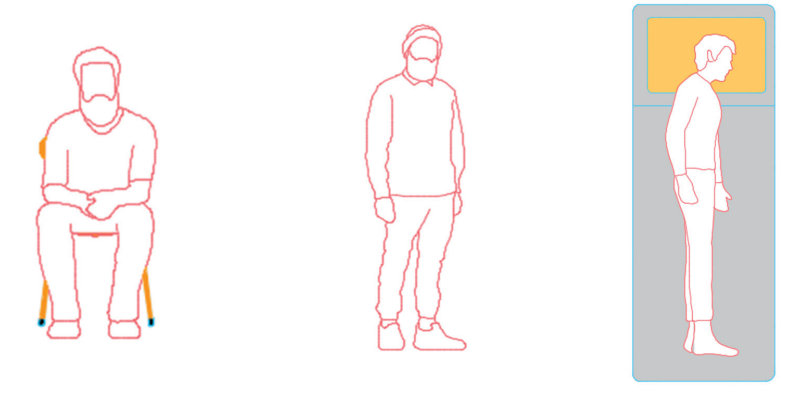

Figure 3. *Cont.*

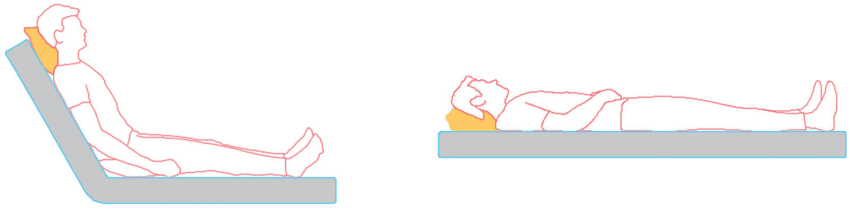

Figure 3. The RR measurement at different body postures.

2.2. Respiratory Rate Derivation

An algorithm was developed on MATLAB (R2018b, MathWorks Inc., Natick, MA, USA) to extract the RR values from the respiratory signals. Firstly, raw data were input into the bridge circuit at a sampling frequency of 100 Hz. The signal was then filtered to remove the direct current (DC) component and some extremely high and low frequencies using a band-pass filter with lower and higher cut-off frequencies of 0.05 Hz and 1.5 Hz. Finally, fast Fourier transform (FFT) was used to determine the respiration frequency, which is the frequency with the highest amplitude. RR was derived as: RR = 60 × respiratory frequency. Figure 4 shows the derivation procedure of the RR from the IJP sensor. Note in Figure 4 that the sharp peak is considered as noise since it exceeds the amplitudes of adjacent respiratory cycles with time period of less than 0.1 s, which is impossible for a respiratory cycle even for maximum inhalation or exhalation [11].

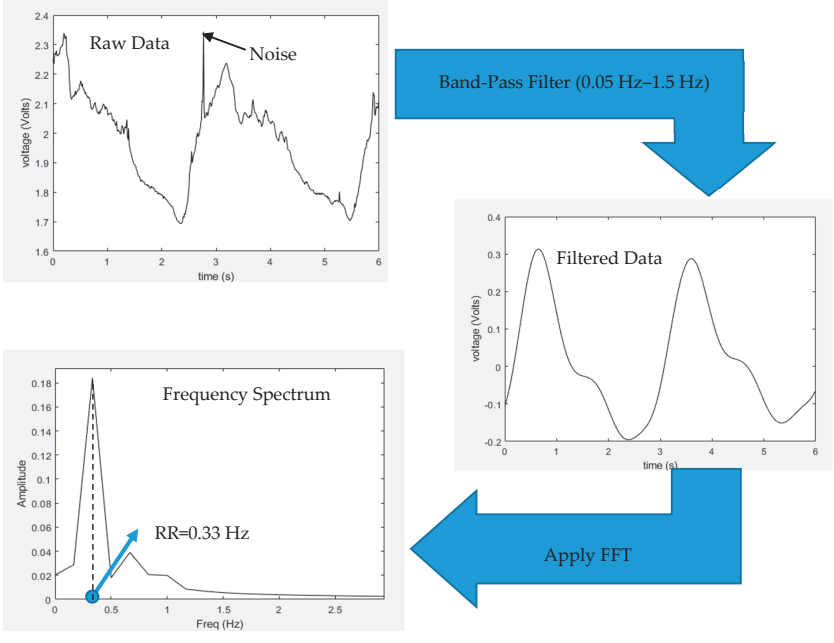

Figure 4. RR derivation flow chart from the IJP sensor. The raw data was input into band-pass filter to filter out the high frequencies and the noise. The RR was then extracted by Simulink (R2018b, MathWorks Inc., Natick, MA, USA). The arrow in the first subfigure shows the spike caused by noise.

2.3. Statistical Analysis

The statistical analysis was performed on SPSS (Version 20, SPSS Inc., Chicago, IL, USA). Firstly, to investigate if the RR measurement was significantly influenced by body postures, repeated trials, and different sensors, analysis of variance (ANOVA) was performed with Levene's test to validate the homogeneity of variance. Significance was defined as p-value less than 0.05. To further investigate the effect of body posture on the measurement accuracy, the difference between RR values derived by IJP sensor and reference sensor was calculated for each measurement in different postures. Moreover, post hoc test based on Tukey's test was used to evaluate the statistical significance of the RR between any two postures to figure out the effect of the posture on the RR.

3. Results

As shown in Figure 5, in each trial and posture, IJP and reference RR sensors derived nearly identical distributions of RR. The details are listed in Table A1, Appendix A. The Levene's test showed that the dataset satisfied the homogeneity of variance ($p > 0.05$). Hence, ANOVA was performed on RR values. The results showed no significant differences in measured RR between IJP and reference sensors, between two measurement trials, and among different body postures (all $p > 0.05$). Moreover, post hoc test showed no significant difference in the RR between any two posture (all $p > 0.05$).

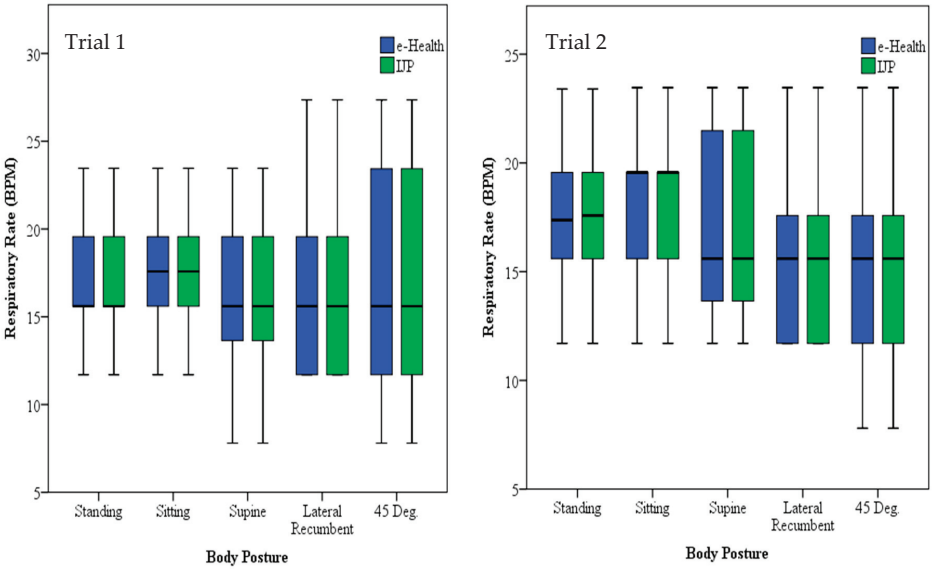

Figure 5. Box and whisker plots of the RR measured by the IJP sensor and the e-Health sensor for each trial at different body postures. The means are represented by the horizontal lines within the boxes while the first and third quartiles are represented by the boxes boundaries whereas the maximum and minimum values are represented by the whiskers.

4. Discussion

4.1. IJP Sensor Accuracy: Comparison with Other Sensors

The ANOVA results showed that IJP sensor had high accuracy, good repeatability, and stability at different body postures. With no observable deviation from the reference sensor at all body postures, the accuracy of the IJP sensor was better than many sensors reported in the literature where the RR

measured by stretchable sensor deviated from the reference value from 1.7% to more than 6% in different postures [4,12,26–30].

4.2. RR Measurements at Different Body Postures

The body posture could significantly influence the lung volume [12,31–33] and the consequent RR detection. The lung has the largest volume capacity at the sitting posture [31]. In lateral recumbent posture, lung and chest wall compliances decrease, which limits the amplitude of thoracic respiration movement [25]. Small respiratory movement amplitude could result in miscounting of RR. In stretchable RR sensors, due to the difference in strain between different postures, the accuracy of RR could be different.

However, in this study, IJP sensor showed high accuracy at different postures. Firstly, the skin-like characteristics of the PDMS surface allow the IJP sensor to closely attach to the body surface and follow the topographical changes [34,35]. Secondly, the polymer-based strain gauge sensors are very sensitive (gauge factor > 100) compared with typical strain gauge ($2 \leq$ gauge factor ≤ 5). Thirdly, silver nanoparticles are highly sensitive which increased the accuracy of the IJP sensor [36]. Finally, during the measurement, test subjects did not move, talk or laugh, which largely reduced the movement artefact in respiratory signals.

4.3. Application of the IJP Sensor

In addition to its accuracy, the IJP sensor is a low-cost sensor with skin-like characteristics that enhances the wearability of the sensor without limiting the daily activities of the patients. All the aforementioned characteristics of the IJP sensor makes it suitable for remote and continuous RR monitoring in low-resources settings and refugee camps, decreasing the pressure on the healthcare facilities in these settings which suffer from limited healthcare resources [37]. Continuous RR measurement in different postures is clinically significant especially for the monitoring of hospitalized patients. Currently, the RR monitoring relies on inaccurate manual counting in a short period (often 30 s or 1 min) or is neglected [38]. The mask-based or contact RR sensors, such as the e-Health sensor in this study, could cause uncomfortableness which makes them inappropriate for long-term continuous RR monitoring. The IJP sensor could accurately and continuously measure RR without any skin allergy or other clinical events, which makes it possible for clinical use. RR measurement at different body postures is important for patients with different physiological conditions. For example, some patients under physiotherapy or with plastic cast need to keep in mainly supine or lateral recumbent postures. Therefore, the IJP sensor provides the possibility of continuous RR monitoring in different patients.

The IJP RR sensor is also applicable for RR monitoring at home without disturbing the users' daily activities. Wearable sensors could provide RR monitoring during the night at the supine and lateral position to inspect the sleep quality and contribute in early diagnostic of several sleep-related issues such as sleep apnea and insomnia [39]. Moreover, such wearable sensors could be used to reduce sudden infant death syndrome by providing comfortable and continuous RR monitoring [40]. Additionally, wearable sensors can be integrated into safety belts in automobiles which eases the monitoring of the RR during driving [11,41]. The IJP sensor accurately measured the RR at all the inspected postures which paved the way for its further application in daily life.

4.4. Limitations and Future Work

The evaluation of the sensor was performed on 15 healthy male subjects only. Firstly, scale-up validation was needed. Secondly, to eliminate the error caused by movement artefact, the IJP sensor was firmly fixed on the xiphoid process. In different body positions, the sensitivity to posture change might be different, which needs further investigation. Thirdly, the evaluation of wider age groups and genders could be performed to investigate if the IJP sensor is suitable for people with different physiological conditions. Furthermore, the study was performed on healthy subjects. The performance of the sensor on subjects with pathological conditions needs further investigation. The IJP sensor is a

low-cost and wearable sensor that provides the possibility of daily RR monitoring. However, motion artefact is a major concern regarding the accuracy of RR monitoring during daily activities [11]. For the further application especially in daily healthcare monitoring, full validation on different levels of motion artefact is needed. Finally, more comfortable mounting mechanism such as the use of biocompatible and skin-friendly adhesive should be investigated.

5. Conclusions

The IJP sensor was able to measure the RR accurately at the five postures (standing, sitting at 90°, Flower's position at 45°, supine and right lateral recumbent), with good repeatability which makes it user-friendly, and very convenient for clinical practices with minimal user efforts and training needs. This IJP sensor is promising for continuous RR monitoring in different clinical and daily situations.

Author Contributions: Conceptualization, A.A.-H., L.A.-G., S.E.B., H.L., and D.Z.; methodology, L.A.-G., H.L., and D.Z.; software, S.E.B..; validation, S.E.B., L.A.-G. and F.H.; formal analysis, L.A.-G., S.E.B., H.L.; investigation, L.A.-G.; resources, A.A.-H., D.Z.; data curation, S.E.B. and F.H.; writing—original draft preparation, L.A.-G., S.E.B.; writing—review and editing, L.A.-G., H.L., A.A.-H.; visualization, L.A.-G.; supervision L.A.-G., H.L., D.Z. and A.A.-H.; project administration, A.A.-H. and L.A.-G.; funding acquisition, A.A.-H. and D.Z. All authors have read and agreed to the published version of the manuscript.

Funding: This research was funded by the Royal Academy of Engineering under grant Ref. IAPP1R2\100204.

Acknowledgments: The authors would like to thank the Royal Academy of Engineering for Funding this project under grant Ref. IAPP1R2\100204. Moreover, the authors would like to thank the Industrial Research and Development Fund in the Higher Council for Science and Technology for their support of the project. In addition, the authors would like to thank Eng. Ali Al-Ghussein from the GJU Innovation and Entrepreneurship laboratory for providing the e-Health sensor.

Conflicts of Interest: The authors declare no conflict of interest.

Appendix A

Table A1. Average RR (breaths per minute, BPM) measured by the IJP and e-Health sensors at five different body postures.

Gender	Age	Standing		Sitting		45 Deg.		Supine		Lateral	
		Our	Ref	Our	Ref	Our	Ref	Our	Ref	Our	Ref
M	24	11.7	11.7	13.65	13.65	11.7	11.7	15.6	15.6	11.7	11.7
M	23	21.51	21.51	21.51	21.51	17.58	17.58	19.56	19.56	23.46	23.46
M	25	21.48	21.48	21.51	21.51	23.46	23.46	21.51	21.51	19.56	19.56
M	25	19.56	19.56	19.56	19.56	17.58	17.58	15.63	15.63	15.6	15.6
M	23	17.58	17.58	21.51	21.51	13.65	13.65	21.51	21.51	17.58	17.58
M	24	15.6	15.6	13.65	13.65	11.7	11.7	13.65	13.65	11.7	11.7
M	24	13.65	13.65	13.65	13.65	9.75	9.75	9.75	9.75	11.7	11.7
M	23	23.4	23.4	23.4	23.4	23.4	23.4	23.4	23.4	23.4	23.4
M	26	15.6	15.6	17.58	17.58	15.6	15.6	15.6	15.6	17.58	17.58
M	21	19.56	19.35	19.56	19.56	21.51	21.51	19.56	19.56	19.56	19.56
M	25	17.58	17.58	19.56	19.56	19.53	19.53	17.58	17.58	15.6	15.6
M	24	23.46	23.46	29.31	29.31	23.46	23.46	23.46	23.46	19.53	19.53
M	24	7.8	7.8	9.75	9.75	9.75	9.75	11.7	11.7	11.7	11.7
M	22	15.6	15.6	15.6	15.6	11.7	11.7	9.75	9.75	11.7	11.7
M	24	17.58	17.58	17.58	17.58	15.6	15.6	15.6	15.6	13.65	13.65

References

1. AL-Khalidi, F.Q.; Saatchi, R.; Burke, D.; Elphick, H.; Tan, S. Respiration rate monitoring methods: A review. *Pediatr. Pulmonol.* **2011**, *46*, 523–529. [CrossRef] [PubMed]
2. Lee, P.J. Clinical evaluation of a novel respiratory rate monitor. *J. Clin. Monit. Comput.* **2016**, *30*, 175–183. [CrossRef] [PubMed]

3. Huang, M.; Xu, W.; Liu, J.; Samy, L.; Vajid, A.; Alshurafa, N.; Sarrafzadeh, M. Inconspicuous on-bed respiratory rate monitoring. In Proceedings of the 6th International Conference on PErvasive Technologies Related to Assistive Environments, Rhodes, Greece, 29–31 May 2013; ACM Press: New York, NY, USA, 2013; pp. 1–8.
4. Nam, Y.; Kong, Y.; Reyes, B.; Reljin, N.; Chon, K.H. Monitoring of Heart and Breathing Rates Using Dual Cameras on a Smartphone. *PLoS ONE* **2016**, *11*, e0151013. [CrossRef]
5. Sharma, H.; Sharma, K.K. ECG-derived respiration using Hermite expansion. *Biomed. Signal Process. Control* **2018**, *39*, 312–326. [CrossRef]
6. Di Fiore, J.M. Neonatal cardiorespiratory monitoring techniques. *Semin. Neonatol.* **2004**, *9*, 195–203. [CrossRef] [PubMed]
7. Koch, E.; Dietzel, A. Stretchable sensor array for respiratory monitoring. In Proceedings of the 2017 19th International Conference on Solid-State Sensors, Actuators and Microsystems (TRANSDUCERS), Kaohsiung, Taiwan, 18–22 June 2017; pp. 2227–2230.
8. Jeong, J.W.; Jang, Y.W.; Lee, I.; Shin, S.; Kim, S. Wearable Respiratory Rate Monitoring using Piezo-resistive Fabric Sensor. In *World Congress on Medical Physics and Biomedical Engineering, 7–12 September 2009, Munich, Germany*; Dössel, O., Schlegel, W.C., Eds.; Springer: Berlin/Heidelberg, Germany, 2009; pp. 282–284. ISBN 978-3-642-03904-1.
9. Ciocchetti, M.; Massaroni, C.; Saccomandi, P.; Caponero, M.; Polimadei, A.; Formica, D.; Schena, E. Smart Textile Based on Fiber Bragg Grating Sensors for Respiratory Monitoring: Design and Preliminary Trials. *Biosensors* **2015**, *5*, 602–615. [CrossRef] [PubMed]
10. Chu, M.; Nguyen, T.; Pandey, V.; Zhou, Y.; Pham, H.N.; Bar-Yoseph, R.; Radom-Aizik, S.; Jain, R.; Cooper, D.M.; Khine, M. Respiration rate and volume measurements using wearable strain sensors. *NPJ Digit. Med.* **2019**, *2*, 8. [CrossRef]
11. Liu, H.; Allen, J.; Zheng, D.; Chen, F. Recent development of respiratory rate measurement technologies. *Physiol. Meas.* **2019**, *40*, 07TR01. [CrossRef]
12. Guan, H.; Yang, X.; Sun, W.; Ren, A.; Fan, D.; Zhao, N.; Guan, L.; Haider, D.; Abbasi, Q. Posture-Specific Breathing Detection. *Sensors* **2018**, *18*, 4443. [CrossRef]
13. Furtak, N.T.; Skrzetuska, E. Development of Screen-Printed Breathing Rate Sensors. *FIBRES Text. East. Eur.* **2013**, *6*, 84–88.
14. Zhu, Y.; Maniyeri, J.; Fook, V.F.S.; Zhang, H. Estimating respiratory rate from FBG optical sensors by using signal quality measurement. In Proceedings of the 2015 37th Annual International Conference of the IEEE Engineering in Medicine and Biology Society (EMBC), Milan, Italy, 25–29 August 2015; pp. 853–856.
15. Wu, D.; Wang, L.; Zhang, Y.; Huang, B.; Wang, B.; Lin, S.; Xu, X. A wearable respiration monitoring system based on digital respiratory inductive plethysmography. In Proceedings of the 2009 Annual International Conference of the IEEE Engineering in Medicine and Biology Society, Minneapolis, MN, USA, 3–6 September 2009; pp. 4844–4847.
16. Hesse, M.; Christ, P.; Hormann, T.; Ruckert, U. A respiration sensor for a chest-strap based wireless body sensor. In Proceedings of the IEEE SENSORS 2014 Proceedings, Valencia, Spain, 2–5 November 2014; pp. 490–493.
17. Sun, X.; Qiu, L.I.; Wu, Y.; Tang, Y.; Cao, G.; State, T.P. SleepMonitor: Monitoring Respiratory Rate and Body Position During Sleep Using Smartwatch. *PACM Interact. Mob. Wearable Ubiquitous Technol.* **2017**, *13*, 104. [CrossRef]
18. Al-Halhouli, A.; Qitouqa, H.; Alashqar, A.; Abu-Khalaf, J. Inkjet printing for the fabrication of flexible/stretchable wearable electronic devices and sensors. *Sens. Rev.* **2018**, *38*, 438–452. [CrossRef]
19. Abu-Khalaf, J.; Al-Ghussain, L.; Al-Halhouli, A. Fabrication of Stretchable Circuits on Polydimethylsiloxane (PDMS) Pre-Stretched Substrates by Inkjet Printing Silver Nanoparticles. *Materials* **2018**, *11*, 2377. [CrossRef] [PubMed]
20. Abu-khalaf, J.M.; Saraireh, R.; Eisa, S.M.; Al-halhouli, A. Experimental Characterization of Inkjet-Printed Stretchable Circuits for Wearable Sensor Applications. *Sensors* **2018**, *18*, 3476. [CrossRef] [PubMed]
21. Abu-khalaf, J.M.; Al-Ghussain, L.; Nadi, A.; Saraireh, R.; Rabayah, A.; Altarazi, S.; Al-Halhouli, A. Optimization of Geometry Parameters of Inkjet-Printed Silver Nanoparticle Traces on PDMS Substrates Using Response Surface Methodology. *Materials* **2019**, *12*, 3329. [CrossRef]

22. Al-Halhouli, A.; Al-Ghussain, L.; El Bouri, S.; Liu, H.; Zheng, D. Fabrication and Evaluation of a Novel Non-Invasive Stretchable and Wearable Respiratory Rate Sensor Based on Silver Nanoparticles Using Inkjet Printing Technology. *Polymers* **2019**, *11*, 1518. [CrossRef]
23. Bayo-Monton, J.L.; Martinez-Millana, A.; Han, W.; Fernandez-Llatas, C.; Sun, Y.; Traver, V. Wearable Sensors Integrated with Internet of Things for Advancing eHealth Care. *Sensors* **2018**, *18*, 1851. [CrossRef]
24. Rákay, R.; Višňovský, M.; Galajdová, A.; Šimšík, D. Testing Properties of E-health System Based on Arduino. *J. Autom. Control.* **2015**, *3*, 122–126.
25. Mezidi, M.; Guérin, C. Effects of patient positioning on respiratory mechanics in mechanically ventilated ICU patients. *Ann. Transl. Med.* **2018**, *6*, 384. [CrossRef]
26. Turnbull, H.; Kasereka, M.C.; Amirav, I.; Sahika, S.E.; Solomon, I.; Aldar, Y.; Hawkes, M.T. Development of a novel device for objective respiratory rate measurement in low-resource settings. *BMJ Innov.* **2018**, *4*, 185–191. [CrossRef]
27. Jarchi, D.; Salvi, D.; Tarassenko, L.; Clifton, D. Validation of Instantaneous Respiratory Rate Using Reflectance PPG from Different Body Positions. *Sensors* **2018**, *18*, 3705. [CrossRef] [PubMed]
28. Van Loon, K.; Breteler, M.J.M.; van Wolfwinkel, L.; Rheineck Leyssius, A.T.; Kossen, S.; Kalkman, C.J.; van Zaane, B.; Peelen, L.M. Wireless non-invasive continuous respiratory monitoring with FMCW radar: A clinical validation study. *J. Clin. Monit. Comput.* **2016**, *30*, 797–805. [CrossRef] [PubMed]
29. Guechi, Y.; Pichot, A.; Frasca, D.; Rayeh-Pelardy, F.; Lardeur, J.-Y.; Mimoz, O. Assessment of noninvasive acoustic respiration rate monitoring in patients admitted to an Emergency Department for drug or alcoholic poisoning. *J. Clin. Monit. Comput.* **2015**, *29*, 721–726. [CrossRef] [PubMed]
30. Shen, C.-L.; Huang, T.-H.; Hsu, P.-C.; Ko, Y.-C.; Chen, F.-L.; Wang, W.-C.; Kao, T.; Chan, C.-T. Respiratory Rate Estimation by Using ECG, Impedance, and Motion Sensing in Smart Clothing. *J. Med. Biol. Eng.* **2017**, *37*, 826–842. [CrossRef] [PubMed]
31. Moreno, F.; Lyons, H.A. Effect of body posture on lung volumes. *J. Appl. Physiol.* **2017**, *16*, 27–29. [CrossRef] [PubMed]
32. Leipälä, J.A.; Bhat, R.Y.; Rafferty, G.F.; Hannam, S.; Greenough, A. Effect of posture on respiratory function and drive in preterm infants prior to discharge. *Pediatr. Pulmonol.* **2003**, *36*, 295–300. [CrossRef] [PubMed]
33. Pal, A.K. Effect of Recumbent Body Positions on Dynamic Lung Function Parameters in Healthy Young Subjects. *J. Clin. Diagn. Res.* **2017**, *11*, CC08. [CrossRef]
34. Sun, J.; Jiang, J.; Bao, B.; Wang, S.; He, M.; Zhang, X.; Song, Y. Fabrication of Bendable Circuits on a Polydimethylsiloxane (PDMS) Surface by Inkjet Printing Semi-Wrapped Structures. *Materials* **2016**, *9*, 253. [CrossRef]
35. Nag, A.; Afasrimanesh, N.; Feng, S.; Mukhopadhyay, S.C. Strain induced graphite/PDMS sensors for biomedical applications. *Sensors Actuators A Phys.* **2018**, *271*, 257–269. [CrossRef]
36. Amjadi, M.; Kyung, K.-U.; Park, I.; Sitti, M. Stretchable, Skin-Mountable, and Wearable Strain Sensors and Their Potential Applications: A Review. *Adv. Funct. Mater.* **2016**, *26*, 1678–1698. [CrossRef]
37. Al-Rousan, T.; Schwabkey, Z.; Jirmanus, L.; Nelson, B.D. Health needs and priorities of syrian refugees in camps and urban settings in jordan: Perspectives of refugees and health care providers | Besoins et priorités sanitaires des réfugiés syriens dans les camps et en milieu urbain en jordanie: Perspectives de. *East. Mediterr. Health J.* **2018**, *24*, 243–253. [CrossRef] [PubMed]
38. Kelly, C. Respiratory rate 1: Why measurement and recording are crucial. *Nurs. Times* **2018**, *114*, 23–24.
39. Kwak, Y.H.; Kim, J.; Kim, K. Sleep monitoring sensor using flexible metal strain gauge. *Jpn. J. Appl. Phys.* **2018**, *57*, 05GD03. [CrossRef]
40. Mathew, J.; Semenova, Y.; Farrell, G. A miniature optical breathing sensor. *Biomed. Opt. Express* **2012**, *3*, 3325. [CrossRef] [PubMed]
41. Hamdani, S.; Fernando, A. The Application of a Piezo-Resistive Cardiorespiratory Sensor System in an Automobile Safety Belt. *Sensors* **2015**, *15*, 7742–7753. [CrossRef]

applied sciences

MDPI

Article

An Automated Data Acquisition System for Pinch Grip Assessment Based on Fugl Meyer Protocol: A Feasibility Study

Abdallah Alsayed [1,*], Raja Kamil [1,2,*], Hafiz Ramli [1] and Azizan As'arry [3]

[1] Department of Electrical and Electronic Engineering, Faculty of Engineering, Universiti Putra Malaysia, Serdang 43400, Selangor, Malaysia; hrhr@upm.edu.my
[2] Laboratory of Computational Statistics and Operations Research, Institute for Mathematical Research, Universiti Putra Malaysia, Serdang 43400, Selangor, Malaysia
[3] Department of Mechanical and Manufacturing Engineering, Faculty of Engineering, Universiti Putra Malaysia, Serdang 43400, Selangor, Malaysia; zizan@upm.edu.my
* Correspondence: eng.abdallah.2013@gmail.com (A.A.); kamil@upm.edu.my (R.K.); Tel.: +6-03-9769-4360 (R.K.)

Received: 27 February 2020; Accepted: 28 March 2020; Published: 15 May 2020

Featured Application: This work was conducted to develop an automated data acquisition system to monitor the pinch grip in rehabilitation and assessment applications after a stroke.

Abstract: The Upper Extremity Fugl Meyer Assessment (UE-FMA) is the most comprehensive assessment for pinch impairment after stroke. The pinch test of UE-FMA is manually performed by pulling a pincer object away from the patient's fingers while providing a visual observation that results in a subjective assessment. In this study, an automated data acquisition system that consists of a linear electric actuator applying automatic pulling to the customized pincer object held by the volunteer was developed. The pinch force was measured such that a strain gauge was placed on the pincer object while pulling force was measured using pulling force load cell connected in between the linear electric actuator and customized pincer object. The pincer object's slip onset was detected using a displacement slip sensor. The mean pinch and pulling force values at the slip onset were 12.17 and 6.25 N for right hands, while mean pinch and pulling force values were 11.67 and 5.92 N for left hands of 50 healthy volunteers, respectively. Based on the paired *t*-test, there is no significant difference between right and left hands. The automated data acquisition system can objectively apply a pulling force, detect the slip onset, and measure the pinch and pulling forces.

Keywords: automated assessment; UE-FMA; pinch force; pulling force; slip onset; strain gauge; stroke

1. Introduction

Globally, stroke is the first leading cause of long-term disability [1]. Many daily activities, for example, pinching an object, require dynamic manipulation of the thumb and index finger. Pinch impairment is defined as the inability of the thumb and index finger to produce strength with sufficient magnitude and directional control, leading to object slipping [2]. Several studies showed that the recovery of pinch grip takes a longer time than handgrip, and it requires long-term rehabilitation after stroke [3]. Besides, a recent study conducted by Katab et al. [4] showed that pinch strength can be used as an alternative assessment to hand strength for assessing muscle strength in patients. Thus, an effective evaluation of pinch grip is needed to determine the pinch deficits accurately and objectively [5]. Accurate and objective pinch assessment can be achieved via automation of traditional standard assessment systems based on available technology. Current technology involves pinch gauge and dynamometers to measure the maximum static pinch force which is not related to

object manipulation involved in daily activities [6]. Therapists are still using the standard manual assessments to evaluate the pinch grip, which is subjective due to the different human interpretations of the procedures as well as the use of qualitative ordinal scoring. There is no single gold standard pinch assessment used in clinical and research practices [7]. Pinch evaluation is usually listed as part of upper limb standard assessments [8–11]. The UE-FMA is arguably the most comprehensive clinical tool for measuring pinch impairment after stroke [12,13]. The UE-FMA provides step-by-step procedures and protocols, which are performed by a UE-FMA therapist. The therapist tests the patient's ability to pinch a pincer object (in which a pencil or pen is customarily used) and exert enough force to stabilize the pincer object against gentle pull generated manually by the therapist, as in Figure 1 [14]. A score of 0, 1, or 2 is assigned, which represents severe impairment, partial impairment, and no impairment rating, respectively. Score 0 is given when the patient cannot execute the pinching at all. Score 1 indicates that the pincer object is not held firmly against the gentle pull such that slippage occurs, while score 2 is given when the pincer object is held firmly without slippage against a gentle pull.

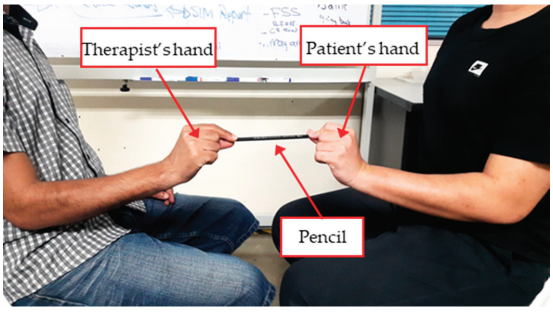

Figure 1. Pinch test as in the UE-FMA protocol.

The motivation of carrying out this study stemmed from the lack of studies related to a complete automated assessment of pinch impairment. In addition, the pinch assessment using UE-FMA is subjective due to the different interpretations of using the original guideline of UE-FMA [15]. These difference in interpretations may result in the following variations in clinical practice:

1. The orientation of the pincer object is not standardized. Some therapists pull the object horizontally, while others pull it vertically.
2. The posture of the patients' shoulder, elbow, forearm, and hand may differ between each clinic resulting in different pinch force exerted at different postures.
3. The amount of pulling force actuated by the therapist is subjective [16]. This opens the possibility for low intra-rater and inter-rater reliability of pinch evaluation.
4. The occurrence of slippage, which results in score of either 1 or 2 is visually observed and sensitive to the therapist experience, skills, and appreciation [17–23].

Due to the previous drawbacks of using the original protocol of UE-FMA assessment, several studies have been conducted to improve the original UE-FMA protocol. In addressing the orientation of the pincer object, Page et al. [24] suggested that the therapist should horizontally pull the pincer object outwards away from the patient's pinch grasp. Horizontal orientation choice is supported by other studies [25–27], which report that the brain response leading to pinch has higher latency responding to the pulling being applied vertically compared to horizontally. Page et al. [24] also proposed the upper limb posture and concurred with an independent study by Sullivan et al. [28]. Both studies recommend that the patient should be sitting on a chair in a 90°. Then, the patient should maintain shoulder at 0°, elbow at 90°, and forearm in resting position. The therapist, if necessary, may support the patient's elbow at 90°. Sullivan has suggested that the therapist can use a bedside

table to support the patient's arm and elbow. The use of bedside table is supported by other studies, which reported that the arm weight leads to abnormal coupling between shoulder abduction and elbow flexion due to abnormal muscle co-activation required to compensate the weight of the arm [29]. Therefore, Ellis and colleagues used arm weight support to reduce the activation of those muscles (e.g., biceps), which otherwise would be involved in pinching [30,31].

Recently, the research community [21,32–39] have been working on automating UE-FMA, but few of them involved the pinch grip. Otten and his colleagues [40,41] implemented a glove with built-in Force Sensing Resistor (FSR) sensors as the data acquisition system to measure the patient's pinch force during the evaluation process. Nevertheless, some post-stroke patients with severe to moderate impairment have muscle contracture and spasticity that lead to difficulties in wearing the glove. In later studies [42,43], the FSR sensor was attached to the pincer object such that the patient is no longer required to wear a glove. The pinch force threshold values that distinguish between slip (score 1) and non-slip (score 2) onsets are useful in determining the baseline measurements to evaluate the effectiveness of pinch rehabilitation for both right and left hands. In both studies, the discrimination between scores 1 and 2 was based on the ability of the subject to exert pinch force up to a threshold value. However, this threshold pinch force value was selected by the therapist which may open the possibility for uncertainty. Moreover, these studies still have not addressed the issues related to subjectivity of the manual pull and the limitations of the FSR sensors used in the data acquisition system.

Generally, FSR sensors (also known as a thin-film sensor) have been used for many applications [44] but they suffer from performance variation as well as low performance [45,46]. The variation in performance is attributed to the conductive material on the sensor layers being sensitive to temperature and deformation on the surface [47]. In addition, the variation in performance can be attributed to the inability to follow the standard calibration procedures resulting in different calibration results compared to those in the manufacturer's datasheet. On the other hand, low performance can be attributed to variation in voltage gain, high hysteresis, nonlinearity, and inaccurate measurements in real-time pinching [48]. Likitlersuang et al. [49] investigated the performance of the thin-film sensor when attached directly to human skin. The results show a large measurement error of 23% using the standard calibration techniques. In addition, the pressure distribution on the sensing area may not be uniform during slippage due to different pinching contact location.

The main objective was to develop an automated data acquisition system for pinch assessment based on the standard UE-FMA protocol. In this study, the following research questions were addressed: (1) Does the slip onset occur at the maximum pinch force? (2) Is there any significant difference between right and left hands in pinch and pulling forces at the slip onset? In this study, the authors hypothesized that the maximum pinch force exerted by the volunteer against the automatic pulling would be located at the slip onset. The authors also hypothesized that the pinch and pulling force measurements of the right hands are significantly higher than pinch and pulling force measurements of left hands at the slip onset for right-handed volunteers.

To address the first question, an automated data acquisition system was developed. The automated system must be able to measure and acquire pinch and pulling forces as well as slip displacement accurately and automatically. The automated system uses linear electric actuator applying automatic pull, customized pinch force load cell measuring the pinch force, pulling force load cell measuring the pulling force, and Linear Variable Differential Transformer (LVDT) displacement sensor detecting the slip onset. The sensors and actuator were calibrated and then integrated together with Arduino® Due board. Subsequently, the data from 50 right-handed male volunteers within the age of 18–24 years were collected according to the UE-FMA protocol to establish the relationship between pulling and pinch forces in order to observe the slip onset. The paired *t*-test was performed on collected data to address the second question.

2. Materials and Methods

2.1. Pinch Data Acquisition System

The experimental setup of the data acquisition system is described in Figure 2. It consists of:

1. Displacement sensor: LVDT sensor (1) with Low Pass Filter (9).
2. Linear actuator system: including linear electric actuator (2) and servo motor driver (8).
3. Customized Pinch force load cell: pincer object (4), Wheatstone bridge (5), and an amplifier (6).
4. Pulling force load cell: load cell (3) and an amplifier (11).
5. Data acquisition card: Arduino® Due board (Arduino LLC, Torino, Italy) (11) and Arduino® IDE 1.8.5 software (arduino.cc) [50].
6. DC power supply (7).

In our previous work [51], a customized pinch force load cell based on strain gauge was designed, fabricated, and calibrated. The customized pinch force load cell is composed of three parts: pincer object, strain gauge, and signal conditioning circuit. The pincer object was fabricated to mimic a pencil, as used in UE-FMA, which represents a cylindrical object with a diameter of 12 mm and 150 mm length. In order for a strain gauge to measure the bending at the pinching location near the free edge of the pincer object, a 4 mm slot cut was created, as shown in Figure 3. The slot cut starts from the free end to the middle of the pincer object, similar to the shape of a tuning fork. The pinching location is within 20 mm from the free edge and is adequate to cover the fingertip length. A 350-ohm strain gauge (SGK-L1-D-K350P-PC11-E) was placed at the maximum stress point. The maximum stress point was determined based on the stress analysis performed using ANSYS® finite element software (Version 15.0, ANSYS Inc, Canonsburg, PA, USA) as shown in Figure 4. The conditioning circuit consists of a quarter Wheatstone bridge and an amplifier. The quarter Wheatstone bridge was implemented to convert the strain gauge resistance change to voltage change when pinching occurs. However, the voltage change was too small. Thus, a commercial amplifier (Wachendorff Strain Gauge Converter®, SENECA s.r.l., Padova, Italy) with a gain of 1000 was used.

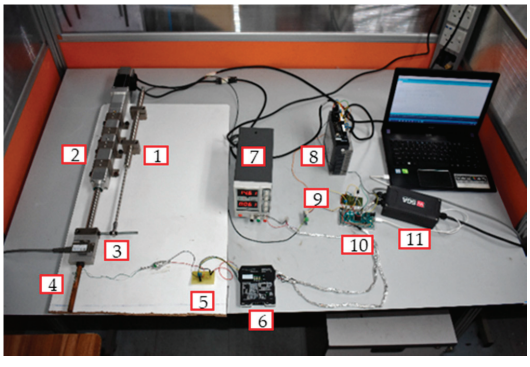

Figure 2. Experimental Setup of data acquisition system for pinch assessment.

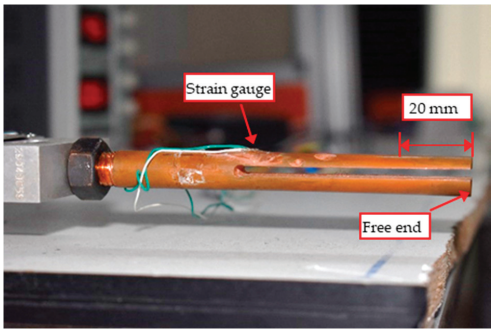

Figure 3. Pinch force load cell.

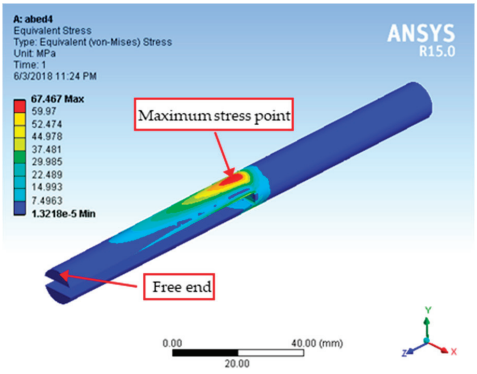

Figure 4. Stress analysis of the pincer object where an external force is applied at the free end.

The standard strain gauge calibration of force–voltage is usually performed for one contact location only. However, in the pinch test of UE-FMA, the contact location may vary due to the different initial pinching location of each volunteer. Furthermore, the contact location may also vary during the automatic pull, which causes slipping. Therefore, a continuous relationship of force–voltage for all possible contact points along the pinching length is required. This can be achieved by performing a multipoint calibration at five contact points away from the free edge (4.1, 5.8, 11.5, 16.5, and 20.2 mm). The multipoint calibration was performed using a mechanical testing system (INSTRON® 3366, Illinois Tool Works Inc, Norwood, MA, USA) by applying dynamic loading (0–50 N), as shown in Figure 5. The pincer object was held stationary on the INSTRON® 3366 base during calibration by applying glue on both sides of the pincer object to prevent any movement, as shown in Figure 5. As a result, five force–voltage curves were generated, as depicted in Figure 6a. The voltage and force data were recorded from the customized pinch force load cell and the INSTRON® 3366 machine. Subsequently, the continuous relationship of force as a function of voltage and position was modeled using linear regression function, as depicted in Figure 6b. The linear correlation coefficient R^2 of 0.9896 indicates high linearity. Using the linear plane model equation (Equation (1)), the force measurements can be estimated at any contact point within pinching length given the measurements of voltage and position, which were collected from the pinch force load cell and the LVDT sensor, respectively.

$$\text{Force} = -0.9447 + 0.02371 \times \text{Voltage} + 0.3632 \times \text{Position}, \quad (1)$$

In performing the hysteresis test to the customized pinch force load cell, dynamic loading (0–50 N) and unloading (from 50 to 0 N) were applied at the contact point 11.5 mm, which is approximately

at the midpoint of the pinching length. Figure A1 (Appendix A) shows the loading and unloading curves of voltage and force measurements recorded from the pinch force load cell and INSTRON® 3366 machine, respectively. The solid line is the force–voltage relationship for dynamic loading, while the dotted line is the force–voltage relationship for dynamic unloading. The hysteresis is defined as the difference in voltage offset between loading and unloading lines at the midpoint on the force axis. The following formula gives the percentage of hysteresis:

$$\text{Hysteresis} = 100\% \times (V_{mu} - V_{ml})/(V_{max} - V_{min}) = 0.287\%. \quad (2)$$

where V_{mu} (892.46 mV) is the voltage value on the unloading line in Figure A1 at midpoint force F_m (23.86 N), V_{ml} (898.1 mV) is the voltage value on the loading line at F_m, V_{max} (1960.86 mV) is the maximum voltage value on the loading line, and V_{min} (0 mV) is the minimum voltage value on the unloading line. The hysteresis of 0.287% can be considered negligible [52]. Furthermore, it is much lower than the hysteresis of thin-film pressure sensors (5%) [53]. Similar hysteresis tests were performed at the other contact points resulting in similarly negligible hysteresis.

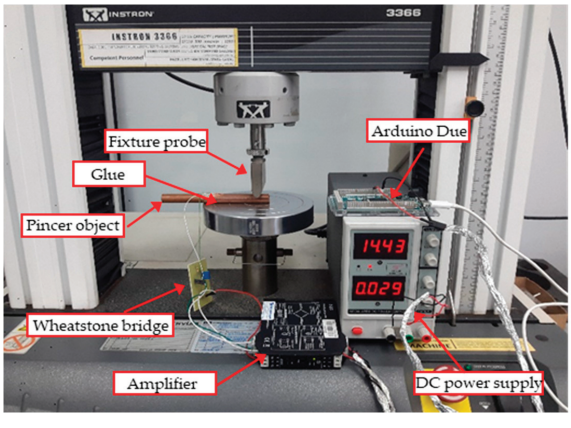

Figure 5. Calibration setup of the pinch force load cell.

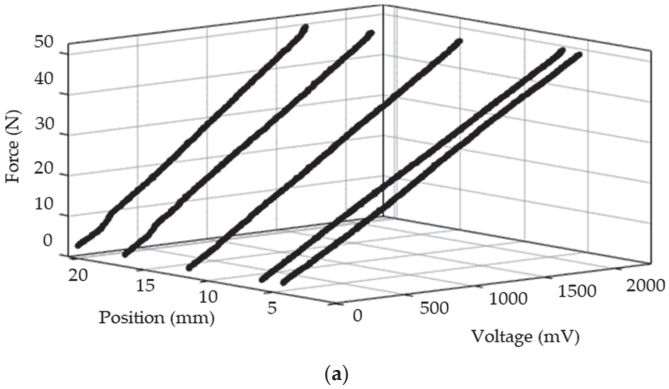

(**a**)

Figure 6. *Cont.*

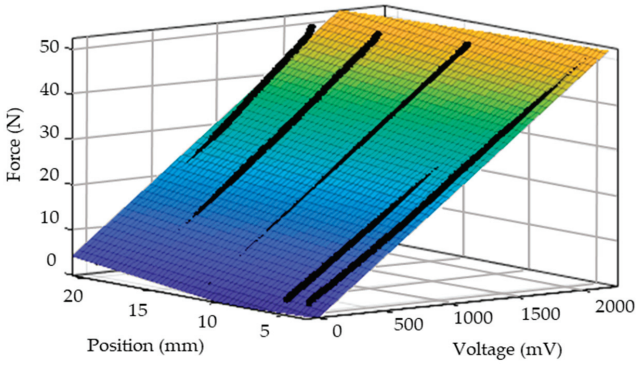

(**b**)

Figure 6. (**a**) Force–voltage curves at five contact points; and (**b**) estimated plane of force as a function of voltage and position.

In performing the repeatability test, a dynamic loading (0–50 N) was applied three times at the contact point 11.5 mm. The Coefficient of Variation (CV) was used to calculate the repeatability. CV is given by the ratio between standard deviation and mean values of three repeated voltage measurements at each force point ranging from F_{min} (2.28 N) to F_{max} (50 N). Then, all CVs are averaged to provide a single CV [49,54]. The "Cfvar" function in SPSS Statistics® V21 was used to calculate the CV. The CV value of 1.43 ± 0.447% was obtained which indicates high repeatability [55]. In addition, it is smaller than the CV value of thin-film pressure sensors (2.1 ± 2.3%) [49].

In replacing the manual gentle pull by the therapist, a linear electric system was used. The linear actuator system consists of a linear electric actuator, AC servo motor, AC servo driver, and Arduino® Due. To run the linear electric actuator, an AC servo motor (SM0602—400 Watt) was coupled in-line to the drive cap of the linear electric actuator. The output analog signal of Arduino® Due controls the AC servo motor through the AC servo driver (M2DV-3D02R). The linear actuator system can exert automatic pulling force ranging from 0 to 63.25 N with a resolution of 0.5 N.

A pulling force is produced when the volunteer pinches the pincer object and then resists the automatic pull generated by the linear actuator system. An off-the-shelf pulling force load cell (STA-1-50 Aluminium S Type Tension) is located between the pincer object and the linear electric actuator to measure the pulling force. The voltage–force relationship of the pulling force load cell was established by the manufacturer, as shown in Figure 7. The pulling force load cell has 0.03% accuracy, 0.01% repeatability, 0.05 N resolution, and $R^2 = 1$ linearity.

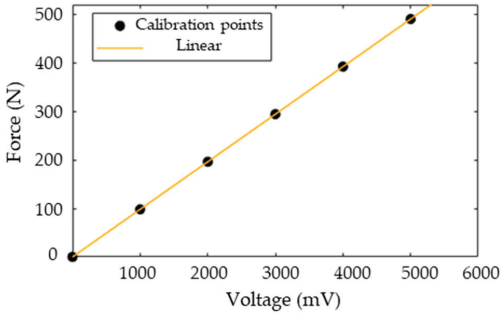

Figure 7. Voltage–force relationship for pulling force load cell.

In detecting the slip onset, the LVDT displacement sensor was used. The LVDT sensor and linear electric actuator were clamped together such that they move in parallel. The output signal of the LVDT sensor was filtered with an analog Low Pass Filter (LPF) of 20 Hz cut off frequency to remove the high-frequency noise. Since the pinching length is only 20 mm, the LVDT sensor was calibrated at 0-, 5-, 10-, 15-, and 20-mm displacement points using a standard digital caliper with 0.05 mm resolution. The calibration process was repeated three times to perform the repeatability test, as mentioned previously for the pinch force load cell. The three voltage–displacement relationships show high linearity of $R^2 = 0.9999$, as shown in Figure 8. The repeatability of the LVDT sensor is 9.57×10^{-5}%, which indicates high repeatability. The analog signals of the customized pinch force load cell, pulling force load cell, and LVDT sensors were converted to digital inside the Arduino® Due and then recorded in a PC installed with Arduino® IDE software. The diagram that illustrates the data acquisition process is shown in Figure 9.

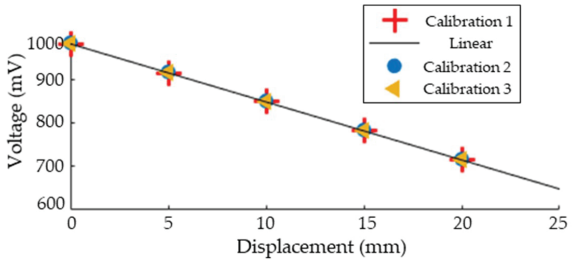

Figure 8. Displacement–voltage relationships of three times calibration.

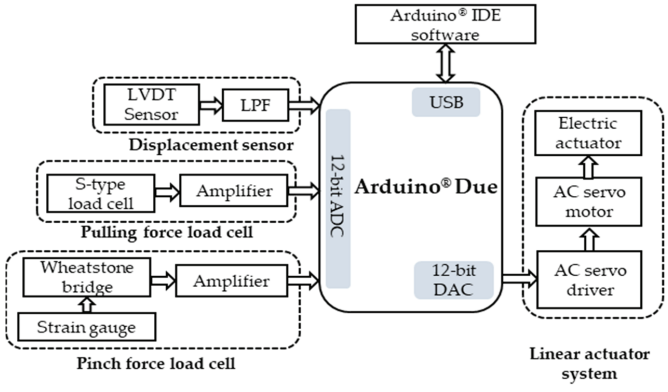

Figure 9. Block diagram of the data acquisition process.

2.2. *Volunteers Recruitment and Experimental Protocol*

Fifty right-handed healthy male students participated. All volunteers had no prior history of upper limb injury and passed the health status questionnaire (SF-36). To avoid bias in the force measurements, the study was conducted on a single-gender because males and females have different pinch strength [56]. Furthermore, the study excluded construction workers and professional sportsmen as they have stronger pinch force than the average male population [57]. The mean age, height, and weight for volunteers were 21.86 ± 1.41 years, 170.41 ± 7.03 cm, and 69.49 ± 17.9 kg, respectively. Ethical approval (Reference number: JKEUPM-2017-248) for this study was obtained from The Ethics Committee for Research Involving Human Subjects of Universiti Putra Malaysia.

In this study, the improved wrist/hand UE-FMA protocol by Page et al. [24] was adopted. The volunteers were instructed to sit at 90° on a chair, shoulder in the neutral position, elbow at 90°,

and forearm in resting position. A bedside table was positioned to support the volunteer's arm and elbow, as shown in Figure 10a. The volunteers were also instructed to clean and dry their hands before commencing the experiment to avoid any influence of moisture through sweat. Then, they were instructed to hold the pincer object comfortably using their thumb and index fingertips, as in Figure 10b. Once the linear actuator started to pull the pincer object, the volunteers attempted to resist this pulling as much as possible. Since no visual feedback was provided, the volunteer had to react and adjust accordingly to the perceived amount of pulling force. To achieve pinch stability, the pinch force had to be adjusted in proportion to the changes in the pulling force. The linear actuator stopped exerting pulling force the moment the pincer object had totally slipped away from the volunteer's fingers, and this was indicated by a 20-mm displacement slip. Figure A2 (Appendix A) demonstrates the flowchart to execute the experiment. The data collection involved both right and left hands. The duration of one trial began when the linear actuator received the control signal from the Arduino® Due, and ended the instant the pincer object slipped totally away. The analysis of the recorded data showed the pinch and pulling force values at the slip onset. The slip onset was defined as the moment when the pincer object started to shift with respect to the starting position, indicating that the object slipped away from the volunteer's fingers. During the trial, one set of measurements, which included the pinch force, pulling force, and displacement, were recorded, resulting in 300 datasets (50 volunteers × 2 hands × 3 trials per hand). To reduce the effect of the physical and mental fatigue, an adequate resting period of 3 min was given between each trial. Cronbach's alpha (α) was used to measure the reliability among the three trials of the hand, which as computed using the following formula [58]:

$$\alpha = \frac{N.\bar{c}}{v + (N-1).\bar{c}} \tag{3}$$

where N is the number of trials, $\bar{c}$ is the average inter-item covariance among the trials, and v is the average variance.

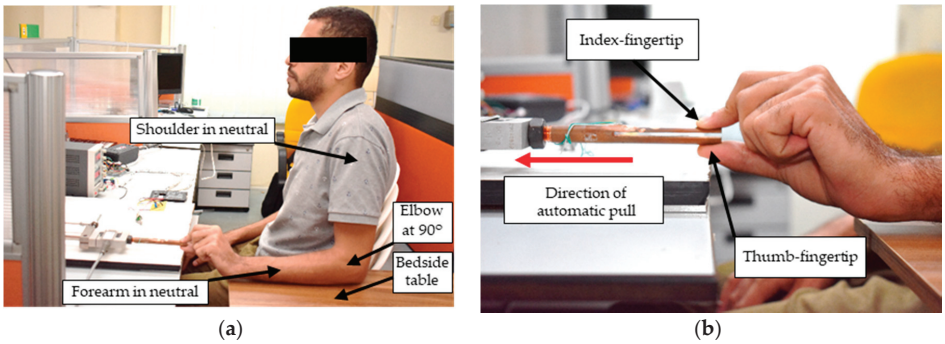

(**a**) (**b**)

Figure 10. (**a**) Body and upper limb positioning during the experiment; and (**b**) thumb and index finger opposed onto the pincer object. Note that the volunteer should resist the automatic pull applied by the linear actuator system.

3. Results

Figure 11a shows data recorded from one trial of one volunteer. The pinch force, pulling force, and displacement signals were recorded from the customized pinch force load cell, pulling force load cell, and the LVDT sensor, respectively. The linear electric actuator started to pull the pincer object, as indicated by a sudden increase in the pinch and pulling force signals at 3 s. The volunteer exerted pinch force increased as the pulling force increased gradually. From this point, the pincer object totally slipped away from volunteer's fingers, as indicated by a sudden increase in displacement measurements at 20 s. For each trial, it was important to extract the pinch and pulling force values at

the slip onset. The slip onset is the point that differentiates between slip and non-slip where the pincer object begins to slip and is the first instance where the displacement started to increase from a relatively flat level. In Figure 11a, it is difficult to determine the slip onset visually due to the small magnitude of the increase in the displacement absolute scale (mm). In addition, the increase in displacement is nonlinear, thus a nonlinear scaling is required. Subsequently, the nonlinear decibel scale (dB) was used such that the logarithm base 10 of the displacement absolute value was multiplied by 20 to provide the necessary scaling. Upon that, the slip onset was precisely determined at 12 s, as shown in Figure 11b. The pinch and pulling force values at the slip onset (12 s) were 15.39 and 7.05 N, respectively.

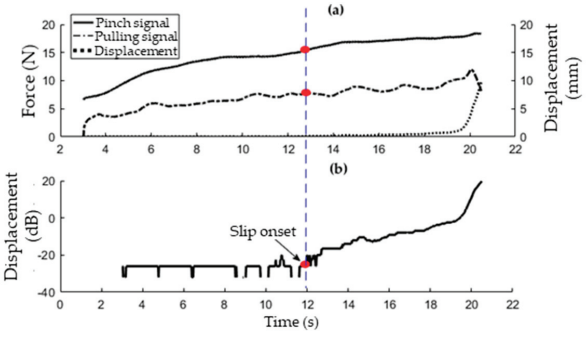

Figure 11. (**a**) One trial recorded from one volunteer; and (**b**) displacement in decibel scale.

Since the static coefficient of friction of copper alloy is constant, it is expected that the relationship between pinch and pulling force prior to slip onset is linear. Figure 12 shows the pinch–pulling force relationship before and after the slip onset. It was observed that the volunteer initially exerted excessive resistance (indicated by a sudden increase in pulling force), because he had to react and adjust the pinch force according to the perceived automatic pull generated by the linear actuator. There was also some nonlinearity observed at 12 and 14.5 N pinch forces that were probably due to the absence of visual feedback as well as the continuous increase in the amount of automatic pull. Prior to the slip onset, the pinch–force relationship had high linearity of $R^2 = 0.8971$, while the linearity decreased to $R^2 = 0.5845$ after the slip onset. This decrease in linearity as due to the inability of the volunteer to exert pinch force according to the continuous increasing of pulling force, which was indicated by the continuous slipping. The COF was computed as the ratio of pulling force to the pinch force at the slip onset, which was equal to 0.45 (7.05/15.39).

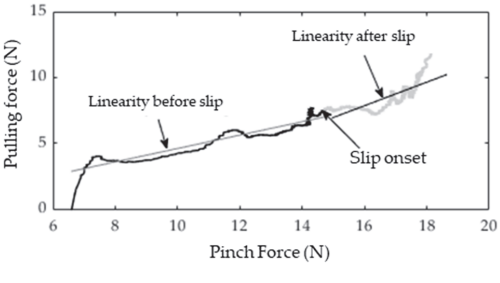

Figure 12. Pinch–pulling force relationship.

For each hand, three trials were recorded, and then the pinch and pulling force values were extracted at the slip onsets using the same criteria involved in the above trial. Figure A3a (Appendix A) shows the three trials collected from the right hand of a volunteer. It can be observed that the pinch force signals were close to each other during the three trials, and they had excellent reliability (Cronbach's

alpha = 0.989). This was also observed for pulling force signals (Cronbach's alpha = 0.969). Based on the displacement measurements after being converted to decibels, the slip onsets were at 17, 14, and 12 s for Trials 1–3, respectively, as shown in Figure A3b. The pinch and pulling force values at the slip onsets as well as the static COFs are summarized in Table 1. The interpretation is that this volunteer could exert an average pinch force of 15.93 N against the maximum automatic pull of 7.65 N without slipping.

Table 1. Measurements recorded from the right hand of a volunteer.

Variables	Trial 1	Trial 2	Trial 3	Average
Pinch force (N)	14.61	17.81	15.39	15.93
Pulling force (N)	7.29	8.61	7.05	7.65
Static COF	0.498	0.483	0.458	0.48

For each hand of the 50 volunteers, the pinch and pulling force values as well as the static COFs of the three trials were averaged, resulting in three averaged values (as demonstrated in Table 1). Figure 13 shows the distribution of averaged values collected from the right and left hands of the 50 volunteers. It is clear that the distribution has an approximately normal bell-shape and no skewness exists. The mean, standard deviation, and range of pinch and pulling force values as well as static COF of right and left hands are summarized in Table 2. It was found that the mean pinch and pulling force values of right hands were slightly higher than those of lefts hands by 4.1% and 5.28%, respectively. However, there were no significant differences between right and left hands based on the paired *t*-test at the confidence level of $p = 0.05$. The paired *t*-test shows a *p*-value of 0.298 and 0.275 for pinch and pulling force, respectively. The average time duration for each hand was around 7 min, which included three trials (around 20 s for each trial depending on the amount of time for the pincer object to slip away from the fingers) with two resting periods in between (3 min for each resting period). Considering each volunteer performed the same experiment with both hands, a total time duration of around 14 min was involved.

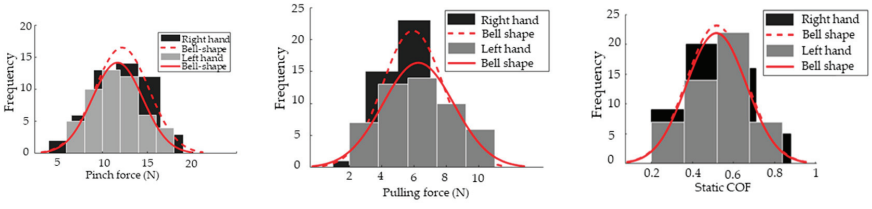

(**a**) (**b**) (**c**)

Figure 13. Distribution of: (**a**) pinch force; (**b**) pulling force; and (**c**) static COF for 50 volunteers.

Table 2. Summary of pinch force, pulling force, and static COF values at slip onset for 50 volunteers.

Variable		Mean	Standard Deviation	Range
Pinch force (N)	Right hand	12.17	3.02	5.36–18.48
	Left hand	11.67	2.82	6.79–17.67
Pulling force (N)	Right hand	6.25	2.19	2.37–10.77
	Left hand	5.92	1.86	1.88–10.67
Static COF	Right hand	0.518	0.146	0.27–0.85
	Left hand	0.517	0.145	0.23–0.81

4. Discussion

In 274 trials (91.3% of total trials), the volunteers could adjust the pinch force in proportion to the changes in pulling force. However, the remaining trials were excluded prior to analysis due to improper adjustment of pinch force to the pulling force. This is considered as human errors such that

the volunteers might not follow the experiment's procedures and instructions probably due to delay in reaction, missing the instructions, or absence of visual feedback. According to the UE-FMA protocol, the subject should resist a gentle pull to avoid slip. This means that the pincer object slips when the subject is no longer able to exert enough pinch force. In this study, it was initially hypothesized that the slip onset was expected at the maximum pinch force just before the point where the pincer object totally slipped. Interestingly, it was found that the slip onset occurred much earlier and was subjected to a sub-maximal pinch force. This result opens up the possibility of using the slip onset as a measurement of pinch improvement such that the patient would develop a stronger pinch force over rehabilitation time at the slip onset. Furthermore, the continuous changes of slip onset would improve the responsiveness of the pinch assessment such that the scoring is not subjected only to score 1 and 2 as in the current UE-FMA scoring criteria.

The pinch–force relationship was found to be linear prior to the slip onset as the static COF between human skin and copper alloy was constant. However, there was some variability in pinch and pulling force, as indicated by peaks approximately at 7.5, 12, and 14.5 N, as depicted in Figure 12. The highest variability was observed at 7.5 N pinch force at the loading phase in which the linear electric actuator started to pull. This is consistent with previous studies stated that the subjects generally show stronger pinch forces at the loading phase [59]. Besides, the pinch force rate (N/s) reached the highest at the loading phase when the volunteer was subjected to unpredictable loading [27]. The study conducted by Takamuku et al. [60] showed that pinch force variability is lower when visual feedback is provided to the subject. In addition, the pinch force control is greatly influenced by the safety margin factor during the unpredictable loading [61]. The safety margin is an additional amount of pinch force applied to guard against slip, which is different from volunteer to volunteer [62]. The other two peaks at 12 and 14.5 N can be interpreted such that the volunteer should adapt his pinch force against the continuous automatic pull without visual feedback; hence, the safety margin is continuously changed to adapt the continuous increase in pulling force. Therefore, it is possible that the volunteer may unconsciously fail to adapt his pinch force to the increase in pulling force at some events. The safety margin is also influenced by the static COF [63], such that it will be high in the case of slippery object as in copper alloy used in our experiment. The pinch–pulling force relationship can be used as an assessment for pinch force control against unpredictable loading for stroke patients.

The CV value (represented by standard deviation divided by the mean) indicates how well the mean values of pinch and pulling forces summarizes the whole dataset. Interpretation of CV may vary; the rule of thumb can be used, which states the CV value of under 1 shows a small variance [64]. In this study, the CV values were 0.248 and 0.35 for pinch and pulling forces of the right hands, respectively. The CV values were 0.241 and 0.31 for pinch and pulling forces of left hands, respectively. Hence, the mean pinch and pulling force values are a reasonable representation of healthy adults in Malaysia. The results also indicate that the pinch and pulling force vary among the volunteers at the slip onset, which is expected as each volunteer has a different body size, hand size, and amount of safety margin. For instance, a bigger fingertip size leads to a larger contact area between the fingertip and the object's surface. Consequently, larger contact area would lead to larger pinch force, as reported in a related study by Derler et al. [65], who showed that there is a positive association between contact area and force exerted by the index finger. In addition, each volunteer has different skin characteristics such as oiliness, moisture, roughness, and age that may affect the friction between fingertip skin and pincer object's surface. In this study, the mean static COFs for right and left hands were computed as 0.518 ± 0.146 and 0.517 ± 0.145, respectively. This is relatively consistent with previous findings related to measuring COF between human skin and copper material, reported by Sivamani et al. [66] (mean COF = 0.55) and Li et al. [67] (mean COF = 0.58).

In the literature, many studies have reported a significant difference in maximum pinch force between right and left hands [68]. Although our results show a slight increase in the means of pinch and pulling force for right hand compared to the left hand, there was no significant difference ($p > 0.05$). Thus, it is not required to distinguish between right and left hands when a single-gender group is

recruited for further research. Furthermore, the unaffected hand can be used as a reference for the affected hand during the rehabilitation of post-stroke patients. The explanation of this result can be that the volunteers did not exert their maximum pinch force at the slip onset. This is consistent with a study conducted by Li and Yu [69], who reported that there is no significant difference between left and right hands when the grip force is at 25%, 50%, and 75% of the maximum force. The results of their study indicate that there is a significant difference only at maximum grip force.

Recently, three main components of the assessment system are required for an assessment system to be fully automated: administration, data acquisition, and rating [19]. Administration involves the instructions and procedures to evaluate the patient, while the data acquisition involves obtaining the outcome measurements from patients. Rating is the criteria to evaluate the outcome measurements of the patients, which are usually designed as an ordinal scale. In this study, only the pinch data acquisition system is automated based on UE-FMA protocol. The limitation of this study is that the administration and rating components are not yet automated. In the future, this limitation will be addressed, such that stroke patients with pinch deficits at different levels of impairment (severe, moderate, and mild) will be recruited to determine the threshold values for each level so that an automated rating process can be performed. In addition, the administration of the pinch test will be automated by including a graphical user interface to visualize the instructions and procedures.

To use the automated data acquisition system in clinical practice based on UE-FMA protocol, the design can be improved to be more compact, less wires, and portable by: (1) replacing the DC power supply with a portable DC battery to power the two amplifiers and LVDT sensor; (2) using a customized small size linear electric actuator as the with pulling force of smaller than 15 N; and (3) using a wireless connection (e.g., ZigBee module) to transmit/receive digitalized signals to/from the PC instead of signal wires. This improvement will be addressed in the future work.

5. Conclusions

In this paper, an automated data acquisition system for pinch assessment based on UE-FMA protocol is presented. The automated system is able to provide objective measurements of pinch and pulling forces and detect slip onset rather than the subjective manual gentle pull and visual observation of slipping occurrence. In addition, the therapist's gentle pull has been replaced with a linear actuator sub-system exerting a consistent amount of pulling force. Right and lefts hands of 50 volunteers were recruited to investigate the pinch and pulling force measurements at the slip onset using the developed system. The pinch–pulling force relationship is linear, which is indicated by a proportional increase of pinch force against the continuous increase of pulling force prior to slip onset. In addition, the volunteers were subjected to submaximal pinch force at the slip onset. The mean pinch force values at the slip onset were 12.17 and 11.67 N for right and left hands, respectively. The mean pulling force values at the slip onset were 6.25 and 5.92 N for right and left hands, respectively. It was found that there is no significant difference in force measurements between right and left hands. A further study can be conducted to investigate the hypothesis of considering slip onset and pinch–pulling force relationship as a pinch assessment for stroke patients.

Author Contributions: A.A. (Abdallah Alsayed) and R.K. designed and developed the pinch assessment system; H.R. performed the integration of sensors and actuator; A.A. (Azizan As'arry) performed CAD and finite element analysis as well as provided access to volunteers; A.A. (Abdallah Alsayed) performed data collection and results analysis; and all authors contributed to writing and editing the paper. All authors have read and agreed to the published version of the manuscript

Funding: This research was funded by Universiti Putra Malaysia, grant number IPS No. 9574400.

Acknowledgments: We would like to thank Yayasan Khazanah Berhad, Malaysia for their technical and financial support.

Conflicts of Interest: The authors declare no conflict of interest.

Data Availability: The data and codes used in this study are available from the corresponding author upon request.

Appendix A

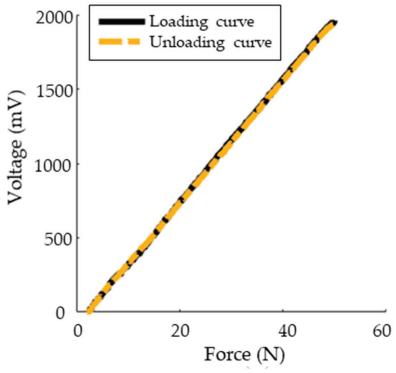

Figure A1. Force–voltage relationship during loading and unloading.

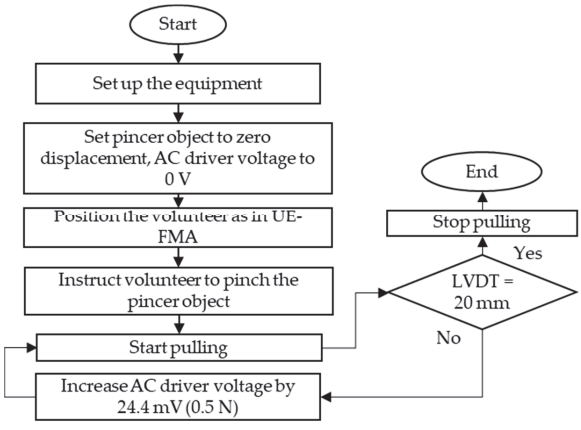

Figure A2. Flowchart of experiment execution.

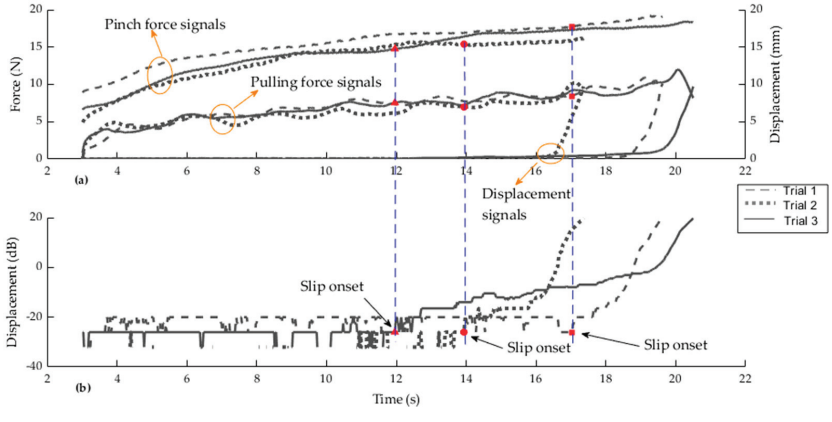

Figure A3. (**a**) Three trials recorded from one volunteer; and (**b**) displacement in decibel scale.

References

1. Miyasaka, H.; Takeda, K.; Ohnishi, H.; Orand, A.; Sonoda, S. Effect of Sensory Loss on Improvements of Upper-Limb Paralysis Through Robot-Assisted Training: A Preliminary Case Series Study. *Appl. Sci.* **2019**, *9*, 3925. [CrossRef]
2. Li, K.; Nataraj, R.; Marquardt, T.L.; Li, Z.-M. Directional coordination of thumb and finger forces during precision pinch. *PLoS ONE* **2013**, *8*, e79400. [CrossRef] [PubMed]
3. Pessina, M.A.; Bowley, B.G.; Rosene, D.L.; Moore, T.L. A method for assessing recovery of fine motor function of the hand in a rhesus monkey model of cortical injury: An adaptation of the Fugl-Meyer Scale and Eshkol-Wachman Movement Notation. *Somatosens. Mot. Res.* **2019**, *36*, 69–77. [CrossRef]
4. El-Katab, S.; Omichi, Y.; Srivareerat, M.; Davenport, A. Pinch grip strength as an alternative assessment to hand grip strength for assessing muscle strength in patients with chronic kidney disease treated by haemodialysis: A prospective audit. *J. Hum. Nutr. Diet.* **2016**, *29*, 48–51. [CrossRef] [PubMed]
5. Murphy, M.A.; Resteghini, C.; Feys, P.; Lamers, I. An overview of systematic reviews on upper extremity outcome measures after stroke. *BMC Neurol.* **2015**, *15*, 29. [CrossRef]
6. Valero-Cuevas, F.J.; Smaby, N.; Venkadesan, M.; Peterson, M.; Wright, T. The strength-dexterity test as a measure of dynamic pinch performance. *J. Biomech.* **2003**, *36*, 265–270. [CrossRef]
7. Harrison, J.K.; McArthur, K.S.; Quinn, T.J. Assessment scales in stroke: Clinimetric and clinical considerations. *Clin. Interv. Aging* **2013**, *8*, 201.
8. Yozbatiran, N.; Der-Yeghiaian, L.; Cramer, S.C. A standardized approach to performing the action research arm test. *Neurorehabilit. Neural Repair* **2008**, *22*, 78–90. [CrossRef]
9. Johansson, G.M.; Häger, C.K. A modified standardized nine hole peg test for valid and reliable kinematic assessment of dexterity post-stroke. *J. Neuroeng. Rehabil.* **2019**, *16*, 8. [CrossRef]
10. Sears, E.D.; Chung, K.C. Validity and responsiveness of the jebsen–taylor hand function test. *J. Hand Surg.* **2010**, *35*, 30–37. [CrossRef]
11. Wolf, S.L.; Catlin, P.A.; Ellis, M.; Archer, A.L.; Morgan, B.; Piacentino, A. Assessing Wolf motor function test as outcome measure for research in patients after stroke. *Stroke* **2001**, *32*, 1635–1639. [CrossRef] [PubMed]
12. Raghavan, P. Upper limb motor impairment after stroke. *Phys. Med. Rehabil. Clin.* **2015**, *26*, 599–610. [CrossRef] [PubMed]
13. Page, S.J.; Fulk, G.D.; Boyne, P. Clinically important differences for the upper-extremity Fugl-Meyer Scale in people with minimal to moderate impairment due to chronic stroke. *Phys. Ther.* **2012**, *92*, 791–798. [CrossRef] [PubMed]
14. Fugl-Meyer, A.R.; Jääskö, L.; Leyman, I.; Olsson, S.; Steglind, S. The post-stroke hemiplegic patient. 1. A method for evaluation of physical performance. *Scand. J. Rehabil. Med.* **1975**, *7*, 13–31. [PubMed]
15. Deakin, A.; Hill, H.; Pomeroy, V.M. Rough guide to the Fugl-Meyer Assessment: Upper limb section. *Physiotherapy* **2003**, *89*, 751–763. [CrossRef]
16. Paternostro-Sluga, T.; Grim-Stieger, M.; Posch, M.; Schuhfried, O.; Vacariu, G.; Mittermaier, C.; Bittner, C.; Fialka-Moser, V. Reliability and validity of the Medical Research Council (MRC) scale and a modified scale for testing muscle strength in patients with radial palsy. *J. Rehabil. Med.* **2008**, *40*, 665–671. [CrossRef]
17. Van Beers, R.J.; Haggard, P.; Wolpert, D.M. The role of execution noise in movement variability. *J. Neurophysiol.* **2004**, *91*, 1050–1063. [CrossRef]
18. Tanaka, K.; Yano, H. Errors of visual judgement in precision measurements. *Ergonomics* **1984**, *27*, 767–780. [CrossRef]
19. Simbaña, E.D.O.; Baeza, P.S.-H.; Jardón, A.; Balaguer, C. Review of Automated Systems for Upper Limbs Functional Assessment in Neurorehabilitation. *IEEE Access* **2019**, *7*, 32352–32367. [CrossRef]
20. de los Reyes-Guzmán, A.; Dimbwadyo-Terrer, I.; Trincado-Alonso, F.; Monasterio-Huelin, F.; Torricelli, D.; Gil-Agudo, A. Quantitative assessment based on kinematic measures of functional impairments during upper extremity movements: A review. *Clin. Biomech.* **2014**, *29*, 719–727. [CrossRef]
21. Yu, L.; Xiong, D.; Guo, L.; Wang, J. A remote quantitative Fugl-Meyer assessment framework for stroke patients based on wearable sensor networks. *Comput. Methods Programs Biomed.* **2016**, *128*, 100–110. [CrossRef] [PubMed]

22. Woytowicz, E.J.; Rietschel, J.C.; Goodman, R.N.; Conroy, S.S.; Sorkin, J.D.; Whitall, J.; Waller, S.M. Determining levels of upper extremity movement impairment by applying a cluster analysis to the Fugl-Meyer assessment of the upper extremity in chronic stroke. *Arch. Phys. Med. Rehabil.* **2017**, *98*, 456–462. [CrossRef] [PubMed]
23. Yu, L.; Wang, J.; Guo, L.; Zhang, Q.; Li, P.; Li, Y.; Yu, X.; Huang, Y.; Wu, Z. Transfer learning based quantitative assessment model of upper limb movement ability for stroke survivors. In Proceedings of the 2017 2nd International Conference on Information Technology (INCIT), Nakhon Pathom, Thailand, 2–3 November 2017; pp. 1–4.
24. Page, S.J.; Levine, P.; Hade, E. Psychometric properties and administration of the wrist/hand subscales of the Fugl-Meyer Assessment in minimally impaired upper extremity hemiparesis in stroke. *Arch. Phys. Med. Rehabil.* **2012**, *93*, 2373–2376. [CrossRef] [PubMed]
25. Westling, G.; Johansson, R. Factors influencing the force control during precision grip. *Exp. Brain Res.* **1984**, *53*, 277–284. [CrossRef]
26. Hu, W.; Wei, N.; Li, Z.-M.; Li, K. Effects of muscle fatigue on directional coordination of fingertip forces during precision grip. *PLoS ONE* **2018**, *13*, e0208740. [CrossRef]
27. Häger-Ross, C.; Cole, K.J.; Johansson, R.S. Grip-force responses to unanticipated object loading: Load direction reveals body-and gravity-referenced intrinsic task variables. *Exp. Brain Res.* **1996**, *110*, 142–150. [CrossRef]
28. Sullivan, K.J.; Tilson, J.K.; Cen, S.Y.; Rose, D.K.; Hershberg, J.; Correa, A.; Gallichio, J.; McLeod, M.; Moore, C.; Wu, S.S. Fugl-Meyer assessment of sensorimotor function after stroke: Standardized training procedure for clinical practice and clinical trials. *Stroke* **2011**, *42*, 427–432. [CrossRef]
29. Frisoli, A.; Procopio, C.; Chisari, C.; Creatini, I.; Bonfiglio, L.; Bergamasco, M.; Rossi, B.; Carboncini, M.C. Positive effects of robotic exoskeleton training of upper limb reaching movements after stroke. *J. Neuroeng. Rehabil.* **2012**, *9*, 36. [CrossRef]
30. Ellis, M.D.; Schut, I.; Dewald, J.P. Flexion synergy overshadows flexor spasticity during reaching in chronic moderate to severe hemiparetic stroke. *Clin. Neurophysiol.* **2017**, *128*, 1308–1314. [CrossRef]
31. Straathof, P.T.; Lobo-Prat, J.; Schilder, F.; Kooren, P.N.; Paalman, M.I.; Stienen, A.H.; Koopman, B.F. Design and control of the A-Arm: An active planar arm support for adults with Duchenne muscular dystrophy. In Proceedings of the 2016 6th IEEE International Conference on Biomedical Robotics and Biomechatronics (BioRob), Singapore, 26–29 June 2016; pp. 1242–1247.
32. Heyer, P.; Orihuela-Espina, F.; Castrejón, L.R.; Hernández-Franco, J.; Sucar, L.E. Sensor Abstracted Extremity Representation for Automatic Fugl-Meyer Assessment. In *Applications for Future Internet*; Springer: Cham, Switzerland, 2017; pp. 152–163.
33. Wang, J.; Yu, L.; Wang, J.; Guo, L.; Gu, X.; Fang, Q. Automated Fugl-Meyer assessment using SVR model. In Proceedings of the 2014 IEEE International Symposium on Bioelectronics and Bioinformatics (IEEE ISBB 2014), Chung Li, Taiwan, 11–14 April 2014; pp. 1–4.
34. Villán-Villán, M.A.; Pérez-Rodríguez, R.; Gómez, C.; Opisso, E.; Tormos, J.M.; Medina, J.; Gómez, E.J. A First Step for the Automation of Fugl-Meyer Assessment Scale for Stroke Subjects in Upper Limb Physical Neurorehabilitation. In Proceedings of the International Conference on Informatics, Management and Technology in Healthcare, Athens, Greece, 9–11 July 2015; pp. 45–48.
35. Oña, E.D.; Jardón, A.; Monge, E.; Molina, F.; Cano, R.; Balaguer, C. Towards Automated Assessment of Upper Limbs Motor Function Based on Fugl-Meyer Test and Virtual Environment. In Proceedings of the International Conference on NeuroRehabilitation, Pisa, Italy, 16–20 October 2018; pp. 297–301.
36. Eichler, N.; Hel-Or, H.; Shimshoni, I.; Itah, D.; Gross, B.; Raz, S. 3D motion capture system for assessing patient motion during Fugl-Meyer stroke rehabilitation testing. *IET Comput. Vis.* **2018**, *12*, 963–975. [CrossRef]
37. Kim, W.-S.; Cho, S.; Baek, D.; Bang, H.; Paik, N.-J. Upper extremity functional evaluation by Fugl-Meyer assessment scoring using depth-sensing camera in hemiplegic stroke patients. *PLoS ONE* **2016**, *11*, e0158640. [CrossRef] [PubMed]
38. Lee, W.W.; Yen, S.-C.; Tay, E.B.A.; Zhao, Z.; Xu, T.M.; Ling, K.K.M.; Ng, Y.-S.; Chew, E.; Cheong, A.L.K.; Huat, G.K.C. A smartphone-centric system for the range of motion assessment in stroke patients. *IEEE J. Biomed. Health Inform.* **2014**, *18*, 1839–1847. [CrossRef] [PubMed]
39. Olesh, E.V.; Yakovenko, S.; Gritsenko, V. Automated assessment of upper extremity movement impairment due to stroke. *PLoS ONE* **2014**, *9*, e104487. [CrossRef] [PubMed]

40. Otten, P.; Kim, J.; Son, S. A framework to automate assessment of upper-limb motor function impairment: A feasibility study. *Sensors* **2015**, *15*, 20097–20114. [CrossRef]
41. Otten, P.; Son, S.H.; Kim, J. Automating stroke patient evaluation using sensor data and SVM. In Proceedings of the 2014 IEEE 7th International Conference on Service-Oriented Computing and Applications, Matsue, Japan, 17–19 November 2014; pp. 223–229.
42. Lee, S.; Lee, Y.-S.; Kim, J. Automated evaluation of upper-limb motor function impairment using Fugl-Meyer assessment. *IEEE Trans. Neural Syst. Rehabil. Eng.* **2017**, *26*, 125–134. [CrossRef]
43. Lee, S.-H.; Song, M.; Kim, J. Towards clinically relevant automatic assessment of upper-limb motor function impairment. In Proceedings of the 2016 IEEE-EMBS International Conference on Biomedical and Health Informatics (BHI), Las Vegas, NV, USA, 24–27 February 2016; pp. 148–151.
44. Kim, Y.M.; Son, Y.; Kim, W.; Jin, B.; Yun, M.H. Classification of children's sitting postures using machine learning algorithms. *Appl. Sci.* **2018**, *8*, 1280. [CrossRef]
45. Paredes-Madrid, L.; Emmi, L.; Garcia, E.; De Santos, P.G. Detailed study of amplitude nonlinearity in piezoresistive force sensors. *Sensors* **2011**, *11*, 8836–8854. [CrossRef]
46. Parmar, S.; Khodasevych, I.; Troynikov, O. Evaluation of flexible force sensors for pressure monitoring in treatment of chronic venous disorders. *Sensors* **2017**, *17*, 1923. [CrossRef]
47. Rivera, J.; Carrillo, M.; Chacón, M.; Herrera, G.; Bojorquez, G. Self-calibration and optimal response in intelligent sensors design based on artificial neural networks. *Sensors* **2007**, *7*, 1509–1529. [CrossRef]
48. Almassri, A.; Wan Hasan, W.; Ahmad, S.; Shafie, S.; Wada, C.; Horio, K. Self-calibration algorithm for a pressure sensor with a real-time approach based on an artificial neural network. *Sensors* **2018**, *18*, 2561. [CrossRef]
49. Likitlersuang, J.; Leineweber, M.J.; Andrysek, J. Evaluating and improving the performance of thin film force sensors within body and device interfaces. *Med. Eng. Phys.* **2017**, *48*, 206–211. [CrossRef] [PubMed]
50. Ide, D.T.A. Available online: https://www.arduino.cc/en/Main/Software (accessed on 1 January 2019).
51. Alsayed, A.; Kamil, R.; Ramli, H.R.; As'arry, A. Design and Calibration of Pinch Force Measurement Using Strain Gauge for Post-Stroke Patients. *Int. J. Integr. Eng.* **2019**, 11. [CrossRef]
52. Oh, J.; Kim, J.O.; Kim, Y.; Choi, H.B.; Yang, J.C.; Lee, S.; Pyatykh, M.; Kim, J.; Sim, J.Y.; Park, S. Highly Uniform and Low Hysteresis Piezoresistive Pressure Sensors Based on Chemical Grafting of Polypyrrole on Elastomer Template with Uniform Pore Size. *Small* **2019**, *15*, 1901744. [CrossRef] [PubMed]
53. Matute, A.; Paredes-Madrid, L.; Gutierrez, E.; Vargas, C.A.P. Characterization of drift and hysteresis errors in force sensing resistors considering their piezocapacitive effect. In Proceedings of the 2017 IEEE SENSORS, Glasgow, UK, 29 October–1 November 2017; pp. 1–3.
54. Reed, G.F.; Lynn, F.; Meade, B.D. Use of coefficient of variation in assessing variability of quantitative assays. *Clin. Diagn. Lab. Immunol.* **2002**, *9*, 1235–1239. [CrossRef]
55. Zheng, Y.; Zhao, M.; Jiang, J.; Song, L. Dynamic Force Transducer Calibration Based on Electrostatic Force. *IEEE Access* **2019**, *7*, 48998–49003. [CrossRef]
56. Maleki-Ghahfarokhi, A.; Dianat, I.; Feizi, H.; Asghari-Jafarabadi, M. Influences of gender, hand dominance, and anthropometric characteristics on different types of pinch strength: A partial least squares (PLS) approach. *Appl. Ergon.* **2019**, *79*, 9–16. [CrossRef]
57. Angst, F.; Drerup, S.; Werle, S.; Herren, D.B.; Simmen, B.R.; Goldhahn, J. Prediction of grip and key pinch strength in 978 healthy subjects. *BMC Musculoskelet. Disord.* **2010**, *11*, 94. [CrossRef]
58. Cronbach, L.J. Coefficient alpha and the internal structure of tests. *Psychometrika* **1951**, *16*, 297–334. [CrossRef]
59. Blennerhassett, J.M.; Carey, L.M.; Matyas, T.A. Grip force regulation during pinch grip lifts under somatosensory guidance: Comparison between people with stroke and healthy controls. *Arch. Phys. Med. Rehabil.* **2006**, *87*, 418–429. [CrossRef] [PubMed]
60. Takamuku, S.; Gomi, H. Better grip force control by attending to the controlled object: Evidence for direct force estimation from visual motion. *Sci. Rep.* **2019**, *9*, 13114. [CrossRef]
61. Roberge, J.-P.; Ruotolo, W.; Duchaine, V.; Cutkosky, M. Improving industrial grippers with adhesion-controlled friction. *IEEE Robot. Autom. Lett.* **2018**, *3*, 1041–1048. [CrossRef]
62. Miall, R.C.; Rosenthal, O.; Ørstavik, K.; Cole, J.D.; Sarlegna, F.R. Loss of haptic feedback impairs control of hand posture. *Exp. Brain Res.* **2019**, *237*. [CrossRef] [PubMed]
63. Barrea, A.; Bulens, D.C.; Lefèvre, P.; Thonnard, J.-L. Simple and reliable method to estimate the fingertip static coefficient of friction in precision grip. *IEEE Trans. Haptics* **2016**, *9*, 492–498. [CrossRef] [PubMed]

64. Hall, D. (e) in Normandy: The sociolinguistics, phonology and phonetics of the Loi de Position. *J. Fr. Lang. Stud.* **2019**, *29*, 1–33. [CrossRef]
65. Derler, S.; Gerhardt, L.-C.; Lenz, A.; Bertaux, E.; Hadad, M. Friction of human skin against smooth and rough glass as a function of the contact pressure. *Tribol. Int.* **2009**, *42*, 1565–1574. [CrossRef]
66. Sivamani, R.K.; Wu, G.C.; Gitis, N.V.; Maibach, H.I. Tribological testing of skin products: Gender, age, and ethnicity on the volar forearm. *Ski. Res. Technol.* **2003**, *9*, 299–305. [CrossRef] [PubMed]
67. Li, W.; Qu, S.; Zhou, Z. Reciprocating sliding behaviour of human skin in vivo at lower number of cycles. *Tribol. Lett.* **2006**, *23*, 165. [CrossRef]
68. Petersen, P.; Petrick, M.; Connor, H.; Conklin, D. Grip strength and hand dominance: Challenging the 10% rule. *Am. J. Occup. Ther.* **1989**, *43*, 444–447. [CrossRef]
69. Li, K.W.; Yu, R. Assessment of grip force and subjective hand force exertion under handedness and postural conditions. *Appl. Ergon.* **2011**, *42*, 929–933. [CrossRef]

applied sciences

MDPI

Article

Investigation of the Functional Decline in Proprioceptors for Low Back Pain Using the Sweep Frequency Method

Reiya Nishio [1,*], Yohei Ito [1], Yoshifumi Morita [1], Tadashi Ito [2], Kazunori Yamazaki [3] and Yoshihito Sakai [4]

[1] Department of Electrical and Mechanical Engineering, Graduate School of Engineering, Nagoya Institute of Technology, Nagoya 466-8555, Japan; y.ito.359@nitech.jp (Y.I.); morita@nitech.ac.jp (Y.M.)
[2] Three-Dimensional Motion Analysis Room, Aichi Prefectural Mikawa Aoitori Medical and Rehabilitation Center for Developmental Disabilities, Okazaki 444-0002, Japan; sanjigen@mikawa-aoitori.jp
[3] Faculty of Clinical Engineering, School of Medical Sciences, Fujita Health University, Toyoake 470-1192, Japan; ymzkk@fujita-hu.ac.jp
[4] Department of Orthopedic Surgery, National Center for Geriatrics and Gerontology, Obu 474-8511, Japan; jsakai@ncgg.go.jp
* Correspondence: r.nishio.115@nitech.jp; Tel.: +81-52-735-5412

Received: 24 October 2019; Accepted: 18 November 2019; Published: 20 November 2019

Abstract: The purpose of this study was to investigate the functional decline in proprioceptors in patients with low back pain (LBP) by evaluating the entire range of response frequencies of proprioceptors. In previous studies, the function of proprioceptors was only evaluated by single frequency vibrations. However, because it is assumed that individual differences exist in response frequencies of proprioceptors, we developed a method using vibration with sweep frequency covering the entire range of response frequencies of proprioceptors. The center of pressure was determined in 35 elderly patients with non-specific LBP (NSLBP) and 28 elderly individuals with non-LBP (NLBP) during upright stances on a balance board without vision. Local vibratory stimulations to lower leg or trunk muscles were continuously varied between 27 and 272 Hz over 60 s to evaluate the proprioceptive predominance of a body location using the relative proprioceptive weighting ratio (RPW). Compared with the NLBP group, the NSLBP group exhibited a lower RPW value for the Vater-Pacini corpuscles. Thus, the NSLBP group relied more on the input of Vater-Pacini corpuscles in the trunk. A reduction in lower leg sensitivity at the Vater-Pacini corpuscles in the NSLBP group was observed.

Keywords: vibratory stimulation device; local muscle vibration; proprioceptors; low back pain; response frequency; postural control; Vater-Pacini corpuscles

1. Introduction

Worldwide, low back pain (LBP) has become the main cause of disability [1]. However, its causes are unidentifiable in 85% of the cases [2]. Postural control impairment is considered one of the main causes of LBP [3]. Postural control is affected by sensory inputs from visual and vestibular senses and somatosensory receptors which provide superficial and proprioception. A previous study indicated that the feedback control on the trunk posture is mainly influenced by the visual and proprioception [4]. Also, another previous study suggested that the ability to select and reweigh sensory inputs to adapt to situations is a critical factor for postural control [5]. In addition, non-specific LBP (NSLBP) may alter postural control by refocusing proprioception from the trunk to the ankles [6]. Furthermore, reduced precision of trunk movement in NSLBP might be explained by proprioceptive deficits [7]. Therefore, NSLBP could be caused by a decline in proprioception leading to problems in postural control and LBP.

Proprioception in the lower leg and trunk muscle plays an important role in maintaining postural stability [8]. Each proprioceptor has a response frequency of vibration. Meissner corpuscles are sensitive to lower vibration frequencies (peaks around 30 Hz), whereas the Vater-Pacini corpuscles are sensitive to higher frequencies (peaks around 240 Hz) [9]. Muscle spindles have a response frequency range of 40–100 Hz [10]. Mechanical vibration is commonly used to test externally induced balance control. This method has been widely used to investigate the role of muscle spindle in research focusing on postural control [11–14]. However, the role of other proprioceptors in NSLBP has not been evaluated. Thus, comparing postural sway of NSLBP during various local frequency vibrations with that of non-LBP (NLBP) will allow determination of the cause of LBP and frequencies of proprioception deficit.

Postural sway of NSLBP during local frequency vibrations of 30, 60 and 240 Hz has been compared with that of NLBP in our previous study. From the result, we found that not only does NSLBP involve the functional impairment of muscle spindles that other groups reported [11–13] but also Vater-Pacini corpuscles were functionally declined because of LBP [15,16]. However, in previous studies, only one frequency of vibration stimulation was applied within the range of response frequencies for each proprioceptor [11–13,15,16]. In addition, other studies investigating muscle spindle response to multiple vibration frequencies reported different results. A previous study using 90 Hz vibration frequency suggested that the weighting of proprioceptive feedback from lumbar muscle spindles did not differ between NSLBP and NLBP [17]. On the other hand, another previous study using 60 Hz vibration frequency suggested that LBP patients rely less on proprioceptive feedback from lumbar muscle spindles [18]. From these results, it is implied that the postural response induced by mechanical vibration varies with the applied vibration frequency even in one proprioceptor. Also, it is assumed that there are individual differences in response frequencies of proprioceptors. To the best of our knowledge, a protocol for measuring postural control while applying local vibration stimulation in the entire response frequency band has not been developed. Thus, we considered that the inspection device and a protocol for evaluating postural response in the range of the entire response frequencies of the proprioceptors are necessary.

Therefore, we developed a new experimental protocol to measure the center of pressure (CoP) of an individual on a gravicorder during local mechanical vibration with sweep frequencies, using our developed variable frequency vibratory stimulation device. This method can be analyzed by applying a vibration stimulus once in the entire frequency range covering the response frequencies of each proprioceptor. For this reason, there is a possibility that this method can identify proprioceptors related to NSLBP and the functionally declined frequency bands of proprioceptors. In addition, the method might be capable of more detailed analyses because the vibration is stimulated with the entire frequency range covering the response frequencies of each proprioceptor. Furthermore, this method is considered to be the shortest for measuring all the response frequency bands of the three proprioceptors. The physical burden on subjects during measurement can also be reduced because the measurement time can be shortened by about 4 min and 30 s compared with the time required for the conventional method with a constant frequency. Our final goal is to develop an inspection device for evaluating the functional decline in proprioceptors. In this study, we aimed to investigate the relationship between proprioception and LBP. Thus, postural sway response in NSLBP and NLBP was measured with our new sweep frequency method and compared with the responses obtained from past studies using the method of constant frequency.

2. Materials and Methods

2.1. Subjects

This study was carried out during a period of 30 months (August 2016–July 2019) in tandem with general clinical practice. Written informed consent was obtained from all participants before inclusion in the study. All investigations were conducted according to the principles expressed in the

Declaration of Helsinki. The Ethics Committee of the National Center for Geriatrics and Gerontology approved the study (IRB approval number: 586).

Sixty-three elderly individuals (age ≧ 65 years: age range 65–90; sex ratio: 36 women/27 men) were recruited, including 35 patients (22 women, 13 men) with NSLBP which lasted over 3 months who visited the National Center for Geriatric and Gerontology for orthopedic treatment. Among the recruited individuals, 28 individuals with NLBP (14 women and 14 men) acted as controls with no history of disabling NSLBP which is defined as LBP when the pathoanatomical cause of the pain cannot be determined [19]. Patients with the following characteristics were excluded—paralysis, astasia, spinal cord tumor, spinal infection and history of spinal surgery. Demographics of all individuals are presented in Table 1.

Table 1. Demographic characteristics and functional outcome of the patients.

Variables	NLBP (n = 28)	NSLBP (n = 35)	p
Age, years	75.9 ± 5.4	75.1 ± 5.2	0.552
Height, cm	154.8 ± 7.7	153.2 ± 7.3	0.410
Weight, kg	59.8 ± 11.4	57.7 ± 10.5	0.609
BMI, kg/m^2	24.8 ± 3.3	24.5 ± 3.7	0.774
VAS, cm	2.4 ± 2.5	6.2 ± 2.4	<0.001
RDQ (score)	9.1 ± 5.8	11.8 ± 4.0	<0.05

BMI: body mass index; NLBP: non-low back pain; NSLBP: non-specific low back pain; VAS: visual analog scale; RDQ: Roland-Morris disability questionnaire; SD: standard deviation. Data are presented as the mean ± SD. All p values were generated using the independent t-test, Mann-Whitney u test.

2.2. Device

Figure 1a,b shows an inspection system for evaluating the functional decline in proprioceptors. The system consists of a PC, an amplifier, four vibrators (NSW1-205-8A, Aurasound, Inc., CA, USA), three hook-and-loop fasteners and a Wii Balance Board (Nintendo Co., Ltd., Kyoto, Japan). Two hook-and-loop fasteners with one vibrator were used for the left and right lower legs and one hook-and-loop fastener with two vibrators was used for the left and right parts of the trunk.

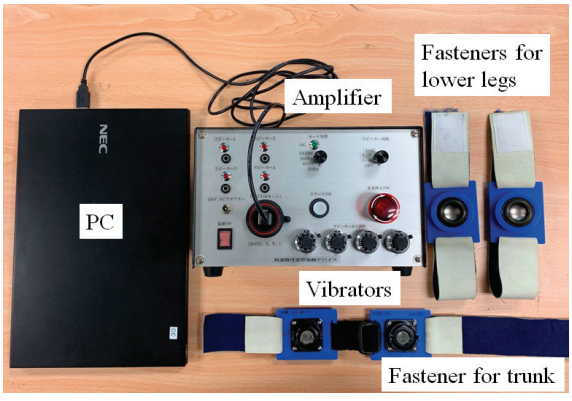

(**a**)

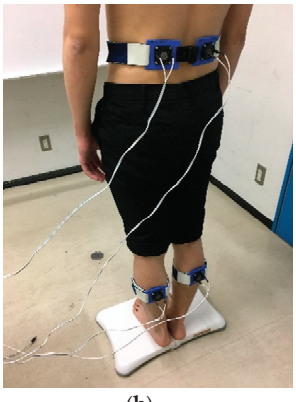

(**b**)

Figure 1. Inspection system for proprioceptive function: (**a**) Variable frequency vibratory stimulation device; and (**b**) experimental setup for a participant.

Vibration signals were generated using the PC. Then, vibrations were output from the vibrators as a mechanical vibration stimulus through the amplifier. In other previous studies, the mechanical vibration stimulus with an amplitude of 0.4 to 1.0 mm was used as the proprioceptive input [10,11,13].

Also, the maximum amplitude of our developed device which can be output without distortion of mechanical vibration at each frequency from 20 to 300 Hz is 0.8 mm. Thus, the amplitude of the vibration was selected at 0.8 mm of a sinusoidal wave. Vibrators were attached to the hook-and-loop fasteners using holders and fixed to the muscle belly of the gastrocnemius (GS) and the lumbar multifidus (LM) muscles. The contact pressure to the body locations of the vibrators was regulated by changing the length of the hook-and-loop fasteners according to the circumference of the fixed body locations. A Wii Balance Board was used as a gravicorder. The CoP was measured instead of the center of gravity. A Wii Balance Board has been reported as a reliable and valid tool for assessing standing balance [20]. It can acquire the time series data of CoP coordinates with a sampling frequency of 100 Hz. Moreover, it is possible to save the CoP as CSV data by running the self-made CoP data collection software on a PC connected with the Wii Balance Board via Bluetooth.

2.3. Experimental Method

The CoP in postural sway while the participant stood barefoot on the Wii Balance Board with his/her eyes closed and feet together was measured. Participants were instructed to remain still and relaxed in the standing position with their arms hanging loosely at their sides. In order to prevent injuries due to falls during measurements, two researchers stood on both sides of a subject with eyes closed. They paid attention to whether or not the subject was likely to fall and gave support if the subject was falling. As the vibration frequency, a sweep frequency (Figure 2) was used. The vibration was continuously changed from 27 Hz to 272 Hz (frequency ascend mode) or 272 Hz to 27 Hz (frequency descend mode) for 60 s, thus covering the response frequency ranges of the three proprioceptors. The relationships of sweep frequency between frequency $f(t)$ and measurement time t are shown in Equations (1) and (2). The coefficient a was determined so that the frequencies at t = 15 s and 75 s were set to 27 Hz and 272 Hz in the frequency ascend mode, respectively. Thus, the coefficient a was found to be 0.03851. Furthermore, the frequency descend mode had the same frequencies at t = 15 s and 75 s (272 Hz and 27 Hz, respectively).

$$f(t) = \begin{cases} 0 \ (0 \le t \le 15) \\ 27e^{a(t-15)} (15 \le t \le 75) \end{cases} \quad \text{(frequency ascend mode)} \tag{1}$$

$$f(t) = \begin{cases} 0 \ (0 \le t \le 15) \\ 27e^{a(75-t)} (15 \le t \le 75) \end{cases} \quad \text{(frequency descend mode)} \tag{2}$$

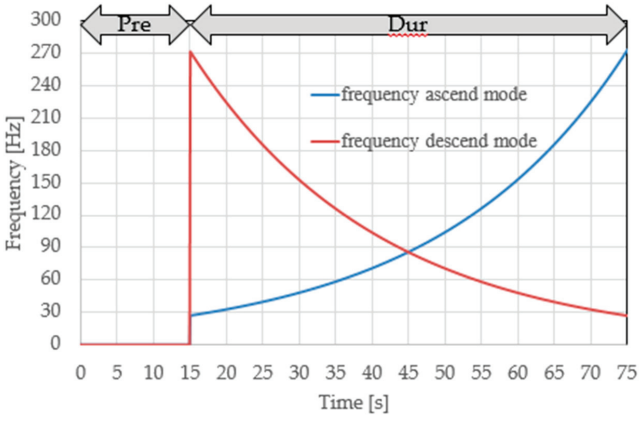

Figure 2. Sweep frequency of vibratory stimulation.

The measurement procedure consisted of two conditions that provided vibration stimulus—GS and LM. The time needed for one condition was 75 s and was divided into two sections. The first 15 s and last 60 s sections are referred to as Pre- and Dur-sections, respectively. In the Pre-section, a participant closed his/her eyes. Then, in the Dur-section, the vibratory stimulation was applied to the GS or LM of the participant with his/her eyes closed. The ascend or descend sweep frequency mode was randomly determined for each subject. A rest interval of 60 s was kept between the conditions. During this time, each participant sat in a chair and remained at rest.

2.4. Data Analysis Method

The postural control performance was evaluated from the CoP data while vibration stimulation was applied. Furthermore, the CoP data divided the Dur-section into three evaluation sections (ES_i, i = 1, 2, 3) determined according to the frequency of vibration stimulation and the response frequencies of the proprioceptors. Table 2 lists the names of each ES, the frequency of the vibration stimulus and the corresponding proprioceptors.

Table 2. Lists of names of each ES, frequency of vibration stimulus and corresponding proprioceptors.

ES_i	Frequency [Hz]	Corresponding Proprioceptors
ES_1	30–43	Meissner corpuscle
ES_2	49–71	Muscle spindles
ES_3	168–247	Vater-Pacini corpuscle

ES: Evaluation section.

Because the previous studies showed that a relationship existed between CoP displacement in an anteroposterior direction and the response of proprioceptors by vibration stimulus, the CoP displacement in the anteroposterior direction was only considered [10]. Previous studies used the relative proprioceptive weighting ratio (RPW) and the root mean square (RMS) of GS and LM as evaluation indexes to evaluate the proprioceptive predominance of body location and the magnitude of CoP in an anteroposterior direction [11,15,18]. The evaluation indexes applicable to the sweep frequency method were introduced as follows.

To obtain information regarding the proprioceptive predominance of body locations, modified RPW was calculated using the following equation.

$$RPW^i = \frac{RMS^i_{GS}}{RMS^i_{GS} + RMS^i_{LM}} \times 100\ [\%] \quad (i = 1,\ 2,\ 3) \tag{3}$$

where the subscript i is used to distinguish the ESs. The higher is the value of RPW^i from 50% to 100%, the higher is the reliability of GS input. On the other hand, the lower is the value of RPW^i from 50% to 0%, the higher is the reliability of LM input [11,15]. RMS^i_* means the effective value of the magnitude of CoP in an anteroposterior direction. In each ES in the Dur-section, the larger the RMS, the higher the amount of transition of postural sway in the anteroposterior direction compared to those in the Pre-section. RMS^i_* was calculated using the following equations.

$$RMS^1_* = \sqrt{\frac{1}{N}\sum_{n=n_1}^{n_2}\left\{Y_{Dur(*)}(n) - \overline{Y}_{pre(*)}\right\}^2} \tag{4}$$

$$RMS^2_* = \sqrt{\frac{1}{N}\sum_{n=n_3}^{n_4}\left\{Y_{Dur(*)}(n) - \overline{Y}_{pre(*)}\right\}^2} \tag{5}$$

$$RMS_*^3 = \sqrt{\frac{1}{N}\sum_{n=n_5}^{n_6}\left\{Y_{Dur(*)}(n) - \overline{Y}_{pre(*)}\right\}^2} \quad (6)$$

where N is the total sampling number of each ES; n is the number of data series; $Y_{Dur(*)}(n)$ is the CoP in the anteroposterior direction in the Dur-section; $\overline{Y}_{pre(*)}$ is the mean value of CoP in the anteroposterior direction in the Pre-section; the superscript "∗" is used to distinguish stimulation body locations, namely, the GS or LM; and subscript numbers are used to distinguish the ESs. In this case, N was equal to 1000 because all ESs were analyzed in 10 s and the sampling frequency was 100 Hz. Table 3 shows the numbers of data series corresponding to the start frequency and the end frequency of ES_i in the case of frequency ascend mode and descend mode. In each of the ascend and descend modes, the numbers of sampling series n corresponding to measurement time t were calculated by Equations (1) and (2) in order to obtain the start and end frequencies of each ES, respectively, as shown in Table 2. To correct the CoP in the Dur-section based on the CoP in the Pre-section, the CoP in the Dur-section was subtracted from the mean value of the CoP in the Pre-section. These values were calculated using MATLAB (MathWorks, Inc., Natick, MA, USA).

Table 3. Numbers of data series corresponding to the start and end frequencies of ES_i.

ES_i	Number of Data Series	Frequency Ascend Mode	Frequency Descend Mode	Corresponding Frequency [Hz]
ES_1	n_1	1750	7250	30
	n_2	2750	6250	43
ES_2	n_3	3000	6000	49
	n_4	4000	5000	71
ES_3	n_5	6250	2750	168
	n_6	7250	1750	247

ES: evaluation section; n: the number of data series; The subscript numbers of ES are indicated as follows: "1: Meissner corpuscle; from 30 to 43 Hz; 2: muscle spindles; from 49 to 71 Hz, 3: Vater-Pacini corpuscle; from 168 to 247 Hz."

2.5. Statistical Analysis

All analyses were performed using IBM SPSS statistical software (Version 25.0; IBM Corp., Armonk, NY, USA). The frequency ascend and descend modes groups were combined into a population of RPW^i and RMS_*^i for statistical analysis to eliminate the order effects due to vibration application. Data were expressed as mean values and standard deviations for the NLBP and NSLBP. First, these data were analyzed to investigate whether they were normally distributed using the Shapiro-Wilk test. Variable data of RPW^i were compared between NLBP and NSLBP using the independent t-test if both the compared data were normally distributed. In statistical analysis, $p < 0.05$(*) were considered statistically significant. In addition, a two-way mixed analysis of variance (ANOVA) was performed with RMS as the dependent variable. The independent variables were group (NSLBP group or NLBP group) and the stimulated body locations (GS or LM). Where significant interaction effects were identified, paired t-tests and univariate analysis with Bonferroni correction were conducted.

3. Results

3.1. Proprioceptive Postural Control

Table 4 shows the results of RPW^i. For each evaluation index, the mean values and SDs analyzed in the 3 sections are shown. The RPW values of NSLBP were smaller than 50%. NSLBP had a significantly smaller RPW compared with NLBP in Vater-Pacini corpuscles ($p < 0.05$). Meanwhile, there were no significant differences in the RPW values of Meissner corpuscles and muscle spindle between NSLBP and NLBP groups (Table 4).

Table 4. Mean values of RPW^{i} with standard deviations.

Variable	NLBP	NSLBP	*p*
RPW^{1} [%]	52.2 ± 13.2	48.2 ± 9.3	0.184
RPW^{2} [%]	53.8 ± 11.8	49.1 ± 10.2	0.092
RPW^{3} [%]	53.3 ± 12.5	46.4 ± 9.8	<0.05

NLBP: non-low back pain; NSLBP: non-specific low back pain; RPW: relative proprioceptive weighting ratio. Data are presented as the mean ± standard deviation or *n* [%]. All *p* values were generated using an independent *t*-test. The superscript numbers indicated the following: "1: Meissner corpuscle; from 30 to 43 Hz; 2: muscle spindles; from 49 to 71 Hz, 3: Vater-Pacini corpuscle; from 168 to 247 Hz."

3.2. Postural Stability

Table 5 shows a result of a two-way mixed ANOVA in RMS^{i}_{*}. There was no significant interaction between the NLBP and NSLPB group and the stimulated body locations in the Meissner corpuscle and muscle spindle. In contrast, the interaction between the NLBP and NSLPB groups and the stimulated body locations in Vater-Pacini corpuscles were significantly observed ($p < 0.05$).

Figure 3 depicts the results of RMS in Vater-Pacini corpuscle. Compared with NLBP group, univariate analysis with Bonferroni correction showed that the NSLBP group exhibited significantly higher RMS values at LM in the Vater-Pacini corpuscle ($F(1,61) = 4.817$, $p < 0.05$), whereas there was no significant difference in the RMS values at GS in the Vater-Pacini corpuscle ($F(1,61) = 0.115$, $p = 0.735$). In addition, the paired *t*-test showed that there was a tendency of significantly higher RMS values at LM than at GS in the NSLBP group ($p = 0.055$). There was no significant difference between GS and LM in the NLBP group ($p = 0.189$).

Table 5. Results of RMS^{i}_{*} and two-way mixed analysis of variance.

Variable	NLBP	NSLBP	F(1, 61)	*p*
RMS^{1}_{GS} [mm]	10.7 ± 7.8	8.9 ± 4.3	2.874	0.095
RMS^{1}_{LM} [mm]	8.7 ± 4.0	9.5 ± 4.3		
RMS^{2}_{GS} [mm]	10.9 ± 7.4	9.6 ± 4.6	2.624	0.110
RMS^{2}_{LM} [mm]	8.8 ± 4.3	9.7 ± 4.5		
RMS^{3}_{GS} [mm]	9.6 ± 4.0	9.2 ± 3.9	5.255	<0.05
RMS^{3}_{LM} [mm]	8.4 ± 3.6	10.8 ± 4.9		

NLBP: non-low back pain; NSLBP: non-specific low back pain; RMS: root mean square of the center of pressure data. Data are presented as the mean ± standard deviation or *n* [%]. All F value and *p* values were generated using the two-way mixed analysis of variance. Independent variables: the NLBP and NSLPB group and the stimulated body locations. The subscripts and superscript numbers indicated the following: "GS: gastrocnemius; LM: lumbar multifidus; 1: Meissner corpuscle; from 30 to 43 Hz; 2: muscle spindles; from 49 to 71 Hz, 3: Vater-Pacini corpuscle; from 168 to 247 Hz."

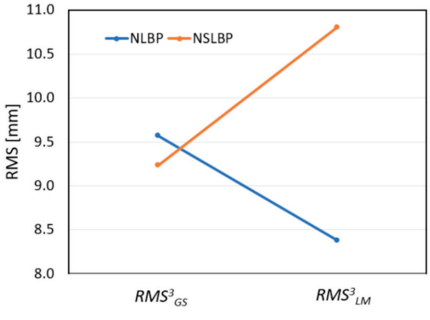

Figure 3. Result of RMS in Vater-Pacini corpuscle. RMS indicates root mean square of the center of pressure data; GS: gastrocnemius; LM: lumbar multifidus.

4. Discussion

To our knowledge, this is the first study to evaluate the postural response when vibration was applied in the entire response frequency range of proprioceptors using sweep frequency. Our main finding was that NSLBP relied more on LM input in the Vater-Pacini corpuscles during vibratory stimulus with a sweep frequency of 168–247 Hz to the lower leg in the standing position.

Past studies have already demonstrated that elderly patients with LBP relied on trunk strategies (Vater-Pacini corpuscles) for postural control during vibratory stimulation [15,16]. Compared with NLBP, lower RPW values in NSLBP during vibratory stimulations of 168 to 247 Hz indicate that NSLBP relies on trunk-muscle proprioceptive inputs. Moreover, the reduction in lower leg sensitivity at the Vater-Pacini corpuscles in the NSLBP group agrees well with the result of previous studies which reported that the NSLBP group decreased its reliance on proprioceptive signals from the lower leg during standing at 240 Hz of constant vibratory stimulus [15,16]. However, statistically significant differences were not observed between the NLBP and NSLBP groups in the Meissner corpuscles and muscle spindle. The decreased reliability on LM inputs in the Meissner corpuscles and muscle spindle may not have been recognized in the NSLBP group because this study was performed under different conditions from measurement methods and subjects in the previous studies [10–12,21–24]. In addition, the differences in age and LBP degree may have affected even the same cases of disease [15,16]. Therefore, the NSLBP group may depend more on the Vater-Pacini corpuscles of their trunk than on the Meissner corpuscles and muscle spindle.

Second, the resulting RMS values were considered. A significant interaction between the NLBP and NSLPB groups and the stimulated body location in Vater-Pacini corpuscles was confirmed. From Figure 3, the NSLBP group exhibited higher RMS values when vibration in the frequency band of the Vater-Pacini corpuscles was applied to LM. This result supports that the NSLBP group relied more on LM input in the Vater-Pacini corpuscles for postural control. These results agree well with those of previous studies where significant differences in postural sways were found between elderly individuals and healthy young adults during quiet standing conditions [25]. Moreover, a decreasing trend in the proprioceptive function in lower leg was observed in the NSLBP group. These findings clearly show the differences in postural control strategies of proprioceptive inputs with respect to NSLBP, suggesting that LBP may influence the postural control strategy of proprioceptive inputs derived from the Vater-Pacini corpuscles of the LM.

For the above reasons, we confirmed that the function of the Vater-Pacini corpuscles was decreased in relation to LBP using the sweep frequency method. Ito et al. reported that patients with NSLBP may have even greater postural instability because the sensitivity of GS at 240 Hz continues to decline [15]. Thus, the reduction possibly causes postural instability because the NSLBP group cannot switch to a more appropriate proprioceptive postural strategy. In addition, the effect of RPW on postural control under proprioceptive stimulation with the response frequency of Vater-Pacini corpuscles may be a good indicator of evaluating the degree of LBP under the sweep frequency method, same as the constant frequency method used in our previous study [15]. These findings could be used to diagnose NSLBP due to the reduced function of proprioceptors. The advantages of using the sweep frequency are as follows. Firstly, the sweep frequency method may eliminate individual differences in the response frequency of proprioceptors. Secondly, the resolution is high because the vibration is applied to the entire frequency band of the response frequency of each proprioceptor. In the future, it may be possible to conduct more detailed proprioceptive examination by analyzing finer frequency bands. Additionally, there is a possibility that the inspection using this method can identify the detailed frequency band of proprioceptors related to NSLBP. Thirdly, the examination time could be shortened. The measurement time of the sweep frequency method can be shortened by 4 min and 30 s compared with the time required for the constant frequency method used in our previous study. Thus, this method can reduce the burden on patients. Therefore, the method using sweep frequency could replace the conventional constant frequency method because it can measure the entire frequency band of proprioceptors in a short time.

Nevertheless, this study has a limitation in that only elderly persons with lumbar spondylosis were surveyed. Therefore, additional studies with healthy older persons and those with more severe disability must be conducted. Finally, the evaluation of the entire range of response frequencies of proprioceptors using sweep frequency could benefit from future studies investigating more optimal stimulation of response frequencies.

5. Conclusions

In this study, we aimed to investigate the functional decline in proprioceptors related to LBP by evaluating the entire range of response frequencies of proprioceptors using sweep frequency. Thus, we developed a variable frequency vibratory stimulation device and measured the CoP of NSLBP and NLBP on a Wii Balance Board during local vibration with sweep frequencies. As a result, compared with the NLBP group, the NSLBP group showed a reduction in lower leg sensitivity at Vater-Pacini corpuscles. Moreover, we believe that the sweep frequency method can replace the conventional constant frequency method because it can measure the entire frequency band of proprioceptors in a short time. Our future work will include investigating the treatment effect of vibration with the frequency evaluated by this device.

Author Contributions: Conceptualization, Y.M. and Y.S.; methodology, Y.M.; software, R.N., Y.I. and K.Y.; validation, T.I.; formal analysis, R.N.; investigation, R.N., Y.I., T.I. and K.Y.; resources, Y.M. and Y.S.; data curation, R.N. and Y.I.; writing—original draft preparation, R.N.; writing—review and editing, Y.I., Y.M., T.I., K.Y. and Y.S.; visualization, R.N.; supervision, Y.M.; project administration, Y.M. and Y.S.; funding acquisition, Y.S.

Funding: This research was funded by Geriatrics and Gerontology research and development cost, grant number 29-6. The APC was funded by Geriatrics and Gerontology research and development cost.

Acknowledgments: The authors thank the staff in the Department of Orthopedic Surgery and the National Center for Geriatric and Gerontology for their help in participant recruitment. This study was supported in part by a grant from the Geriatrics and Gerontology research and development cost.

Conflicts of Interest: The authors declare no conflicts of interest.

References

1. Hoy, D.; March, L.; Brooks, P.; Blyth, F.; Woolf, A.; Bain, C.; Williams, G.; Smith, E.; Vos, T.; Barendregt, J.; et al. Global burden of low back pain: Estimates from the Global Burden of Disease 2010 study. *Ann. Rheum. Dis.* **2014**, *76*, 968–974. [CrossRef] [PubMed]
2. Andrea, R.; Cholewicki, J.; Polzhofer, G.K.; Greene, H.S. Impaired postural control of the lumbar spine is associated with delayed muscle response times in patients with chronic idiopathic low back pain. *Spine* **2001**, *26*, 724–730. [CrossRef]
3. Henry, S.; Hitt, J.; Jones, S.; Bunn, J. Decreased limits of stability in response to postural perturbations in subjects with low back pain. *Clin. Biomech.* **2006**, *21*, 881–892. [CrossRef] [PubMed]
4. Willigenburg, N.W.; Kingma, I.; van Dieën, J.H. How is precision regulated in maintaining trunk posture? *Exp. Brain Res.* **2010**, *203*, 39–49. [CrossRef] [PubMed]
5. Sean, C.; Tim, K.; John, J.J. Modeling the dynamics of sensory reweighting. *Biol. Cybern.* **2006**, *95*, 123–134. [CrossRef]
6. Johansson, R.; Magnusson, M. Human postural dynamics. *Crit. Rev. Biomed. Eng.* **1991**, *18*, 413–437.
7. Willigenburg, N.W.; Kingma, I.; Hoozemans, M.J.; van Dieën, J.H. Precision control of trunk movement in low back pain patients. *Hum. Mov. Sci.* **2013**, *32*, 228–239. [CrossRef]
8. Bloem, B.R.; Allum, J.M.; Carpenter, M.G.; Honegger, F. Is lower leg proprioception essential for triggering human automatic postural responses? *Exp. Brain Res.* **2000**, *130*, 375–391. [CrossRef]
9. Kuroki, S.; Hagura, N.; Nishida, S.; Haggard, P.; Watanabe, J. Sanshool on The Fingertip Interferes with Vibration Detection in a Rapidly-Adapting (RA) Tactile Channel. *PLoS ONE* **2016**, *11*. [CrossRef]
10. Pyykko, I.; Jantti, P.; Aalto, H. Postural control in elderly subjects. *Age Ageing* **1990**, *19*, 215–221. [CrossRef]
11. Brumagne, S.; Janssens, L.; Janssens, E.; Goddyn, L. Altered postural control in anticipation of postural instability in persons with recurrent low back pain. *Gait Posture* **2008**, *28*, 657–662. [CrossRef] [PubMed]

12. Goossens, N.; Janssens, L.; Pijnenburg, M.; Severijns, P.; Van, R.C.; Meugens, P.; Brumagne, S. Test-Retest Reliability and Concurrent Validity of an fMRI-Compatible Pneumatic Vibrator to Stimulate Muscle Proprioceptors. *Multisens. Res.* **2016**, *29*, 465–492. [CrossRef] [PubMed]
13. Capicíková, N.; Rocchi, L.; Hlavacka, F.; Chiari, L.; Cappello, A. Human postural response to lower leg muscle vibration of different duration. *Physiol. Res.* **2006**, *55*, 129–134.
14. Nima, T.; Hossein, E.; Marco, M.; Jane, M. Proprioceptive impairments in high fall risk older adults: The effect of mechanical calf vibration on postural balance. *BioMed. Eng. Online* **2018**, *17*, 51. [CrossRef]
15. Ito, T.; Sakai, Y.; Morita, Y.; Yamazaki, K.; Igarashi, K.; Nishio, R.; Sato, N. Proprioceptive Weighting Ratio for Balance Control in Static Standing Is Reduced in Elderly Patients with Non–Specific Low Back Pain. *Spine* **2018**, *43*, 1704–1709. [CrossRef]
16. Ito, T.; Sakai, Y.; Yamazaki, K.; Igarashi, K.; Sato, N.; Yokoyama, K.; Morita, Y. Proprioceptive change impairs balance control in older patients with low back pain. *J. Phys. Ther. Sci.* **2017**, *29*, 1788–1792. [CrossRef]
17. Willigenburg, N.W.; Kingma, I.; van Dieën, J.H. Precision control of an upright trunk posture in low back pain patients. *Clin. Biomech.* **2012**, *27*, 866–871. [CrossRef]
18. Brumagne, S.; Cordo, P.; Verschueren, S. Proprioceptive weighting changes in persons with low back pain and elderly persons during upright standing. *Neurosci. Lett.* **2004**, *366*, 63–66. [CrossRef]
19. Chris, M.; Martin, U.; Rachelle, B. Non-specific low back pain. *Lancet* **2017**, *389*, 736–747. [CrossRef]
20. Clark, R.A.; Mentiplay, B.F.; Pua, Y.H.; Bower, K.J. Reliability and validity of the Wii Balance Board for assessment of standing balance: A systematic review. *Gait Posture* **2018**, *61*, 40–54. [CrossRef]
21. Claeys, K.; Brumagne, S.; Dankaerts, W.; Kiers, H.; Janssens, L. Decreased variability in postural control strategies in young people with non-specific low back pain is associated with altered proprioceptive reweighting. *Eur. J. Appl. Physiol.* **2011**, *111*, 115–123. [CrossRef] [PubMed]
22. Brumagne, S.; Janssens, L.; Knapen, S.; Claeys, K.; Suuden-Johanson, E. Persons with recurrent low back pain exhibit a rigid postural control strategy. *Eur. Spine J.* **2008**, *17*, 1177–1184. [CrossRef] [PubMed]
23. Mientjes, M.I.; Frank, J.S. Balance in chronic low back pain patients compared to healthy people under various conditions in upright standing. *Clin. Biomech.* **1999**, *14*, 710–716. [CrossRef]
24. Ito, T.; Sakai, Y.; Nakamura, E.; Yamazaki, K.; Yamada, A.; Sato, N.; Morita, Y. Relationship between paraspinal muscle cross-sectional area and relative proprioceptive weighting ratio of older persons with lumbar spondylosis. *J. Phys. Ther. Sci.* **2015**, *27*, 2247–2251. [CrossRef] [PubMed]
25. Ito, T.; Sakai, Y.; Yamazaki, K.; Nishio, R.; Ito, Y.; Morita, Y. Postural Strategy in Elderly, Middle-Aged, and Young People during Local Vibratory Stimulation for Proprioceptive Inputs. *Geriatrics* **2018**, *3*, 93. [CrossRef]

applied sciences

MDPI

Article

Temporal EEG Imaging for Drowsy Driving Prediction

Eric Juwei Cheng [1,*], Ku-Young Young [1] and Chin-Teng Lin [2]

[1] Department of Electrical Engineering, National Chiao Tung University, Hsinchu 300, Taiwan; kyoung@mail.nctu.edu.tw

[2] Centre for Artificial Intelligence, University of Technology Sydney, Sydney 2007, Australia; chintenglin@gmail.com

* Correspondence: fred7018@gmail.com

Received: 21 October 2019; Accepted: 21 November 2019; Published: 25 November 2019

Abstract: As a major cause of vehicle accidents, the prevention of drowsy driving has received increasing public attention. Precisely identifying the drowsy state of drivers is difficult since it is an ambiguous event that does not occur at a single point in time. In this paper, we use an electroencephalography (EEG) image-based method to estimate the drowsiness state of drivers. The driver's EEG measurement is transformed into an RGB image that contains the spatial knowledge of the EEG. Moreover, for considering the temporal behavior of the data, we generate these images using the EEG data over a sequence of time points. The generated EEG images are passed into a convolutional neural network (CNN) to perform the prediction task. In the experiment, the proposed method is compared with an EEG image generated from a single data time point, and the results indicate that the approach of combining EEG images in multiple time points is able to improve the performance for drowsiness prediction.

Keywords: electroencephalography; deep learning; driving fatigue; feature extraction; convolutional neural network

1. Introduction

The prevention of drowsy driving has become a major challenge in safety driving issues. Many drivers experience driving in drowsy conditions, especially in long-term driving. Continuous, unexciting driving reduces the vigilance of drivers and increases the risk of traffic accidents. To address this problem, the development of brain-computer interfaces (BCIs) to investigate the human's cognitive state is an urgent necessity. Electroencephalography (EEG) is one of the most direct and effective physiological measures for the estimation of brain dynamics. Recent EEG studies have demonstrated that changes in alertness during driving are related to changes in global brain dynamics [1,2]. It has also been shown that EEG is a robust measurement for the estimation of a driver's cognitive state [3–6]. In addition, EEG provides abilities of convenient measurement in real timeand is therefore widely used in real applications [3,7–9].

Although EEG has many advantages for the analysis of brain dynamics, the use of EEG-based BCIs in real applications remains challenging. The raw EEG signals acquired from the electrodes are often obscured by physiological artifacts such as eye movement and muscle movement, which is undesirable in the BCI system [10]. Therefore, removing these unwanted artifactsto capture brain activity has become a crucial issue in EEG-based BCI applications. Many studies have shown that independent component analysis (ICA) can effectively separate the artifacts from raw EEG data [11–14]. The mixture signal is decomposed into many statistically independent components by ICA. A non-artifact signal is obtained by excluding the components that are associated with artifacts. Although ICA is a powerful tool for extracting brain activity from raw EEGsignal, it cannot support real-time applications because the separated artifacts need to be removed manually. This drawback limits the utility of ICA for

real-world BCI applications. An automatic processing BCI is strongly required for drowsy driving prediction since traffic accidents always occur in a very short time. Therefore, this study does not apply any artifact removal process to the raw EEG data during the experiment, ensuring that the proposed method does not use manual processes for the drowsy driving prediction task.

For EEG signals without artifact removal, how to correctly extract the informative features of EEG signals becomes a major challenge in BCI applications. A popular approach for feature extraction is transforming the EEG signals into a frequency domain [15,16]. Fast Fourier transform (FFT) is applied to compute the power spectra of the multi-channel time-series EEG signals into the frequency domain; then, the average of the power spectra value for each frequency is collected to obtain a feature vector for classification [3,17]. The main disadvantage of such an approach is that it only considers the frequency information. EEG is measured over the scalp in a three-dimensional space. It is obvious that the spatial information of EEG cannot be well described by a feature vector. Instead of the 1D feature vector, there is an increasing trend to use 2D feature maps for the analysis of EEG, which have achieved good performance in their application areas [18,19].

As the most popular machine learning technique in recent years, deep learning has achieved significant success in a variety of research fields, such as speech [20], images [21–23] and video [24]. The ability of deep learning techniques to learn unknown features from incoming data has gained considerable attention in EEG studies [25–27]. There is an increasing trend to use convolutional neural networks (CNNs) to analyze EEGs due to their state-of-the-art performance in the computer vision field. A popular approach is transforming the EEG measurement into a 2D feature map and then passing it into a CNN model for classification [28–31].

For drowsy driving prediction, it is difficult to identify the drowsy state using the single time point of EEG data because drowsiness is an ambiguous event. The driving performance may not immediately decrease with increasing drowsiness levels, which means that drivers maintain normal driving performance even though their vigilance level has started to decrease. To overcome these difficulties, this study proposes a new EEG image method that combines multiple frames of EEG images to examine the temporal activity of EEG data. Such approach not only focus on the current EEG data, but also considers the brain activity of the previous time period. The evaluation results show that the proposed method can improve the performance of EEG image-based BCI systems in drowsiness prediction.

2. Experimental Setup

2.1. Virtual Reality (VR)-Based Driving Environment

In our previous studies, to observe the subject's drowsy state during the driving task, a virtual reality (VR)-based realistic driving environment was developed to simulate a long-term driving situation [2,13,32–35]. As shown in Figure 1, the surrounding scenes were projected from six projectors to constitute a surrounding vision. A night-time driving scene at a fixed velocity of 100 km/h on a four-lane highway is set up in the VR experiment. Before the experiment was started, participants were directed to enter the real car mounted on a motion platform and then steer the vehicle according to the instructions. All participants were required to take a 5-min pre-test session to ensure that they clearly understood the instruction and did not suffer from simulator sickness. The highway scene was connected to a physiological measuring system, where the EEG and participants' performance were continuously and simultaneously measured and recorded.

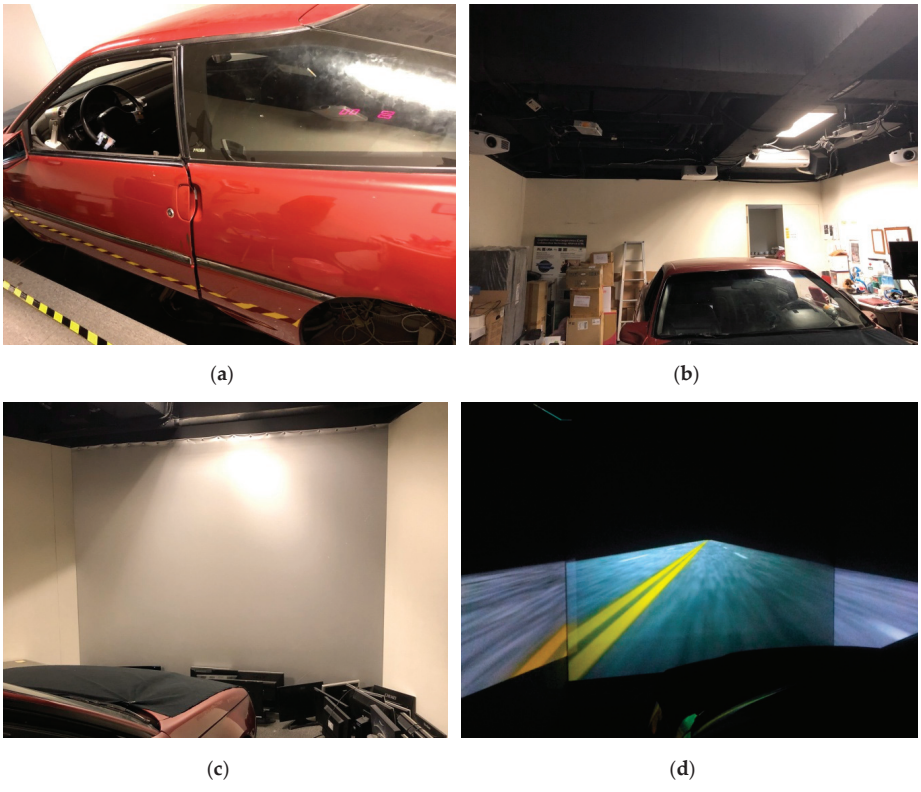

Figure 1. The virtual reality (VR)-based driving environment. (**a**) Vehicle used for the driving task. (**b**) Projector platform. (**c**) The surrounding scene. (**d**) Front view of the VR scene.

2.2. Driving Fatigue Paradigm

The event-related lane-keeping driving task was adopted in this study for the evaluation of the brain dynamics occurring during the driving task, as illustrated in Figure 2. The participants were instructed to perform a 90-min driving task without breaking or resting in the VR driving environment. The driving experiment began in the early afternoon (13:00–14:00) after lunch because people often feel sleepy during this time [36]. During the sustained attention driving task, the VR paradigm randomly simulated a lane-departure event that caused the car to drift away from the center of the cruising lane. The participants were required to quickly steer the car back whenever the car started to deviate from the original cruising lane. There was no feedback to wake the participants even if they did not respond to the lane-departure event. The car continued to move along the curb until the participants steered it to return to the center of the cruising lane. Figure 2 describes a complete trial in the driving paradigm that includes the one-second baseline recording, deviation onset, response onset, and response offset. The time interval between the random lane-departure event was set to 5–10 s.

2.3. Participants

Thirty-eight right-handed, healthy young adults aged 20–30 years participated in the driving experiment. All subjects were required to have a driving license and sufficient sleep in the two preceding weeks. According to self-reporting, no subject had a history of psychological disorders. Before the experiment, the subjects were asked to answer a questionnaire about their sleep patterns to ensure that they had a normal cognitive state during the driving task, and they needed to complete a

consent form explaining the experimental protocol that was approved by the Institutional Review Board of the Taipei Veterans General Hospital, Taiwan. The EEG signals of the subjects were captured from a Quik-Cap (CompumedicalNeuroScan) with 32 Ag/AgCl electrodes, including 30 EEG electrodes and two reference electrodes. The EEG electrodes were placed in accordance with a modified international 10–20 system. The impedance of all electrodes was kept under 5 kΩ during the experiments.

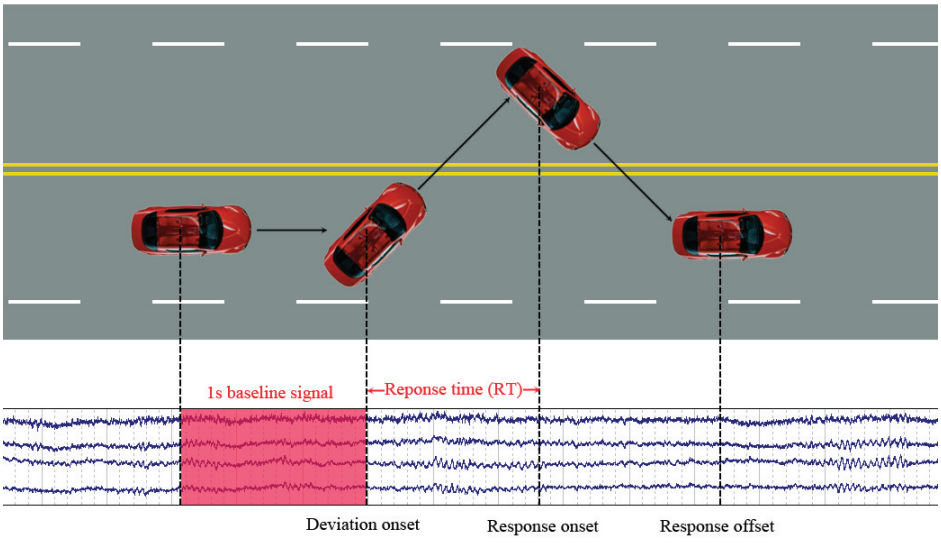

Figure 2. The event-related lane departure paradigm [2]. A complete trial consists of three steps: (**1**) deviation onset—the lane-departure event occurs, (**2**) response onset—the driver starts to steer the wheel back, and (**3**) the response offset—the car returns to the original cruising lane. Response time (RT) is defined as the time period between the deviation onset and the response onset. This study uses the 1 s baseline signal before the lane-departure event for predicting drowsiness according to the value of RT.

2.4. Drowsiness Measurement

The driving performance was defined based on the response time (RT), which represented the time between the deviation onset and the response onset. As the lane-departure event occurred, it was expected that the participant would take a long time to steer the car back to the center of the cruising lane if he/she was in a drowsy state; then, the response time (RT) in the trial could be very long. By contrast, when the participant was alert, he/she could respond to the lane-departure event in a short time. Previous studies have shown that baseline EEG activity is strongly correlated with changes in RT [34]. In this study, the 1s baseline signal (red region shown in Figure 2) was used to perform the drowsy prediction based on the trial's RT.

3. Approach

The general flowchart of our method is presented in Figure 3. Before data analysis, the acquired EEG records were processed using a 1-Hz high-pass and 50-Hz low-pass infinite impulse response filter to remove the noise and then down-sampled to 250-Hz to reduce the dimensions of the data. The power spectral activities of EEG signals were computed using FFT. To transform the EEG signal to a 2D image, we needed to address the following issues: (1) transforming the power spectrum of EEG signals to image values and (2) interpolating the points of the image data to a color image. The detailed approach is explained in the following sections.

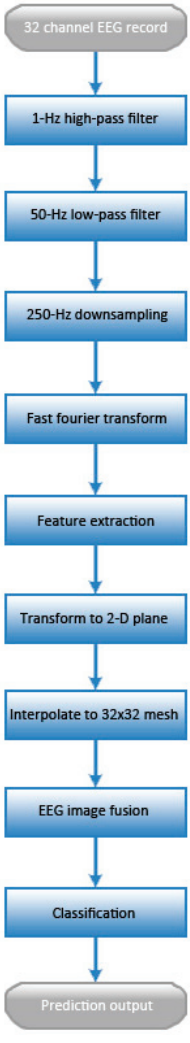

Figure 3. Flowchart of the proposed drowsiness prediction system.

3.1. Feature Extraction

To extract the physiological features, the 30-channel time-series EEG signal was transformed into a frequency domain via a 256-point FFT. Based on the findings in previous studies [14,37,38], the frequency band in the, theta (4–8 Hz), alpha (8–13 Hz), and beta (13–20 Hz) was suitable for estimating the driver's vigilance level. Our past studies also observed that the increasing power of theta band and alpha band had positive correlation with RT, and beta band had high correlation to kinesthetic stimuli which can affect the prediction performance [13,17]. The mean power of these frequency bands of interest was combined to form a feature vector. As depicted in Figure 4, this feature vector was considered a pixel value of the RGB image. Each channel of the colour image corresponds to a frequency band of interest.

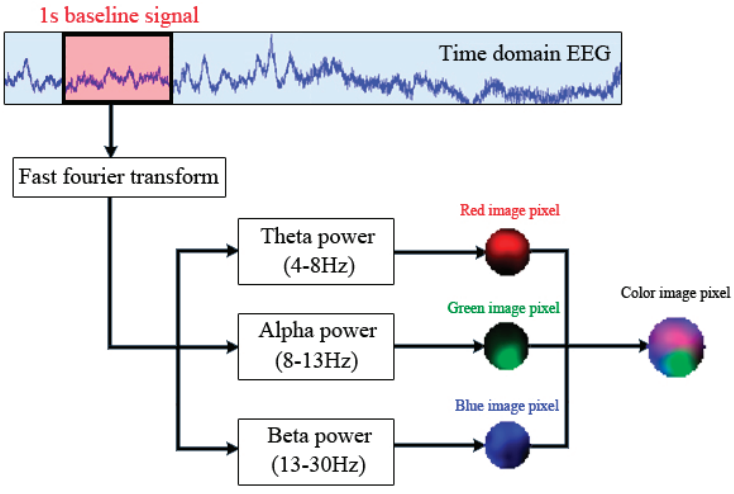

Figure 4. Schematic illustration used to transform the time domain electroencephalography (EEG) signals into a pixels in a color image.

3.2. Interpolation of the EEG Measurement to Image Pixels

As described in the previous section, we obtained 30 data points corresponding to the location of the EEG electrodes. First, we converted the magnitude of the power spectrum of the EEG signals into an image pixel value. Equation (1) shows the sigmoid function utilized to normalize the value of the EEG power spectrum to [0,1]:

$$P_t = \frac{1}{1 + e^{-0.5t}}, \tag{1}$$

where P_t is the normalized image pixel value, and t is the magnitude of the frequency response in the dB. Next, we needed to interpolate the scattered image data points to a color image. Figure 5 illustrates the interpolation scheme of the EEG image. The finite element method, a numerical technique that is usually applied for the approximate solution of engineering problems that are difficult to solve analytically, was adopted to perform the interpolation task. The Clough–Tocher scheme was used to interpolate a 32×32 mesh from the 30 image data points [39]. In this study, the EEG electrodes were placed in accordance with a modified international 10–20 system, which means that the location corresponding to each image point is known. Three topographical maps corresponding to the three frequency bands of interest were acquired by the Clough–Tocher scheme. The three spatial maps were then merged to create a 32×32 color image. Figure 6 demonstrates several samples of the EEG image.

3.3. Temporal EEG Image

One of the challenges in drowsy driving prediction is that some drowsy trials may have similar patterns of the alert trials. The driving performance might not degrade immediately, even if the alertness level of the drivers begins falling, which means that drivers can respond well to lane-departure events before they fall asleep (but the drowsy pattern of the EEG has appeared). In that case, the generated EEG images between the drowsy trial and its previous alert trials can be very similar. As the drivers wake up by themselves, their vigilance level dramatically recovers, and the RT returns to the alert state; then, the EEG pattern becomes completely different from the drowsy trials. Based on these findings, the drowsy state should be estimated not only using the current trial but also by examining the previous trials. This study proposes a temporal EEG image that is generated by a linear combination of a sequence of EEG images, as shown in Equation (2):

$$I'_t = \sum_{t=1}^{N} c_t I_t$$
$$\sum_{t=1}^{N} c_t = 1 \tag{2}$$

where I'_t is the generated temporal EEG image, I_t is the array of the EEG image data, c is a scalar coefficient and $c_i < c_j$ when $i < j$. N in this study is set to five. Figure 7 illustrates the schematic diagram of the temporal EEG image. Instead of asingle frame EEG image I_N, this approach estimates the drowsiness state using I'_N, which includes the information of the brain activity from multiple time points.

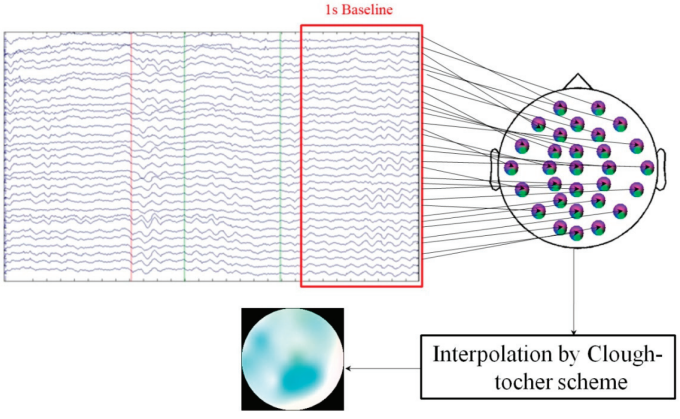

Figure 5. Interpolation scheme of the EEG image. The transformed image data points described in Figure 4 are arranged corresponding to the location of the EEG electrodes. These image pixels are interpolated over a 32 × 32 color image via Clough–Tocher scheme.

(**a**) (**b**)

Figure 6. Examples of the generated EEG images. (**a**) The alert trials. (**b**) The drowsy trials.

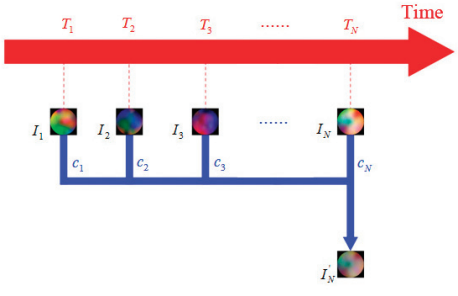

Figure 7. The schematic diagram of the temporal EEG image. I_N is the single frame EEG image generated from the current trial. Temporal EEG image I'_N is acquired by linearly combining I_N and its previous trials.

3.4. Classification Using the CNN Model

This study applies a CNN including six convolution layers, three max-pooling layers, and a layer to the classification of the input EEG image, as shown in Figure 8. A popular open source deep learning framework named Caffe is employed for implementing the CNN model [40]. The parameter setting of the overall CNN architecture is presented in Table 1. A set of filters is used to convolve the input EEG images for feature extraction. The convolved images are then subsampled by the max-pooling layer to derive compacted features. The convolution and pooling progress are repeated several times through CNN layers. The lower-level features of the input data are extracted via the early layers, and those features are collected in the later layers to hierarchically learn the higher-level features. Finally, the acquired high-level features are concatenated and passed into the fully-connected layer for the classification. The final prediction result is determined according to the output of the fully-connected layer. We only use the alert and drowsy classes in this study, so the output size of the fully-connected layer is 2×1.

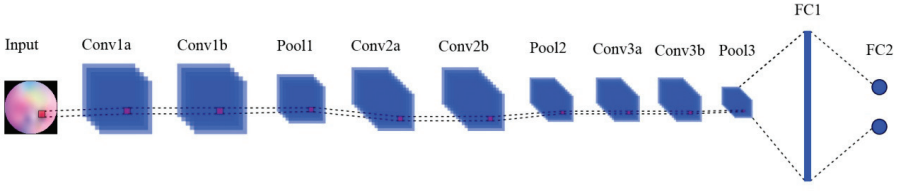

Figure 8. The convolutional neural network (CNN) architecture used in the experiment.

Table 1. Parameter setting of the CNN model.

Layer Name	Kernel Size	Stride	Num of Filters
Conv1a	3×3	1	16
Conv1b	3×3	1	16
Pool1	2×2	1	-
Conv2a	3×3	1	32
Conv2b	3×3	1	32
Pool2	2×2	2	-
Conv3a	3×3	1	32
Conv3b	3×3	1	32
Pool3	2×2	2	-
FC1	500	-	-
FC2	2	-	-

4. Experiment

The EEG dataset used in this study includes 10,395 alert trials and 3080 drowsy trials collected from 38 subjects. According to the suggestion of the previous research, if the drivers are fully aware of the driving situation, the average time for them to respond to the lane-departure event is approximately 0.7 s [41]. According to the previous studies [42–44], drivers provide poor performance when they don't respond the lane-departure event in three times the mean alert RT. Therefore, this study adopts three times the average response time as the classification boundary of the drowsy prediction task. The EEG trials are considered as alert trials as long as their RT are less than 2.1 s. In addition, the EEG trials with an RT larger than 2.5 s are labelled as drowsy trials, and the EEG trials with an RT between 2.1 s and 2.5 s are not used in this experiment. The evaluation of our approach is performed using leave-one-subject-out cross-validation. We select the data from one subject for testing and the data from the remaining subjects for training. This process is repeated for each of the 38 subjects. To evaluate the predictive performance of the proposed method, the temporal EEG image method is compared with the single frame EEG image method—directly using the current trial of the EEG image for drowsiness prediction.

Table 2 shows the comparison result of the temporal EEG image method and the single frame EEG image method. The average accuracy is an average of the accuracy of individual categories. It is apparent that the temporal EEG image method outperforms the single frame EEG image methods. In both methods, a similar accuracy of the alert class is given, but our approach achieves significant improvement in the accuracy of the drowsy class. Based on the aim of drowsiness prediction, the prediction rate of the drowsy class is more important than the alert class. Furthermore, the results also demonstrate that our approach has better prediction performance than the single frame EEG image method in most subjects, which proves that the improvement of our approach has universality in general users. Table 3 shows the evaluation result of EEGnet and hierarchical convolutional neural network (HCNN), which are CNN-based approach for EEG analysis and achieve good performance in their applications [45]. The results demonstrate that the proposed method yields superior prediction performance than EEGnet and HCNN.

Table 2. The prediction result of the single frame EEG image and temporal EEG image.

Subject	Single Frame EEG Image			Temporal EEG Image		
	Alert (%)	Drowsy (%)	Total Accuracy (%)	Alert (%)	Drowsy (%)	Total Accuracy (%)
S1	97.30	23.06	79.12	97.94	19.17	78.11
S2	88.21	20.13	52.25	82.72	29.78	53.95
S3	93.50	27.60	72.47	97.85	21.47	73.07
S4	96.76	9.30	71.85	97.79	14.19	73.33
S5	96.61	80.69	92.22	97.13	86.67	94.20
S6	96.72	84.03	93.22	98.21	96.25	97.66
S7	95.14	50.26	87.21	95.46	60.54	89.33
S8	98.30	27.69	87.31	96.42	66.15	91.60
S9	96.67	32.55	81.06	95.15	58.91	86.17
S10	96.50	12.10	80.25	96.21	8.39	79.09
S11	95.31	14.67	68.21	96.27	14.21	68.44
S12	95.60	15.80	66.30	94.50	25.71	68.90
S13	95.76	9.66	74.94	98.02	7.82	76.02
S14	92.04	17.44	80.25	96.24	16.46	83.53
S15	91.04	19.47	83.18	93.56	18.07	85.20
S16	94.10	18.25	80.62	95.06	20.00	81.62
S17	93.87	16.77	81.96	95.27	18.60	84.12
S18	92.30	16.13	85.02	92.79	16.45	85.46
S19	85.97	33.50	65.05	87.51	42.92	69.49
S20	92.40	21.44	76.24	95.15	20.17	77.94
S21	94.30	34.61	79.34	94.19	54.41	84.12
S22	92.98	21.86	76.20	94.49	21.86	77.07
S23	87.12	32.38	67.30	90.21	28.57	67.72
S24	95.68	20.28	76.46	94.83	30.35	78.27
S25	95.08	40.58	83.78	94.53	55.34	86.35
S26	92.02	37.11	85.08	91.68	48.67	86.22
S27	91.65	52.52	82.21	91.89	62.82	84.24
S28	97.60	26.50	85.55	97.29	30.25	85.73
S29	96.24	16.12	80.08	97.63	12.65	80.21
S30	94.79	12.10	74.83	95.24	13.45	75.34
S31	93.38	18.96	82.42	94.32	17.76	82.95
S32	87.57	23.57	73.37	87.92	29.76	74.78
S33	89.67	19.24	65.37	92.60	15.19	65.42
S34	89.21	25.00	84.49	90.36	22.00	85.26
S35	90.14	15.85	78.29	91.04	18.54	79.29
S36	88.33	23.57	52.43	79.65	35.63	54.75
S37	95.76	12.37	80.15	94.91	16.67	80.75
S38	69.29	40.23	53.27	52.73	53.60	53.22
Average	92.76	26.93	76.83	92.76	32.35	78.39

Table 3. The prediction result of EEGnet and HCNN.

Subject	EEGnet [45]			HCNN [28]		
	Alert (%)	Drowsy (%)	Total Accuracy (%)	Alert (%)	Drowsy (%)	Total Accuracy (%)
S1	94.39	13.33	73.99	99.07	11.11	76.92
S2	84.92	24.53	52.1	90.48	17.33	50.72
S3	93.84	16.4	68.7	95.51	21.33	71.43
S4	92.79	14.19	69.8	94.23	13.95	70.75
S5	90.81	18.89	70.66	99.45	86.11	95.72
S6	88.65	20.28	69.49	98.37	93.55	96.89
S7	91.26	23.24	79.29	94.82	32.43	83.88
S8	93.21	17.69	81.17	97.08	15.38	84.05
S9	92.46	16.73	73.69	98.2	12.73	77.03
S10	89.77	20.16	76.19	92.97	16.13	77.98
S11	91.8	12.12	64.8	92.54	12.72	65.5
S12	91.75	14.91	63.16	93.12	12.5	63.12
S13	96.4	9.08	75.1	94.31	11.76	74.18
S14	90.62	15.12	78.6	96.77	14.63	83.69
S15	91.18	16.67	82.93	89.96	21.05	82.33
S16	93.46	13.81	79.21	89.44	27.84	78.41
S17	91.69	15.91	80.66	84.43	17.2	74.65
S18	92.65	17.26	81.56	88.52	11.29	81.14
S19	91.41	14.75	60.44	94.92	17.5	63.63
S20	91.52	15.25	74.01	92.42	16.95	75.1
S21	94.09	19.31	75.16	97.34	20.59	77.92
S22	86.52	19.15	70.37	89.3	18.64	72.36
S23	85.65	19.63	61.56	96.35	7.94	64.09
S24	90.76	15.25	71.37	92.16	16.31	72.68
S25	87.33	20.58	73.38	97.69	22.33	81.95
S26	87.91	17.23	78.93	90.18	36.14	83.31
S27	89.78	15.95	71.84	96.08	28.24	79.59
S28	92.19	16.5	79.14	95.83	20	82.76
S29	92.37	13.27	76.15	95.79	12.24	78.66
S30	91.32	14.03	72.52	92.7	15.13	73.82
S31	91.95	16.27	80.71	92.19	17.91	81.15
S32	91.32	21.9	75.65	90.28	16.67	73.66
S33	100	0	64.89	90.41	11.39	62.67
S34	58.14	35	56.42	86.29	20	81.34
S35	83.3	29.76	74.62	88.68	17.07	77.08
S36	100	0	43.43	88.37	22.32	51.001
S37	83.62	17.22	71.61	92.02	22.22	79.4
S38	80	20.12	46.12	87.88	13.95	46.05
Average	90.02184	16.88132	71.03737	93.05658	21.64684	74.91082

5. Discussion and Conclusions

It is challenging to classify EEG data without an artifact removal process because drivers' brain activity can change over time due to many factors, such as their mental state and body movement, which result in the temporal fluctuations of the EEG signals. However, there still contains important information associated with the drowsiness level of drivers, and thus, the temporal analysis of the EEG signals becomes a crucial issue. This study proposes a temporal EEG image algorithm that combines a sequence of EEG images to form a new EEG image that contains brain dynamics from multiple time points. Our experimental results show that the proposed method achieves good performance in the drowsiness prediction.

Support vector machines (SVMs) are also employed for comparison with our approach because they are popular classifiers for EEG analysis. In our experiment, the computational cost is expensive and a bad prediction result is obtained if we use the EEG image as the input of SVM. Thus, the power spectrum of EEG is selected as the input of the SVM. Similar to the experiment described in the previous sections, the input data do not apply any artifact removal process. The experimental results indicate

that SVM provides a biased prediction result towards the alert class. That is, it always predicts an alert regardless of the input and results in a perfect detection of alert trials but no detection of drowsy trials. We found that SVM only provides meaningful prediction results in a balanced training dataset that has a similar number of alert trials and drowsy trials. In real-world applications, BCI systems usually have to perform drowsiness prediction under imbalanced-datasets, which means that SVM cannot provide reasonable reliability in real-world BCI applications.

To find a suitable CNN model for the drowsiness prediction task, this study introduces two CNN architectures for further evaluation: (1) AlexNet—a very popular CNN architecture that is larger than the CNN architecture used in this study [18], (2) 3D CNN—by performing 3D convolutions, which is capable of learning features from both spatial and temporal dimensions. For AlexNet, the EEG measurement is transformed into 227×227 to fit the input size of AlexNet. For 3D CNN, different from our approach using a linear combination of a sequence of EEG images, these EEG images are directly fed into the 3D CNN model since they are 3D input data. Our results show that both AlexNet and 3D CNN cannot achieve better performance than the proposed CNN architecture in the present study. That is, high-complexity CNN is not required for the drowsiness prediction task.

The detection of drowsy trials remains a challenge because different subjects have different drowsy EEG patterns. A further investigation of brain dynamics is the key to improving the prediction performance of the BCI system.

Author Contributions: E.J.C. conceived the main idea and wrote the paper. K.-Y.Y. provided the academic support and checked the manuscript, C.-T.L. provided the funding support and performed the experiment.

Funding: This work was supported in part by the Australian Research Council under Grant DP180100670 and Grant DP180100656, Taiwan Ministry of Science and Technology under AQ1 Grant MOST 106-2218-E-009-027-MY3 and MOST 108-2221-E-009-120-MY2 and W911NF-10-2-0022.

Conflicts of Interest: The authors declare no conflict of interests.

References

1. Chuang, S.-W.; Ko, L.-W.; Lin, Y.-P.; Huang, R.-S.; Jung, T.-P.; Lin, C.-T. Co-modulatory spectral changes in independent brain processes are correlated with task performance. *Neuroimage* **2012**, *62*, 1469–1477. [CrossRef] [PubMed]
2. Huang, C.S.; Pal, N.R.; Chuang, C.H.; Lin, C.T. Identifying changes in EEG information transfer during drowsy driving by transfer entropy. *Front. Hum. Neurosci.* **2015**, *9*, 570. [CrossRef] [PubMed]
3. Liu, Y.T.; Lin, Y.Y.; Wu, S.L.; Chuang, C.H.; Lin, C.T. Brain Dynamics in Predicting Driving Fatigue Using a Recurrent Self-Evolving Fuzzy Neural Network. *IEEE Trans. Neural Netw. Learn. Syst.* **2015**, *27*, 347–360. [CrossRef] [PubMed]
4. Baulk, S.D.; Reyner, L.A.; Horne, J.A. Driver sleepiness—Evaluation of reaction time measurement as a secondary task. *Sleep* **2001**, *24*, 695–698. [CrossRef]
5. Banks, S.; Catcheside, P.; Lack, L.; Grunstein, R.R.; McEvoy, R.D. Low levels of alcohol impair driving simulator performance and reduce perception of crash risk in partially sleep deprived subjects. *Sleep* **2004**, *27*, 1063–1067. [CrossRef]
6. Campagne, A.; Pebayle, T.; Muzet, A. Correlation between driving errors and vigilance level: Influence of the driver's age. *Physiol. Behav.* **2004**, *80*, 515–524. [CrossRef]
7. Arunkumar, N.; Ramkumar, K.; Venkatraman, V.; Abdulhay, E.; Fernandes, S.L.; Kadry, S.; Segal, S. Classification of focal and non-focal EEG using entropies. *Pattern Recognit. Lett.* **2017**, *94*, 112–117.
8. Long, J.; Li, Y.; Wang, H.; Yu, T.; Pan, J.; Li, F. A hybrid brain computer interface to control the direction and speed of a simulated or real wheelchair. *IEEE Trans. Neural Syst. Rehabil. Eng.* **2012**, *20*, 720–729. [CrossRef] [PubMed]
9. Xiong, Y.; Gao, J.; Yang, Y.; Yu, X.; Huang, W. Classifying driving fatigue based on combined entropy measure using EEG signals. *Int. J. Control Autom.* **2016**, *9*, 329–338. [CrossRef]
10. Winkler, I.; Haufe, S.; Tangermann, M. Automatic classification of artifactual ICA-Components for artifact removal in EEG signals. *Behav. Brain Funct.* **2011**, *7*, 30. [CrossRef]

11. Hyvärinen, A.; Karhunen, J.; Oja, E. *Independent Component Analysis*; Wiley-Interscience: New York, NY, USA, 2001.
12. Tran, Y.; Craig, A.; Boord, P.; Craig, D. Using independent component analysis to remove artifact from electroencephalographic measured during stuttered speech. *Med. Biol. Eng. Comput.* **2004**, *42*, 627–633. [CrossRef] [PubMed]
13. Lin, C.-T.; Wu, R.-C.; Liang, S.-F.; Chao, W.-H.; Chen, Y.-J.; Jung, T.-P. EEG-based drowsiness estimation for safety driving using independent component analysis. *IEEE Trans. Circuits Syst. I Regul. Pap.* **2005**, *52*, 2726–2738.
14. Jung, T.P.; Humphries, C.; Lee, T.W.; Makeig, S.; McKeown, M.J.; Iragui, V.; Sejnowski, T.J. Extended ICA removes artifacts from electroencephalographic recordings. *Adv. Neural Inf. Process. Syst.* **1998**, *10*, 894–900.
15. Garipelli, G.; Chavarriaga, R.; R Millán, J. Single trial analysis of slow cortical potentials: A study on anticipation related potentials. *J. Neural Eng.* **2013**, *10*, 036014. [CrossRef]
16. Pfurtscheller, G.; Neuper, C. Motor imagery and direct brain- computer communication. *Proc. IEEE* **2001**, *89*, 1123–1134. [CrossRef]
17. Chuang, C.H.; Lai, P.C.; Ko, L.W.; Kuo, B.C.; Lin, C.T. Driver's cognitive state classification toward brain computer interface via using a generalized and supervised technology. In Proceedings of the 2010 International Joint Conference on Neural Networks (IJCNN), Barcelona, Spain, 18–23 July 2010; pp. 1–7.
18. Tabar, Y.R.; Halici, U. A novel deep learning approach for classification of EEG motor imagery signals. *J. Neural Eng.* **2016**, *14*, 016003. [CrossRef]
19. Carvalho, S.R.; Filho, I.C.; Resende, D.O.; Siravenha, A.C.; De Souza, C.R.B.H.; Debarba, B.D.; Gomes, R.; Boulic, A. Deep Learning Approach for Classification of Reaching Targets from EEG Images. In Proceedings of the 2017 30th SIBGRAPI Conference on Graphics, Patterns and Images (SIBGRAPI), Niteroi, Brazil, 17–20 October 2017.
20. Hinton, G.; Deng, L.; Yu, D.; Dahl, G.A.; Mohamed, N.; Jaitly, A.; Senior, V.; Vanhoucke, P.; Nguyen, T.; Sainath, B. Kingsbury, Deep neural networks for acoustic modeling in speech recognition. *IEEE Signal. Process. Mag.* **2012**, *29*, 82–97. [CrossRef]
21. Krizhevsky, A.; Sutskever, I.; Hinton, G. Imagenet classification with deep convolutional neural networks. In Proceedings of the NIPS, Doha, Qatar, 12–15 November 2012.
22. Taigman, Y.; Yang, M.; Ranzato, M.; Wolf, L. DeepFace: Closing the Gap to Human-Level Performance in Face Verification. In Proceedings of the IEEE Conference on Computer Vision and Pattern Recognition (CVPR), Columbus, OH, USA, 24–27 June 2014.
23. Sun, Y.; Wang, X.; Tang, X. Deep Learning Face Representation from Predicting 10,000 Classes. In Proceedings of the IEEE Conference on Computer Vision and Pattern Recognition (CVPR), Columbus, OH, USA, 24–27 June 2014.
24. Karpathy, A.; Toderici, G.; Shetty, S.; Leung, T.; Sukthankar, S.; Li, F.-F. Large-scale video classication with convolutional neural networks. In Proceedings of the IEEE Conference on Computer Vision and Pattern Recognition (CVPR), Columbus, OH, USA, 24–27 June 2014.
25. Jirayucharoensak, S.; Pan-Ngum, S.; Israsena, P. Eeg-based emotion recognition using deep learning network with principal component based covariate shift adaptation. *Sci. World J.* **2014**, *2014*, 627892. [CrossRef]
26. Zheng, W.-L.; Zhu, J.-Y.; Peng, Y.; Lu, B.-L. EEG-based emotion classification using deep belief networks. In Proceedings of the 2014 IEEE International Conference on Multimedia and Expo (ICME), Chengdu, China, 14–18 July 2014.
27. Hosseini, M.-P.; Soltanian-Zadeh, H.; Elisevich, K.; Pompili, D. Cloud-based deep learning of big eeg data for epileptic seizure prediction. In Proceedings of the 2016 IEEE Global Conference on Signal and Information Processing (GlobalSIP), Washington, DC, USA, 7–9 December 2016.
28. Li, J.; Zhang, Z.; He, H. Hierarchical convolutional neural networks for EEG-based emotion recognition. *Cogn. Comput.* **2017**, *10*, 368–380. [CrossRef]
29. Bashivan, P.; Rish, I.; Yeasin, M.; Codella, N. Learning representations from EEG with deep recurrent-convolutional neural networks. *Int. Conf. Learn. Represent.* **2016**, *1511*, 06448.
30. Emami, A.; Kunii, N.; Matsuo, T.; Shinozaki, T.; Kawai, K.; Takahashi, H. Seizure detection by convolutional neural network-based analysis of scalp electroencephalography plot images. *NeuroImage Clin.* **2019**, *22*, 101684. [CrossRef]

31. Comaniciu, A.; Najafizadeh, L. Enabling Communication for Locked-in Syndrome Patients using Deep Learning and an Emoji-based Brain Computer Interface. In Proceedings of the 2018 IEEE Biomedical Circuits and Systems Conference (BioCAS), Cleveland, OH, USA, 24 December 2018.
32. Lin, F.-C.; Ko, L.-W.; Chuang, C.-H.; Su, T.-P.; Lin, C.-T. Generalized EEG-based drowsiness prediction system by using a self-organizing neural fuzzy system. *IEEE Trans. Circuits Syst. I Reg. Pap.* **2012**, *59*, 2044–2055. [CrossRef]
33. Huang, R.-S.; Jung, T.-P.; Delorme, A.; Makeig, S. Tonic and phasic electroencephalographic dynamics during continuous compensatory tracking. *NeuroImage* **2008**, *39*, 1896–1909. [CrossRef] [PubMed]
34. Chuang, C.H.; Ko, L.W.; Jung, T.P.; Lin, C.T. Kinesthesia in a sustained-attention driving task. *Neuroimage* **2014**, *91*, 187–202. [CrossRef] [PubMed]
35. Lin, C.T.; Wu, R.C.; Jung, T.P.; Liang, S.F.; Huang, T.Y. Estimating Driving Performance Based on EEG Spectrum Analysis. *EURASIP J. Appl. Signal. Process.* **2005**, *19*, 3165–3174. [CrossRef]
36. Ueno, H.; Kaneda, M.; Tsukino, M. Development of drowsiness detection system. In Proceedings of the VNIS'94-1994 Vehicle Navigation and Information Systems Conference, Yokohama, Japan, 6 August 2002.
37. Jap, B.T.; Lal, S.; Fischer, P.; Bekiaris, E. Using EEG spectral components to assess algorithms for detecting fatigue. *Expert Syst.* **2009**, *36*, 2352–2359. [CrossRef]
38. Bashivan, P.; Bidelman, G.M.; Yeasin, M. Spectrotemporal dynamics of the EEG during working memory encoding and maintenance predicts individual behavioral capacity. *Eur. J. Neurosci.* **2014**, *40*, 3774–3784. [CrossRef]
39. Alfeld, P. A trivariate clough-tocher scheme for tetrahedral data. *Comput. Aided Geom. Des.* **1984**, *1*, 169–181. [CrossRef]
40. Jia, Y.; Shelhamer, E.; Donahue, J.; Karayev, S.; Long, J.; Girshick, R.; Guadarrama, S.; Darrell, T. Caffe: Convolutional architecture for fast feature embedding. *arXiv* **2014**, arXiv:1408.5093.
41. Marc, G. How Long Does It Take to Stop? Methodological Analysis of Driver Perception-Brake Times. *Transp. Hum. Factors* **2000**, *2*, 195–216.
42. Lin, C.T.; Huang, K.C.; Chuang, C.H.; Ko, L.W.; Jung, T.P. Can arousing feedback rectify lapses in driving? Prediction from EEG power spectra. *J. Neural Eng.* **2013**, *10*, 056024. [CrossRef] [PubMed]
43. Huang, K.C.; Jung, T.P.; Chuang, C.H.; Ko, L.W.; Lin, C.T. Preventing lapse in performance using a drowsiness monitoring and management system. In Proceedings of the 2012 Annual International Conference of the IEEE Engineering in Medicine and Biology Society, San Diego, CA, USA, 12 November 2012.
44. Lin, C.-T.; Huang, K.-C.; Chao, C.-F.; Chen, J.-A.; Chiu, T.-W.; Ko, L.-W.; Jung, T.-P. Tonic and phasic EEG and behavioral changes induced by arousing feedback. *NeuroImage* **2010**, *52*, 633–642. [CrossRef] [PubMed]
45. Lawhern, V.J.; Solon, A.J.; Waytowich, N.R.; Gordon, S.M.; Hung, C.P.; Lance, B.J. EEGNet: A compact convolutional neural network for EEG-based brain computer interfaces. *J. Neural Eng.* **2018**, *15*, 056013. [CrossRef] [PubMed]

applied sciences

MDPI

Article

Interval-Based LDA Algorithm for Electrocardiograms for Individual Verification

Chulseung Yang [1], Gi Won Ku [1], Jeong-Gi Lee [1] and Sang-Hyun Lee [2,*]

[1] Korea Electronics Technology Institute, Buk-gu, Gwangju 61011, Korea; yangcs@keti.re.kr (C.Y.); giwon9@keti.re.kr (G.W.K.); jklee@keti.re.kr (J.-G.L.)

[2] Department of Computer Engineering, Honam University, Gwangsan-gu, Gwangju 62399, Korea

* Correspondence: leesang64@honam.ac.kr

Received: 8 July 2020; Accepted: 27 August 2020; Published: 31 August 2020

Abstract: This paper presents an interval-based LDA (Linear Discriminant Analysis) algorithm for individual verification using ECG (Electrocardiogram). In this algorithm, at first, unwanted noise and power-line interference are removed from the ECG signal. Then, the autocorrelation profile (ACP) of the ECG signal, which is a mathematical representation of the degree of similarity between a given time series and a lagged version of itself over successive time intervals, is calculated. Finally, the interval-based LDA algorithm is applied to extract unique individual feature vectors that represent distance and angle characteristics on short ACP segments. These feature vectors are used during the processes of enrollment and verification of individual identification. To validate our algorithm, we conducted experiments using the MIT-BIH ECG and achieved EERs (Equal Error Rate) of 0.143%, showing that the proposed algorithm is practically effective and robust in verifying the individual's identity.

Keywords: Individual verification; Electrocardiogram (ECG); Interval based LDA; biometrics

1. Introduction

Since the invention of electrocardiogram (ECG) recording in 1903 [1], a considerable number of studies using the electrocardiogram have been performed in the fields of diagnosing cardiac-related diseases [2–5], detecting sleep apnea [6], monitoring driver drowsiness [7], and measuring blood pressure [8], because of its advantage of noninvasive convenience. Recently, researchers started to use the ECG biometrics to verify individual identity [9]. The ECG is a suitable tool because the signal itself constantly changes depending on the sympathetic/parasympathetic activities and it is resistant to attacks and duplication [10–12].

According to the latest US Federal Trade Commission report published in March 2019 [13], identity theft and cybercrime ranked third among the issues most complained about. Such kinds of identity fraud and hacking are becoming seriously dangerous. Unfortunately, they are unavoidable as long as we use password-based identity authentication systems. Therefore, new types of biometrics such as facial characteristics [14], gait [15], fingerprints and iris scans [16], vein pattern [17], etc., have been developed. Nevertheless, References [18,19] show that they are still vulnerable to a replay/falsification attack even though they perform better with very low identification errors. To avoid problems related to such attacks, the biometrics should be a variable, so that they cannot be stolen, duplicated, or shared. Thus, many studies are showing a great interest in the ECG signal as a promising alternative biometric [20–23].

The ECG signal is non-stationary and thus continuously changes over time. The two limbs of the autonomic nervous system (i.e., sympathetic and parasympathetic nerves) are the most important factors determining the changes in the heart rate. This type of variability is called intra-subject variability [24–26], that is, the changes occur for the same individual over time. There is also

inter-subject variability found in the ECG's waveform that depends on the position, size, and anatomy of the heart, age, gender, relative body weight, chest configuration, and various other factors [27,28]. Therefore, the ECG signal varies from person to person, implying that we can use it as a biometric for the verification of an individual's identity.

There have been numerous attempts at applying ECG inter-subject variation for individual verification/identification [20–23,29–32], which can be classified into two categories: the fiducial dependent approach [20–23] and the fiducial independent approach [29–32]. The fiducial dependent approach relies on local features, such as time duration and amplitude differences between specific points of interest in an ECG, so it is less affected by heart rate variations. However, it has the possibility of missing the overall morphological information that might be useful in identifying individuals. Many studies have focused on fiducial dependent features such as time intervals, angles, and amplitudes between specific fiducial points on the QRS complex [20,33–35].

On the contrary, the fiducial independent approach is to find the feature of the ECG signal in the frequency domain rather than the time domain, or to extract the whole morphological features that appear to offer excellent discrimination information among individuals. Many algorithms based on frequency transformation have been proposed for extracting fiducial independent features from ECG signals, in which they use wavelet transform or DCT (Discrete Cosine Transform) to convert ECG signals in the time domain to the frequency domain [36–40]. The autocorrelation method also has been gaining considerable attention because of its excellent performances reported in many studies. It eliminates the need for fiducial point localization in the ECG signal by using an autocorrelation (AC) of the segmented ECG signal followed by DCT or LDA [41–43]. More recently, Safie [44] introduced a new feature extraction method, known as Pulse Active Ratio (PAR), that is implemented on electrocardiogram signals for biometric authentication. The Pulse Active Ratio uses pulse width modulation (PWM) to generate new ECG feature vectors and thereby can adapt to changes in heart rate. However, such fiducial independent approaches require tremendous computational effort because the parameters should be generated and compared for every person listed in the database during the verification stage. Furthermore, the database is often updated with intra-subject variability, in which the computational cost increases exponentially as the size of the database increases. This computational cost problem can be mitigated significantly by combining the above-mentioned two approaches.

In this paper, we propose an interval-based Linear Discriminant Analysis (LDA) algorithm, a type of hybrid algorithm that combines the complementary strengths of both fiducial dependent and fiducial independent features, and thereby is able to achieve higher accuracy of identification. The main characteristics of the proposed algorithm are as follows: (i) the use of an autocorrelation profile (ACP) of ECG signal; (ii) the use of short segments of the ACP to extract the interval-based feature vectors, which can be updated every 5 s, showing higher adaptability to intra-subject variation; (iii) the enrollment and verification of the individual's interval-based feature vectors; and (iv) the update of interval-based feature vectors when the user's identity claim is accepted.

The remainder of the paper is organized as follows. The proposed LDA algorithm based on the short ACP segments to determine the feature vectors on an interval basis as enrollment process, the verification process, and the algorithm to update the feature vectors are described in Section 2. In Section 3, the experimental results are compared with the existing ECG identification algorithms based on the same public database. Finally, the conclusion is drawn in Section 4.

2. Materials and Methods

The ECG signal reflects the electrical activity of the heart. A basic ECG signal cycle is shown in Figure 1 with a single lead ECG sensor. The signal cycle consists of the P wave, followed by the QRS complex, and the T wave [1,33].

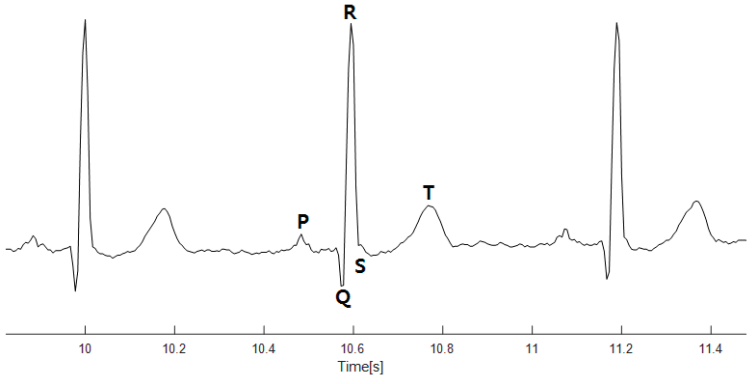

Figure 1. Basic ECG signal cycle.

Figure 2 shows a simplified block diagram of the proposed interval-based LDA algorithm. This algorithm mainly consists of signal preprocessing, enrollment, and verification.

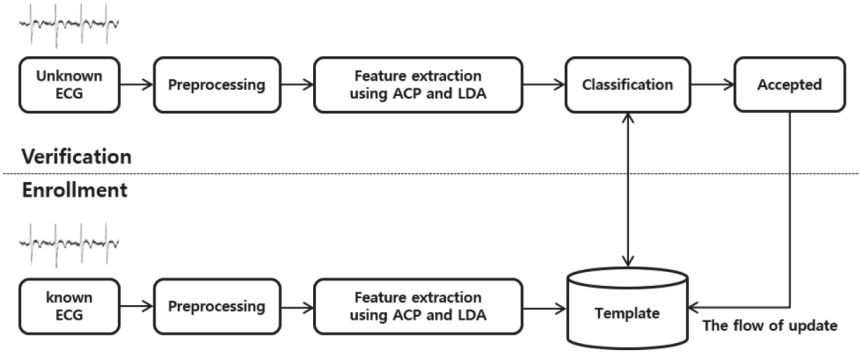

Figure 2. Simplified block diagram of the proposed interval-based LDA algorithm.

In the preprocessing stage, the raw ECG signal's noise is removed or suppressed. For biometric authentication, every user can use his/her ECG sensor in one of the two operation modes, that is, enrollment or verification mode.

In the enrollment mode/stage, a distinctive feature set is extracted from the ACP (autocorrelation profile) of the ECG on an interval basis to create an association between the user and his/her biometric characteristics. Subsequently, the extracted feature set is stored in a template. This process is called training in the enrollment mode. The template is updated over time, mainly to handle the intra-subject variation of cardiac signals. Longer training of the ECG signal leads to lower chances of false rejection (FR). In this study, the enrollment is performed for 2 min to provide a stable signature.

Similarly, during the verification mode/stage, the newly acquired unknown input is compared with the template stored in the database to verify a claimed identity. The verification decision is made through a matching process based on a feature vector threshold. The obtained matching score is finally compared with the threshold to either accept or reject the target user's identity claim.

2.1. Preprocessing

We used the ECG data from the MIT-BIH public database to test the proposed algorithm. The MIT-BIH database (MITDB) [34] is the standard ECG database universally used for ECG analyses that contains 48 records of heartbeats collected from 47 subjects; each record was sampled at 360 Hz

and is approximately 30 min long. The subjects were 25 men with ages ranging from 32 to 89 years and 22 women with ages ranging from 23 to 89 years. The data were obtained with a two-channel ambulatory Holter monitor at the Bath Israel Deaconess Medical Center from 1975 to 1979. In most database records, the upper signal is a modified limb lead II(MLII) obtained by placing the electrode on the chest, and the lower signal is usually a V1(occasionally V2 or V5 or V4). Normal QRS complexes are usually prominent in the upper signal, thus, we only used the single lead data (the upper signal, MLII) in the experiment.

To minimize the negative effect of random noises, we applied the scheme proposed by Sornmo [35] in our study, in which noisy ECG signals are passed through the bandpass filters (BPF) spanning from 0.5 to 200 Hz to reject the DC components and high-frequency noise. Subsequently, we implemented a notch filter and a short-time Fourier transform (STFT) to eliminate the power line interference and its harmonics. Figure 3 shows the preprocessing procedures.

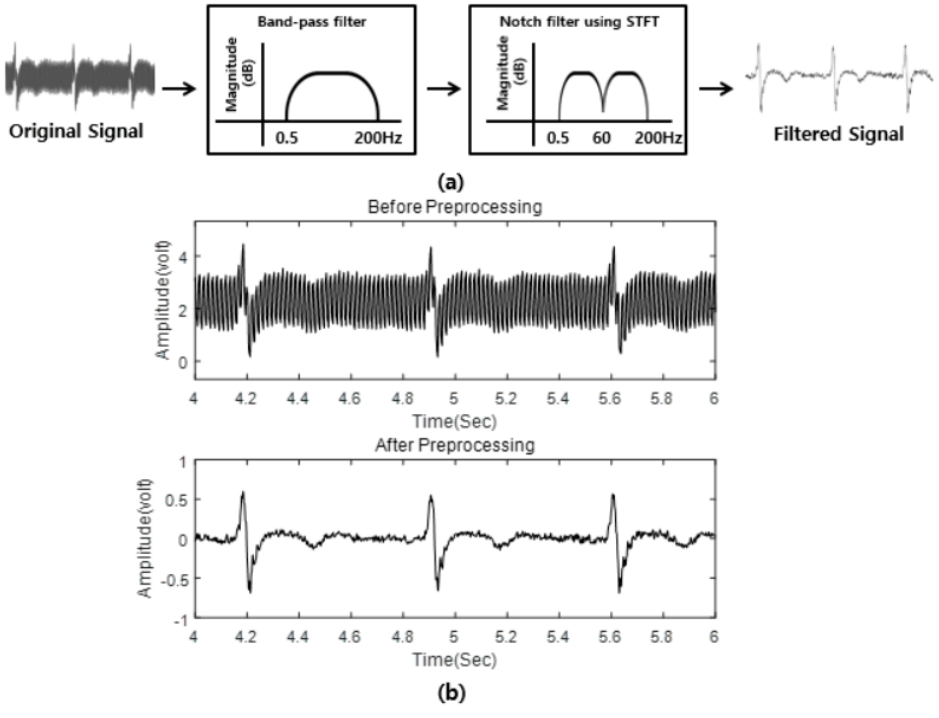

Figure 3. ECG signal preprocessing. (**a**): The simplified block diagram of signal preprocessing, where the BPF and notch filter are applied to remove the noise and power line interference related harmonics on ECG signals. (**b**): An example of an ECG signal before and after the preprocessing.

2.2. Feature Extraction

Let the noise-filtered ECG signals be $x(n)$, with the time index n. The proposed method strongly relies on the small pieces of $x(n)$, called classes, and calculates the ACP (autocorrelation profile) of each class. Then, each calculated ACP is sliced into short-time ACP segments; each segment is called ACPlet. By dividing each ACP into multiple ACPlets, we may easily capture the temporal pattern of the ACP in detail. The features we used are mainly based on the amplitude and angle patterns of the ACPlets to identify the similarities between an unknown ACP input and the reference profile.

2.2.1. Calculating the Reference Profile, $\overline{\Phi}(m)$

As mentioned in the previous section, during the enrollment mode, 2 min long ECG signals received from the ECG sensor are considered to be the training set $x(n)$. The training set $x(n)$ is then divided into several classes with a length of N. Each class of $x(n)$ is labeled $x_c(n)$ with the class "c", as follows

$$x_c(n) = x(n) \cdot R_N(n - N \cdot c) \text{ for a given class } c = 0, 1, \cdots, C-1 \tag{1a}$$

where

$$R_N(n) = \begin{cases} 1, & 0 \le n \le N-1 \\ 0, & \text{otherwise} \end{cases} \tag{1b}$$

Subsequently, the ACP $\Phi_c(m)$ of $x_c(n)$ can be computed by the following Equation (2a).

$$\Phi_c(m) = \sum_{n=0}^{N-1} x_c(n) \cdot x_c(n+m) \text{ for } 0 \le m \le Q-1 \text{ and a given class c} \tag{2a}$$

where $x(n+m)$ is the time-shifted version of ECG with a time lag m and Q is the length of the QRS complex. Figure 4 shows how the signals $x_c(n)$ and $x_c(n+m)$ are defined to obtain the ACP, that is, $\Phi_c(m)$.

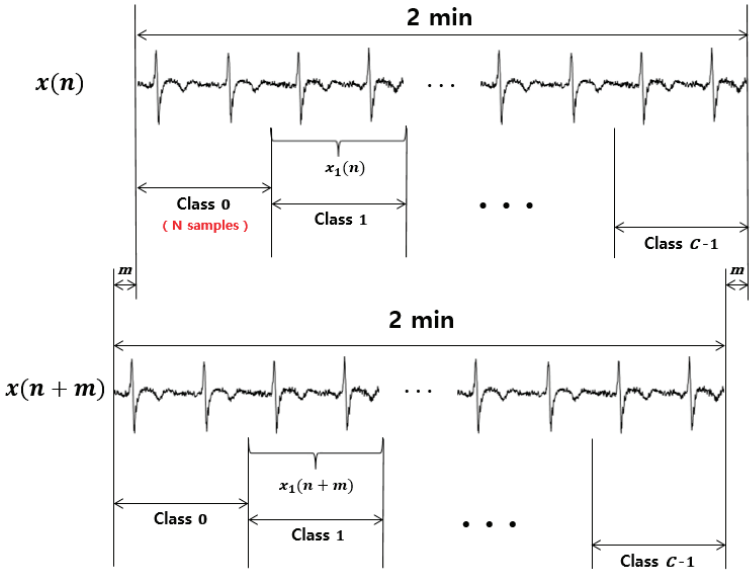

Figure 4. The two-minute-long training set $x(n)$ and its time-shifted version $x(n+m)$. The training set $x(n)$ is divided into C classes, each of which is N samples long. For example, $x_1(n)$ and $x_1(n+m)$ are the 1st class of $x(n)$ and $x(n+m)$, respectively.

Based on the previous research, the QRS complex is considered to be the most prominent waveform of ECG for individual verification [41,45,46]. Hence, the time shift parameter m of $\Phi_c(m)$ was chosen between 0 to $Q-1$. In this paper, the length Q, which depends on the individual, was calculated using the QRS detection method based on the Pan-Tompkins algorithm [47]. Depending on the individual, the different length of Q helps in achieving a high identification accuracy and robustness of the proposed algorithm.

Based on the assumption that the training set $x(n)$ includes C classes, we define a set of ACPs for C classes as follows:

$$\Phi_0(m), \Phi_1(m), \cdots, \Phi_c(m), \cdots, \Phi_{C-1}(m) \tag{2b}$$

Subsequently, the reference profile $\overline{\Phi}(m)$ is defined as the average of all ACPs contained in the training set $x(n)$, given by:

$$\overline{\Phi}(m) = \frac{1}{C}\sum_{c=0}^{C-1}\Phi_c(m) \tag{3}$$

where C is the total number of classes in the training set $x(n)$ for 2 min.

2.2.2. Interval-Based Feature Extraction

Figure 5 shows an example of ACPs for two different subjects (subject A and subject B). We assumed that each subject has C classes and those C classes are displayed together within the same time period Q.

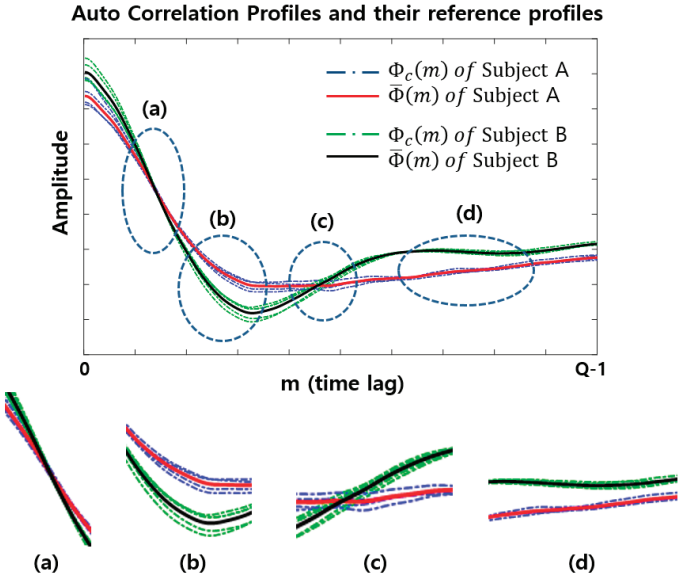

Figure 5. An example of a set of ACPs, displayed together within the same time period of Q, for two different subjects (subject A and subject B) when C = 5. (**a**–**d**) illustrate the differences in amplitude and angle patterns of ACPlet generated when the ACPs are segmented into six ACPlets, even though the two subjects have a very similar ACP shape.

From Figure 5, the intervals (a) and (c) are when the two subjects are difficult to distinguish by using only the amplitude patterns of $\Phi_c(m)$, but these two subjects are more easily distinguished using the angle patterns of $\Phi_c(m)$. It is obvious from the two profiles of (a) and (c) that their angle patterns are significantly different, in which the angle pattern is defined as the angles between the horizontal x-axis and the ACPlet. On the other hand, (b) and (d) are the intervals when the two subjects can be easily distinguished using the amplitude patterns of $\Phi_c(m)$.

These results lead to the idea of an interval-based feature vector. Accordingly, to facilitate the identification between different subjects, each class needs to be sliced into short-time ACP segments, i.e., the ACPlets. Therefore, in this work, the two features of amplitude and angle patterns of ACP produced for every ACPlet are used to distinguish the ECG signals.

2.2.3. Deciding the Optimal Interval Size for Interval-Based Feature Vector

In Section 2.2.2, we realized that dividing ACPs with a short interval and applying different feature vectors to each ACPlet yields a better identification; however, the interval size should be decided appropriately. The optimal interval size is determined based on the maximum interval that satisfies a mean square error (MSE) criterion between the ACPlets and their linearly fitted lines, such that each ACPlet provides clear angle information.

Based on the assumption of the optimal interval size L, the reference profile $\overline{\Phi}(m)$ can be equally divided into Q/L profiles $f_i(v)$, defined as follows:

$$\overline{\Phi}(m) = \{\ f_1(v), f_2(v), \cdots, f_i(v), \cdots, f_{NI}(v)\ \} \text{ for a given } L \tag{4}$$

where $i\left(=\frac{Q}{L}\right)$ is the number of intervals and $0 \le v \le L-1$.

Here, let define $\hat{\Phi}(m)$ as the set of $g_i(v)$ that is the $f_i(v)$ linearly fitted, as follows:

$$\hat{\Phi}(m) = \{\ g_1(v), g_2(v), \cdots, g_i(v), \cdots, g_{NI}(v)\ \} \tag{5}$$

where $0 \le v \le L-1$.

Thus, the optimal interval L is the maximum length that satisfies the following MSE (ζ) criterion between the two profiles $\overline{\Phi}(m)$ and $\hat{\Phi}(m)$.

$$L = \max_{l}\left[\sum_{i=1}^{NI}\sum_{v=0}^{l-1}(\ f_i(v) - g_i(v)\ )^2 \le \varepsilon\right] \text{for } 2 \le l \le \frac{Q}{2} \tag{6}$$

where ε is the minimum tolerance of the MSE and NI (=Q/L) is the number of intervals. The symbol represented in the above process is illustrated in Figure 6.

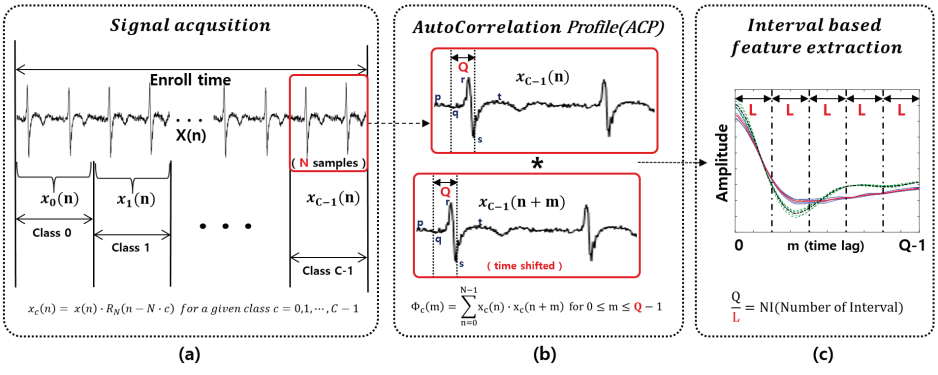

Figure 6. Symbol descriptions: (**a**) N is the update cycle of the verification process; (**b**) Q is the time-shifting size of the ACP process; (**c**) L is the size of an interval and the maximum length that satisfies the MSE (ζ) criterion.

Figure 7 shows typical examples of the MSE ζ and identification accuracy η as a function of NI (Number of Interval). In Figure 7, MSE ζ represents the ratio based on the assumption that MSE ζ is 100% when NI is set to 2, where (a) represents the minimum tolerance ε, which is experimentally set to 20%; (b) is the NI value satisfying (a), which corresponds to Q/L; and (c) is the identification accuracy when the NI value corresponds to (b).

The Figure 7 shows that the MSE ζ decreases as NI increases, where a higher NI is proportional to identification accuracy η but requires more computations for the verification process. Accordingly, there is a trade-off between the NI and computational cost. We also observed that the IDA improves

with increasing NI; however, the improvement is not significant. For instance, as the NI increases from Q/L to 50, only an improvement of less than 0.2% is obtained. In conclusion, the performance of the proposed algorithm is not highly sensitive to the NI as long as it is greater than Q/L. Finally, the NI is set to Q/L when MSE ζ corresponds to ε, since there is no big difference in the final performance as long as the NI is greater than Q/L.

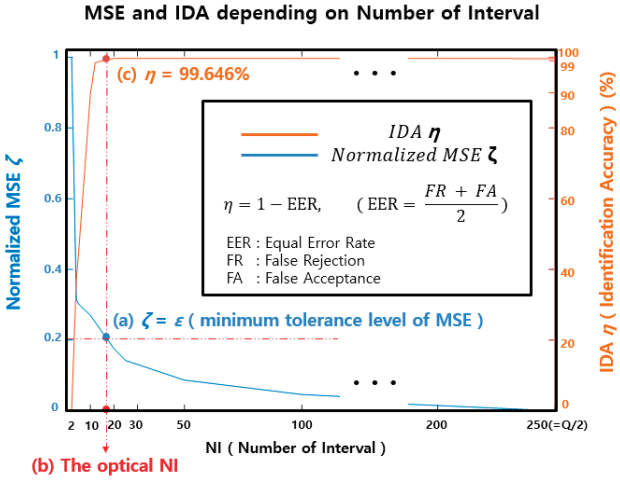

Figure 7. The relationship between the MSE (Mean Squared Error) ζ and the IDA (Identification Accuracy) η according to NI (Number of Interval) values to show the decision of the optimal NI. In this experiment, the optimal NI is set as the value when η = 99.646% and $\zeta = \varepsilon$

2.3. Threshold Values for Classification

Our algorithm requires two types of interval-based thresholds for the robust verification of intra-subject variation. One threshold is for the amplitude feature vector and another is for the angle feature vector, denoted $TH_\phi(i,v)$ and $TH_\theta(i)$, respectively, where the variable i indicates the interval index. These thresholds are used to check the similarity between the amplitude and angle feature vectors of the newly incoming ACPlets to those stored in the template.

2.3.1. Threshold of Amplitude Similarity: $TH_\phi(i,v)$

Step 1: Consider a subject A for the training set and let define the ACP as $\phi_c^A(m)$ that consists of the ACPlets $\phi_c^A(i,v)$ for $c \in \{0,\ldots,C-1\}$:

$$\phi_c^A(m) = \left\{\phi_c^A(1,v), \phi_c^A(2,v), \cdots, \phi_c^A(i,v), \cdots, \phi_c^A(NI,v)\right\} \tag{7}$$

In matrix form,

$$\begin{bmatrix} \phi_0^A(m) \\ \phi_1^A(m) \\ \vdots \\ \phi_c^A(m) \\ \vdots \\ \phi_{C-1}^A(m) \end{bmatrix} = \begin{bmatrix} \phi_0^A(1,v) & \phi_0^A(2,v) & \cdots & \phi_0^A(i,v) & \cdots & \phi_0^A(NI,v) \\ \phi_1^A(1,v) & \phi_1^A(2,v) & \cdots & \phi_1^A(i,v) & \cdots & \phi_1^A(NI,v) \\ \vdots & \vdots & & \vdots & & \vdots \\ \phi_c^A(1,v) & \phi_c^A(2,v) & \vdots & \phi_c^A(i,v) & \vdots & \phi_c^A(NI,v) \\ \vdots & \vdots & \cdots & \vdots & \cdots & \vdots \\ \phi_{C-1}^A(1,v) & \phi_{C-1}^A(2,v) & \cdots & \phi_{C-1}^A(i,v) & \cdots & \phi_{C-1}^A(NI,v) \end{bmatrix} \tag{8}$$

Step 2: Calculate the average in a vertical way to obtain the reference profile, $\overline{\phi}^A(m)$:

$$\overline{\phi}^A(m) = \left[\overline{\phi}^A(1,v)\ \overline{\phi}^A(2,v)\ \cdots \overline{\phi}^A(i,v)\ \cdots \overline{\phi}^A(NI,v)\right] \tag{9}$$

where

$$\overline{\phi}^A(i,v) = \frac{1}{C}\sum_{c=0}^{C-1}\phi_c^A(i,v) \text{ for a given } i \text{ and } v \tag{10}$$

Step 3: Define $\Delta\phi_c^A(i,v)$ as the amplitude distance between $\overline{\phi}^A(i,v)$ and $\phi_c^A(i,v)$:

$$\Delta\phi_c^A(i,v) = \left|\overline{\phi}^A(i,v) - \phi_c^A(i,v)\right| \tag{11}$$

where the distance $\Delta\phi_c^A(i,v)$ is large if the descriptors are further apart in the descriptor space and small if they are closer together.

We obtain:

$$\begin{array}{c} TH_{\phi_{max}}(i,v) = max\left\{\Delta\varnothing_c^A(i,v)\middle|\ \forall c \in \{0,1,\cdots C-1\}\right\}, \\ \text{and } TH_{\phi}(i,v) = \mu_{\phi}^A(i,v) + \sigma_{\phi}^A(i,v) \text{ for a given } i \text{ and } v \end{array} \tag{12}$$

where

$$\begin{array}{c} \mu_{\phi}^A(i,v) = mean\left\{\Delta\phi_c^A(i,v)\middle|\ \forall c \in \{0,1,\cdots C-1\}\right\} \\ \sigma_{\phi}^A(i,v) = std\left\{\Delta\phi_c^A(i,v)\middle|\ \forall c \in \{0,1,\cdots C-1\}\right\} \end{array} \tag{13}$$

Note that the amplitude distance $\Delta\phi_c^A(i,v)$ is small and thus $TH_{\phi}(i,v)$ is most likely smaller than $TH_{\phi_{max}}(i,v)$, since this parameter reflects the distance between intra-subjects.

2.3.2. Threshold of Angle Similarity: $TH_{\theta}(i)$

We calculated the scatter within class representing the degree of dispersion in a class which is called intra-subject variability, and the scatter between classes representing the degree of dispersion between different classes, which is called inter-subject variability, to obtain $TH_{\theta}(i)$ [43].

Step 1: Consider a data set of (x,y) and (x,r) for a given $i_o \in i$, where

$$\begin{array}{c} x = \{\forall v\}, \\ y = \left\{\phi_c^A(i_o,v)\middle|\ i_o \in i,\ \forall v\right\} \text{ for a given class } c \\ r = \left\{\overline{\phi}^A(i_o,v)\middle|\ i_o \in i, \forall v\right\} \end{array} \tag{14}$$

Step 2: Calculate the scatter within class and scatter between classes of the dataset (x,y) and (x,r).

$$\begin{array}{c} S_W = S_{(x,y)} + S_{(x,r)} \\ S_{(x,y)} = \sum\left(y-u_y\right)\left(y-u_y\right)^T \\ S_{(x,r)} = \sum\left(r-u_r\right)\left(r-u_r\right)^T \\ S_B = \left(u_y-u_r\right)\left(u_y-u_r\right)^T \end{array} \tag{15}$$

where u_y and u_r indicates the mean of y and r, respectively.

Step 3: Calculate the weight vector matrix in terms of S_W and S_B. Subsequently, use the eigenvector with the highest eigenvalue as the most discriminant projection vector.

$$\begin{array}{c} W = \frac{S_B}{S_W} \\ WV = \lambda V \end{array} \tag{16}$$

where V is the eigenvector when λ corresponds to the highest eigenvalue.

Let's define $\theta_c^A(i_o)$ as the angle θ of the x-axis to the most discriminant projection vector V of the dataset, (x, y) and (x, r).

$$\theta_c^A(i_o) = tan^{-1}(V) \tag{17}$$

Step 4: Define $\theta_c^A(i_o)$ as the angle distance per interval between dataset (x, y) and (x, r) for a given c and i_o.

We obtain:

$$\begin{array}{c} TH_{\theta_{max}}(i_o) = max\Big\{\ \theta_c^A(i_o)\Big|\ \forall c \in \{0, 1, \cdots C-1\ \}\Big\} \\ TH_{\theta_{min}}(i_o) = min\Big\{\ \theta_c^A(i_o)\Big|\ \forall c \in \{0, 1, \cdots C-1\ \}\Big\} \end{array} \tag{18}$$

and

$$TH_{\theta_1}(i_o) = \mu_\theta^A(i_o) + \sigma_\theta^A(i_o),\ \ TH_{\theta_2}(i_o) = \mu_\theta^A(i_o) - \sigma_\theta^A(i_o) \tag{19}$$

where

$$\begin{array}{c} \mu_\theta^A(i_o) = mean\Big\{\ \theta_c^A(i_o)\Big|\ \forall c \in \{0, 1, \cdots C-1\ \}\Big\} \\ \sigma_\theta^A(i_o) = std\Big\{\ \theta_c^A(i_o)\Big|\ \forall c \in \{0, 1, \cdots C-1\ \}\Big\} \end{array} \tag{20}$$

Similar to the amplitude distance $\Delta\phi_c^A(i, v)$, the angle distance $\theta_c^A(i_o)$ is mostly between $TH_{\theta_1}(i_o)$ and $TH_{\theta_2}(i_o)$ and almost always between $TH_{\theta_{min}}(i)$ and $TH_{\theta_{max}}(i)$. Based on this process and the subsequent updating process, the range of the intra-subject variation can be determined and the advantage of the constantly changing ECG signal can be reaped, which is beneficial for the verification using ECG.

2.4. Verification

In addition to the biometric data for subject A, the template database includes information about the identifier related to the subject A. The term "biometric data" is referred to as the $\left\{\ \overline{\phi}^A(i, v)\ \middle|\forall i \in \text{training set}\ \right\}$ stored along with the $TH_\phi(i, v)$ and $TH_\theta(i)$ in the template database. During the verification stage, the system validates the identity claimed by an unknown person by checking the similarity of the person's biometric data to the enrolled data retrieved by the identifier input by subject A.

Consider an unknown subject B to be verified. If an unknown person B is detected by the biometric system during the verification, first, a biometric input is extracted from the person by calculating the feature vector, $\left\{\ \phi_c^B(i, v)\ \middle|\forall i, c \in \text{verification mode}\ \right\}$. Subsequently, the system calculates the difference between the unknown input and templates, resulting in the amplitude and angle distances in the same manner as during enrollment.

Next, the system calculates the similarity to determine how close the subjects A and B are. The computation is carried out by applying a similarity threshold to the distances and normalizing the resulting value to the range [0,1], where 0 means "no match at all" and 1 means "perfect match". In this paper, two similarity measures are considered, and those are the similarities of the amplitude and angle distances, denoted as S_ϕ and S_θ , respectively.

Subsequently, we define a matching score S to quantify the match between the unknown and template subject by concatenating the two similarities into $S = 0.5S_\phi + 0.5S_\theta$, where both similarities are equally weighted. Given a matching score S, the system checks whether the score S is above a certain threshold S_{TH} for the signature classification. A detailed explanation of the verification is given below.

Step 1: First, consider an unknown subject B to be verified and let its ACP be $\Phi_c^B(m)$, which belongs to class c. It can be represented by the set of the ACPlets of

$$\Phi_c^B(m):\ \Phi_c^B(m) = \Big\{\phi_c^B(1, v), \phi_c^B(2, v), \cdots, \phi_c^B(i, v), \cdots,\ \phi_c^B(NI, v)\Big\} \tag{21}$$

Step 2: Compute the amplitude distance $\Delta\varnothing_c^B(i,v)$ between

$$\overline{\phi}^A(i,v) \text{ and } \phi_c^B(i,v), \text{ given by : } \Delta\phi_c^B(i,v) = \left|\overline{\phi}^A(i,v) - \phi_c^B(i,v)\right| \tag{22}$$

where this distance shows how close the amplitudes of $\overline{\phi}^A(i,v)$ and $\phi_c^B(i,v)$ are. Smaller $\Delta\varnothing_c^B(i,v)$ leads to a higher possibility that the unknown subject B is to be subject A.

Step 3: Calculate the similarity of the amplitude distance: S_ϕ

The similarity of the amplitude distance (S_ϕ) can be obtained by applying the threshold of the amplitude similarity to $\Delta\varnothing_c^B(i,v)$ as follows:

$$\begin{array}{l} for\ i = 1\ : NI \\ \quad for\ v = 0\ : L-1 \\ \quad\quad \Omega(\mathrm{i,v}) = \frac{TH_\phi(i,v)}{\Delta\varnothing_c^B(i,v)} \text{ for a given class} \\ \quad\quad \Omega(\mathrm{i,v}) = 0 \text{ if } \Delta\varnothing_c^B(i,v) > TH_{\phi_{max}}(i,v) \\ \quad\quad \Omega(\mathrm{i,v}) = 1 \text{ if } \Delta\varnothing_c^B(i,v) \le TH_\phi(i,v) \\ \quad end \\ end \\ \mathrm{S}_\varnothing = \frac{1}{(\ NI \cdot L\ )} \sum_{i=1}^{NI}\sum_{v=0}^{L-1} \Omega(i,v) \text{ for a given class} \end{array} \tag{23}$$

Given $\Delta\varnothing_c^B(i,v)$, if $\Delta\varnothing_c^B(i,v) \le TH_\phi(i,v)$, the corresponding ACP pixel is counted as "accepted", i.e., the similarity $\Omega(i,v) = 1$. Else if $\Delta\varnothing_c^B(i,v) > TH_{\phi_{max}}(i,v)$, the corresponding ACP pixel is counted as "declined", that is, the similarity score $\Omega(i,v) = 0$. If $TH_\phi(i,v) < \Delta\varnothing_c^B(i,v) \le TH_{\phi_{max}}(i,v)$, the corresponding ACP pixel is counted as "partially accepted" and the similarity score is given by $\Omega(\mathrm{i,v}) = \frac{\mathrm{TH}_\phi(\mathrm{i,v})}{\Delta\varnothing_c^B(\mathrm{i,v})}$, which ranges from 0 to 1. Finally, the similarity of the amplitude distance (S_ϕ) is determined as the average of the similarity score calculated on a pixel-by-pixel basis.

Step 4: Compute the angle distance $\theta_c^B(i)$

Define $\theta_c^B(i_o)$ as the angle θ of the x-axis to the most discriminant projection vector of the datasets, (x, z) and (x, r) where

$$\begin{array}{c} x = \{\forall v\}, \\ z = \left\{\varnothing_c^B(i_o,v)\middle| i_o \in i, \forall v\right\} \text{ for a given class } c \\ r = \left\{\overline{\varnothing}^A(i_o,v)\middle| i_o \in i, \forall v\right\} \end{array} \tag{24}$$

The method of finding the most discriminant projection vector is the same as the method used to calculate the most discriminant vector in the enrollment mode. Subsequently, define $\theta_c^B(i_o)$ as the angle distance per interval between datasets (x, z) and (x, r) for a given c and i_o.

Step 5: Calculate the similarity of angle distance: S_θ

The similarity of angle distance (S_θ) can be obtained by applying the threshold of the angle similarity to $\theta_c^B(i)$ as follows:

$$\begin{array}{c} \text{for } i = 1\ : NI \\ if\ \theta_c^B(i) \le TH_{\theta_1}(i), \Lambda(i) = \frac{TH_{\theta_1}(i)}{\theta_c^B(i)} \\ if\ \theta_c^B(i) \ge TH_{\theta_2}(i), \Lambda(i) = \frac{TH_{\theta_2}(i)}{\theta_c^B(i)} \\ \Lambda(i) = 0 \text{ if } \left(\theta_c^B(i) < TH_{\theta_{min}}(i) \text{ or } \theta_c^B(i) > TH_{\theta_{max}}(i)\right) \\ \Lambda(i) = 1 \text{ if } TH_{\theta_1}(i) \le \theta_c^B(i) \le TH_{\theta_2}(i) \text{ for a given class} \\ \text{end} \\ S_\theta = \frac{1}{NI}\sum_{i=1}^{NI} \Lambda(i) \text{ for a given class} \end{array} \tag{25}$$

Given $\theta_c^B(i)$, if $TH_{\theta_{min}}(i) \leq \theta_c^B(i) < TH_{\theta_1}(i)$ or $TH_{\theta_2}(i) < \theta_c^B(i) \leq TH_{\theta_{max}}(i)$, the corresponding ACP interval is counted as "partially accepted", that is, the similarity score is $\Lambda(i) = \frac{TH_\theta(i)}{\theta_c^B(i)}$, which has the range [0,1], or else if $\theta_c^B(i) < TH_{\theta_{min}}(i)$ or $\theta_c^B(i) > TH_{\theta_{max}}(i)$, the corresponding ACP interval is counted as "declined", that is, the similarity score $\Lambda(i) = 0$, or else if $TH_{\theta_1}(i) \leq \theta_c^B(i) \leq TH_{\theta_2}(i)$, the corresponding ACP interval is counted as "accepted" and the similarity score is given by $\Lambda(i) = 1$. The similarity of the angle (S_θ) is determined as the average of the similarity scores calculated on an interval-by-interval basis.

Step 6: Calculate the matching score

For every incoming class, we define a matching score $S = 0.5S_\phi + 0.5S_\theta$ with a range from 0 to 1, where 1 means a perfect match. Given a matching score S, the system finally determines whether the score S is above a certain threshold S_{TH}, called as the matching threshold, for signature identification.

2.5. Updating Template

As mentioned in Section 1, an individual ECG signal changes over time due to intra-subject variability. Therefore, if a subject uses a fixed template for a long time, the subject may be falsely rejected during the verification. To solve this problem, we applied an updating process by continuously performing the training process for every class. For instance, for a new C^{th} class incoming shortly after the training process of class $c \in \{0, 1, \ldots C-1\}$, if the matching score S is larger than the threshold S_{TH}, the new C^{th} class is accepted as a new member for the template update. Subsequently, the newly accepted class is appended to the training set, and thus the latest accepted C classes $c \in \{1, 2, \ldots C-1\}$ are considered to be the new training set for the update. The template update for subject A is described below.

2.5.1. Calculating the Amplitude and Angle Distances

The latest accepted C classes are re-indexed using $c \in \{0, 1, \ldots C-1\}$.

(i) Use the C classes as the new training set for subject A and find the ACP as $\Phi_c^A(m)$ which consists of the ACPlets $\varnothing_c^A(i, v)$:

$$\Phi_c^A(m) = \left\{\phi_c^A(1, v), \phi_c^A(2, v), \cdots, \phi_c^A(i, v), \cdots, \phi_c^A(NI, v)\right\} \tag{26}$$

(ii) Next, find the profile $\overline{\Phi}^A(m)$:

$$\overline{\Phi}^A(m) = \left[\overline{\phi}^A(1, v) \;\; \overline{\phi}^A(2, v) \cdots \overline{\phi}^A(i, v) \cdots \overline{\phi}^A(NI, v)\right] \tag{27}$$

where

$$\overline{\phi}^A(i, v) = \frac{1}{C}\sum_{c=0}^{C-1} \phi_c^A(i, v) \text{ for a given } i \text{ and } v \tag{28}$$

(iii) Finally, compute the amplitude distance $\Delta\varnothing_c^A(i, v)$ and angle distance $\theta_c^A(i)$:

$$\begin{aligned} \Delta\phi_c^A(i, v) &= \left|\overline{\phi}^A(i, v) - \phi_c^A(i, v)\right| \text{ and} \\ \theta_c^A(i) &= tan^{-1}(V) \end{aligned} \tag{29}$$

where V is the most discriminant projection vector between $\overline{\phi}^A(i, v)$ *and* $\phi_c^A(i, v)$.

2.5.2. Updating the Threshold of Amplitude Similarity

$$\begin{gathered}\mu_{\phi}(i,v) = mean\Big\{\ \Delta\varnothing_c^A(i,v)|\ \forall c \in \{0,1,\cdots C-1\ \}\Big\}\\ \sigma_{\phi}(i,v) = std\Big\{\ \Delta\varnothing_c^A(i,v)|\ \forall c \in \{0,1,\cdots C-1\ \}\Big\}\\ TH_{\phi_{max}}(i,v) = max\Big\{\ \Delta\varnothing_c^A(i,v)|\ \forall c \in \{0,1,\cdots C-1\ \}\Big\}\\ TH_{\phi}(i,v) = \mu_{\phi}(i,v) + \sigma_{\phi}(i,v)\end{gathered} \tag{30}$$

2.5.3. Updating the Threshold of Angle Similarity

$$\begin{gathered}\mu_{\theta}(i) = mean\{\ \theta_c^A(i)|\ \forall c \in \{0,1,\cdots C-1\ \}\Big\}\\ \sigma_{\theta}(i) = std\{\ \theta_c^A(i)|\ \forall c \in \{0,1,\cdots C-1\ \}\Big\}\\ TH_{\theta_{max}}(i) = max\{\ \theta_c^A(i)|\ \forall c \in \{0,1,\cdots C-1\ \}\Big\}\\ TH_{\theta_{min}}(i) = min\{\ \theta_c^A(i)|\ \forall c \in \{0,1,\cdots C-1\ \}\Big\}\\ TH_{\theta_1}(i) = \mu_{\theta}(i) + \sigma_{\theta}(i)\ \ TH_{\theta_2}(i) = \mu_{\theta}(i) - \sigma_{\theta}(i)\end{gathered} \tag{31}$$

By updating the threshold of the amplitude/angle similarity using the above process, the ECG changes due to intra-subject variation can be continuously reflected in the template. In this study, the verification/updating template is repeatedly performed for every class and each class is specified to be 5 s long, which is fast enough for real-life applications.

3. Experiment and Results

An experiment was carried out using a public open database, available on the PhysioNet website [34], to evaluate the proposed algorithm.

The MIT-BIT arrhythmia database (MITDB) contains 48 records of heartbeats collected from 47 subjects (records 201 and 202 are from the same male subject). Each record is approximately 30 min long and was sampled at 360Hz. The subjects are 25 men with ages between 32 and 89 years old and 22 women with ages between 23 to 89 years old. The data were obtained using a two-channel ambulatory Holter monitor at the Beth Israel Deaconess Medical Center from 1975 until 1979. This database is the most referred database related to arrhythmic studies. In this study, this database was used to evaluate the efficiency of the proposed algorithm. Two 2-min intervals were randomly selected for each data. The first 2-min interval of each data was used for training and the second data was used for verification. Only single lead data was used in the experiment.

The error rate can be calculated for each subject, as shown in Figure 8. The FR (False Rejection) means that the subject was rejected despite being himself. The FA (False Acceptance) means that the subject was accepted despite being someone else. The distance threshold was chosen to be the intersection of FR (False Rejection) and FA (False Acceptance), depending on the subject. The threshold and EER for each subject are calculated based on the intersection of FR and FA. If there is only one intersection point, the threshold and EER are determined based on the intersection point, whereas if there are more than two points, the threshold is determined by the average value of the largest and smallest value, and certainly, EER is calculated as 0, as shown in Figure 8.

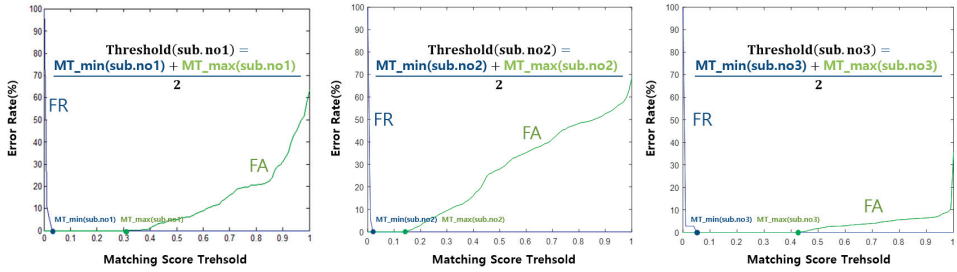

Figure 8. Examples of false rejection and acceptance rates for Subject no. 1, no. 2, and no. 3.

Figure 9a shows an example of obtaining the EER for each individual. A histogram of the EER (Equal Error Rates) is shown in Figure 9b. The average EER is 0.143%, which indicates the efficiency of the overall algorithm, as shown in Equation (32). Only a single user was enrolled at any point in time. In other words, at any point in time, we had one client and 46 imposters.

$$\text{Total efficiency of verification} = \frac{1}{\text{No. of subject}} \sum_{\text{Sub}=1}^{\text{No. of subject}} \text{EER}_{\text{Sub}} \tag{32}$$

where Sub indicates the subject number.

To demonstrate the efficiency of our proposed algorithm, we compared it with related works that used the same database (MIT-BIH), as shown in Table 1. Table 1 shows that the EER (Equal Error Rate) in Reference [48] is higher than the proposed algorithm despite using ECG data from two leads. Recently, most ECG wearable devices, such as smart watches, only use one lead; thus, the proposed algorithm is more suitable for real-life applications. In Reference [48], a fixed shifting size was used for the autocorrelation, while in the proposed algorithm, we used a flexible shifting size for the autocorrelation as the QRS width for the individual, which requires less computational effort. Although fused information from two ECG leads was used in Reference [49], their IDA (Identification Accuracy) is lower than the proposed algorithm; however, the enroll time is 5 min, which is longer than our algorithm. A fiducial point dependent method was used in References [28,50–52] which is vulnerable to noise. Only 10–20 s data were used for enrollment and verification in References [52,53]. However, we used two 2-min data for enrollment and verification to verify the stability of the proposed algorithm. Only a direct contact sensor was used in References [28,48–53] to verify the algorithms. In contrast, we used a non-contact single lead senor for real-life applications. In this paper, in the case of a fiducial dependent approach, although it has the advantage of being able to identify a subject in a relatively short time with less computational effort, it is easily affected by external noise. On the other hand, a fiducial independent approach has the advantage of being less affected by external noise, but it takes higher computational effort and longer authentication time. To compensate for the advantages and disadvantages of the above two methods, the amount of calculation was reduced through the amplitude feature using ACP and the identification accuracy was improved through the interval-based angle feature.

However, in this study, the matching score was calculated using the same weight for the two features, resulting in a disadvantage in terms of the weakness in various environmental variables. Therefore, we intend to explore the application of variable weights for future research to design a robust algorithm for environment variables.

Table 1. Comparison of the proposed algorithm with related research using the same public database.

Ref.	NS	ST	DB	Method	EER	IDA
[48]	56	2-lead Direct Contact type	MITDB NSRDB PTB database	Normalized AC and LDA	3.8 %	96.2 %
[49]	145	2-lead Direct Contact type	(a) MITDB (b) NSRDB (c) LTSTDB	WT and ICA	(a) 0.43 % (b) 0.67 % (c) 1.89 %	(a) 99.57 % (b) 99.33 % (c) 98.11 %
[28]	50	2-lead Direct Contact type (Only single lead of data used)	MITDB NSRDB	Delineation of P and T wave, Correlation	1.01 %	98.99 %
[50]	73	2-lead Direct Contact type (Only single lead of data used)	(a) MITDB (b) IIT(BHU) database (laboratory experiment)	Delineation of P and T wave, Eigenbeat feature extraction	(a) 8.58 % (b) 4.45 %	(a) 91.42 % (b) 95.55 %
[51]	47	2-lead Direct Contact type (Only single lead of data used)	MITDB	Sum of Gaussian, QDA	3 %	97 %
[52]	83	2-lead Direct Contact type (Only single lead of data used), AliveCor single lead Contact type [54]	(a) MITDB NSRDB (b) Laboratory experiment database	FP (Time and amplitude), Proposed hierarchical algorithm	(a) 9.795 % (b) 8.18 %	(a) 90.205 % (b) 91.82 %
[53]	65	2-lead Direct Contact type (Only single lead of data used)	(a) MITDB (b) NSRDB	DWT	(a) 6.9 % (b) 0.6 %	(a) 93.1 % (b) 99.4 %
Proposed method	72	2-lead Direct Contact type (Only single lead of data used)	MITDB	Unnormalized AC and Interval based LDA algorithm	0.143 %	99.857 %

NS number of subject, ST sensor type, DB database, EER equal error rate, IDA identification accuracy, AC autocorrelation, LDA linear discriminant analysis, WT wavelet transform, ICA independent component analysis, QDA quadratic discriminant analysis, DWT discrete wavelet transform.

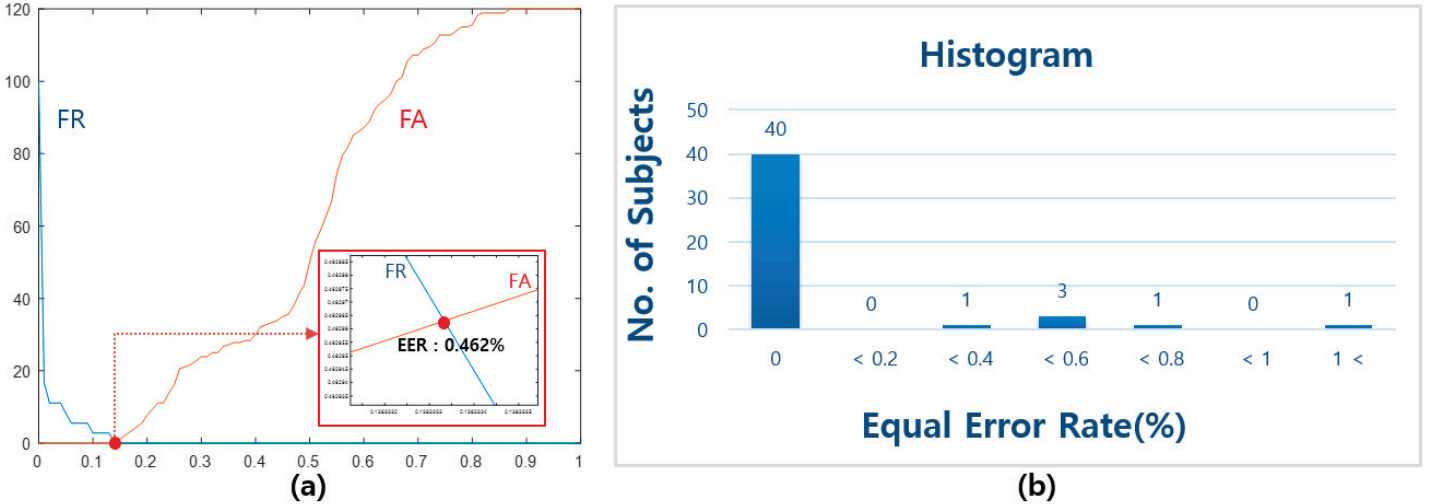

Figure 9. (**a**) Example of the EER depending on individuals (subject no. 41); (**b**) a histogram of the EER (Equal Error Rates) (average EER is 0.143%).

4. Conclusions

In this paper, a novel interval-based LDA algorithm is proposed. The implementation experiments of the proposed algorithm show higher identification accuracy compared to the existing ECG-based identification algorithm using the fiducial point dependent method or fiducial independent method. Based on this algorithm, we can complement each method's disadvantages by using both a fiducial point dependent method (amplitude distance by pixel) and fiducial point independent method (angle distance by feature vector). In addition, our proposed algorithm is able to maintain identification accuracy by tracking the ECG that changes in real-time using a template updating process.

This algorithm was tested with a public ECG database (MIT-BIH) and we compared its performance with related studies using the same database. The results show that the proposed algorithm is more reliable than other algorithms in terms of EER (Equal Error Rate). However, this algorithm has the disadvantage that it requires 5 s for each identification. Therefore, as future research, we intend to reduce the identification time and proceed to commercialize this as a product through multimodal identification combined with other biometrics.

Author Contributions: Conceptualization, C.Y. and G.W.K.; methodology, C.Y., J.-G.L. and G.W.K.; software, G.W.K.; validation, C.Y., J.-G.L. and S.-H.L.; formal analysis, C.Y. and S.-H.L.; investigation, C.Y. and G.W.K.; resources, C.Y. and G.W.K.; data curation, G.W.K.; writing-original draft preparation, C.Y.; writing-review and editing, S.-H.L.; visualization, C.Y. and G.W.K.; supervision, S.-H.L.; project administration, C.Y. and S.-H.L. All authors have read and all agree upon the published version of the manuscript.

Funding: This research was funded by the Technological Innovation R&D Program (S2827786) funded by the Ministry of SMEs and Startups (MSS, Korea).

Conflicts of Interest: The authors declare no conflict of interest.

References

1. Geddes, L.A.; Roeder, R.A. The first electronic electrocardiograph. *Cardiovasc. Eng. Int. J.* **2002**, *2*, 73–79. [CrossRef]
2. Myers, G.B.; Klein, H.A.; Stofer, B.E. The electrocardiographic diagnosis of right ventricular hypertrophy. *Am. Heart J.* **1948**, *35*, 1–40. [CrossRef]
3. Casale, P.N.; Devereux, R.B.; Alonso, D.R.; Campo, E.; Kligfield, P. Improved sex-specific criteria of left ventricular hypertrophy for clinical and computer interpretation of electrocardiograms: Validation with autopsy findings. *Circulation* **1987**, *75*, 565–572. [CrossRef] [PubMed]
4. Addison, P.S.; Watson, J.N.; Clegg, G.R.; Holzer, M.; Sterz, F.; Robertson, C.E. Evaluating arrhythmias in ECG signals using wavelet transforms. *IEEE Eng. Med. Biol. Mag.* **2000**, *19*, 104–109. [CrossRef] [PubMed]
5. Acharya, R.; Kannathal, N.; Krishnan, S.M. Comprehensive analysis of cardiac health using heart rate signals. *Physiol. Meas.* **2004**, *25*, 1139.
6. Bsoul, M.; Minn, H.; Tamil, L. Apnea MedAssist: Real-time Sleep Apnea Monitor Using Single-Lead ECG. *IEEE Trans. Inf. Technol. Biomed.* **2011**, *15*, 416–427. [CrossRef] [PubMed]
7. Karthikeyan, P.; Murugappan, M.; Yaacob, S. Detection of human stress using short-term ECG and HRV signals. *J. Mech. Med. Biol.* **2013**, *13*, 1350038. [CrossRef]
8. Kaniusas, E.; Pfutzner, H.; Mehnen, L.; Kosel, J.; Tellez-Blanco, C.; Varoneckas, G.; Alonderis, A.; Meydan, T.; Vazquez, M.; Rohn, M.; et al. Method for continuous nondisturbing monitoring of blood pressure by magnetoelastic skin curvature sensor and ECG. *IEEE Sens. J.* **2006**, *6*, 819–828. [CrossRef]
9. Saul, J.P.; Rea, R.F.; Eckberg, D.L.; Berger, R.D.; Cohen, R.J. Heart rate and muscle sympathetic nerve variability during reflex changes of autonomic activity. *Am. J. Physiol. Circ. Physiol.* **1990**, *258*, H713–H721. [CrossRef]
10. Pomeranz, B.; Macaulay, R.J.; Caudill, M.A.; Kutz, I.; Adam, D.; Gordon, D.; Kilborn, K.M.; Barger, A.C.; Shannon, D.C.; Cohen, R.J.; et al. Assessment of autonomic function in humans by heart rate spectral analysis. *Am. J. Physiol. Circ. Physiol.* **1985**, *248*, H151–H153. [CrossRef]
11. Agrafioti, F.; Gao, J.; Hatzinakos, D.; Yang, J. Heart biometrics: Theory, methods and applications. In *Biometrics*; InTech: Shanghai, China, 2011; pp. 199–216.

12. Biel, L.; Pettersson, O.; Philipson, L.; Wide, P. ECG analysis: A new approach in human identification. In Proceedings of the 16th IEEE Instrumentation and Measurement Technology Conference, Venice, Italy, 24–26 May 1999.
13. US Federal Trade Commission. Consumer Sentinel Network Data Book for January–December 2018. Available online: https://www.ftc.gov/system/files/documents/reports/consumer-sentinel-network-data-book-2018/consumer_sentinel_network_data_book_2018_0.pdf (accessed on 26 August 2020).
14. Burge, M.; Burger, W. Ear Biometrics. In *Biometrics*; Springer US: Boston, MA, USA, 1996; pp. 273–285.
15. Hossain, S.M.E.; Chetty, G. Next generation identity verification based on face-gait Biometrics. In Proceedings of the International Conference on Biomedical Engineering and Technology, Kuala Lumpur, Malaysia, 4–5 June 2011.
16. Prabhakar, S.; Pankanti, S.; Jain, A.K. Biometric recognition: Security and privacy concerns. *IEEE Secur. Priv.* **2003**, *1*, 33–42. [CrossRef]
17. Sanchit; Ramalho, M.; Correia, P.L.; Soares, L.D. Biometric identification through palm and dorsal hand vein patterns. In Proceedings of the 2011 IEEE EUROCON—International Conference on Computer as a Tool, Lisbon, Portugal, 27–29 April 2011; pp. 1–4.
18. Boulgouris, N.V.; Plataniotis, K.N.; Micheli-Tzanakou, E. (Eds.) *Biometrics: Theory, Methods, and Applications*; John Wiley & Sons, Inc.: Hoboken, NJ, USA, 2009; Volume 9, ISBN 9780470522356.
19. Jain, A.K.; Arun, R.; Salil, P. An introduction to biometric recognition. *IEEE Trans. Circuits Syst. Video Technol.* **2004**, *14*, 4–20. [CrossRef]
20. Israel, S.A.; Irvine, J.M.; Cheng, A.; Wiederhold, M.D.; Wiederhold, B.K. ECG to identify individuals. *Pattern Recognit.* **2005**, *38*, 133–142. [CrossRef]
21. Irvine, J.; Israel, S.; Wiederhold, M.; Wiederhold, B. A new biometric: Human identification from circulatory function. In Proceedings of the Joint Statistical Meetings of the American Statistical Association, San Francisco, CA, USA, 3–7 August 2003.
22. Zhang, Z.; Wei, D. A New ECG Identification Method Using Bayes' Teorem. In Proceedings of the Tencon 2006 IEEE Region 10 Conference, Hong Kong, China, 14–17 November 2006.
23. Singh, Y.N.; Gupta, P. ECG to Individual Identification. In Proceedings of the 2008 IEEE Second International Conference on Biometrics: Theory, Applications and Systems, Arlington, VA, USA, 29 September–1 October 2008.
24. Simon, B.P.; Eswaran, C. An ECG Classifier Designed Using Modified Decision Based Neural Networks. *Comput. Biomed. Res.* **1997**, *30*, 257–272. [CrossRef] [PubMed]
25. Hoekema, R.; Uijen, G.J.H.; van Oosterom, A. Geometrical aspects of the interindividual variability of multilead ECG recordings. *IEEE Trans. Biomed. Eng.* **2001**, *48*, 551–559. [CrossRef] [PubMed]
26. Tan, R.; Perkowski, M. ECG Biometric Identification Using Wavelet Analysis Coupled with Probabilistic Random Forest. In Proceedings of the 2016 15th IEEE International Conference on Machine Learning and Applications (ICMLA), Anaheim, CA, USA, 18–20 December 2016.
27. Agrafioti, F.; Hatzinakos, D.; Bui, F.M. Cardiac biometric security in welfare monitoring. In Proceedings of the 2012 IEEE International Conference on Acoustics, Speech and Signal Processing (ICASSP), Kyoto, Japan, 25–30 March 2012.
28. Singh, Y.N.; Gupta, P. Correlation-based classification of heartbeats for individual identification. *Soft Comput.* **2011**, *15*, 449–460. [CrossRef]
29. Fratini, A.; Sansone, M.; Bifulco, P.; Cesarelli, M. Individual identification via electrocardiogram analysis. *Biomed. Eng. Online* **2015**, *14*, 78. [CrossRef]
30. Singh, Y.N.; Singh, S.K. Evaluation of Electrocardiogram for Biometric Authentication. *J. Inf. Secur.* **2011**, *03*, 39–48. [CrossRef]
31. Guennoun, M.; Abbad, N.; Talom, J.; Rahman, S.M.M.; El-Khatib, K. Continuous authentication by electrocardiogram data. In Proceedings of the 2009 IEEE Toronto International Conference Science and Technology for Humanity (TIC-STH), Toronto, ON, Canada, 26–27 September 2009.
32. Kyoso, M.; Uchiyama, A. Development of an ECG identification system. In Proceedings of the 2001 Conference Proceedings of the 23rd Annual International Conference of the IEEE Engineering in Medicine and Biology Society, Istanbul, Turkey, 25–28 October 2001.
33. Kass, R.E.; Colleen, E.C. (Eds.) *Basis and Treatment of Cardiac Arrhythmias*; Springer Science & Business Media: Berlin/Heidelberg, Germany, 2005; Volume 171.

34. Physionet, Physiobank Archives, Massachusetts Institute of Technology Cambridge, January 2011. Available online: https://www.physionet.org/physiobank/database/#ecg (accessed on 26 August 2020).
35. Sörnmo, L.; Laguna, P. *Bioelectrical Signal Processing in Cardiac and Neurological Applications*; Academic Press: New York, NY, USA, 2005; Volume 8.
36. Chan, A.D.C.; Hamdy, M.M.; Badre, A.; Badee, V. Wavelet Distance Measure for Person Identification Using Electrocardiograms. *IEEE Trans. Instrum. Meas.* **2008**, *57*, 248–253. [CrossRef]
37. Ye, C.; Coimbra, M.T.; Vijaya Kumar, B.V.K. Arrhythmia detection and classification using morphological and dynamic features of ECG signals. In Proceedings of the 2010 Annual International Conference of the IEEE Engineering in Medicine and Biology, Buenos Aires, Argentina, 31 August–4 September 2010.
38. Belgacem, N. ECG Based Human Authentication using Wavelets and Random Forests. *Int. J. Cryptogr. Inf. Secur.* **2012**, *2*, 1–11. [CrossRef]
39. Choudhary, T.; Manikandan, M.S. A novel unified framework for noise-robust ECG-based biometric authentication. In Proceedings of the 2015 2nd International Conference on Signal Processing and Integrated Networks (SPIN), Noida, India, 19–20 February 2015.
40. Gutta, S. Biomedical Signal Processing and Inference in Wearable Sensing Applications. Ph.D. Thesis, Oklahoma State University, Stillwater, OK, USA, 1 December 2016.
41. Plataniotis, K.N.; Hatzinakos, D.; Lee, J.K.M. ECG Biometric Recognition Without Fiducial Detection. In Proceedings of the 2006 Biometrics Symposium: Special Session on Research at the Biometric Consortium Conference, Baltimore, MD, USA, 19–21 September 2006.
42. Matta, R.; Lau, J.K.H.; Agrafioti, F.; Hatzinakos, D. Real-Time Continuous Identification System Using ECG Signals. In Proceedings of the 2011 Canadian Conference on Electrical and Computer Engineering, Niagara Falls, ON, Canada, 8–11 May 2011; pp. 1313–1316.
43. Wang, Y.; Agrafioti, F.; Hatzinakos, D.; Plataniotis, K.N. Analysis of Human Electrocardiogram for Biometric Recognition. *EURASIP J. Adv. Signal Process.* **2007**, *2008*, 148658. [CrossRef]
44. Safie, S.I.; Soraghan, J.J.; Petropoulakis, L. Pulse Active Ratio (PAR): A new feature extraction technique for ECG biometric authentication. In Proceedings of the 2011 IEEE International Conference on Signal and Image Processing Applications (ICSIPA), Kuala Lumpur, Malaysia, 16–18 November 2011.
45. Mücke, D. *Elektrokardiographie Systematisch*; UNI-MED-Verlag: Bremen, Germany, 1996.
46. Khalil, I.; Sufi, F. Legendre Polynomials based biometric authentication using QRS complex of ECG. In Proceedings of the 2008 International Conference on Intelligent Sensors, Sensor Networks and Information Processing, Sydney, Australia, 15–18 December 2008.
47. Pan, J.; Tompkins, W.J. A Real-Time QRS Detection Algorithm. *IEEE Trans. Biomed. Eng.* **1985**, *BME-32*, 230–236. [CrossRef] [PubMed]
48. Agrafioti, F.; Hatzinakos, D. ECG biometric analysis in cardiac irregularity conditions. *Signal, Image Video Process.* **2009**, *3*, 329–343. [CrossRef]
49. Ye, C.; Coimbra, M.T.; Kumar, B.V.K.V. Investigation of human identification using two-lead Electrocardiogram (ECG) signals. In Proceedings of the 2010 Fourth IEEE International Conference on Biometrics: Theory, Applications and Systems (BTAS), Washington, DC, USA, 27–29 September 2010.
50. Singh, Y.N.; Singh, S.K. Identifying Individuals Using Eigenbeat Features of Electrocardiogram. *J. Eng.* **2013**, *2013*, 539284. [CrossRef]
51. Sarkar, A.; Abbott, A.L.; Doerzaph, Z. ECG biometric authentication using a dynamical model. In Proceedings of the 2015 IEEE 7th International Conference on Biometrics Theory, Applications and Systems (BTAS), Arlington, VA, USA, 8–11 September 2015.
52. Arteaga-Falconi, J.S.; Al Osman, H.; El Saddik, A. ECG Authentication for Mobile Devices. *IEEE Trans. Instrum. Meas.* **2016**, *65*, 591–600. [CrossRef]
53. Dar, M.N.; Akram, M.U.; Usman, A.; Khan, S.A. ECG biometric identification for general population using multiresolution analysis of DWT based features. In Proceedings of the 2015 Second International Conference on Information Security and Cyber Forensics (InfoSec), Cape Town, South Africa, 15–17 November 2015.
54. *Heart Monitor AC-002 User Manual*; AliveCor, Inc.: San Francisco, CA, USA, 2015.

applied sciences

MDPI

Article

Spectral and Nonlinear Analysis of Electrodermal Activity in Adolescent Anorexia Nervosa

Zuzana Visnovcova [1,2], Lucia Bona Olexova [1,2], Nikola Sekaninova [1,2], Igor Ondrejka [3], Igor Hrtanek [3], Dana Cesnekova [3], Simona Kelcikova [4], Ivan Farsky [5] and Ingrid Tonhajzerova [1,2,*]

1 Biomedical Center Martin, Jessenius Faculty of Medicine in Martin, Comenius University in Bratislava, 03601 Martin, Slovakia; zuzana.visnovcova@uniba.sk (Z.V.); olexova10@uniba.sk (L.B.O.); sekaninova1@uniba.sk (N.S.)

2 Department of Physiology, Jessenius Faculty of Medicine in Martin, Comenius University in Bratislava, 03601 Martin, Slovakia

3 Psychiatric Clinic, Jessenius Faculty of Medicine in Martin, Comenius University in Bratislava, University Hospital Martin, Kollarova 2, 03659 Martin, Slovakia; igor.ondrejka@uniba.sk (I.O.); igor.hrtanek@uniba.sk (I.H.); cesnekova.danka@gmail.com (D.C.)

4 Department of Midwifery, Jessenius Faculty of Medicine in Martin, Comenius University in Bratislava, 03601 Martin, Slovakia; simona.kelcikova@uniba.sk

5 Department of Nursing, Jessenius Faculty of Medicine in Martin, Comenius University in Bratislava, 03601 Martin, Slovakia; ivan.farsky@uniba.sk

* Correspondence: ingrid.tonhajzerova@uniba.sk; Tel.: +421-2633425

Received: 8 June 2020; Accepted: 25 June 2020; Published: 29 June 2020

Abstract: Anorexia nervosa (AN) is an eating disorder with increasing prevalence in childhood and adolescence. Sympathetic dysregulation is supposed to be the underlying mechanism of increased cardiovascular risk in AN. Thus, we assess the electrodermal activity (EDA) as a non-invasive index of sympathetic cholinergic activity using linear and nonlinear analysis in adolescent AN with the aim of detecting potential biomarkers for AN-linked cardiovascular risk. We examined 25 adolescent girls with AN and 25 age-matched controls. EDA was continuously recorded during a 5-min resting phase. Evaluated parameters were: time-domain (skin conductance level, non-specific skin conductance responses), frequency-domain (EDA in very low, low, sympathetic, high and very high frequency bands) and nonlinear (approximate, sample, symbolic information entropies, detrended fluctuation analysis (DFA)) parameters of EDA and peripheral skin temperature. Our findings revealed lower EDA values indicating a decrease in the sympathetic nervous activity in female adolescents with the acute phase of AN. Further, we found higher nonlinear index DFA in AN vs. controls. We assumed that nonlinear index DFA could provide novel and independent information on the complex sympathetic regulatory network. We conclude that the parameters of complex EDA analysis could be used as sensitive biomarkers for the assessment of sympathetic cholinergic dysregulation as a risk factor for AN-linked cardiovascular morbidity.

Keywords: anorexia nervosa; electrodermal activity; time-domain analysis; frequency-domain analysis; nonlinear analysis

1. Introduction

Anorexia nervosa (AN) is one of the most frequent eating disorders with the highest morbidity and mortality among intake malfunctions [1,2]. Patients with AN are characterised by low weight as a result of the restriction of food intake, fear of weight gain, and distortion of self-image, including fear of being or becoming fat [3,4]. Rates of lifetime prevalence of AN range from 1.4% to 3.3% in

women [5]. AN mainly presents in mid- to late adolescence, although its occurrence in childhood and early adolescence is increasing [6].

In general, the autonomic nervous system (ANS) plays a crucial role in the maintenance of the homeostasis, flexibility and adaptability of the human body. It is assumed that disturbances of the ANS may participate in underlying mechanisms of cardiovascular disorders associated with AN [7]. For example, several studies revealed lower heart rate associated with higher heart rate variability indicating cardiovagal dominance, and sympathetic vascular underactivity indexed by lower blood pressure variability [7–11]. However, studies regarding other biosignals in AN are scarce.

Electrodermal activity (EDA) represents a non-invasive index of sympathetic cholinergic activity. Specifically, changes in sympathetic activity lead to altered activity of eccrine sweat glands, which is related to skin´s ability to conduct electricity and thus to EDA variations [12,13]. Moreover, the eccrine sweat glands are involved in thermoregulation of organisms, and cover the majority of the organism, but are the densest on palms and soles. Indeed, these localizations are mainly used in psychophysiological research, because it is assumed that they are associated with emotion-evoked sweating [13].

From the physiological aspect, the skin is relatively non-conductive, due to its most upper layer of derma—the *stratum corneum*. A variable amount of sweat is released from the ducts of the eccrine sweat glands, which open onto the skin surface. The degree of sympathetic activation affects the amount of filled sweat ducts, and the amount of produced sweat; in turn, this activation influences the degree of skin conduction. Variations of the amount of sweat in the ducts relates to the conductivity of the skin and its measurable changes in EDA [14]. Additionally, Posada-Quintero et al. (2016) revealed that variation in the dynamics of the sympathetic activity evaluated by EDA represent one of the important prognostic and diagnostic tools in diseases associated with autonomic dysfunction [15].

With respect to methodology, Lanata et al. (2012) evaluated changes of EDA by standard time and frequency indices and nonlinear parameters, such as deterministic chaos, recurrence plot, and detrended fluctuation analysis in the healthy group during exposure of sets of images from the International Affective Picture System (IAPS) [16]. This study revealed that nonlinear indices of EDA contribute to better extraction of EDA features, such as characteristics of sympathetic activity without significant differences in two types of used measuring devices (special textile gloves vs. bipolar electrodes) [16]. Our previous study evaluated the difference between standard and nonlinear parameters of EDA (approximate and symbolic information entropy) after cognitive stressors (recovery phase) in healthy young adults. Specifically, whereas skin conductance amplitude remained increased in the recovery phase compared to the baseline period, nonlinear indices decreased under the baseline value. It is assumed that this could be caused by complex mechanisms consisting of feedback loops forming a chaotic system on the central level [17].

Recently, evaluation of EDA in AN has been attracting more attention from scientists. Several studies found a lower amplitude of skin conductance response (SCR) in adult females suffering from AN versus age-matched healthy control (HC) in resting conditions [18–20]. Similarly, Crifaci et al. (2013) revealed a decrease of SCR, but a higher level of frequency of SCR in AN group with respect to healthy volunteers during baseline [10]. Additionally, Soussignan et al. (2011) observed significantly larger SCR during exposure to pictures of food and odorous foods in HC versus AN women [21]. Finally, AN women had lower SCR during rest and the Iowa Gambling Task compared to the HC group [22]. According to these results, Tchanturia et al. (2007) assumed that SCR represents a sensitive indicator of response to stimuli in AN patients [22]. While the variations of SCR in adult AN patients are relatively obvious [18,20], the changes of spectral components and nonlinear features of EDA in adolescent females suffering from AN remain unclear. Moreover, studies evaluating variables of EDA by time, spectral and nonlinear indices in AN adolescents are rare. There exist only a few studies concerning changes of these parameters, and only in healthy adults [15–17,23,24]. For example, time and spectral indices of EDA for frequency bands (range from 0.0 Hz to 0.5 Hz) increased during applications of various stressors (changes of position, cold pressor, and Stroop test) assuming that the

EDA evaluation by different parameters could provide an important quantitative tool for evaluating sudomotor activity regulated by the sympathetic nervous system [15].

Based on these studies, we hypothesized that complex EDA analysis (time-domain, spectral and non-linear) could provide important information related to sympathetic nervous activity in adolescent anorexic patients. Thus, we aimed to evaluate EDA by different parameters of the spectral and nonlinear analysis indicating complex sympathetic cholinergic regulatory network in adolescent anorexia nervosa. To the best of our knowledge, this is the first study to use complex EDA analysis with the aim of detecting potential biomarkers for complex sympathetic cholinergic dysregulation as a risk factor for AN-linked cardiovascular morbidity already present in adolescent age.

2. Materials and Methods

The study was approved by the Ethics Committee of Jessenius Faculty of Medicine in Martin, Comenius University in Bratislava in accordance with the 1964 Helsinki declaration and its later amendments. All participants and their parents/legal representatives were carefully instructed about the study protocol and gave written informed consent to participate in the study before the examination.

2.1. Study Population

The studied group consisted of 25 girls suffering from newly diagnosed AN recruited from inpatients admitted to the Psychiatric Clinic of Jessenius Faculty of Medicine and University Hospital in Martin (mean age: 14.8 ± 0.4 years), and control group of 25 healthy age-matched controls (mean age: 15.1 ± 0.3 years). Exclusion criteria were the following for both groups: history of recent acute illness or chronic cardiovascular, respiratory, endocrine, neurological, metabolic, and infectious diseases, smoking, medication/psychoactive substances, or dietary supplementation potentially affecting the ANS. Moreover, mental disorders and weight abnormalities (underweight/overweight/obesity) were considered as exclusion criteria in control group. The weight was defined according to extended International Obesity Task Force body mass index (BMI) cut-offs for thinness, overweight, and obesity using age- and sex- specific BMI cut-offs, which correspond to the adult BMI range between 18.5 and 25 kg/m^2 for normal weight, and the threshold of 30 kg/m^2 for obesity [25].

2.2. Diagnosis of Anorexia Nervosa

The diagnosis of anorexia nervosa without other comorbid mental disorders (e.g., depressive disorder) was assessed by a thorough clinical investigation based on a unstructured diagnostic interview by a staff child/adolescent psychiatrist according to the Diagnostic and Statistical Manual of Mental Disorders, DSM-5 (American Psychiatric Association, 2013). The AN patients were examined before pharmacotherapy and starting of nonpharmacological regimen interventions, including re-feeding, during the first days of hospitalization.

2.3. The Study Protocol and Evaluated Parameters

The examinations were performed in the Psychophysiological laboratory (Biomedical Center Martin, Jessenius Faculty of Medicine in Martin) under standard conditions with the minimalization of stimuli: a quiet room, 22 °C, in the morning between 8:00 and 11:30 a.m., after a normal breakfast.

Firstly, anthropometric parameters were assessed by body composition analyser InBody 120 (Biospace Co. Ltd, Seoul, Korea). Then, participants were instructed to sit comfortably and rest in a special armchair for 10 min to avoid potential effects of stress (laboratory environment and examining person). After the introductory 10 min, EDA was recorded using FlexComp Infinity Biofeedback (Thought Technology, Canada) with a sampling frequency of 256 Hz. The EDA signal was monitored by two bipolar electrodes composed of 10-mm diameter Ag-AgCl placed on the middle phalanges of two fingers on the non-dominant hand. In accordance with some other studies [26,27], the special EDA conductive gel was not used. Special FlexComp biofeedback electrodes containing a metallic disk set were used without conductive gel as recommended by Thought Technology, Ltd. [28]. These

special electrodes were carefully cleaned with an alcohol wipe after each examination of the subject. In addition, peripheral skin temperature was recorded using FlexComp Infinity Biofeedback (Thought Technology, Canada). The temperature of the periphery was monitored by a sensor attached to the second phalange of one finger on the non-dominant hand. The baseline phase of the study lasted for 5 min.

2.4. Anthropometric Measures

Body composition was analysed using InBody 120 (Biospace Co. Ltd, Seoul, Korea) with multi-segmental multi-frequency (20/100 kHz) bioimpedance analysis, using eight tactile electrodes (thumbs and fingers of the hands, balls of the feet and heels) in a standing position. Thereafter, software Lookin'Body120 (Biospace Co. Ltd, Korea) processed the obtained data. The following body composition parameters were evaluated: weight (kg) and body mass index (BMI, kg/m^2) calculated as the weight (kg) divided by the square of height (m), waist circumference (WC, cm). Body surface area (BSA, m^2) was calculated using the Mosteller equation as:

$$BSA = \sqrt{h \times w/3600}, \quad (1)$$

where h is height (cm) and w is weight (kg) [29].

3. Data Analysis

3.1. Time-Domain Parameters of EDA

The tonic EDA, needed for analysis, was extracted by 10th order low-pass finite impulse response filter (cut off 0.0004 Hz) [15]. Next, the skin conductance level (SCL) was evaluated as a mean amplitude of tonic EDA. SCL informs about quantitative changes in the cholinergic sympathetic nervous system. The physiological values of SCL depend on the size of the sensors used. For 10 mm sensors, the range is from 0 to 30 micro Siemens [14,30].

Non-specific skin conductance responses (NS.SCRs) were obtained as the rate of spontaneous skin conductance responses that occur without external stimuli during examination [31]. Typical values ranged from 1 to 3 per min during baseline. The higher values of NS.SCRs indicate intensified arousal conditions [14]. Thus, the time-domain parameters provide information about changes associated with the sympathetic nervous system [15].

3.2. Power Spectral Analysis of EDA

At first, the data was filtered with an 8th-order Chebyshev Type I low-pass filter. Consequently, the signals were down-sampled to 2 Hz. Then, to eliminate any trend the data was high-pass filtered with an 8th-order Butterworth filter. The power spectra of signals were evaluated using Welch´s periodogram method with a 50% overlap. The mean power spectrum of the analysed unit was computed by fast Fourier transform (using a Blackman window length of 128 samples), and spectral powers [μS^2] in the appropriate frequency bands (VLF: 0.000–0.045 Hz; EDA-Symp: 0.045–0.25 Hz (sum of low (0.045–0.15 Hz) and high 1 (0.15–0.25 Hz) frequencies); HF: 0.25–0.40 Hz and VHF: 0.40–0.50 Hz) were obtained according to Posada-Quintero et al. [15].

From a physiological perspective, the frequency-domain parameters express the spectral distribution of sympathetic arousal in the skin surface [15].

3.3. Nonlinear Indices of EDA

3.3.1. Entropy

Entropy describes the unpredictability, randomness and uncertainty of a system. Entropy represents random and asymmetrical fluctuations in a given time series, and thus the complexity of

the sympathetic cholinergic regulatory system [32]. The fundament of entropy indices calculation is the evaluation of probabilities distribution of the expected value in the time series [32,33].

3.3.2. Approximate and Sample Entropy of EDA

Approximate (ApEn) and Sample (SampEn) entropies describe the probability that the vectors of length m chosen from a time-series of length N that are related within a given tolerance range r, remain similar for the vector of length m + 1.

$$\text{ApEn (m, r, N)} = \Phi^{m}(r) - \Phi^{m+1}(r), \tag{2}$$

$$\text{SampEn (m, r, N)} = \log\left(\Phi^{m}(r) / \Phi^{m+1}(r)\right), \tag{3}$$

where N—number of points, m—length of sequence (for N = 300 length of sequence m = 2), r—tolerance of similarity (r ϵ< 0.1 SD; 0.25 SD>). Minimum values of ApEn and SampEn (around zero) indicate regular system. In contrast, the increasing ApEn and SampEn refer to a random and more complex system [32,34].

3.3.3. Symbolic Information Entropy

The analysis of symbolic information entropy (SIE) has been demonstrated to be sufficient for the investigation of complex systems and is able to describe nonlinear aspects within a time series. The concept of SIE is based on coarse-graining of the time series into symbolic sequences with a certainly given alphabet. This data was transformed by four numbers (0, 1, 2, 3) to classify the dynamic changes of the time series, then these symbols were used to generate SIE [17,24]. The numbers characterize changes of the time series, i.e., 0 and 1 indicate slow and fast increasing of the data, respectively; 2 and 3 specify fast and slowly decreasing signal, respectively. The patterns are divided into vectors of length L = 2 and they are paired into the class according to letters of the vector. For instance, vector 13 means the change of SCL from fast elevation to a slow decrease in the waveform. Index SIE characterizes the randomness and messiness of the system. Symbolic information entropy can be defined as

$$\text{SIE(m)} = -\Sigma^{M}{}_{i=1}\,(p_i * P_i), \tag{4}$$

where if $p_i > 0$, then $P_i = \log_2(p_i)$, else $P_i = 0$. The higher values of SIE represent more irregular, messy and unpredictable signals, whereas the values around zero characterize higher regularity [17,24].

3.3.4. Detrended Fluctuation Analysis of EDA

Detrended fluctuation analysis (DFA) is a scaling analysis method for evaluating the statistical self-similarity properties of the time series. DFA is used to confirm the existence of persistent long-term range associations in EDA data. Exponent α represents the slope of the trend line relating log $\underline{F(n)}$ to log (n) in the range of time-scales. It is estimated by linear regression. Generally, two scaling exponents—α1 and α2 are evaluated, which represent relationships over short (≤30 s) and long (>30 s) timescales, respectively [35]. At first, the analyzed data (length of N) was integrated and divided into boxes of equal length n. In individual boxes of n, a least square line fits the signals. The y coordinate of the straight stretches is marked by $y_n(k)$. Subsequently, we subtracted the local trend $y_n(k)$ from y(k) in each box, i.e., we detrended them. Finally, the root-mean-square fluctuation of this combined and detrended signals was computed according to Lanata et al. (2012) [16]:

$$F(n) = \sqrt{\frac{1}{N}\sum_{k=1}^{N}[y(k) - y_n(k)]^2}, \tag{5}$$

Figure 1 summarizes the EDA evaluated parameters using linear and nonlinear analysis.

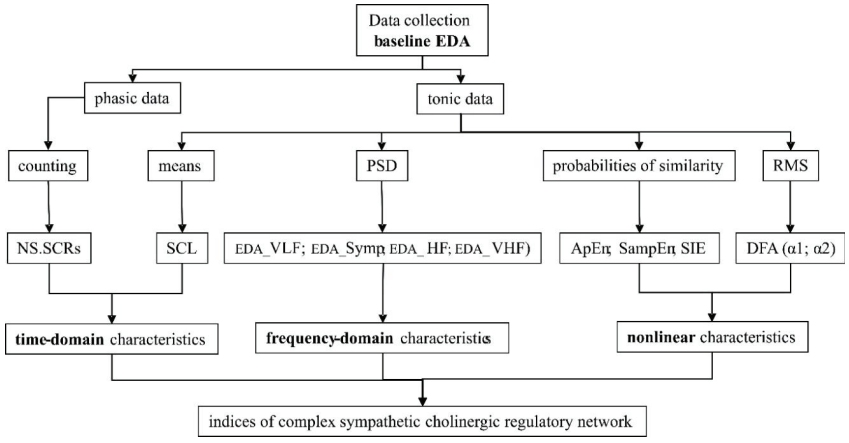

Figure 1. Evaluation of electrodermal activity (EDA) parameters. SCL—skin conductance level; NS.SCRs—nonspecific skin conductance responses; PSD—power spectral density; EDA-VLF—electrodermal activity in very low frequency band; EDA-Symp—EDA in the sum of low and high 1 frequency bands; EDA-HF—EDA in high 2 frequency band; EDA-VHF—EDA in very high frequency band; ApEn—approximate entropy; SampEn—sample entropy; SIE—symbolic information entropy; RMS—root mean square; DFA—detrended fluctuation analysis; α1, α2—indices of detrended fluctuation analysis short-term and long-term correlations, respectively.

4. Statistical Analysis

Statistical analysis was performed by SYSTAT (SSI, Richmond, CA, USA). The Lilliefors´ normality statistical test was used for evaluation data distributions (Gaussian/non-Gaussian). The Mann–Whitney test was used for between-group comparison of EDA indices and the peripheral temperature (PT) because data were not normally distributed. Anthropometric parameters were normally distributed and analyzed by unpaired Student´s *t*-test. The associations between the parameters of EDA and the peripheral temperature, and correlations between anthropometric characteristics (BMI, BSA) and EDA parameters were analyzed using Spearman´s rank-order correlation test. A value of $p < 0.05$ (two-tailed) was considered statistically significant. Anthropometric parameters were expressed as a mean ± standard error of the mean (SEM). Values of EDA and PT were expressed as median (interquartile range).

5. Results

Anthropometric characteristics of both groups (AN and controls) are summarized in Table 1.

Table 1. Anthropometric characteristics of groups.

	Anorexia Nervosa (N = 25)	Controls (N = 25)	*p* Value
Age (years)	14.76 ± 0.38	15.12 ± 0.32	0.580
Weight (kg)	46.04 ± 1.56	57.76 ± 2.58	0.0001
Height (m)	1.65 ± 1.28	1.66 ± 1.90	0.816
BMI (kg/m^2)	16.88 ± 0.48	20.88 ± 0.66	0.0001
BSA (m^2)	1.45 ± 0.03	1.62 ± 0.04	0.001
WC (cm)	64.79 ± 1.41	75.80 ± 1.99	0.0001

Values are expressed as mean ± SEM. BMI—body mass index; BSA—body surface area; WC—waist circumference. *p* values express the comparison between groups. Probabilities $p < 0.05$ were considered as significant.

5.1. Comparison between Groups of Time-Domain EDA Parameters

Index SCL was significantly lower in the AN group compared to controls ($p = 0.041$). No significant differences were found in index NS.SCRs (Table 2).

Table 2. Parameters of electrodermal activity and peripheral temperature.

Parameter	Anorexia Nervosa (n = 25)	Controls (n = 25)	*p* Value
Time-domain indices of EDA			
SCL (μS)	0.67 (0.32–2.21)	2.10 (0.97–3.23)	0.041
NS.SCRs	0.50 (0.00–1.00)	1.00 (0.00–2.00)	0.257
Frequency-domain indices of EDA			
EDA-VLF (μS^2)	18.85 (0.28–56.66)	238.84 (41.39–798.81)	0.001
EDA-Symp (μS^2)	16.33 (3.09–103.79)	815.60 (125.69–1427.03)	0.0001
EDA-HF2 (μS^2)	1.45 (0.37–5.94)	1.73 (0.44–5.07)	0.684
EDA-VHF (μS^2)	1.45 (0.37–5.94)	0.21 (0.03–1.07)	0.765
Nonlinear indices of EDA			
ApEn	0.59 (0.41–0.82)	0.67 (0.45–0.82)	0.674
SampEn	0.48 (0.28–1.18)	0.48 (0.27–0.81)	0.562
SIE	2.14 (2.06–2.65)	2.35 (1.51–2.76)	0.734
α1	1.01 (0.65–1.20)	0.94 (0.77–1.17)	0.779
α2	0.49 (0.07–0.73)	0.11 (0.05–0.31)	0.032
Index of peripheral temperature			
PT (°C)	30.53 (25.93–33.46)	31.43 (28.94–32.54)	0.487

5.2. Comparison between Groups of Spectral-Domain EDA Parameters

Index EDA in the very low frequency band was significantly lower for AN group compared to HC ($p = 0.001$). EDA-Symp was significantly lower during baseline for AN vs. HC groups ($p = 0.0001$). No significant differences were found in indices EDA in the high and very high frequency bands (Table 2).

5.3. Comparison between Groups of Nonlinear EDA Parameters

Only nonlinear index α2 was significantly higher for AN group compared to HC ($p = 0.032$). No significant differences were found in remaining nonlinear parameters—ApEn, SampEn, SIE and α1 between groups (Table 2).

5.4. Comparison between Groups of Peripheral Temperature

Peripheral temperature was without significant differences between groups (Table 2).

Values are expressed as median (interquartile range). SCL—skin conductance level; NS.SCRs—nonspecific skin conductance responses; EDA-VLF—electrodermal activity in very low frequency band; EDA-Symp—EDA in the sum of low and high 1 frequency bands; EDA-HF—EDA in high 2 frequency band; EDA-VHF—EDA in very high frequency band; ApEn—approximate entropy; SampEn—sample entropy; SIE—symbolic information entropy; α1, α2—indices of detrended fluctuation analysis short-term and long-term correlations, respectively; PT—peripheral temperature. The *p* value expresses the comparison between groups. Probabilities $p < 0.05$ were considered to be significant.

5.5. Correlation Analysis

Correlation analysis in the total group revealed significant positive correlations between BMI and SCL, and between BMI and PT ($r = 0.292$, $p = 0.042$; $r = 0.302$, $p = 0.041$, respectively). Index SCL was significantly positively correlated with indices of spectral-domain EDA-VLF and EDA-Symp ($r = 0.556$, $p = 0.0001$; $r = 0.277$, $p = 0.050$, respectively). No significant correlations were found in the remaining parameters.

6. Discussion

To the best of our knowledge, this study was the first to describe features of the sympathetic cholinergic regulatory system using spectral and nonlinear characteristics of EDA in AN adolescents before starting a treatment. The results can be summarized as follows: (1) several indices of time (SCL)

and frequency (EDA-VLF and EDA-Symp) analysis were significantly lower, indicating insufficient sympathetic cholinergic activity already in adolescent anorexia nervosa; (2) in contrast, the index of DFA–α2 showed a different pattern compared to the time and spectral EDA characteristics—it was increased in anorectic patients thus providing independent and novel information related to altered complexity in sympathetic cholinergic regulatory network in anorexia; (3) correlation analysis revealed that BMI is positively associated with SCL and PT indicating possible alteration of sympathetically mediated and thermoregulatory mechanisms in AN, which could be induced by extensive reduction in body weight. Several mechanisms are proposed.

First, reduced SCL is in accordance with other studies that revealed a lower mean of tonic EDA in AN adults [18,20] and extend these findings into the adolescent age group. Additionally, our study revealed statistically important decrease of EDA in spectral-domain (EDA-VLF, EDA-LF and EDA-Symp) in AN compared to controls. Moreover, we found a positive correlation between SCL and EDA-VLF, and between SCL and EDA-Symp. Thus, we assume that EDA evaluation by SCL, EDA-VLF and EDA-Symp indices represents a sufficient non-invasive tool for assessment of sympathetic cholinergic underactivity linked to AN. Our previous study revealed reduced sympathetic activity based on blood pressure variability analysis in newly diagnosed AN girls, indicating nutritional trajectory as an adaptation process associated with bodyweight control from "normal weight to underweight" [8]. Thus, we assume that acute phase of adolescent AN is characterized by sympathetically mediated autonomic hypoactivation which could only partially be ascribed to the reduced body weight measured by BMI associated with reduced basal metabolism. Specifically, neurobiological features such as hormonal deficiencies (e.g., decreased level of leptin and increased level of ghrelin), neurotransmitters (e.g., serotonin and dopamine) [36–38] and electrolyte dysfunctions (e.g., mainly potassium) [39] could play an important role in AN-linked sympathetic underactivity. Notably, leptin as an important molecular signal of energy abundance is closely linked to sympathetic regulation [40,41], and reduced leptin concentrations associated with sympathetic hypoactivity were found in anorexia nervosa [42].

Further, psychopathological features linked to AN could also importantly contribute to sympathetic hypoactivity in AN. A recent study found an inverse correlation between the negative beliefs concerning the consequences of not controlling thoughts and SCL, suggesting that metacognitive variables (i.e., the inescapability of negative thoughts and the need for thought control) could have a key role in modulating patients' sympathetic hypoactivation. Moreover, this worry could be considered a cognitive strategy to avoid intense emotions. From this perspective the dysfunctional metacognitions about worry might yield also a reduced sympathetic activity in anorexia nervosa [20]. Therefore, it is questionable whether AN-linked sympathetic hypoactivity is predominantly a result of neurobiological changes or is more a reflection of psychopathological features associated with AN.

Due to the fact that biological signals are very difficult to interpret and with various timing and diverse structure, we used nonlinear methods of analysis, which better characterize complex qualitative features of the system. Contrary to time and frequency domain indices, we revealed that the index α2 was significantly higher in AN group compared to controls. Thus, we assume that the α2 index could provide independent information about the complexity of the sympathetic cholinergic regulatory network compared to other time and frequency parameters of EDA. With respect to another biosignal (heart rate), Ishizawa et al. (2008) revealed increased complexity of heart rate variability based on DFA in AN group [9]. Additionally, Jelinek et al. (2017) found an increase of α2-HRV during orthostasis in AN compared to controls [43]. It seems that this important issue remains for further research to elucidate pathways linking sympathetic complexity and anorexia nervosa.

In light of these findings, we could speculate about the complex mechanisms. The excitatory and inhibitory influences of the sympathetic regulation derive from different structures of the central nervous system. We assume that the control mechanisms and neural pathways' influence on the central regulation of EDA are complex. Boucsein et al. (1992) define two potential independent paths affecting sweat production and thus skin conductance: A) cortical level—central control of EDA applies to inclination of cortical centers and basal ganglia as brain structures encompassed in

motor control [44]. Notably, cortical pathways encompass excitatory control via pyramidal pathways and the premotor cortex [26,44,45]; B) subcortical level—EDA control encompasses effects from the hypothalamus and the limbic system related to thermoregulatory sweating. Additionally, the inhibitory effects of EDA are mediated by the hippocampus, whereas the excitatory effects are mediated by the amygdala [26,44,45]. Furthermore, the EDA is changed by control effects of reticular formation in the brainstem [26]. Therefore, we assume that the complexity of the brain regulatory regions (prefrontal cortex, hypothalamus) and the existence of feedback loops create a chaotic system influencing EDA.

Conversely, decreased prefrontal cortex (PFC) activity has often been observed among AN patients compared to healthy controls using functional neuroimaging techniques [46–49]. The PFC is a key area for executive functioning, which includes inhibitory control, working memory, and planning. Behavioural studies have revealed that AN patients often have complications with tasks requiring inhibitory control, including response inhibition and task switching [50]. Thus, inhibitory control might be a key element influencing the salient characteristics of AN. Functional imbalance between reward and inhibitory control in the cerebral cortex, especially the PFC, might be related to AN susceptibility and pathology. However, regional structural relevance regarding functional abnormalities in AN remains largely unknown [51–53]. Moreover, the PFC is one of the last brain regions to fully develop relative to subcortical areas [53]. PFC organization undergoes dynamic variations in terms of synaptic density throughout prepubescence and adolescence [54]. This might represent one of key pathomechanisms leading to both AN onset in adolescence and abnormalities in complex feedback regulatory loops resulting in AN-linked sympathetic disruption.

Taken together, the conventional and nonlinear EDA parameters reveal different features of the complex sympathetic cholinergic system consisting of multiple feedback regulatory loops in adolescent AN. While time and spectral parameters of EDA characterize quantitative features of sympathetic cholinergic regulation indicating sympathetic hypoarousal in adolescent AN, the parameter of DFA–α2 could provide novel and distinct information about the qualitative feature complexity of the sympathetic regulatory network, as well.

7. Conclusions

Our study revealed decreased time and spectral indices of EDA indicating sympathetic underactivity in never-treated AN presenting at adolescent age. However, the nonlinear parameter α2 showed a different pattern, indicating abnormal complexity of the sympathetic cholinergic regulatory network in adolescent AN. We suggest that the complex EDA analysis seems to be a sensitive tool for evaluating the activity of the sympathetic cholinergic modulation in AN adolescents. Further, the discrete alteration of the complex sympathetic regulatory network indexed by EDA might represent a risk factor for greater cardiovascular complications already present in adolescent AN.

Future studies should be directed to clarify pathomechanisms linking AN and increased cardiovascular risk, and reveal a complex profile of the sympathetic nervous activity in anorexic patients, particularly in adolescent age. Further clinical research is necessary to identify biomarkers for the assessment of sympathetic complex dysfunction, which could be used for early prevention and personalized treatment of cardiovascular diseases in AN patients.

8. Limitations of the Study

In present study, the cohort consisted of a relatively small homogenous sample of female adolescents with newly diagnosed AN; therefore, it is needs to be validated in a larger cohort with respect to gender. Further, EDA represents a noninvasive index of the sympathetic cholinergic system; therefore, it is not possible to apply these results in terms of general sympathetic dysregulation associated with anorexia nervosa. In this aspect, future research based on continual analysis of additional parameters evaluating the sympathetic control and exploring complex relations between EDA signal and other sympathetically-mediated biosignals (e.g., pre-ejection period, blood pressure variability) under physiological and pathological conditions is needed.

Author Contributions: Z.V., researcher in the field of normal and pathological physiology. She wrote and contributed to the preparation of all parts of the original and revised manuscript and participated in final version of the manuscript. L.B.O., N.S., young researchers in the field of normal and pathological physiology. A significant contribution of all named authors was searching and selection of the scientific studies according to the topic of manuscript, writing and final editing of the original and revised manuscript. I.O., I.H., D.C., clinicians in pediatric psychiatry. They significantly participated in writing and final supervision of the manuscript parts related to the pedopsychiatric topic. S.K., researcher in the field of midwifery and I.F. researcher in the field of nursing. They were involved in searching and selection of the scientific studies according to the topic of manuscript. I.T., professor of normal and pathological physiology, and head of research team. She contributed significantly to the preparation of all parts of the manuscript, final version, supervision and approval of the original and revised manuscript. All authors have read and agreed to the published version of the manuscript.

Funding: This work was funded by the Slovak Scientific Grant Agency under grants VEGA 1/0044/18 and VEGA 1/0190/20, Ministry of Health of the Slovak Republic under the project registration number 2018/20-UKMT-16.

Conflicts of Interest: The authors declare no conflict of interest.

Abbreviations

AN	anorexia nervosa
EDA	electrodermal activity
DFA	detrended fluctuation analysis
ANS	autonomic nervous system
IAPS	International Affective Picture System
SCR	skin conductance response
HC	healthy controls
BMI	body mass index
DSM-5	Diagnostic and Statistical Manual of Mental Disorders
Ag-AgCl	silver-silver chloride
WC	waist circumference
BSA	body surface area
h	height
w	weight
SCL	skin conductance level
NS.SCRs	non-specific skin conductance responses
PSD	power spectral density
EDA-VLF	electrodermal activity in very low frequency band
EDA-Symp	electrodermal activity in the sum of low and high 1 frequency bands
EDA-HF	electrodermal activity in high 2 frequency band
EDA-VHF	electrodermal activity in very high frequency band
ApEn	approximate entropy
SampEn	sample entropy
SIE	symbolic information entropy
RMS	root mean square
$\alpha 1$	indices of detrended fluctuation analysis short-term correlation
$\alpha 2$	indices of detrended fluctuation analysis long-term correlation
VLF	very low frequency band
HF	high frequency band
VHF	very high frequency band
N	number of points
r	tolerance range
m	length of sequence
L	length of vector
p	probability
y	coordinate of the strait stretches
F	fluctuation of combined and detrended signal
SEM	standard mean error
PT	peripheral temperature
PFC	prefrontal cortex

References

1. Arcelus, J.; Mitchell, A.J.; Wales, J.; Nielsen, S. Mortality rates in patients with anorexia nervosa and other eating disorders: A meta-analysis of 36 studies. *Arch. Gen. Psychiatry* **2011**, *68*, 724–731. [CrossRef] [PubMed]
2. Lavender, J.M.; Wonderlich, S.A.; Engel, S.G.; Gordon, K.H.; Kaye, W.H.; Mitchell, J.E. Dimensions of emotion dysregulation in anorexia nervosa and bulimia nervosa: A conceptual review of the empirical literature. *Clin. Psychol. Rev.* **2015**, *40*, 111–122. [CrossRef] [PubMed]
3. American Psychiatric Association. *Diagnostic and Statistical Manual of Mental Disorders*, 5th ed.; American Psychiatric Publishing: Arlington, VA, USA, 2013.
4. Attia, E. Anorexia Nervosa: Current Status and Future Directions. *Annu. Rev. Med.* **2010**, *61*, 425–435. [CrossRef]
5. Favaro, A.; Ferrara, S.; Santonastaso, P. The spectrum of eating disorders in young women: A prevalence study in a general population sample. *Psychosom. Med.* **2003**, *65*, 701–708. [CrossRef] [PubMed]
6. Madden, S.; Morris, A.; Zurynski, Y.A.; Kohn, M.; Elliot, E.J. Burden of eating disorders in 5–13-year-old children in Australia. *Med. J. Aust.* **2009**, *190*, 410–414. [CrossRef]
7. Mazurak, N.; Enck, P.; Muth, E.; Teufel, M.; Zipfel, S. Heart rate variability as a measure of cardiac autonomic function in anorexia nervosa: A review of the literature. *Eur. Eat. Disord. Rev.* **2011**, *19*, 87–99. [CrossRef]
8. Tonhajzerova, I.; Mestanikova, A.; Jurko, A.; Grendar, M.; Langer, P.; Ondrejka, I.; Jurko, T.; Hrtanek, I.; Cesnekova, D.; Mestanik, M. Arterial stiffness and haemodynamic regulation in adolescent anorexia nervosa versus obesity. *Appl. Physiol. Nutr. Metab.* **2020**, *45*, 81–90. [CrossRef]
9. Ishizawa, T.; Yoshiuchi, K.; Takimoto, Y.; Yamamoto, Y.; Akabayashi, A. Heart Rate and Blood Pressure Variability and Baroreflex Sensitivity in Patients With Anorexia Nervosa. *Psychosom. Med.* **2008**, *70*, 695–700. [CrossRef]
10. Crifaci, G.; Billeci, L.; Tartarisco, G.; Balocchi, R.; Pioggia, G.; Brunori, E.; Maestro, S.; Morales, M.A. ECG and GSR measure and analysis using wearable systems: Application in anorexia nervosa adolescents. In Proceedings of the International Symposium on Image and Signal Processing and Analysis (ISPA), Trieste, Italy, 4–6 September 2013; pp. 499–504. [CrossRef]
11. Sachs, K.V.; Harnke, B.; Mehler, P.S.; Krantz, M.J. Cardiovascular complications of anorexia nervosa: A systematic review. *Int. J. Eat. Disord.* **2016**, *49*, 238–248. [CrossRef]
12. Figner, B.; Murphy, R.O. Using Skin conductance in judgment and decision making research. In *A Handbook of Process Tracing Methods for Decision Research*; Schutle-Mecklenbeck, M., Kuehberger, A., Ranyard, R., Eds.; Psychology Press: New York, NY, USA, 2010; pp. 163–184.
13. Dawson, M.E.; Schell, A.M.; Filion, D.L. The Electrodermal System. In *Handbook of Psychophysiology*; Cacioppo, J.T., Tassinary, L.G., Berntson, G.G., Eds.; Cambridge University Press: Cambridge, MA, USA, 2000; pp. 200–223.
14. Dawson, M.E.; Schell, A.M.; Filion, D.L. The Electrodermal System. In *Handbook of Psychophysiology*; Cacioppo, J.T., Tassinary, L.G., Berntson, G.G., Eds.; Cambridge University Press: New York, NY, USA, 2007; pp. 159–181.
15. Posada-Quintero, H.F.; Florian, J.P.; Orjuela-Cañón, A.D.; Aljama-Corrales, T.; Charleston-Villalobos, S.; Chon, K.H. Power Spectral Density Analysis of Electrodermal Activity for Sympathetic Function Assessment. *Ann. Biomed. Eng.* **2016**, *44*, 3124–3135. [CrossRef]
16. Lanatà, A.; Valenza, G.; Scilingo, E.P. A novel EDA glove based on textile-integrated electrodes for affective computing. *Med. Biol. Eng. Comput.* **2012**, *50*, 1163–1172. [CrossRef]
17. Visnovcova, Z.; Mestanik, M.; Gala, M.; Mestanikova, A.; Tonhajzerova, I. The complexity of electrodermal activity is altered in mental cognitive stressors. *Comput. Biol. Med.* **2016**, *79*, 123–129. [CrossRef] [PubMed]
18. Bellodi, L.; Martoni, R.M.; Galimberti, E.; Cavallini, M.C. Low baseline startle in anorexia nervosa patients. *Prog. Neuro-Psychopharmacol. Biol. Psychiatry* **2013**, *40*, 26–29. [CrossRef]
19. Clarke, J.; Ramoz, N.; Fladung, A.K.; Gorwood, P. Higher reward value of starvation imagery in anorexia nervosa and association with the Val66Met BDNF polymorphism. *Transl. Psychiatry* **2016**, *6*, e829. [CrossRef]
20. Palomba, D.; Venturini, M.; Rausa, M.; Contin, S.A.; Penolazzi, B.; Schumann, R.; Ballardini, D. Reduced sympathetic activity and dysfunctional metacognition in patients with anorexia nervosa: A preliminary study. *J. Evid. Based Psychother.* **2017**, *17*, 1–20. [CrossRef]

21. Soussignan, R.; Schaal, B.; Rigaud, D.; Royet, J.P.; Jiang, T. Hedonic reactivity to visual and olfactory cues: Rapid facial electromyographic reactions are altered in anorexia nervosa. *Biol. Psychol.* **2011**, *86*, 265–272. [CrossRef]
22. Tchanturia, K.; Liao, P.C.; Uher, R.; Lawrence, N.; Treasure, J.; Campbell, I.C. An investigation of decision making in anorexia nervosa using the Iowa Gambling Task and skin conductance measurements. *J. Int. Neuropsychol. Soc.* **2007**, *13*, 635–641. [CrossRef]
23. Piacentini, R. *Emotions at Fingertips: Revealing Individual Features in Galvanic Skin Response Signals—Roberto Piacentini—Google Books*; Sapienza Università di Roma: Roma, Italy, 2004.
24. Yang, Z.; Liu, G. An entropy measure of emotional arousal via skin conductance response. *J. Fiber Bioeng. Inform.* **2014**, *7*, 67–80.
25. Cole, T.J.; Lobstein, T. Extended international (IOTF) body mass index cut-offs for thinness, overweight and obesity. *Pediatr. Obes.* **2012**, *7*, 284–294. [CrossRef] [PubMed]
26. Blain, S.; Power, S.D.; Sejdic, E.; Mihailidis, A.; Chau, T. A cardiorespiratory classifier of voluntary and involuntary electrodermal activity. *Biomed. Eng. Online* **2010**, *9*, 11. [CrossRef] [PubMed]
27. Poh, M.Z.; Swenson, N.C.; Picard, R.W. A wearable sensor for unobtrusive, long-term assessment of electrodermal activity. *IEEE Trans. Biomed. Eng.* **2010**, *57*, 1243–1252. [PubMed]
28. FlexComp Infinity Hardware Manual. Available online: https://bio-medical.com/media/support/t7555m.pdf (accessed on 23 June 2020).
29. Mosteller, R. Simplified calculation of body-surface area. *N. Engl. J. Med.* **1987**, *317*, 1098.
30. Venables, P.H.; Gartshore, S.A.; O'Riordan, P.W. The function of skin conductance response recovery and rise time. *Biol. Psychol.* **1980**, *10*, 1–6. [CrossRef]
31. Boucsein, W.; Fowles, D.C.; Grimnes, S.; Ben-Shakhar, G.; Roth, W.T.; Dawson, M.E.; Filion, D.L. Publication recommendations for electrodermal measurements. *Psychophysiology* **2012**, *49*, 1017–1034. [PubMed]
32. Pincus, S.M. Approximate entropy as a measure of system complexity. *Proc. Natl. Acad. Sci. USA* **1991**, *88*, 2297–2301. [CrossRef] [PubMed]
33. Richman, J.S.; Moorman, J.R. Physiological time-series analysis using approximate and sample entropy. *Am. J. Physiol. Hear. Circ. Physiol.* **2000**, *278*, H2039–2049. [CrossRef] [PubMed]
34. Pincus, S.M.; Goldberger, A.L. Physiological time-series analysis: What does regularity quantify? *Am. J. Physiol. Hear. Circ. Physiol.* **1994**, *266*, H1643–1656. [CrossRef]
35. Peng, C.K.; Havlin, S.; Stanley, H.E.; Goldberger, A.L. Quantification of scaling exponents and crossover phenomena in nonstationary heartbeat time series. *Chaos* **1995**, *5*, 82–87. [CrossRef]
36. Ravaldi, C.; Vannacci, A.; Ricca, V. Cardiac complications of anorexia nervosa. *Recenti Prog. Med.* **2003**, *94*, 267–270.
37. Vanderdonckt, O.; Lambert, M.; Cornejo Montero, M.; Boland, B.; Brohet, C. The 12-lead electrocardiogram in anorexia nervosa: A report of 2 cases followed by a retrospective study. *J. Electrocardiol* **2001**, *34*, 233–242. [CrossRef]
38. Tanaka, M.; Nakahara, T.; Muranaga, T.; Kojima, S.; Yasuhara, D.; Ueno, H.; Nakazato, M.; Inui, A. Ghrelin concentrations and cardiac vagal tone are decreased after pharmacologic and cognitive-behavioral treatment in patients with bulimia nervosa. *Horm. Behav.* **2006**, *50*, 261–265. [CrossRef] [PubMed]
39. Ballardini, D.; Schumann, R. *La Riabilitazione Psiconutrizionale nei Disturbi Dell'alimentazione*; Carocci Faber: Roma, Italy, 2011; ISBN 9788874666218.
40. Zigman, J.M.; Elmquist, J.K. Minireview: From anorexia to obesity—The Yin and Yang of body weight control. *Endocrinology* **2003**, *144*, 3749–3756. [CrossRef] [PubMed]
41. Rahmouni, K. Leptin-induced sympathetic nerve activation: Signaling mechanisms and cardiovascular consequences in obesity. *Curr. Hypertens. Rev.* **2010**, *6*, 104–109. [CrossRef]
42. Murialdo, G.; Casu, M.; Falchero, M.; Brugnolo, A.; Patrone, V.; Cerro, P.F.; Ameri, P.; Andraghetti, G.; Briatore, L.; Copello, F.; et al. Alterations in the autonomic control of heart rate variability in patients with anorexia or bulimia nervosa: Correlations between sympathovagal activity, clinical features, and leptin levels. *J. Endocrinol. Investig.* **2007**, *30*, 356–362. [CrossRef] [PubMed]
43. Jelinek, H.; Cornforth, D.; Tarvainen, M.; Spence, I.; Russell, J. Decreased sample entropy to orthostatic challenge in anorexia nervosa. *J. Metab. Syndr.* **2017**, *6*. [CrossRef]
44. Sequeira, H.; Roy, J.-C. Cortical and hypothalamo-limbic control of electrodermal responses. In *Progress in Electrodermal Research*; Springer: Plenum Press: New York, NY, USA, 1993; pp. 93–114.

45. Boucsein, W. *Electrodermal Activity*; Plenum University Press: New York, NY, USA, 1992.
46. Lock, J.; Garrett, A.; Beenhakker, J.; Reiss, A.L. Aberrant brain activation during a response inhibition task in adolescent eating disorder subtypes. *Am. J. Psychiatry* **2011**, *168*, 55–64. [CrossRef]
47. Nagamitsu, S.; Araki, Y.; Ioji, T.; Yamashita, F.; Ozono, S.; Kouno, M.; Iizuka, C.; Hara, M.; Shibuya, I.; Ohya, T.; et al. Prefrontal brain function in children with anorexia nervosa: A near-infrared spectroscopy study. *Brain Dev.* **2011**, *33*, 35–44. [CrossRef]
48. Oberndorfer, T.A.; Kaye, W.H.; Simmons, A.N.; Strigo, I.A.; Matthews, S.C. Demand-specific alteration of medial prefrontal cortex response during an inhibition task in recovered anorexic women. *Int. J. Eat. Disord.* **2011**, *44*, 1–8. [CrossRef]
49. Suda, M.; Brooks, S.J.; Giampietro, V.; Friederich, H.C.; Uher, R.; Brammer, M.J.; Williams, S.C.R.; Campbell, I.C.; Treasure, J. Functional neuroanatomy of body checking in people with anorexia nervosa. *Int. J. Eat. Disord.* **2013**, *46*, 653–662. [CrossRef]
50. Galimberti, E.; Martoni, R.M.; Cavallini, M.C.; Erzegovesi, S.; Bellodi, L. Motor inhibition and cognitive flexibility in eating disorder subtypes. *Prog. Neuropsychopharmacol. Biol. Psychiatry* **2012**, *36*, 307–312. [CrossRef]
51. Castro-Fornieles, J.; Bargalló, N.; Lázaro, L.; Andrés, S.; Falcon, C.; Plana, M.T.; Junqué, C. A cross-sectional and follow-up voxel-based morphometric MRI study in adolescent anorexia nervosa. *J. Psychiatr. Res.* **2009**, *43*, 331–340. [CrossRef] [PubMed]
52. Chui, H.T.; Christensen, B.K.; Zipursky, R.B.; Richards, B.A.; Hanratty, M.K.; Kabani, N.J.; Mikulis, D.J.; Katzman, D.K. Cognitive function and brain structure in females with a history of adolescent-onset anorexia nervosa. *Pediatrics* **2008**, *122*, e426–e437. [CrossRef] [PubMed]
53. Somerville, L.H.; Casey, B.J. Developmental neurobiology of cognitive control and motivational systems. *Curr. Opin. Neurobiol.* **2010**, *20*, 236–241. [CrossRef] [PubMed]
54. Chowdhury, U.; Gordon, I.; Lask, B.; Watkins, B.; Watt, H.; Christie, D. Early-onset anorexia nervosa: Is there evidence of limbic system imbalance? *Int. J. Eat. Disord.* **2003**, *33*, 388–396. [CrossRef] [PubMed]

applied sciences

MDPI

Article

Feature Assessment of Toe Area Activity during Walking of Elderly People with Stumbling Experiences through Wearable Clog-Integrated Plantar Visualization System

Yingjie Jin [1,*], Miho Shogenji [2] and Tetsuyou Watanabe [3,*]

1 Graduated School of Natural Science and Technology, Kanazawa University, Kakuma-machi, Kanazawa 9201192, Japan
2 Faculty of Health Sciences, Institute of Medical, Pharmaceutical and Health Sciences, Kanazawa University, 5-11-80 Kodatsuno, Kanazawa 9200942, Japan; shogen@mhs.mp.kanazawa-u.ac.jp
3 Faculty of Frontier Engineering, Institute of Science and Engineering, Kanazawa University, Kakuma-machi, Kanazawa 9201192, Japan
* Correspondence: e.k-kin@stu.kanazawa-u.ac.jp (Y.J.); twata@se.kanazawa-u.ac.jp (T.W.)

Received: 21 January 2020; Accepted: 12 February 2020; Published: 17 February 2020

Abstract: In this study, we investigated the relationship between toe-area activity and stumbling experiences utilizing our developed sensing system, in order to assess toe-area activity in elderly people with stumbling experiences. The sensing system enables the visualization of the plantar aspect while walking on any surface and under any condition. An image of the plantar aspect is received at a reflecting surface and captured by a camera attached to a clog. The toe-area activity was evaluated by comparing the difference between the toe contact areas at heel-strike and push-off. Thirteen young individuals (nine men and four women, age 22.4 ± 2 years) and nine elderly individuals (five men and four women, age 65.3 ± 2 years) participated in the experiment by walking along a straight line wearing the plantar sensing system on their feet. The analysis found that a low value of the mean toe activity for multiple walking cycles was associated with high stumbling risk, irrespective of age, whereas large variations in toe activity was associated with aging. These results indicate that toe activity can predict stumbling risk irrespective of age. We also found that a large value of the maximum toe activity during multiple walking cycles indicates aging, whereas a low value is associated with high stumbling risk.

Keywords: wearable sensors; gait analysis; stumbling; plantar visualization

1. Introduction

The Cabinet Office of the Government of Japan [1] has reported falls as the fourth leading reason for elderly individuals above 65 years requiring support from caregivers. The demand for risk assessment to prevent falls increases with age. Fall risk assessment considers different types of factors [2]. This study focused on the motion of the plantar region, especially the toe area. Examination of the sole of the foot, or the plantar aspect, which is often conducted as a self-health check in Oriental medicine, is expected to reveal significant health-related information, such as irregularity in toe-area shape corresponding to stumbling risks. However, the number of observational methods used to obtain quantitative data is limited. Measurement systems for observing parts of the foot involved in walking are classified into two types.

The first type comprises pressure-sensor-based systems. Pressure profiles during walking can be obtained by embedding pressure sensors into the insoles found in every shoe. There are several commercially available pressure sensors for investigating the relationship between plantar pressure

and walking speed [3,4], age [5], and foot type [6]. Majumder et al. [7] predicted falls using sensory data from a smartphone and four pressure sensors on a shoe. Ayena et al. [8] assessed the risk of falls at home using a system similar to that of Majumder et al. [7]. Yu et al. [9] developed a shoe system that monitored walking with shoe-integrated force sensors. Crea et al. [10] developed a pressure-sensitive insole based on optoelectronic technology.

The second type of measurement system comprises the inertial measurement unit (IMU)-sensor-based systems [11]. Hung and Suh [12] reduced the position error of shoes estimated by IMU sensors by utilizing additional camera information. Do and Suh [13] developed a walking measurement system that employed inertial sensors and a camera with floor markers to estimate step length and foot angle. An optical sensor was utilized in this case, although the targets did not correspond to plantar observation. Foxlin [14] tracked pedestrians with shoe-mounted IMU sensors. Ojeda and Borenstein proposed a personal dead-reckoning navigation system with a shoe-mounted IMU sensor. Sim et al. [15] proposed an algorithm to detect falls with acceleration sensors on a shoe. Rampp et al. [16] estimated a stride parameter that utilized IMU sensors on a shoe. Mariani et al. [17] used IMU sensors on a shoe to assess 3D spatial parameters of gait.

There are also systems that have both pressure and IMU sensors. Scheoers et al. [18] proposed a shoe fitted with force and IMU sensors. Bamberg et al. [19] proposed a wireless wearable sensor system with an accelerometer, a gyroscope, and a ground force reaction sensor embedded in a shoe. Bebek et al. [20] developed a personal navigation system with pressure and IMU sensors, while Chen et al. [21] detected an abnormality in shoes with four force and IMU sensors. Hegde et al. [22] developed the SmartStep shoe with embedded pressure and acceleration sensors. Kawsar et al. [23] presented an activity detection system that utilized pressure data from a shoe and accelerometers and gyroscope data from a smartphone.

Several studies have focused on toe plantar flexor strength, which is closely related to toe activity. Tsuyuguchi et al. [24] and Kim et al. [25] showed that toe grip strength is an independent risk factor for falling. Mickle et al. [26] showed that the reduction of toe flexor strength and the presence of toe deformities increased the risk of falling among older people. Hiura et al. [27] investigated the relationship between walking ability and falls in elderly Japanese people. Their results showed that lower toe-gap force was significantly associated with falling. Uritani et al. [28] presented a study showing that timed up-and-go test (a measure of functional ability) results were significantly correlated with toe grip strength. Branthwaite et al. [29] assessed the effect of toe flexor exercises on apical plantar pressure, and showed that such exercises can improve forefoot stability and gait efficiency. Takatori et al. [30] showed that the toe elevation angle of participants who had experienced a fall was significantly smaller compared with that of participants who did not fall.

Plantar pressure is another important indicator in walking evaluation, such as for the diagnosis and determination of the course of a disease. Bus et al. [31] showed that the claw/hammer toe deformity is associated with a distal-to-proximal transfer of load in the forefoot, and elevated the plantar pressure at the sub-metatarsal heads in neuropathic diabetic patients. Morag et al. [32] developed predictive models to identify the potential etiological factors associated with elevated plantar pressure. Payne et al. [33] investigated the factors associated with increased plantar pressure on the diabetic foot. Buldt et al. [34] compared plantar pressure among healthy individuals with normal, planus, or cavus feet. Mickle et al. showed that high plantar pressure may increase the risk of falls.

However, the above observation methods can provide only specific data, including pressure or IMU data; thus, they yield a limited amount of information. Examples of unobservable information obtained by conventional measurements include accurate contact area, skin deformation, and skin color. It is difficult for pressure sensors to detect or identify the exact contact area when the load is low (for example, during the swing phase). Thus, we propose a novel wearable sensing system for direct observation of the plantar aspect while walking on any surface and condition [35]. The plantar image is reflected by a reflective film and captured by a camera embedded in a clog (shoe). Passive joints are embedded in the camera holder and around the tarsometatarsal joints to facilitate

walking while wearing the system. However, the main contribution of this sensing system is the investigation of fall or stumbling risks, which were not considered previously. As a first step, we focus on toe activity, which is closely related to walking issues such as stumbling, which in turn is directly connected to falling [36,37]. We did not find research that collected and analyzed visual data on toe movements in the above literature, because of the difficulty in directly obtaining visual data from the sensor. The utilization of the developed system is expected to provide clearer information on toe movements, especially in the swing phase. The movements in the swing phase are difficult to observe by conventional IMU or pressure sheet sensors.

In this study, we investigated the relationship between toe-area activity and stumbling utilizing the developed sensing system. Specifically, we identify the features of toe-area activity while walking in elderly people with a history of stumbling. The main difference of this study from the previous one [35] is the utilization of the sensing system. The previous study provided only primary results among young male participants, whereas this study investigated the effects of aging to identify new features of walking in elderly people with a stumbling history. We also improved the sensing system. The difference between the actual sensing system and previous system [35] is the data processing method: the partially manual data processing used in the previous study was changed to fully automatic data processing to determine the contact area in the toe and the corresponding criterion for evaluation. The remainder of this paper is organized as follows. Section 2 presents the developed clog-integrated plantar visualization system. The experimental investigation and data analysis method for evaluating toe activity are presented in Section 3. The results are provided in Section 4 and discussed in Section 5. A summary of the study is presented in Section 6.

2. Clog-Integrated Plantar Visualization System

Overview of the System

Figure 1a shows an overview of the sensing system. The system was constructed by covering the sensing area, shown in Figure 1b, with the upper part of the clog (Crocs, Niwot, CO, USA). A schematic view of the lower part (sensing area) of the system, which consists of a reflecting surface and camera, is shown in Figure 1b. The image of the plantar aspect was reflected by the reflecting surface and captured by the camera fixed at the holder. Transparent silicone and acrylic plates were utilized as the foot sole to enable visualization of the planta. The sensing area was surrounded by a frame manufactured by a 3D printer (Raise 3D N2) to support the weight of the wearer (exerted through the acrylic plates) and minimize the total weight of the clog.

(**a**) (**b**)

Figure 1. Overview of the system: (**a**) photo of the clog-integrated plantar visualization system and (**b**) dimensions of the underpart of the plantar observation system.

A schematic illustration of the sensing system is shown in Figure 2. The embedding of the camera to capture the visual information from the plantar aspect was a crucial step. Positioning the camera at the bottom of the clog for direct visualization of the planta is difficult because the space under the insole is very narrow. If the area under the plantar aspect is too thick, it becomes difficult to walk,

which makes the observation of walking difficult. Multiple cameras or a camera with an extremely wide field of view and short focal length could be utilized in this setting. However, the use of multiple cameras is unsuitable because they should be sufficiently small to be embedded into or attached to the bottom space of the clog; the processing costs would also increase. Thus, the use of only one camera is ideal to reduce costs and simplify the system. The reflecting surface was placed at the insole of the clog while the camera was set outside the clog to capture the reflected plantar image (Figure 2). The camera was positioned in such a way that the main target areas could be clearly observed. Usually, the heel area of the foot is utilized only during heel-strike, and not during push-off or other swing-phase parts (see Figure 3 for the definition of phases and their components). Therefore, the primary observation target is the toe area, particularly the big toe used during push-off motion.

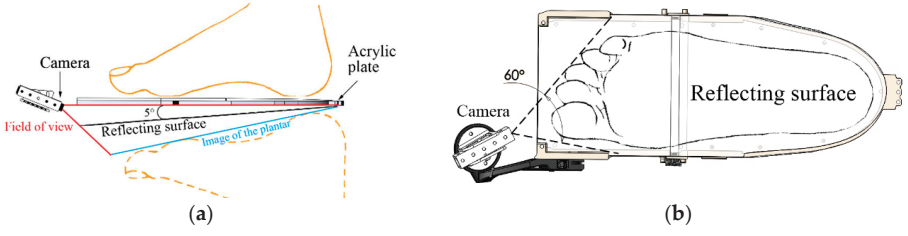

Figure 2. Schematic illustration of the plantar observation system: (**a**) side view and (**b**) bottom view.

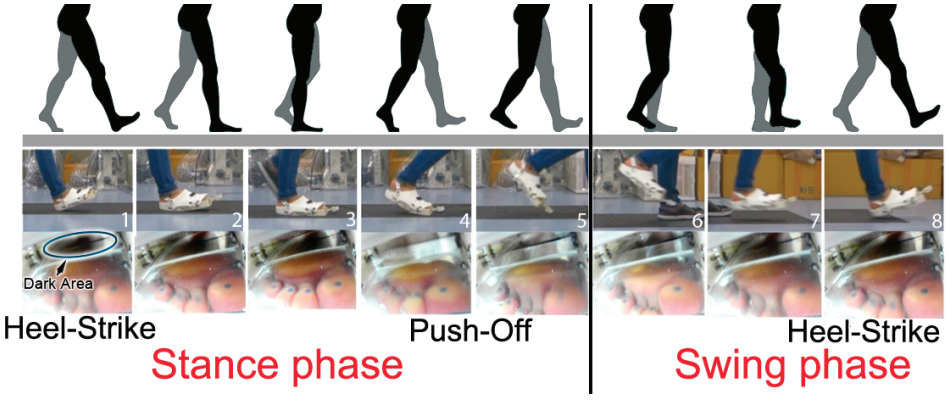

Figure 3. Phases and phase components of a walking cycle and representative images captured by the developed plantar observation system.

An endoscopic camera (GIWOX; resolution: 640 × 480 pixels, focal length: 6 cm to infinity, angle of view: 60°) with a short focal length was utilized to obtain a wide field of view. A 0.6 mm thick reflecting film was utilized to ensure that the thickness of the clog sole was close to its original thickness. Sequential images showing a single walking cycle are presented in Figure 3. The toe area is visible in all phases, while the heel area (dark area in the figure) is visible at heel-strike.

Two passive joints were embedded into the clog (Figure 4). One was installed in the clog near the tarsometatarsal joints to minimize the effect of the 3D-printed solid part on walking and enable the foot to bend naturally. The maximum allowable joint angle was set to 40°. The heel area cannot be observed during push-off because of the passive joints. The other passive joint was installed where the holder is attached to the clog to minimize the disturbance on walking by the camera holder. The camera holder rotates during push-off and the heel area is not observable.

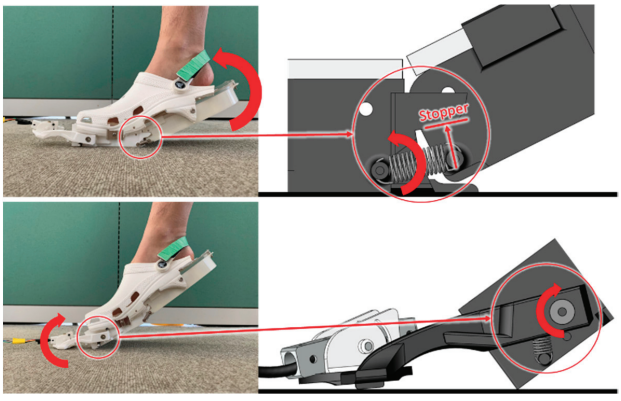

Figure 4. Passive joints to allow the foot to bend at the tarsometatarsal joints and toward the camera.

The system currently costs less than $70, and the sensor for one foot weighs 448 g (the weight of the original clog is 190 g). The camera cable was connected to a Wi-Fi transmitter (F99 WIFI; weight: 27.5 g, size: $63 \times 35 \times 18$ mm^3) with a built-in battery, which was attached to the shank of the wearer to wirelessly transmit the captured images. The electric power reserve of the sensor was sufficient to complete a test lasting approximately 1 h. Hence, the proposed system has the potential for use in a wide variety of experimental environments.

3. Methods

3.1. Participants

The participants were 13 young and healthy individuals (nine men and four women, age 22.4 ± 2 years, weight = 58.3 ± 10.6 kg, height = 165.6 ± 8.9 cm, and foot size = 24–27 cm), and 9 elderly individuals (five men and four women, age 65.3 ± 2 years, weight = 61.4 ± 10.9 kg, height = 163.6 ± 10.8 cm, and foot size = 24–27 cm) without any diseases, impediments, or history of walking problems. The procedure and purpose of the experiments were approved by the Medical Ethics Committee of Kanazawa University (No. 33). Information on the stumbling experiences of participants were obtained via a questionnaire; individuals who had stumbled within a period of three months were designated as individuals with stumbling experience. The participants were separated into two groups according to their responses: those without stumbling experiences (eight young and five elderly individuals) and those with stumbling experiences (five young and four elderly individuals). The toe-area activities of the two groups were compared. The information on participants is summarized in Table 1.

Table 1. Information of participants.

	Young	**Elderly**
Number of participants	13 (M:9 F:4)	9 (M:5 F:4)
Without stumbling experience	8 (M:5 F:3)	5 (M:3 F:2)
With stumbling experience	5 (M:4 F:1)	4 (M:2 F:2)
Information of participants		
Age	22.4 ± 2 years	65.3 ± 2 years
Weight	58.3 ± 10.6 kg	61.4 ± 10.9 kg
Height	165.6 ± 8.9 cm	163.6 ± 10.8 cm
Foot Size	24–27 cm	24–27 cm

M: Male; F: Female.

3.2. Procedure

The participants walked a straight line along a 6.5 m long flat road wearing the developed plantar sensing system on their right foot and a normal shoe on their left foot. The thickness of the sole of the left shoe was the same as that of the sensing system so that there was no impact on walking. There was initially a start and stop zone, measuring 1 m each; and the walking data obtained in the remaining 4.5 m, which corresponds to three walking cycles, were analyzed. The camera cable was attached to the leg of participants to avoid disturbing the walking motion. Before the experiment, we conducted a practice session enabling participants to adapt to the plantar sensing system. This minimized the effects of differences between the left and right footwear on the results. The participants practiced walking while wearing the experimental system until they could walk normally without the feeling of strangeness, and the motion of the left foot (wearing a normal shoe) was close to that of the right foot (wearing the developed sensing system). The practice session was also aimed at minimizing the effect of the camera holder on walking. We determined the position and angle of the camera based on the principle of specular reflection and the horizontal angle of view of the camera. Before each experiment, we controlled the camera position and angle so that the image captured includes all the areas of the forepart of the foot and was focused. We also checked whether the average image intensity was in the range of the desired reference values: 0.53 ± 0.02, which were determined through trial and error based on the results of preliminary experiments. If not, we adjusted the camera's auxiliary brightness so that the average image intensity was within the desired range. With these methods, we obtained the plantar images for all the participants under almost the same illumination conditions and foot positions. The participants were instructed to walk while facing forward as much as possible to avoid looking at their feet during the experiment. Each participant performed the experiment three times; thus, we analyzed nine walking cycles for each participant.

3.3. Data Analysis: Toe-Area Activity

First, each frame containing the toe area was extracted from the captured video streams. Second, the toe area was extracted from the image frame and evaluated. Third, the contact area in the toe area was derived. The information about the contact area was obtained using the skin color of the bare foot. The skin turns white when in contact with something because the blood flow inside capillary vessels is blocked. Thus, the white area in the image corresponds to the contact area. The RGB (red, green, blue) image was transformed into the hue, saturation, value (HSV) image, and the extracted area that satisfied $0.055 < H < 0.167,\ 0.05 < S < 0.75,\ 0.4 < V$ corresponded to the white area. It should be noted that the contact area can be detected by the naked eye. Therefore, the range of H, S, V values for detecting the contact area was manually determined through trial and error, utilizing sample images obtained at preliminary experiments. The same range of HSV values was applied to all the data for all participants. Fourth, using binarization, the extracted area was assigned a value of one, whereas the other areas were assigned a value of zero. Finally, the small noise area was removed. Figure 5 outlines the overall procedure. Figure 6 shows the time series for the contact area in the toe area for the two young study groups over one walking cycle in a single trial. The first peak resulted from pushing-off before taking-off, while the second peak indicates the heel-strike. The difference in the values of the contact areas at the two peaks was large for the group with no stumbling experiences and small for the group with stumbling experiences. We assumed that the former group moved or rotated their toes while pushing off, thus increasing the contact area, whereas the latter group did not. We examined the difference in the two peaks corresponding to toe-area activity, called the difference of two peak-contact areas (DPCA). The DPCA was normalized for variations in the width of the contact area (Figure 5) to compare the value for each group considering individual differences. The normalized DPCA (NDPCA) is defined as follows:

$$\mathrm{NDPCA} = \frac{A_{\mathrm{peak1}} - A_{\mathrm{peak2}}}{A_{\mathrm{peak1}} - A_{\mathrm{min}}} \tag{1}$$

where A_{peak1} denotes the contact area at the first peak, A_{peak2} denotes the contact area at the second peak, and A_{min} denotes the minimum contact area. In short, we used the DPCA as an indicator of toe movement, and the min–max normalization of the DPCA was performed using the maximum and minimum difference between the contact area in each cycle. This eliminated data from individual differences, and finally, the NDPCA was obtained. The NDPCA was automatically derived by the method presented in the Appendix A.

	Algorithm: Extraction of the contact area of the toe area
	Given Image captured by the camera at each frame
1	Select the toe area from the captured image.
2	An RGB image is transformed into an HSV image.
3	Extracted area satisfies $0.055 < H < 0.167$, $0.05 < S < 0.75$, $0.4 < V$.
4	Binarization: Extracted area value = 1, the other area value = 0.
5	Remove the small area.
6	Count the area with a value = 1.
End	

Figure 5. Procedure to derive the toe contact area.

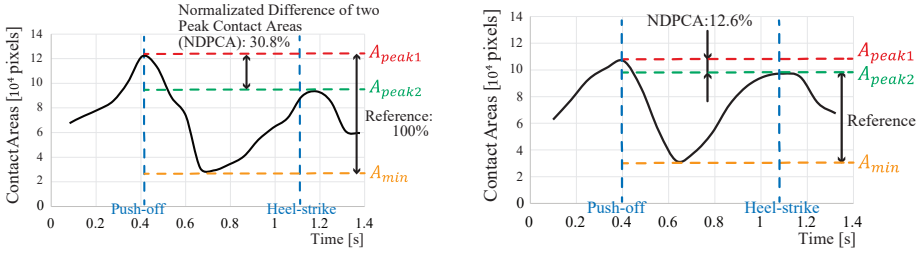

(**a**) (**b**)

Figure 6. Time series of the toe contact area for (**a**) the group without stumbling experiences and (**b**) the group with stumbling experiences. Both subfigures display one example obtained from a single trial for a single young individual. NDPCA: normalized difference of two peak-contact areas.

4. Results

The mean, maximum, minimum, and standard deviation values of NDPCAs for nine walking cycles were used as evaluation values for each participant. There were no significant differences between the groups with regard to gender proportion, as shown in Table 2; thus, we evaluated the results according to stumbling experiences and aging effect.

Table 2. Effect of gender on NDPCA.

NDPCA (Mean ± Std.)	Male	Female	*p*-Value *
Young	0.318 ± 0.073	0.300 ± 0.024	0.536
Elderly	0.317 ± 0.047	0.301 ± 0.059	0.690

* *p* is probability value.

Figure 7 and Table 3 show the calculated NDPCAs. Assessment of the mean NDPCAs showed statistically significant differences between the groups with and without stumbling experiences, regardless of the difference in age between groups. Note that the bars shown in Figure 7 represent not standard error but standard deviation, and thus there could be an overlap in the bars for the groups even if there was a statistically significant difference between them. Toe-area activity (NDPCA) was high for the group with no stumbling history, and low for the group with a stumbling history. The results also showed no significant difference in the NDPCA between the elderly and young people in both groups. We evaluated the maximum and minimum NDPCAs to observe extreme cases in toe activity. The order of the mean value of the maximum NDPCA was highest for elderly individuals without stumbling experience, followed by elderly individuals with stumbling experience, and then young individuals without and with stumbling experience. A statistically significant difference was observed between young and elderly groups ($p < 0.01$), between young and elderly groups with stumbling experiences, and between groups with and without stumbling experiences irrespective of age. A difference was also observed between the young and elderly groups with no stumbling experiences, although it was not statistically significant. No statistically significant difference was observed for any pairs in the minimum NDPCAs. The variations in toe activity were evaluated via the standard deviation of NDPCA. A difference between the young and elderly groups without stumbling experiences was observed, although it was not statistically significant.

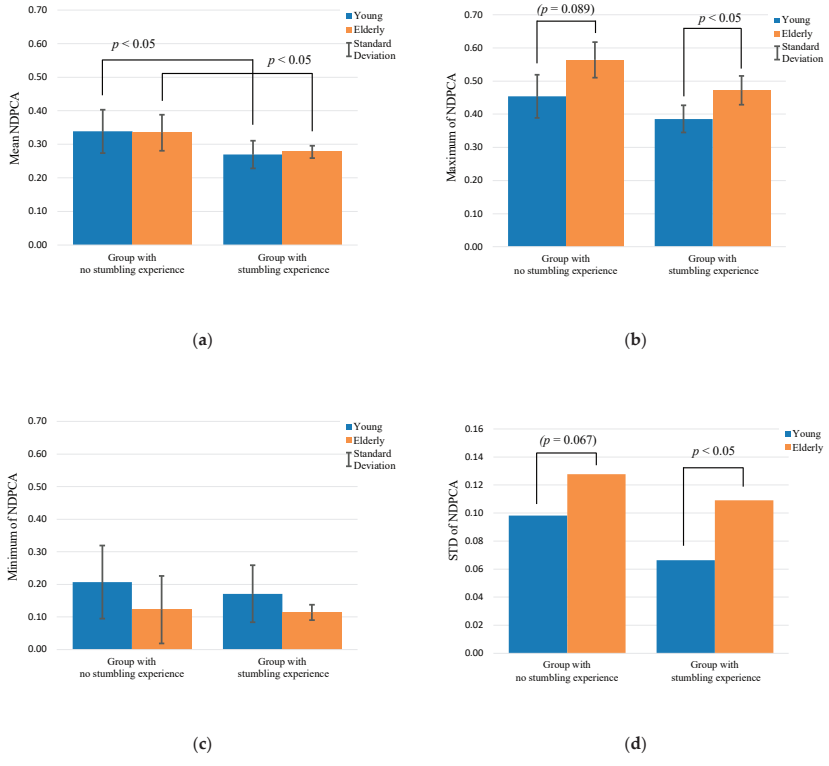

Figure 7. Main results of NDPCA: (**a**) Mean NDPCA; (**b**) Maximum NDPCA; (**c**) Minimum NDPCA; (**d**) Standard deviation of NDPCA.

Table 3. Mean, maximum, minimum, and standard deviation of the NDPCA for groups with and without stumbling histories.

	Young	Elderly	*p*-Value
Mean NDPCA			
Without stumbling experience	0.339 ± 0.064	0.335 ± 0.054	0.451
With stumbling experience	0.269 ± 0.041	0.278 ± 0.019	0.348
***p*-value**	**0.020** *	**0.039** *	/
Maximum NDPCA			
Without stumbling experience	0.454 ± 0.065	0.564 ± 0.053	**0.012** *
With stumbling experience	0.385 ± 0.041	0.471 ± 0.043	**0.038** *
***p*-value**	**0.089**	**0.017** *	/
Minimum NDPCA			
Without stumbling experience	0.207 ± 0.112	0.123 ± 0.104	0.101
With stumbling experience	0.171 ± 0.087	0.113 ± 0.023	0.110
***p*-value**	0.268	0.572	/
NDPCA Standard Deviation			
Without stumbling experience	0.098	0.128	**0.067**
With stumbling experience	0.063	0.109	**0.048** *
***p*-value**	**0.096**	0.151	/

* Significant at $p < 0.05$.

5. Discussion

Toe-activity analysis: Using videos, various toe movements were observed during walking. Some participants without stumbling history showed noticeable toe movements in the swing phase. Preservation of posture in the swing phase by participants with stumbling experiences was observed. These factors monitored by our proposed system are difficult to measure with conventional pressure sheet sensors. These factors also explain why we focused on the first and second peaks (contact areas at the start and end of the swing phase) and the difference between them to evaluate toe activity.

Effects of toe activity on stumbling: All the evaluation values shown in Figure 7 and Table 3 exhibit the same tendency—that is, higher toe activity decreased the stumbling risk. This tendency was particularly clear at the mean and maximum NDPCAs, as the statistically significant differences were evident. Zhang et al. [38] assessed the effects of restricting the flexion–extension motion of the first metatarsophalangeal (MTP) joint on the walking gait of humans, and found a high risk of slipping and falling when the MTP joint is constrained. They also found that the flexion–extension motion of the MTP joint is important for normal walking. This supports our finding that low toe activity was associated with high stumbling risk. Tsuyuguchi et al. [24] and Kim et al. [25] investigated the relationship between the risk of falling and toe flexor strength of middle-aged and elderly individuals. Their results showed that toe flexor strength is related to the incidence of falls. Given that high toe activity corresponds to high flexion–extension ability, it was assumed that the risk of stumbling and falling could be estimated by the NDPCA. Kurihara et al. [39] reported a strong correlation between maximum isometric toe flexor strength and the cross-sectional area of intrinsic and extrinsic plantar muscles. Guillén-Rogel et al. [40] reported a moderate correlation between toe flexor strength and ankle dorsiflexion range of motion (DF ROM). Mecagni et al. [41] reported correlations between ankle ROM and balance among community-dwelling elderly women. The aforementioned studies show that toe flexor strength is closely related to balance in walking because the ankle DF ROM can reflect toe flexor strength. We believe that high NDPCA corresponds to high ankle mobility, which means that individuals with high NDPCA have better walking dynamics than those with low NDPCA. Furthermore, low NDPCA indicates that the flexion–extension motion of the MTP joint is not working properly, and that the DF ROM is low, which increases the risk of falling and stumbling. A well-known criterion for evaluating stumbling is the minimum toe clearance (MTC), which is the minimum distance between the toe and the floor. Moosabhoy et al. [42] investigated the sensitivity of MTC to the hip, knee, and ankle joint angles of the swing leg, and found that MTC was most sensitive to the ankle joint

angle. Therefore, we speculate that toe activity may be related to MTC. The relationship between toe activity and MTC needs to be clarified in future studies.

Aging effect: The mean NDPCA evaluates the toe activity for nine walking cycles. The difference in mean NDPCAs between healthy elderly and young individuals was very small when the groups with and without stumbling histories were compared. This indicates that the mean NDPCA is a valid parameter for evaluating stumbling risk, irrespective of age. With regard to the maximum NDPCA, a high value is associated with aging (whereas a low value indicates high stumbling risk). We speculate that the high value of the maximum NDPCA resulted from a temporary action that compensated for the decline in muscle strength—in other words, a temporary increase in kicking force to raise the foot high and prevent stumbling. A low value of the minimum NDPCA was also associated with aging, although statistically significant differences were not observed. We speculate that the low value of the minimum NDPCA indicates low toe activity, which is caused by aging and leads to high stumbling risk. A large value obtained by subtracting the minimum NDPCA from the maximum NDPCA indicates considerable fluctuations in toe activity, which indicates aging. In the same context, we also evaluated the standard deviation of NDPCA. For elderly individuals with stumbling experience, the standard deviation of NDPCA was higher than that of young people. This highlights the fact that their toe activities were more volatile and may increase their risk of stumbling. The considerable variations in NDPCA could be attributed to the decline in muscle strength due to aging.

Limitations and further applications: The developed sensing system has many potential applications in future research. These include the analysis of the plantar surface during walking by participants with conditions such as toe deformity and weakness [43] or plantar calluses [44], and the exploration of the plantar region to investigate plantar flexion [26] or diabetes [45]. However, the developed sensing system still has some deficiencies that need to be addressed. We provided only one size of sensor. For a few participants in certain testing environments, foot motion around the MTP joints was affected by the rigidity of the clog. Given that this study is based on image analysis, the sensor was sensitive to the illumination of the experimental environment. Illumination may affect the validity of the image data. Color-based image extraction was also affected by the camera settings. This issue can be resolved by locking the white balance of the camera and adjusting the average brightness. The effect of ambient lighting can be reduced by using the auxiliary lighting provided by the endoscope. Further improvements and application of the sensing system to other studies will be part of our future research. The experimental setup for the left and right footwear was different, but the disparity between results was minimized by conducting a practice walking session with participants. The practice session also minimized the difference in weight and toe length (due to the camera holder) between normal shoes and the developed system. However, the influence of these disparities cannot be completely eliminated. In the future, the investigation could be performed using the same experimental setup for the right and left feet, optimizing materials and topology for reducing the weight, and shortening of the length of the camera holder. Consolidating the validity of the obtained results by increasing the number of participants and its application to the assessment of stumbling or fall risk might also be part of our future work. In this study, we investigated only the case in which participants walked straight ahead. The investigation of the plantar aspects of several types of walking, including turning and speed change [46], will be considered in future works. The developed plantar visualization system has potential applications in different types of clinical measurements of fall risk, including the single-leg-stance test and postural sway test. Further investigation of other measurements will be part of future work.

6. Conclusions

This study investigated the relationship between toe activity during walking and stumbling experiences using a clog-integrated plantar visualization system [35]. The system can accurately observe features such as the contact area, skin deformation, and skin color. We focused on the contact area in the toe area and evaluated toe-area activity as participants walked in a straight line.

The participants were separated into four groups: young individuals with and without stumbling experiences and elderly individuals with and without stumbling experiences. The difference between the two peaks at the toe contact area was normalized and calculated to evaluate the toe-area activity. The two peaks correspond to heel-strike and push-off. We evaluated the mean, maximum, minimum, and standard deviation of the toe-area activity for multiple walking cycles. We found that the mean toe-area activity was high for the group with no stumbling experiences, and low for the group with stumbling experiences, irrespective of age. In contrast, the deviations in toe-area activity were high in the elderly group and low in the young group, irrespective of stumbling histories. Therefore, the mean toe-area activity is useful for evaluating stumbling risk, irrespective of age. We also found that a large value of the maximum toe-activity indicates aging, whereas a low value indicates stumbling risk.

Author Contributions: Conceptualization, M.S. and T.W.; Data curation, Y.J.; Formal analysis, Y.J. and T.W.; Funding acquisition, T.W.; Investigation, Y.J. and T.W.; Methodology, Y.J., M.S. and T.W.; Project administration, T.W.; Software, Y.J.; Supervision, M.S. and T.W.; Validation, M.S. and T.W.; Writing—original draft, Y.J.; Writing—review & editing, T.W. All authors have read and agreed to the published version of the manuscript.

Funding: This research was partly funded by Mitutoyo Association for Science and Technology, grant number R1810.

Conflicts of Interest: The authors declare no conflict of interest.

Appendix A

Automatic Deviation of NDPCA

To automatically determine the NDPCA, we developed a method to separate the continuous time-series data of the contact area in the toe area into wave data for one walking cycle; detect the extreme points; and identify the first and second peaks as well as the troughs.

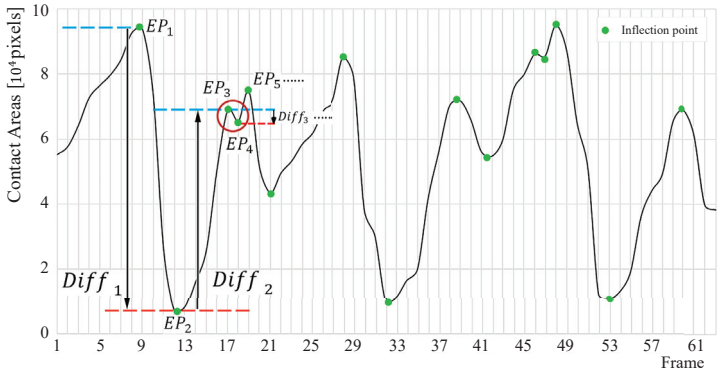

Figure A1. Extreme points extracted by determining the change in the toe contact area.

As shown in Figure A1, the calculation of the DPCA requires the two peaks (A_{peak1}, A_{peak2}) and the minimum point (A_{min}) of each walking cycle from the time-series data. We derived these extreme points by determining where the time derivative of the pixel time-series data was zero. The local peak or maximum is where the time derivative changes from positive to negative. Conversely, the point where the time derivative changes from negative to positive is the local trough or minimum. Figure A1 shows the extreme points (in green) derived from three walking cycles. Some of the extreme points were unnecessary for the calculation of the NDPCA (e.g., EP_2 and EP_3, where EP_i denotes the ith extreme point) and were deleted before calculation. The unnecessary extreme points are characterized

by a small difference between contact areas of adjacent points, as seen in the red circle in Figure A1. Thus, we checked the distance between two adjacent extreme points, $Diff_i$, defined by

$$Diff_i = \left| EP_i - EP_{i+1} \right| \text{ for } i = 1,\ 2,\ 3 \ldots \tag{A1}$$

We then removed the unnecessary extreme points. If $Diff_i$ was less than the threshold θ, then EP_i was removed. The threshold was determined through trial and error, based on the preliminary experiments. Here, the difference between $Diff_{\max}$ and $Diff_{\min}$ was used as the reference for considering the individual difference and normalizing the range of time-series data. In addition, if both EP_i and EP_{i+2} were the same type of extreme points (i.e., peak or trough), then EP_i was removed. The condition for removing EP_i was defined as

$$Diff_i < \theta (i = 1,\ 2,\ 3 \ldots) \tag{A2}$$

where

$$\begin{gathered} \theta = 0.25(Diff_{max} - Diff_{min}) \\ Diff_{max} = \text{Max}(Diff_i)\ (i = 1,\ 2,\ 3 \ldots) \\ Diff_{min} = \text{Min}(Diff_i)\ (i = 1,\ 2,\ 3 \ldots) \end{gathered} \tag{A3}$$

Figure A2 shows time-series data after removing the unnecessary extreme points in Figure A2. Each walking cycle has three extreme points associated with two peaks (A_{peak1} and A_{peak2}) and one trough between the two peaks. The trough between A_{peak1} and A_{peak2} is the minimum point (A_{min}). A_{peak1} and A_{peak2} correspond to the values of the contact areas at push-off and heel-strike, respectively, and A_{min} corresponds to the moment when the contact area during the swing phase is the smallest. The swing phase is detected upon detection of A_{min}. Given that the order of appearance of A_{peak1}, A_{min}, and A_{peak2} is known, the peaks corresponding to A_{peak1} and A_{peak2} are recognized by the location of A_{min}. One walking cycle ends at the trough that occurs after A_{peak2}. The NDPCA is calculated using A_{peak1}, A_{peak2}, and A_{min} in Equation (A2). The overall automatic gait recognition procedure is summarized in Figure A3.

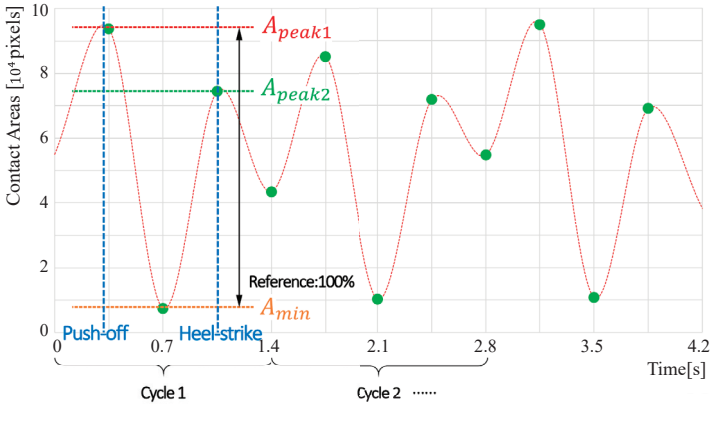

Figure A2. First and second peaks and troughs extracted from the calculation for three cycles.

Algorithm 2: Automatic NDPCA derivation		
	Given	Time-series data from Algorithm 1
1	Find all extreme points.	
2	Remove the extreme points that are not needed to identify the walking cycle and the NDPCA.	
3	Identify the walking cycle and the first and second peaks as well as the troughs.	
4	Derive the NDPCA for each cycle.	
End		

Figure A3. Procedure for deriving the NDPCA automatically.

References

1. Cabinet Office, Government of Japan. Annual Report on the Aging Society. 2016. Available online: https://www8.cao.go.jp/kourei/english/annualreport/2016/2016pdf_e.html (accessed on 15 January 2020).
2. Oliver, D.; Daly, F.; Martin, F.C.; McMurdo, M.E.T. Risk factors and risk assessment tools for falls in hospital in-patients: A systematic review. *Age Ageing* **2004**, *33*, 122–130. [CrossRef]
3. Taylor, A.J.; Menz, H.B.; Keenan, A.-M. The influence of walking speed on plantar pressure measurements using the two-step gait initiation protocol. *Foot* **2004**, *14*, 49–55. [CrossRef]
4. Burnfield, J.M.; Few, C.D.; Mohamed, O.S.; Perry, J. The influence of walking speed and footwear on plantar pressures in older adults. *Clin. Biomech.* **2004**, *19*, 78–84. [CrossRef] [PubMed]
5. Preis, S.; Klemms, A.; Müller, K. Gait analysis by measuring ground reaction forces in children: Changes to an adaptive gait pattern between the ages of one and five years. *Dev. Med. Child Neurol.* **2008**, *39*, 228–233. [CrossRef] [PubMed]
6. Chuckpaiwong, B.; Nunley, J.A.; Mall, N.A.; Queen, R.M. The effect of foot type on in-shoe plantar pressure during walking and running. *Gait Posture* **2008**, *28*, 405–411. [CrossRef]
7. Majumder, A.J.A.; Zerin, I.; Uddin, M.; Ahamed, S.I.; Smith, R.O. Smartprediction: A Real-time Smartphone-based Fall Risk Prediction and Prevention System. In Proceedings of the 2013 Research in Adaptive and Convergent Systems, Montreal, OC, Canada, 1–4 October 2013; pp. 434–439.
8. Ayena, J.C.; Otis, M.J.D.; Menelas, B.A.J. An efficient home-based risk of falling assessment test based on Smartphone and instrumented insole. In Proceedings of the 2015 IEEE International Symposium on Medical Measurements and Applications (MeMeA) Proceedings, Turin, Italy, 7–9 May 2015; pp. 416–421.
9. Yu, H.; Wang, D.; Yang, C.-J.; Lee, K.-M. A walking monitoring shoe system for simultaneous plantar-force measurement and gait-phase detection. In Proceedings of the 2010 IEEE/ASME International Conference on Advanced Intelligent Mechatronics, Montreal, ON, Canada, 6–9 July 2010; pp. 207–212.
10. Crea, S.; Donati, M.; De Rossi, S.M.M.; Oddo, C.M.; Vitiello, N. A wireless flexible sensorized insole for gait analysis. *Sensors* **2014**, *14*, 1073–1093. [CrossRef]
11. Yang, S.; Li, Q. Inertial sensor-based methods in walking speed estimation: A systematic review. *Sensors* **2012**, *12*, 6102–6116. [CrossRef]
12. Hung, T.N.; Suh, Y.S. Inertial sensor-based two feet motion tracking for gait analysis. *Sensors* **2013**, *13*, 5614–5629. [CrossRef]
13. Do, T.N.; Suh, Y.S. Gait Analysis Using Floor Markers and Inertial Sensors. *Sensors* **2012**, *12*, 1594–1611. [CrossRef]
14. Foxlin, E. Pedestrian Tracking with Shoe-Mounted Inertial Sensors. *IEEE Comput. Graph. Appl.* **2005**, *25*, 38–46. [CrossRef]
15. Sim, S.Y.; Jeon, H.S.; Chung, G.S.; Kim, S.K.; Kwon, S.J.; Lee, W.K.; Park, K.S. Fall detection algorithm for the elderly using acceleration sensors on the shoes. In Proceedings of the Annual International Conference of the IEEE Engineering in Medicine and Biology Society, EMBS, Boston, MA, USA, 30 August–3 September 2011; pp. 4935–4938.
16. Rampp, A.; Barth, J.; Schülein, S.; Gaßmann, K.G.; Klucken, J.; Eskofier, B.M. Inertial Sensor-Based Stride Parameter Calculation from Gait Sequences in Geriatric Patients. *IEEE Trans. Biomed. Eng.* **2015**, *62*, 1089–1097. [CrossRef]

17. Mariani, B.; Hoskovec, C.; Rochat, S.; Büla, C.; Penders, J.; Aminian, K. 3D gait assessment in young and elderly subjects using foot-worn inertial sensors. *J. Biomech.* **2010**, *43*, 2999–3006. [CrossRef]
18. Schepers, H.M.; Koopman, H.F.J.M.; Veltink, P.H. Ambulatory assessment of ankle and foot dynamics. *IEEE Trans. Biomed. Eng.* **2007**, *54*, 895–902. [CrossRef] [PubMed]
19. Bamberg, S.J.M.; Benbasat, A.Y.; Scarborough, D.M.; Krebs, D.E.; Paradiso, J. A Gait analysis using a shoe-integrated wireless sensor system. *IEEE Trans. Inf. Technol. Biomed.* **2008**, *12*, 413–423. [CrossRef] [PubMed]
20. Bebek, Ö.; Suster, M.A.; Rajgopal, S.; Fu, M.J.; Huang, X.; Cavusoglu, M.C.; Young, D.J.; Mehregany, M.; van den Bogert, A.J.; Mastrangelo, C.H. Personal Navigation via High-Resolution Gait-Corrected Inertial Measurement Units. *IEEE Trans. Instrum. Meas.* **2010**, *59*, 3018–3027. [CrossRef]
21. Chen, M.; Huang, B.; Xu, Y. Intelligent shoes for abnormal gait detection. In Proceedings of the IEEE International Conference on Robotics and Automation, Pasadena, CA, USA, 19–23 May 2008; pp. 2019–2024.
22. Hegde, N.; Sazonov, E.S. SmartStep 2.0—A completely wireless, versatile insole monitoring system. In Proceedings of the 2015 IEEE International Conference on Bioinformatics and Biomedicine (BIBM), Washington, DC, USA, 9–12 November 2015; pp. 746–749.
23. Kawsar, F.; Hasan, M.K.; Love, R.; Ahamed, S.I. A Novel Activity Detection System Using Plantar Pressure Sensors and Smartphone. In Proceedings of the IEEE 39th Annual Computer Software and Applications Conference, Taichung, Taiwan, 1–5 July 2015; pp. 44–49.
24. Tsuyuguchi, R.; Kurose, S.; Seto, T.; Takao, N.; Tagashira, S.; Tsutsumi, H.; Otsuki, S.; Kimura, Y. Toe grip strength in middle-aged individuals as a risk factor for falls. *J. Sports Med. Phys. Fit.* **2018**, *58*, 1325–1330.
25. Kim, Y.-W.; Kwon, O.-Y.; Cynn, H.-S.; Weon, J.-H.; Yi, C.-H.; Kim, T.-H. Comparison of Toe Plantar Flexors Strength and Balancing Ability between Elderly Fallers and Non-fallers. *J. Phys. Ther. Sci.* **2011**, *23*, 127–132. [CrossRef]
26. Mickle, K.J.; Munro, B.J.; Lord, S.R.; Menz, H.B.; Steele, J.R. ISB Clinical Biomechanics Award 2009. *Clin. Biomech.* **2009**, *24*, 787–791. [CrossRef] [PubMed]
27. Hiura, M.; Nemoto, H.; Nishisaka, K.; Higashi, K.; Katoh, T. The Association Between Walking Ability and Falls in Elderly Japanese Living in the Community Using a Path Analysis. *J. Community Health* **2012**, *37*, 957–962. [CrossRef] [PubMed]
28. Uritani, D.; Fukumoto, T.; Matsumoto, D.; Shima, M. The Relationship Between Toe Grip Strength and Dynamic Balance or Functional Mobility Among Community-Dwelling Japanese Older Adults: A Cross-Sectional Study. *J. Aging Phys. Act.* **2016**, *24*, 459–464. [CrossRef] [PubMed]
29. Branthwaite, H.; Grabtree, G.; Chockalingam, N.; Greenhalgh, A. The Effect of Toe Flexion Exercises on Grip. *J. Am. Podiatr. Med. Assoc.* **2018**, *108*, 355–361. [CrossRef]
30. Takatori, K.; Matsumoto, D. Relationships Between Simple Toe Elevation Angle in the Standing Position and Dynamic Balance and Fall Risk Among Community-Dwelling Older Adults. *PM&R* **2015**, *7*, 1059–1063.
31. Bus, S.A.; Maas, M.; de Lange, A.; Michels, R.P.J.; Levi, M. Elevated plantar pressures in neuropathic diabetic patients with claw/hammer toe deformity. *J. Biomech.* **2005**, *38*, 1918–1925. [CrossRef] [PubMed]
32. Morag, E.; Cavanagh, P.R. Structural and functional predictors of regional peak pressures under the foot during walking. *J. Biomech.* **1999**, *32*, 359–370. [CrossRef]
33. Payne, C.; Turner, D.; Miller, K. Determinants of plantar pressures in the diabetic foot. *J. Diabetes Complicat.* **2002**, *16*, 277–283. [CrossRef]
34. Buldt, A.K.; Forghany, S.; Landorf, K.B.; Levinger, P.; Murley, G.S.; Menz, H.B. Foot posture is associated with plantar pressure during gait: A comparison of normal, planus and cavus feet. *Gait Posture* **2018**, *62*, 235–240. [CrossRef]
35. Jin, Y.; Shogenji, M.; Watanabe, T. Clog-integrated plantar visualization system for evaluating activity during walking. In Proceedings of the 2017 IEEE International Conference on Advanced Intelligent Mechatronics (AIM), Munich, Germany, 3–7 July 2017; pp. 862–867.
36. Byju, A.G.; Nussbaum, M.A.; Madigan, M.L. Alternative measures of toe trajectory more accurately predict the probability of tripping than minimum toe clearance. *J. Biomech.* **2016**, *49*, 4016–4021. [CrossRef]
37. Santhiranayagam, B.K.; Sparrow, W.A.; Lai, D.T.H.; Begg, R.K. Non-MTC gait cycles: An adaptive toe trajectory control strategy in older adults. *Gait Posture* **2017**, *53*, 73–79. [CrossRef]
38. Zhang, J.; Si, Y.; Zhang, Y.; Liu, Y. The effects of restricting the flexion–extension motion of the first metatarsophalangeal joint on human walking gait. *Biomed. Mater. Eng.* **2014**, *24*, 2577–2584. [CrossRef]

39. Kurihara, T.; Yamauchi, J.; Otsuka, M.; Tottori, N.; Hashimoto, T.; Isaka, T. Maximum toe flexor muscle strength and quantitative analysis of human plantar intrinsic and extrinsic muscles by a magnetic resonance imaging technique. *J. Foot Ankle Res.* **2014**, *7*, 26. [CrossRef]
40. Guillén-Rogel, P.; San Emeterio, C.; Marín, P.J. Associations between ankle dorsiflexion range of motion and foot and ankle strength in young adults. *J. Phys. Ther. Sci.* **2017**, *29*, 1363–1367. [CrossRef] [PubMed]
41. Mecagni, C.; Smith, J.P.; Roberts, K.E.; O'Sullivan, S.B. Balance and ankle range of motion in community-dwelling women aged 64 to 87 years: A correlational study. *Phys. Ther.* **2000**, *80*, 1004–1011. [CrossRef] [PubMed]
42. Moosabhoy, M.A.; Gard, S.A. Methodology for determining the sensitivity of swing leg toe clearance and leg length to swing leg joint angles during gait. *Gait Posture* **2006**, *24*, 493–501. [CrossRef] [PubMed]
43. Menz, H.B.; Zammit, G.V.; Munteanu, S.E. Plantar pressures are higher under callused regions of the foot in older people. *Clin. Exp. Dermatol.* **2007**, *32*, 375–380. [CrossRef]
44. Fox, J.; Docherty, C.L.; Schrader, J.; Applegate, T. Eccentric plantar-flexor torque deficits in participants with functional ankle instability. *J. Athl. Train.* **2008**, *43*, 51–54. [CrossRef]
45. Mueller, M.J.; Hastings, M.; Commean, P.K.; Smith, K.E.; Pilgram, T.K.; Robertson, D.; Johnson, J. Forefoot structural predictors of plantar pressures during walking in people with diabetes and peripheral neuropathy. *J. Biomech.* **2003**, *36*, 1009–1017. [CrossRef]
46. Verlinden, V.J.A.; van der Geest, J.N.; Hoogendam, Y.Y.; Hofman, A.; Breteler, M.M.B.; Ikram, M.A. Gait patterns in a community-dwelling population aged 50 years and older. *Gait Posture* **2013**, *37*, 500–505. [CrossRef]

applied sciences

MDPI

Article

A Novel Artificial Pancreas: Energy Efficient Valveless Piezoelectric Actuated Closed-Loop Insulin Pump for T1DM

Alp Kaçar [1,*], Mehmet Bülent Özer [2] and Yiğit Taşcıoğlu [3]

[1] Department of Mechanical Engineering, TOBB University of Economics and Technology, Ankara 06530, Turkey
[2] Department of Mechanical Engineering, Middle East Technical University, Ankara 06800, Turkey; ozerb@metu.edu.tr
[3] Department of Mechanical Engineering, TED University, Ankara 06420, Turkey; yigit.tascioglu@tedu.edu.tr
* Correspondence: a.kacar@etu.edu.tr

Received: 16 June 2020; Accepted: 29 July 2020; Published: 30 July 2020

Abstract: The objective of this work is to develop a closed-loop controlled insulin pump to keep the blood glucose level of Type 1 diabetes mellitus (T1DM) patients in the desired range. In contrast to the existing artificial pancreas systems with syringe pumps, an energy-efficient, valveless piezoelectric pump is designed and simulated with different types of controllers and glucose-insulin models. COMSOL Multiphysics is used for piezoelectric-fluid-structural coupled 3D finite element simulations of the pump. Then, a reduced-order model (ROM) is simulated in MATLAB/Simulink together with optimal and proportional-integral-derivative (PID) controllers and glucose–insulin models of Ackerman, Bergman, and Sorensen. Divergence angle, nozzle/diffuser diameters, lengths, chamber height, excitation voltage, and frequency are optimized with dimensional constraints to achieve a high net flow rate and low power consumption. A prototype is manufactured and experimented with different excitation frequencies. It is shown that the proposed system successfully controls the delivered insulin for all three glucose–insulin models.

Keywords: piezo-fluid-structural coupled simulation; APS; valveless micropump; closed-loop insulin pump

1. Introduction

Piezoelectric pumps are a compact and lightweight alternative in microfluidic flow control. However, artificial pancreas systems (APSs) typically use syringe pumps for insulin delivery. In this paper, we propose a closed-loop controlled valveless insulin pump to keep the blood glucose level of Type 1 diabetes mellitus (T1DM) patients in the desired range. Our objective is to develop a piezoelectric pump that delivers the right amount of insulin while maintaining energy efficiency. Design and optimization of the pump are accomplished by using multi-physics finite element simulations, and the resulting performance is evaluated by numerical tests on mathematical glucose–insulin models and also by laboratory experiments with a preliminary prototype. The rest of this section reviews the related work in the subject matter. Section 2 presents a mathematical model of the pump and three glucose–insulin models with different complexity. Section 3 explains piezoelectric-fluid-structural coupled finite element implementation and simulation-based design optimization in COMSOL to achieve a high flow rate and low power consumption. The designed closed-loop controllers are outlined in Section 4. Sections 5 and 6 present model-based simulations in MATLAB/Simulink and the experiments, respectively. Finally, in Section 7, we discuss current and future work.

1.1. Diabetes Mellitus

Insufficient insulin production in islet cells in the pancreas or tissue resistance against secreted insulin leads to excessive glucose concentration in the blood, which is called diabetes mellitus [1]. Insulin and glucagon, the two necessary secretions of the pancreas, regulate the glucose level in the body. Insulin is secreted to stimulate the cells to absorb the extra glucose for the energy needed, and glucagon is secreted to increase the blood glucose level up to its desired level required for the regulation of the system [2].

According to the findings of the IDF (International Diabetes Federation) in 2017, approximately 425 million adult people (20–79 years) were living with diabetes, and this will rise to 629 million by 2045 [3]. Furthermore, diabetes caused 4 million deaths and at least 727 billion dollars in health expenditure in 2017 and 12% of total spending on adults [3]. Furthermore, statistics of the WHO (World Health Organization) predict a dramatic increase of the adult diabetes population from 4% (in 2000, 171 million people) to 5.4% (366 million worldwide) by the year 2030 [4].

1.2. Closed-Loop Insulin Pumps

Manual injection with an insulin pen or pump causes patients to appear twice in a discrete control loop: as the glucose metabolic system which must be controlled and as the controller itself (cognitive system). Since it is difficult to take all external disturbances and internal systems into consideration, the discrete control method is generally followed by hypoglycemic or hyperglycemic events. Thus, to avoid patients having to determine each insulin dose manually, and to limit the variation in blood glucose concentration, an artificial pancreas needs to be developed as an essential scientific research aim. The required insulin dose is calculated using a control algorithm based on continuous glucose measurements obtained via a sensor without human input, and the precise insulin dose is automatically administered via a pump that continuously delivers insulin [5]. Improvement in glycemic control, in terms of glycated HbA1c (hemoglobin A1c) concentration and a reduction in hypoglycemia, and automatic changes in the basal insulin infusion rate at the time of exercise without any extra high-carbohydrate intake are essential advantages of APSs [6].

A T1DM patient needs to calculate his/her meal intake and required exercise interval in order to inject insulin, and glucose level also needs to be measured several times during a loop [4]. In this manual loop, the whole responsibility is on the patient, and if the patient cannot balance the glucose level correctly, it may cause many different diseases. Consequently, using a closed-loop system controlled by an artificial pancreas is quite beneficial for T1DM patients [6]. Artificial pancreases should be convenient to use, accessible, long-lasting, secure, safe, and affordable. Furthermore, they should also consume low energy. In this study, being low-cost and disposable, and consuming low energy are the primary focused features of an artificial pancreas.

Most of the APSs in the market includes a syringe pump such as Medtronic's MiniMed 670G [7], Beta Bionics' iLet [8], and Tandem's t:slim X2 [9]. However, the clinical use of syringe pumps is associated with several risk factors, including overdose or underdose due to lack of control of the infusion speed, bleeding from backflow, and introduction of air. Overdose is the most problematic and significant one among all. It can lead to severe complications such as hypersecretion, respiratory depression, and hypoxia [10]. Additionally, the use of syringe pumps may not be ideal due to their large size and high-power demands for APS applications, where portability and mobility are important requirements. The novel artificial pancreas, which we propose in this study, functions with a piezoelectric actuated pump and can eliminate the accuracy, portability, and power efficiency issues of the old methods and serve as a solution.

1.3. Piezoelectric Actuated Pumps

A piezoelectric material is a smart mechanical material that can deform when the voltage is applied to it [11]. Piezoelectric actuation is advantageous from many aspects such as high actuation

force, fast mechanical response, ease of integration, compact design, and low power consumption compared to the power required for the actuation of syringe pumps. Piezoelectric actuators can be used in different configurations such as in cylinder shape encircling a tube and moving the fluid in the tube under compressions and expansions along the radial direction [12] or a disc shape piezoelectric actuator moving the fluid with a dome deflected shape [13–17]. Moreover, even valveless designs of the disc configuration are possible for improved reliability due to the elimination of valves [13]. To manipulate, transport, and control the exact amount of fluid in the order of microliters and milliliters, micropumps are of great importance in the microfluidic systems [14]. In order to predict the flow rate and working of the micropump, analytical and numerical results are compared to each other [15].

Furthermore, Laser and Santiago [16] have categorized the micropumps in terms of valves, chamber, thickness, voltage, frequency, pressure, and flow values. Optimization of diffuser dimensions such as diffuser length, diffuser neck width, and diffuser angle is necessary in order to enhance the performance of the micropump on the net flow [17]. Finally, in order to design and manufacture a low-cost micropump that is useful in a variety of applications, the overall micropump design should enable the use of mass fabrication methods [14].

1.4. Insulin/Glucose Models

Modeling of glucose–insulin control systems has gained significant importance in the last 50 years [18], and various glucose–insulin kinetic models have been found in order to capture the glucose–insulin mechanism [19]. Even though there is a wide range of models from simple expressions to complex mathematical models, there are three general groups for mathematical models including linear models (Ackerman [18], Ceresa [20]), nonlinear models (Bergman [21,22], Furler [23]), and comprehensive models (Sorensen [24], Cobelli [25], and Hovorka [26]) [19]. In this work, the Ackerman model is used for optimal controller design, the Bergman model is used for PID controller parameters, and finally, the Sorensen model is used for validation and reliability of models.

2. Mathematical Modeling

2.1. The Piezoelectric Pump Analytical Modeling

The insulin rate that needs to be pumped for an adult is defined as a minimum of 1.67 μL/min [27]. To pump this amount with piezoelectric disk deflection, the valve selection of the pump is one of the most sensitive parts. Neither active nor passive valves were used in this study because the opening-closing speed and back-pressure constraints of the active valves were inadequate for the designed pump, and passive valves are not only difficult to manufacture but also inapplicable in terms of numerical implementation. Instead, a valveless design was desired to be used. In this valveless design, literature reviews of 3D conical, 2D cone-shaped, or planar cone projected options were examined [16]. When the voltage sent to piezoelectric disk is positive, and it does an upward displacement, insulin is pumped from both inlet and outlet, but more from the outlet. When the voltage is negative, the piezoelectric disk will be in downward displacement, and it will pump insulin from the reservoir from both the inlet and outlet, but more from the inlet. According to the difference in pumping frequency, the speed difference between inlet and outlet can be defined. This is illustrated in Figure 1 below. Nozzle and diffuser cone angle, in other words, divergence angle ($2\theta°$), differs from 5° to 70°. Optimum angle needs to be calculated for each system, but studies have searched for angle-length variances as well [28].

The deformation of the piezoelectric pump d_z was calculated using Timoshenko's theory of thin circular plates with small deflection [29].

$$d_z(r,t) = A_0(t)\left[1-\left(\frac{r}{R}\right)^2\right]^2 \quad (1)$$

where r is the radial coordinate, R is the radius of the piezoelectric disk, and A_0 is the time-dependent deflection of the piezoelectric disc. Maximum of d_z is used to calculate the volume. The elliptic conical form is used to calculate the approximate delivered insulin volume analytically. This volume is considered a quarter of one period.

$$V = \frac{\pi 4 R^2 h}{6}, \tag{2}$$

where h is the maximum deflection (d_z) of the piezoelectric disk. The total flow rate from both inlet and outlet can be calculated as follows:

$$Q_{total} = \frac{V}{t_{quarter}}, \text{ where } Q_{total} = Q_{inlet} + Q_{outlet}, \tag{3}$$

and $t_{quarter}$ represents time (e.g., 1/400 s for 100 Hz). In order to validate numerical results easily, Q_{total} equation is used to compare total flow rates in a quarter of one period. Therefore, Equation (3) does not calculate the net flow. The net flow occurs from the difference of Q_{inlet} and Q_{outlet} instead. The following net flow rate equation is calculated in Section 3 using summation of inlet and outlet flow rate difference [30].

$$Q_{net} = \frac{1}{2} \sum_{0}^{1/FR} Q_{inlet} - Q_{outlet}, \tag{4}$$

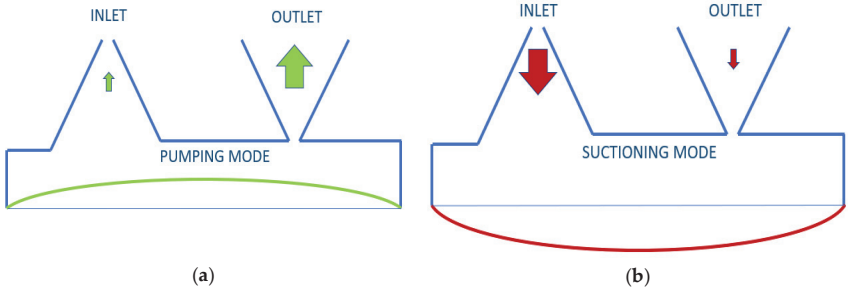

Figure 1. Working principle of valveless piezoelectric pump illustration: (**a**) pumping mode; (**b**) suctioning mode.

2.2. Insulin/Glucose Plant Modeling

Plant models were developed to see T1DM patients' blood glucose levels in the simulation environment and to calculate the controller parameters. These models differ in terms of complexity and accuracy. One linear, one nonlinear, and one comprehensive model were chosen among a great many models in the literature. The Ackerman model was used in the design of an optimum controller as a linear model; the Bergman model was selected as the nonlinear model with medium-level detail applied on all of the controllers. Finally, the Sorensen model was used as the model which shows the insulin glucose level in each part of the body in a detailed way [6].

Ackerman [18,31,32], developed a model utilizing four first-order rate constants for the glucose–insulin interactions. The model is described on two poles; the first one is G = blood glucose level; another one is H = hormone level. g and h parameters in the linear model are defined by considering the differences in fasting values for $g \equiv G - G_0$ and $h \equiv H - H_0$.

$$\frac{dg}{dt} = m_1 g - m_2 h + J(t), \tag{5}$$

$$\frac{dh}{dt} = -m_3 h + m_4 g + K(t); \tag{6}$$

m_1 represents glucose activity, m_2 is a parameter for the removal of glucose due to blood hormone concentration, m_3 is defined for the duration of insulin action, and m_4 is for the removal of hormone for high glucose concentration (typically 0 for T1DM). $J(t)$ and $K(t)$ are rates of exogenous glucose and hormone, respectively.

Although the model of insulin and glucose dynamics adapted from Bergman et al. [21] define a similar model with Ackerman [18] for glucose–insulin interactions, it has three compartments for plasma insulin $I(t)$, remote insulin $X(t)$, and plasma glucose $G(t)$. p_1 is a parameter at which glucose is removed from the plasma space independent of the influence of insulin, and the rate of insulin appearance and remote insulin disappearance are governed by p_3 and p_2, respectively. The time constant for insulin disappearance is defined with n. Subscript B is defined for basal plasma concentrations, and (0) is the level of the parameter at $t = 0$, and external insulin infusion is defined as $u(t)$, and meal intake is defined with $p(t)$ [23,24].

$$\frac{dG(t)}{dt} = -(p_1 + X(t))\, G(t) + p_1 G_B + p(t), \text{ where } G(0) = G_b, \tag{7}$$

$$\frac{dX(t)}{dt} = -p_2 X(t) + p_3[I(t) - I_B], \text{ where } X(0) = 0, \tag{8}$$

$$\frac{dI(t)}{dt} = -n[I(t) - I_B] + u(t), \text{where } I(0) = I_b, \tag{9}$$

Finally, the Sorensen model is used for advanced glucose–insulin metabolism modeling. Sorensen [24] used the compartment modeling technique. Six compartments are used: brain, heart/lungs, gut (stomach–intestine), liver, kidney, and periphery (muscle–adipose). Mass balance for glucose of brain is $\frac{dG_{BV}}{dt}$ and $\frac{dG_{BI}}{dt}$, heart and lungs: $\frac{dG_H}{dt}$, gut: $\frac{dG_G}{dt}$, liver: $\frac{dG_L}{dt}$, kidney: $\frac{dG_K}{dt}$. The periphery is defined, and periphery equations are given below. First subscripts are defined as follows: B is the brain, G is the gut, H is the heart, L is the liver, K is the kidney, and P is the periphery. Second subscripts are as follows: I is interstitial fluid space, and V is vascular blood space; also B is defined as basal value, and N is defined as normalized value by using basal values [33].

$$\frac{dG_{PI}}{dt} = \frac{V_{PI}}{T_P^G V_{PI}} \cdot (G_{PV} - G_{PI}) - \frac{\Gamma_{PGU}}{V_{PI}}, \tag{10}$$

On the other hand, mass balance for insulin of the brain is $\frac{dI_B}{dt}$, and for heart and lungs $\frac{dI_H}{dt}$. In terms of insulin intake, $i(t)$, gut $\frac{dI_G}{dt}$, liver $\frac{dI_L}{dt}$, and kidney $\frac{dI_K}{dt}$. The periphery is represented as follows:

$$\frac{dI_{PI}}{dt} = \frac{V_{PI}}{T_P^I V_{PI}^I} \cdot (I_{PV} - I_{PI}) - \frac{\Gamma_{PIC}}{V_{PI}}, \tag{11}$$

Another part of the model is metabolic sources and sinks for glucose compartment such as peripheral glucose uptake, hepatic glucose production and uptake, and kidney glucose excretion. Additionally, for insulin compartment, liver insulin clearance, peripheral insulin clearance, and kidney insulin clearance variables are used while defining the glucagon model [19]. Sorensen model parameters are defined with delivered insulin $i(t)$, blood glucose concentration G, blood insulin concentration I, vascular blood flow rate Q, metabolic secreting rate Γ, volume V, and trans-capillary diffusion rate T [24]. All glucose–insulin mathematical models were designed with T1DM parameters in MATLAB-Simulink, and minute-based open-loop simulations and step responses were identified. The model parameters of Ackerman can be found in Section 4, the Bergman Model was taken from [22], and the Sorensen model was taken from [19] Appendix B5.

3. Numerical Implementation

3.1. Piezoelectric Pump Finite Element Implementation

Solid mechanics and electrostatics equations were used to calculate piezoelectric dynamics numerically in the stress-charge form.

$$\{T\} = \left[c^E\right]\{S\} - [e]^t\{E\}, \tag{12}$$

$$\{D\} = [e]\{S\} + \left[\varepsilon^S\right]\{E\}, \tag{13}$$

where T is stress vector, S is elastic strain vector, $[c^E]$ is elastic stiffness under constant electric field, $[e]$ is a coupling matrix, and superscript t on $[e]$ means transpose of the matrix $[e]$. D is electric flux density of piezoelectric material, E is electric field intensity, and $\left[\varepsilon^S\right]$ is dielectric permittivity under constant strain [34]. The values of these parameters are presented in Table 1 with other material properties. The dimensions of the pump are illustrated in the same table as well. Some of dimensions are optimized in Section 3.2, so initial values are given.

Table 1. Material properties [34,35].

Material/Dimensions	Parameter	Value	Unit
PZT-5J	Density	7800	kg/m^3
Diameter (D_p): 25 mm *Thickness* (t_p): 0.4 mm	Elasticity matrix $\left[c^E\right]$	$\begin{bmatrix} 8.2 & 3.4 & 3.0 & 0 & 0 & 0 \\ 3.4 & 8.2 & 3.0 & 0 & 0 & 0 \\ 3.0 & 3.0 & 5.9 & 0 & 0 & 0 \\ 0 & 0 & 0 & 2.1 & 0 & 0 \\ 0 & 0 & 0 & 0 & 2.1 & 0 \\ 0 & 0 & 0 & 0 & 0 & 2.4 \end{bmatrix} 10^{10}$	N/m^2
Chamber Dimensions: *Inlet/Outlet Diameter* (D_{out}): 3 mm *Nozzle Small Radius* (r_d): 50 µm	Piezoelectric Coupling Matrix $[e]^t$	$\begin{bmatrix} 0 & 0 & -10.48 \\ 0 & 0 & -10.48 \\ 0 & 0 & 16.58 \\ 0 & 0 & 0 \\ 0 & 14.25 & 0 \\ 14.25 & 0 & 0 \end{bmatrix}$	C/m^2
Nozzle Big Radius (R_d): 0.25 mm (Initial) *Chamber Height* (*mu*): 0.5 mm (Initial)	Permittivity $\left[\varepsilon^S\right]/\varepsilon_0$, where $\varepsilon_0 = 8.85 * 10^{-12}\ F/m$	$\begin{bmatrix} 1641 & 0 & 0 \\ 0 & 1641 & 0 \\ 0 & 0 & 1143 \end{bmatrix}$	1
Nozzle Length (L): 0.5 mm (Initial)	Damping (Isotropic Loss Factor) η_s	0.02	1
Divergence Angle (θ): 11° (Initial)	Dielectric Loss (Isotropic Loss Factor) for Electrical Permittivity εS	0.02	1
Brass	Density	8500	kg/m^3
Diameter (D_c): 27 mm	Young modulus	90,000	MPa
Thickness(t_b): 0.2 mm	Poisson's ratio	0.32	1
Insulin	Density	997	kg/m^3
	Kinematic viscosity	0.0014	kg/m.s

For numerical simulation of the piezoelectric actuator, solid mechanics and two-way electrostatic coupling were used, and appropriate dimensions were determined through iterative design and simulations. Piezoelectric material used in the simulations were decided to be the 27 × 0.5 mm piezoelectric disk of the STEMinc (Davenport, FL, USA) [35] company. Last but not least, the optimum design was found by conducting a three-way analysis (e.g., electrostatics, structural mechanics, and laminar flow) to the system. The requirements for a valveless design are as follows: the flow velocity needs to reach to 1 m/s but should be less than 8 m/s, the piezoelectric disk diameter should be 27 mm, the maximum piezoelectric disk displacement should be 50 µm and minimum displacement should be 2.5 µm, net flows should be at least 2.5 mL/h (~0.1 µL/s), the size of the pump should fit the palm of a hand, the maximum voltage supply should be 100 Vp-p, and, finally, 0.1 A continuous, the instantaneous current (transient) value of one ampere, should be the maximum value needed for current.

Planar/horizontal design was implemented, as shown in Figure 2, and when this design was finished and after defining a starting point, parameter ranges such as diffuser/nozzle angle, nozzle's wide diameter, nozzle length, and length of the chamber were decided accordingly. Between the range of minimum 1 degree and maximum 30 degrees, 10-degree nozzle angle; between the range of minimum 0.1 mm and maximum 1 mm, 1 mm nozzle length; and, finally, between the range of minimum 0.5 mm and maximum 2 mm, 0.5 mm nozzle diameter were used for simulation iterations.

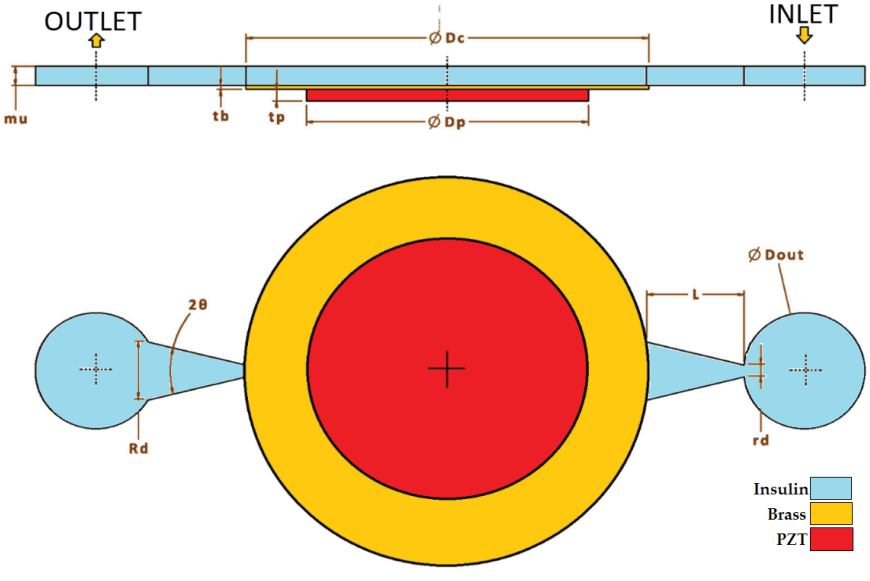

Figure 2. Geometry and dimensions.

The input signal to the piezoelectric pump is defined as follows, where V is voltage, FR is the frequency (in Hz) of applied voltage and t is time:

$$V(t) = V \sin(2\pi \cdot FR \cdot t), \tag{14}$$

By using COMSOL Multiphysics 5.4 [34], analyses were made in different domains both in a single and a coupled way, and with different time steps, mesh sizes, and discretization values. Different relative tolerance values were tried as well. According to the results of Eigenfrequency study analysis, the piezoelectric actuator's first natural frequency was calculated as 6373 Hz without fluid. Then the transient analysis setup was started. Damping was defined to the linear elastic material, dielectric loss was defined to the piezoelectric disk, a fixed constraint was defined to the outer surface of the brass located under the piezo, and lastly, the ground was defined to the one surface of the piezoelectric material and terminal to the other surface. Force, displacement, and voltage were assigned as 0 for initial conditions. In the piezoelectric actuator's first mode shape, it was seen that it had displacements as shown in Figure 3. According to the piezoelectric actuator data [35], expected displacement could reach up to 50 µm at 155 Vp-p; hence, arrangements that provide this displacement were determined. The applied voltage was 100 Vp-p, and the frequency was 100 Hz. How voltage and frequency affected the net flow in the optimization part can also be seen in Section 3.2.

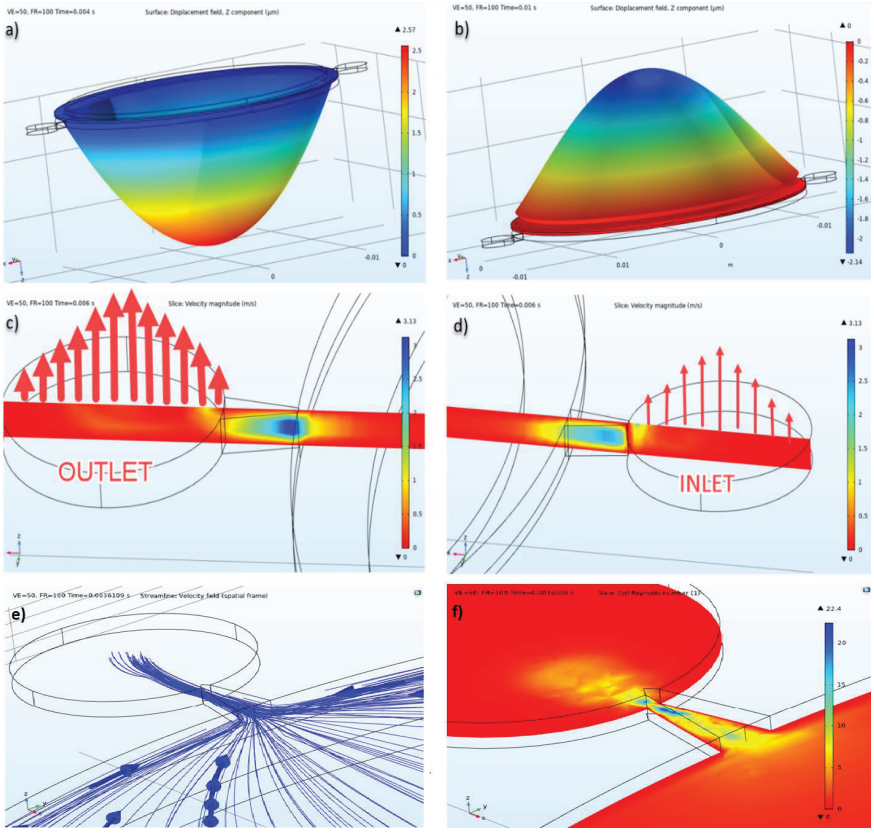

Figure 3. (**a**) Displacement of the piezoelectric actuator at pumping mode, (**b**) suction mode, (**c**) inlet velocity illustration, (**d**) outlet velocity illustration at the same time, (**e**) velocity field streamlines, (**f**) cell Reynold's number.

Insulin flow is defined as an incompressible flow, at 293.15 K temperature, under 1 atm reference pressure, and without a turbulence model. Cell Reynold's numbers shown in Figure 3f verified that there was no need for a turbulence model. As an initial condition, velocity and pressure were given as 0 (zero). As a boundary condition, after defining the stable wall, the wall condition was given as no-slip, and it was defined with inlet and outlet, as seen in Figure 3. For inlet and outlet, 0 Pa pressure condition was given, and no constraint was defined for flow direction. Absolute tolerance was given as 0.001, and the PARDISO solver was used in a coupled analysis study. The results of displacement of the piezoelectric actuator under insulin pressure, the pressure inside the pump chamber, the current passing through the terminal in the electrical circuit, and velocity values in inlet and outlet were calculated and presented in different plots of this study.

3.2. Piezoelectric Pump Optimization

Analyses were done between 100 K to 500 K mesh elements for coupled analysis to prove mesh independency. After mesh convergence analyses, <1% for structure-based error and ~8% flow-based error were calculated for 200 K. The analysis time measured a minimum 2.5 h to 262 h for 100 K to 500 K grid analysis with 1% relative tolerance and 1/40 step size (40 time steps per cycle); as a result, the 200 K grid had an acceptable error, so it was used. There were many analyses done, as well, for different

time-steps from 20 steps per cycle to 1600 steps per cycle. These analyses took a minimum of 1.5 h to 48 h for 100 K grid size and 1% relative tolerance. Error was calculated with respect to 1600 steps per cycle. The error was, respectively, >41% for 20 step, 8.5% for 40 step, 7.5% for 100 step, and <1.5% for 400 step per one cycle. i7-7700-32GB hardware was used for this analysis and time optimization.

Nozzle/diffuser divergence angle, nozzle/diffuser wide radius, nozzle/diffuser length, and chamber height were optimized. According to [13] and [30], when the chamber diameter increases, the efficiency of nozzle/diffuser and the net flow increases. When diameter of the piezoelectric disk increases, the expected deformation of the piezoelectric disk increases as well. These parameters were optimized for best efficiency, maximum deflection, maximum velocity, and net flow, as well as manufacturability considerations. Analyses were performed to achieve the most efficient nozzle and diffuser design. Since chamber diameter was fixed by piezoelectric actuator selection, only chamber height (*mu*) was optimized in a range of 0.2 mm to 2.5 mm, and the one with the highest net flow rate using Equation (4) was 1 mm, shown in Figure 4a.

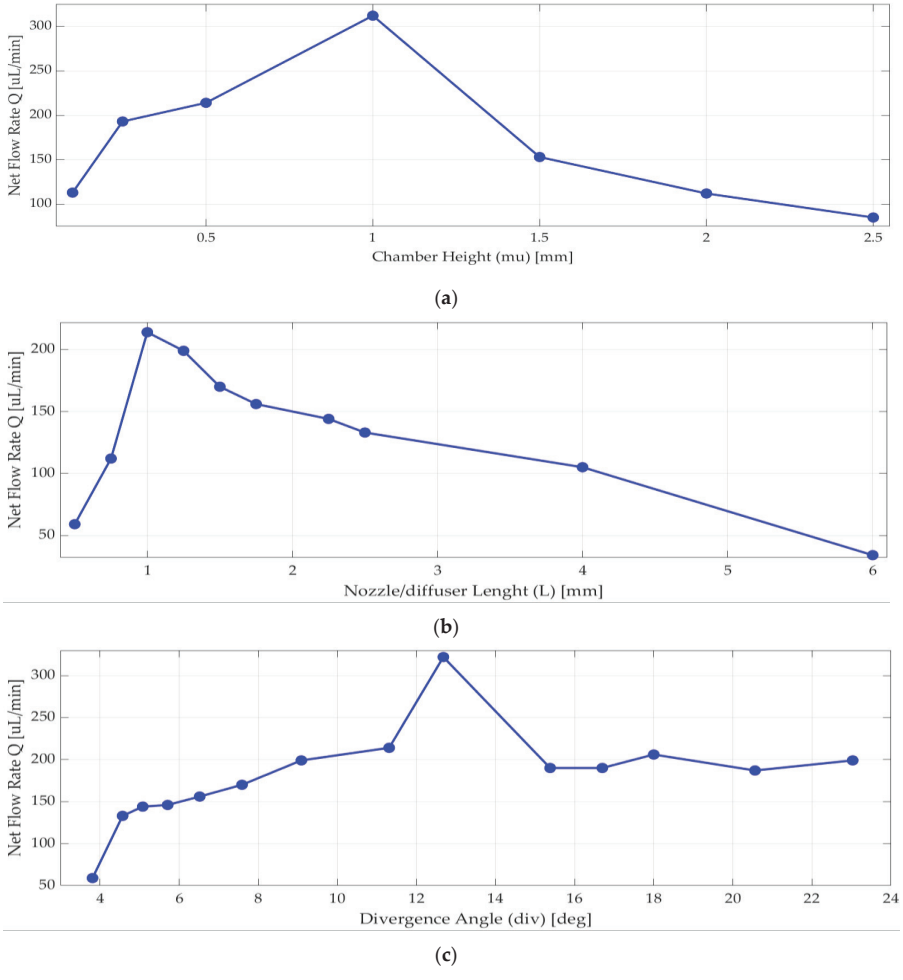

Figure 4. Numerical simulation results for net flow rate versus (**a**) chamber height; (**b**) length of nozzle/diffuser, (**c**) divergence angle.

As seen in Figure 4b, nozzle/diffuser length affects the net flow rate, so more than 10 different lengths were analyzed. The net flow rate significantly changed around 1 mm. There are many published pieces of research about nozzle and diffuser design [13,30,36,37] that are typically above 4 degrees half angle. When the nozzle and diffuser angle increases, the net flow rate increases too. However, there are some velocity values and venturi effects that may constrict the flow, so analyses were done to have the most efficient planar nozzle/diffuser. As seen in Figure 4c above, the most efficient nozzle and diffuser selected half-angle value θ was in between 12 and 14 degrees.

In addition to that, voltage and frequency parameters sweep was done. The piezoelectric actuator terminal was connected to an electrical circuit, and there was a voltage source in the circuit. Different voltages and frequencies were applied to the voltage source (see Figure 5). When the voltage increased, displacement and net flow increased explicitly. It was observed that the flow rate peaked at 100 Hz for the frequency range between 20 Hz and 200 Hz. (see Figure 5).

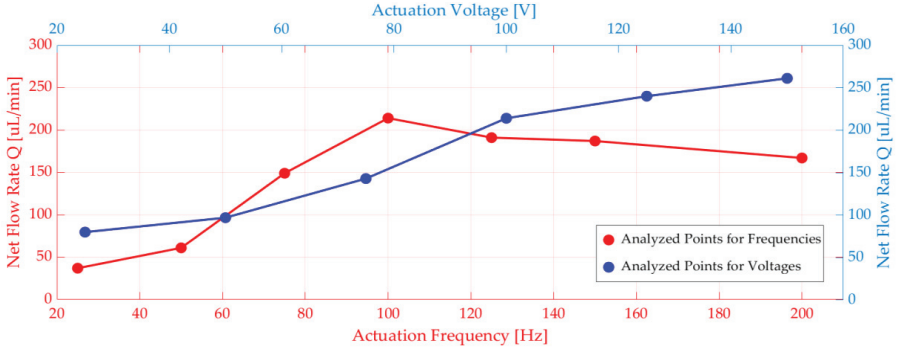

Figure 5. Numerical simulations of net flow rate versus voltage and frequency.

Another case considered was the calculation of the current drawn by the piezoelectric disk. There is an electrical circuit defined in COMSOL workspace, and the cable connected between the electrical source and the piezoelectric actuator was used as a resistor; the current through the cable was calculated. As expected, it increased when the voltage increased. Using the voltage and the current values, power consumption was calculated for different voltage and frequencies applied to the system. It is shown in Figure 6 below.

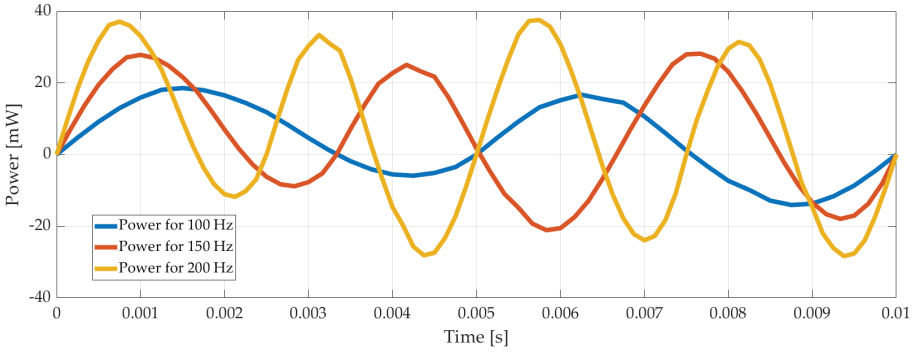

Figure 6. Power consumption of the pump with time for 100 Vp-p, 100 Hz, 150 Hz, and 200 Hz.

Last but not least, outlet and inlet flow rates were recorded, as illustrated in Figure 7 for 3 µm displacement amplitude of the piezoelectric disc. The net flow was calculated with Equation (4) as 220 µL/min in average.

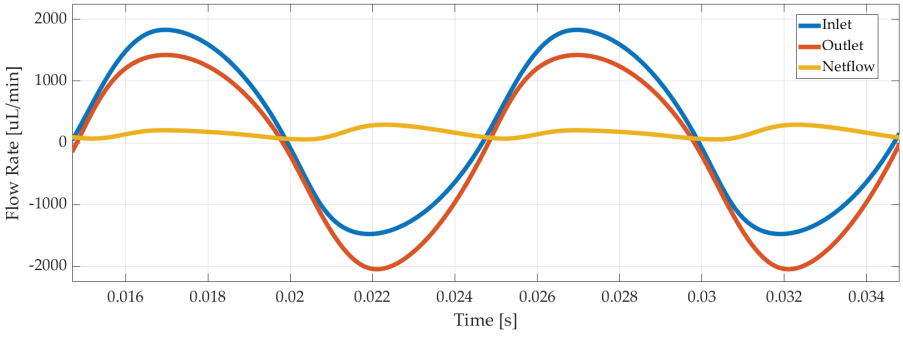

Figure 7. Numerical simulation results of inlet, outlet, and net flow rate of the piezoelectric pump.

4. Controller Design

First, Ackerman [18], Sorensen [24], and Bergman [21] glucose–insulin models were implemented in MATLAB-Simulink. Additionally, for each of these three models, a PID controller was designed. Additionally, the optimum controller gains, calculated by using Ackerman model, were implemented on all these models. It is known that daily insulin delivery and human glucose levels should be in the desired range [3] of 70–130 mg/dl. The three models used in this study have parameters for different patients. It is easy to observe that Ackerman's model can be used as a state-feedback controller design. Bergman's minimal model is easier to adopt, and using this simpler non-linear model can be less time-consuming than a more complicated non-linear model. The Sorensen model is comprehensive and detailed, so insulin and glucose levels all-around the body can be simulated with it. It is also very complex and contains several parameters.

After the glucose–insulin models are established, control of glucose level is the next step. For those controllers, there are two types of control reference methods: target tracking (e.g., 90 mg/dl) and reference tracking (e.g., 80–110mg/dl) [19]. For this article, PID with bang–bang coupling, and optimal controllers were selected from control algorithms, and the target tracking method was used [6].

To design the optimal controller, state–space forms had to be established. Since Sorensen and Bergman's models are nonlinear, the optimal controller was designed regarding Ackerman's linear model. Ackerman equations are formed in the state–space form as shown using Equations (5) and (6).

$$\begin{bmatrix} \dot{x_1} \\ \dot{x_2} \end{bmatrix} = \begin{bmatrix} -m_1 & -m_2 \\ m_4 & -m_3 \end{bmatrix} \begin{bmatrix} x_1 \\ x_2 \end{bmatrix} + \begin{bmatrix} 0 \\ 1 \end{bmatrix} u. \tag{15}$$

After the state–space model is defined, a performance criterion is defined considering the deviation from the target of blood glucose level and delivered insulin; also, δ is taken as the balance between them. δ defines the coefficiency of the effect of input, which typically describes the delivered insulin.

$$P.I. = \int_{\circ}^{\infty} \left(x_1 - x_{ref}\right)^2 + \delta\, u^2\,, \tag{16}$$

While Q is defined as 1, and P is as δ, Ricatti's equation is applied for A and B from (15) as follows:

$$A^T R + RA - RBP^{-1} B^T R + Q = 0 \text{ where } R = \begin{bmatrix} r_{11} & r_{12} \\ r_{12} & r_{22} \end{bmatrix}. \tag{17}$$

For calculated R, $m_1 = 0.005$, $m_2 = 0.001$, $m_3 = 0.002$, $m_4 = 0$, for $\delta = 0.25, 0.5, 0.75, 1$ parameters applied, and from the gain equation, K is observed and u_0 input is derived from following equation. On the other hand, u is defined as pump working time, which represents the power consumption of

the pump as well, so $\delta = 0.25$ represents a less power efficient pump, and $\delta = 1$ represents a more power-efficient pump.

$$u_0 = -K^T x \text{ where } K = RBP^{-1}, \tag{18}$$

Finally, the PID algorithm is established, and the reference glucose and actual glucose measurement information is transmitted to the PID controller and delivered to the bang–bang controller and ROM of the piezoelectric actuated pump at the input of the plant model. The flowing insulin is transmitted to the insulin/glucose model. PID controller parameters *Kp*, *Ki*, *Kd*, is optimized for the best performance for overshoot $Me = 40\%$ rising time $tr = 5$ mins and settling time $ts = 15$ mins for all glucose–insulin models [38].

5. Model-Based Simulation and Results

Based on the results of COMSOL simulations, a reduced-order model (ROM) of the pump was generated in the form of a look-up table. This model output time-dependent net flow and electrical current from excitation voltage and frequency inputs. Figure 8 shows an overview of the closed-loop control simulations in MATLAB/Simulink, where the pump supplied insulin to Ackerman, Bergman, and Sorensen glucose–insulin models with T1DM parameters. The R2019b version of MATLAB was used, and the solver settings were configured as 6×10^{-7} minutes minimum step size, auto solver selection, 1×10^{-4} relative tolerance, adaptive zero-crossing, 1440 min. (i.e., one day) stop time.

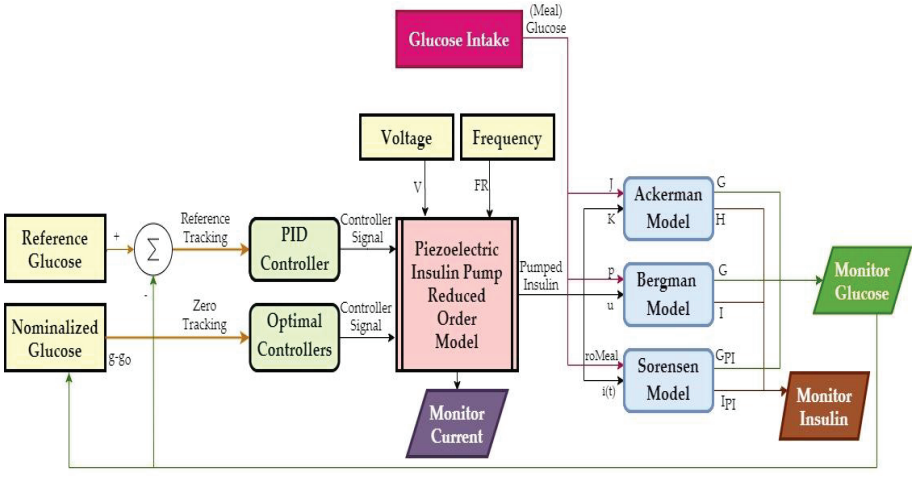

Figure 8. Overview of the closed-loop control simulations.

The glucose intake model supplied glucose input to the glucose–insulin models. On top of the 100 mg/dL basal glucose, a 150 mg/dL increase lasted for 18 min after each meal. This increase was supplied via a 1/(2s + 1) delay transfer function. Voltage and frequency of the pump excitation signal were constant, and the controllers switched the pump on/off based on the difference between the reference and measured glucose. Pump displacement and the electrical current were monitored as well as the inlet and outlet flow rates. The amount of delivered insulin was calculated from the net flow rate and the volume integral of the outlet.

As explained in Section 1.4, the simpler models, Ackerman and Bergman, are used for controller design, whereas the comprehensive Sorensen model is used for validation. Figure 9 shows the results of model-based simulations with three meal disturbances at 400, 750, and 1150 minutes. The PID controller successfully maintained the blood glucose level of the Sorensen model at around 90 mg/dL (Figure 9) and kept the insulin level at 18 mU/dL (Figure 10a). On the other hand, the δ value of the optimal controller had a negligible effect on the insulin level. This was shown with the Bergman model,

as seen in Figure 10b, where the insulin level decreased minimally with increasing δ. The corresponding difference between the glucose levels was smaller than 0.05 mg/dL.

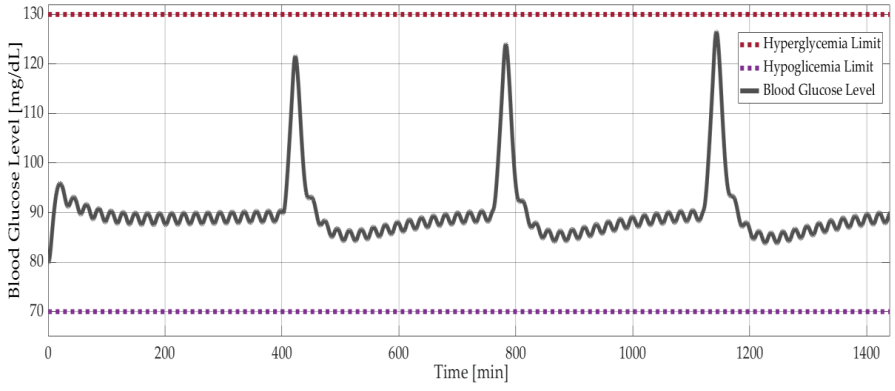

Figure 9. Model-based simulation results: Blood glucose level versus time with PID controlled Sorensen model.

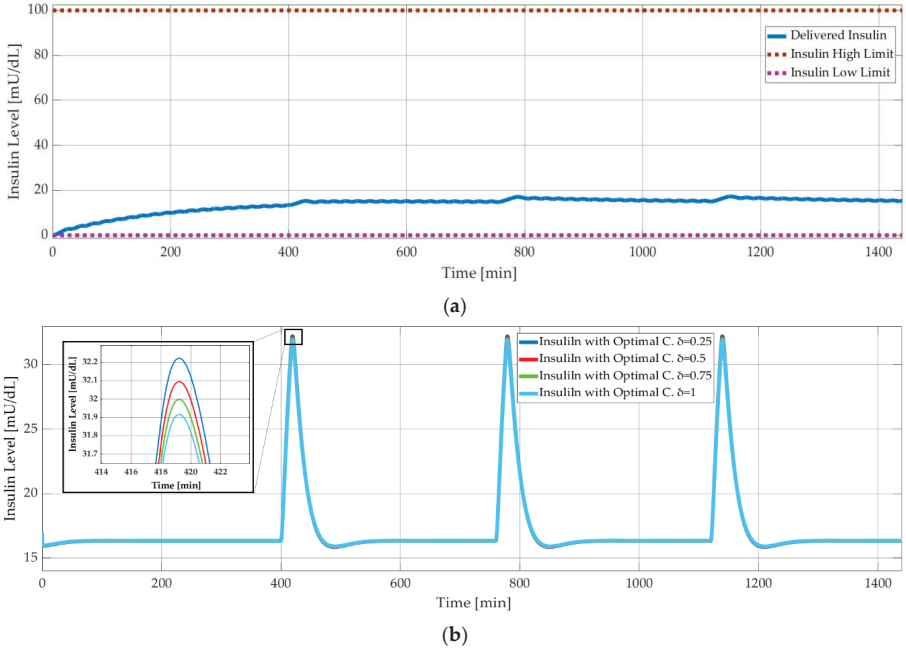

Figure 10. Model-based simulation results: (**a**) insulin level versus time with PID controlled Sorensen model; (**b**) insulin level versus time with optimal controlled Bergman model.

6. Experimental Verification and Results

The prototype pump consisted of two 3D printed closures (Figure 11a) and the piezoelectric actuator (STEMinc SMBA27T05PP), as seen in Figure 11b. Wires of the actuator were soldered and then it was glued at the brass substrate and sealed between the closures. The sealing was tested with compressed air at 100 kPa. Plastic hoses with a 3 mm inner diameter were attached to the inlet and outlet of the pump, as shown in Figure 11c.

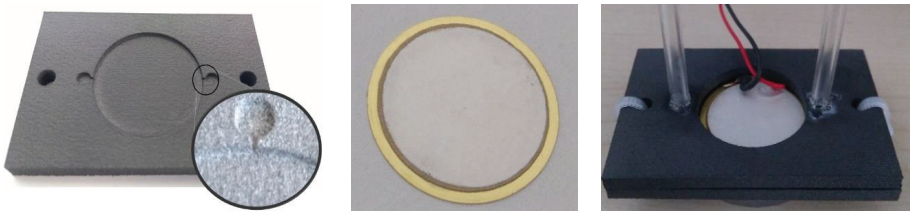

(**a**) (**b**) (**c**)

Figure 11. Pump prototype: (**a**) 3D printed bottom closure, (**b**) the piezoelectric actuator, (**c**) assembled and sealed pump.

The test stand is shown in Figure 12. The signal generator could provide a 2 Vp-p sinus signal with an adjustable frequency between 1 Hz and 3 kHz. The amplitude could be increased up to 100 Vp-p at the Falco Systems WMA-300 amplifier. An amperemeter (Keithley 2000 Series Digital Multimeter) was connected in series between the amplifier and the pump to measure the electrical current. A Polytec CLV-2534 laser vibrometer measured the velocity of the piezoelectric actuator and displays on the oscilloscope.

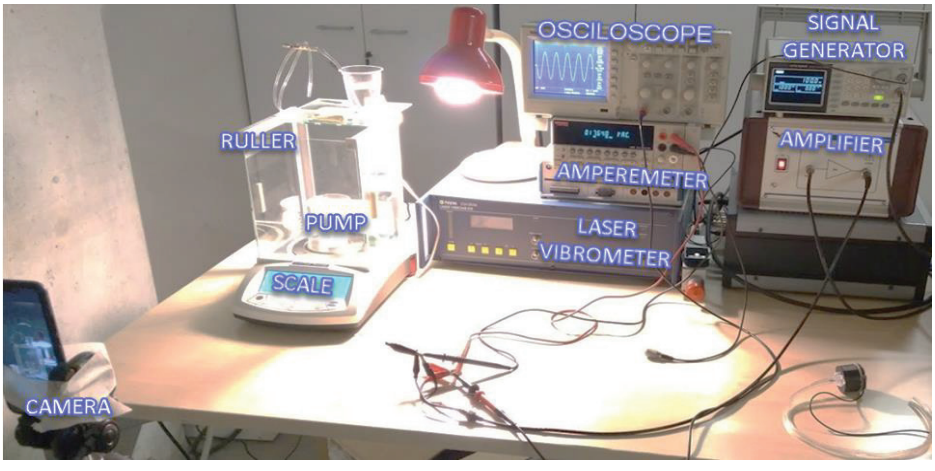

Figure 12. Experiment setup and architecture.

Water was used to simulate insulin in the experiments. The hoses were attached side-by-side to a vertical ruler to ensure equal water level at the initial condition (i.e., 0 Pa boundary condition). A 100 Vp-p sinusoidal voltage with different frequencies was applied to the pump until the head difference reached 1 mm. The change in boundary conditions was ignored in this interval when calculating net flow rates.

Figure 13 shows the measured maximum displacement of the actuator at different frequencies alongside the corresponding numerical results, since the differences between numerical simulation results and experiments were less than 10%.

Measured RMS electrical current versus excitation frequency is plotted in Figure 14 with the corresponding numerical results. On average, the experiments showed 22% higher current draw than the simulations. At 100 Hz with 100 Vp-p 0.7 mA RMS current corresponded to 18 mW RMS power consumption.

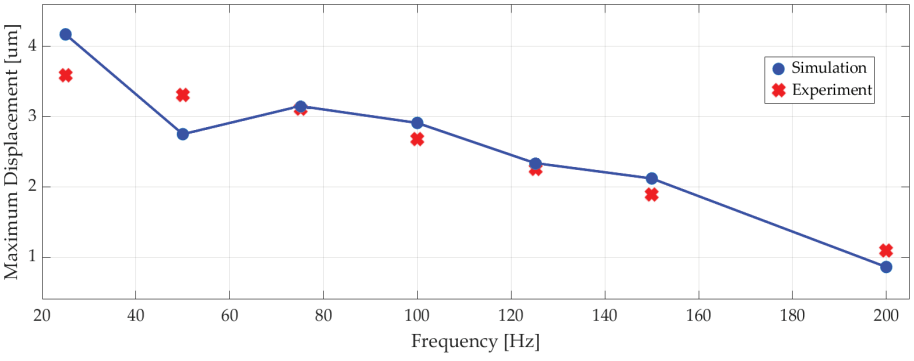

Figure 13. The experimental and simulated maximum displacement of the piezoelectric actuator at different excitation frequencies.

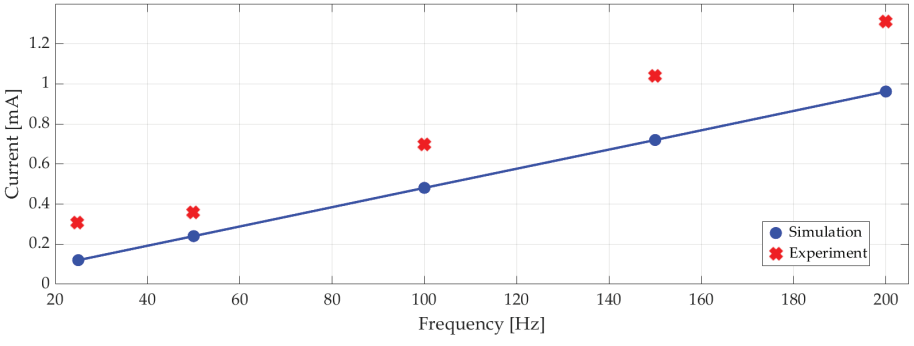

Figure 14. Experimental and simulated electrical current (RMS) at different excitation frequencies.

7. Discussion and Future Work

In this paper, we demonstrated a novel artificial pancreas system with a valveless piezoelectric pump. Although the pump is mechanically simple, its design requires detailed analysis to ensure efficient operation. We optimized our design, based on high net flow rate and low power consumption objectives, by using numerical multi-physics simulations in COMSOL. Once satisfied, we derived a reduced-order mathematical model of the pump in MATLAB/Simulink for model-based closed-loop control of blood glucose level in T1DM. In these simulations, the pump supplies insulin to three commonly used insulin–glucose models, namely, Ackerman, Bergman, and Sorensen. It must be noted that these models have parameters of different T1DM patients. The input to the controllers is the difference between the target glucose level and measured blood glucose level of the patient. The reference value is given and the instantaneous value is the output of the insulin–glucose model. A standalone APS gets the instantaneous value from a sensor known as a continuous glucose monitor. Integrating a continuous glucose monitor model in our simulations is a part of future work.

The produced prototype includes two closures and a piezoelectric actuator. A multi-jet fusion 3D printer successfully printed the closures with embedded inlet and outlet nozzles, which require high precision. The piezoelectric actuator is selected due to availability and it consists of a PZT disk attached to a thin brass substrate. Although the PZT is lead-based, and potentially toxic, it is not exposed to insulin in our design since the brass side faces the chamber. Lead-free piezoelectric materials, such as alkaline niobates or bismuth titanate [39], are interesting alternatives for future work. Another option is to use a separating layer, like a non-toxic coating or diaphragm, between the actuator and the chamber.

The prototype pump does not include embedded electronics at this stage because it is experimented in a laboratory test setup. This enables us to test the pump with a range of inputs and to observe a multitude of outputs during development phase. A fully coupled simulation model of the APS is one of the major contributions of this work. Hence, the experiments serve as a basis and validation for the development of the simulation model as well as the pump. The main drawback of the existing test setup is the lack of an accurate flow sensor. Because of this, instead of measuring the net flow rate we measured the maximum displacement of the actuator and compared with the simulations to find that the values are within 10% of each other at the experimented frequencies. This discrepancy can be extended to net flow rate, but supporting this with experimental proof is our first priority in future work.

In the literature, there are several studies [13,30] that investigate the dynamics of valveless piezoelectric pumps. Our contribution here is that we coupled the piezoelectric pump dynamics with three types of well-known glucose–insulin models. Furthermore, we applied PID and optimal controllers on the blood glucose level control problem. For blood glucose level control with an APS, it is crucial to show that the proposed pump can deliver insulin with the flow rates required by the blood glucose controller. The Ackerman's and Bergman's glucose–insulin models are relatively simple so that they are used for the design of optimal and PID controllers, respectively. The comprehensive Sorensen model is used for performance assessment in model-based simulations. Because of its complexity, the Sorensen model requires more computational power and time. This issue must be considered when electing an embedded controller for a standalone APS.

We showed with analysis and experiment that a valveless piezoelectric pump is significantly more energy-efficient compared to a syringe pump, which is typically used in APS applications. Both the numerical and experimental studies of the proposed pump predicted a power requirement of nearly 20 mW for a flow rate in the range of 200–300 μL/min. A commercial syringe pump's technical specification document states that almost 5 W is required for pumping (additional power requirement on top of the standby condition of the pump) [40]. Such orders of magnitude decreases in the power requirement are essential for APS applications where portability and battery life considerations are crucial.

Author Contributions: Conceptualization, A.K. and M.B.Ö.; methodology, A.K., Y.T., and M.B.Ö.; mathematical modeling, A.K.; numerical implementation, A.K.; writing—original draft preparation, A.K.; writing—review and editing, M.B.Ö. and Y.T. All authors have read and agreed to the published version of the manuscript.

Funding: This research received no external funding.

Conflicts of Interest: The authors declare no conflict of interest.

References

1. Ntaganda, J.M.; Minani, F.; Banzi, W.; Mpinganzima, L.; Niyobuhungiro, J.; Gahutu, J.B.; Rutaganda, E.; Kambutse, I.; Dusabejambo, V. Simplified mathematical model of glucose-insulin system. *Am. J. Comput. Math.* **2018**, *8*, 233–244. [CrossRef]
2. Saleem, M.U.; Farman, M.; Meraj, M.A. Stability analysis of sorensen's model for controllability and observability. *Proc. Pak. Acad. Sci. Part B* **2017**, *54*, 133–145.
3. IDF. *IDF Diabetes Atlas*, 9th ed.; IDF: Brussels, Belgium, 2019.
4. Kovacs, L.; Kulcsar, B.; Bokor, J.; Benyo, Z. Model-based nonlinear optimal blood glucose control of Type I diabetes patients. In Proceedings of the 2008 30th Annual International Conference of the IEEE Engineering in Medicine and Biology Society, Vancouver, BC, Canada, 20–25 August 2008; pp. 1607–1610. [CrossRef]
5. Lunze, -I.K.; Singh, T.; Walter, M.; Brendel, M.D.; Leonhardt, S. Blood glucose control algorithms for type 1 diabetic patients: A methodological review. *Biomed. Signal Process. Control* **2013**, *8*, 107–119. [CrossRef]
6. Nath, A.; Biradar, S.; Balan, A.; Dey, R.; Padhi, R. Physiological models and control for type 1 diabetes mellitus: A brief review. *IFAC PapersOnLine* **2018**, *51*, 289–294. [CrossRef]
7. MiniMed^{TM} 670G Insulin Pump System. Available online: https://www.medtronicdiabetes.com/products/minimed-670g-insulin-pump-system (accessed on 1 June 2020).

8. Beta Bionics: Introducing the iLet. Available online: http://www.betabionics.com/ (accessed on 1 June 2020).
9. T:slim X2 Insulin Pump w/ Dexcom G6 CGM. Available online: https://www.tandemdiabetes.com/products/t-slim-x2-insulin-pump (accessed on 1 June 2020).
10. Jung, B.; Seo, K.-S.; Kwon, S.J.; Lee, K.; Hong, S.; Seo, H.; Kim, G.-Y.; Park, G.-M.; Jeong, J.; Seo, S.W. Efficacy evaluation of syringe pump developed for continuous drug infusion. *J. Dent. Anesthesia Pain Med.* **2016**, *16*, 303–307. [CrossRef]
11. Yang, J. *An Introduction to the Theory of Piezoelectricity*; Kluwer Academic Publishers: Boston, MA, USA, 2005; Volume 9.
12. Lumentut, M.; Friswell, M.I. A smart pipe energy harvester excited by fluid flow and base excitation. *Acta Mech.* **2018**, *229*, 4431–4458. [CrossRef]
13. Singh, S.; Kumar, N.; George, D.; Sen, A.K. Analytical modeling, simulations and experimental studies of a PZT actuated planar valveless PDMS micropump. *Sens. Actuators A Phys.* **2015**, *225*, 81–94. [CrossRef]
14. Khalilian, S. Development of a Low Cost Micro-Pump. Master's Thesis, University of Calgary, Calgary, AB, Canada, 2012; pp. 1–185. [CrossRef]
15. Atul, S.T.; Lenin Babu, M.C. Characterization of valveless micropump for drug delivery by using piezoelectric effect. In Proceedings of the 2016 International Conference on Advances in Computing, Communications and Informatics (ICACCI), Jaipur, India, 21–24 September 2016; pp. 2138–2144. [CrossRef]
16. Laser, D.J.; Santiago, J.G. A review of micropumps. *J. Micromech. Microeng.* **2004**, *14*, R35–R64. [CrossRef]
17. Nisar, A.; Afzulpurkar, N.; Tuantranont, A.; Mahaisavariya, B. Three dimensional transient multifield analysis of a piezoelectric micropump for drug delivery system for treatment of hemodynamic dysfunctions. *Cardiovasc. Eng.* **2008**, *8*, 203–218. [CrossRef]
18. Yipintsoi, T.; Gatewood, L.C.; Ackerman, E.; Spivak, P.L.; Molnar, G.D.; Rosevear, J.W.; Service, F.J. Mathematical analysis of blood glucose and plasma insulin responses to insulin infusion in healthy and diabetic subjects. *Comput. Boil. Med.* **1973**, *3*, 71–78. [CrossRef]
19. Chee, F.; Fernando, T. *Closed-Loop Control of Blood Glucose*; Springer: Berlin/Heidelberg, Germany, 2007; Volume 368.
20. Ceresa, F.; Ghemi, F.; Martini, P.F.; Martino, P.; Segre, G.; Vitelli, A. Control of blood glucose in normal and in diabetic subjects: Studies by compartmental analysis and digital computer technics. *Diabetes* **1968**, *17*, 570–578. [CrossRef]
21. Bergman, R.N.; Phillips, L.S.; Cobelli, C. Physiologic evaluation of factors controlling glucose tolerance in man: Measurement of insulin sensitivity and beta-cell glucose sensitivity from the response to Intravenous glucose. *J. Clin. Investig.* **1981**, *68*, 1456–1467. [CrossRef] [PubMed]
22. Roy, A.; Parker, R.S. Dynamic modeling of exercise effects on plasma glucose and insulin levels. *J. Diabetes Sci. Technol.* **2007**, *1*, 338–347. [CrossRef] [PubMed]
23. Furler, S.M.; Kraegen, E.W.; Smallwood, R.H.; Chisholm, D. Blood glucose control by intermittent loop closure in the basal mode: Computer simulation studies with a diabetic model. *Diabetes Care* **1985**, *8*, 553–561. [CrossRef] [PubMed]
24. Sorensen, J.T. A Physiologic Model of Glucose Metabolism in Man and Its Use to Design and Assess Improved Insulin Therapies for Diabetes. Ph.D. Thesis, University of California, Berkeley, CA, USA, 1985; p. 557.
25. Cobelli, C.; Mari, A. Control of diabetes with artificial systems for insulin delivery algorithm independent limitations revealed by a modeling study. *IEEE Trans. Biomed. Eng.* **1985**, *32*, 840–845. [CrossRef]
26. Hovorka, R.; Shojaee-Moradie, F.; Carroll, P.V.; Chassin, L.J.; Gowrie, I.J.; Jackson, N.C.; Tudor, R.S.; Umpleby, A.M.; Jones, R.H. Partitioning glucose distribution/transport, disposal, and endogenous production during IVGTT. *Am. J. Physiol. Metab.* **2002**, *282*, E992–E1007. [CrossRef]
27. Kaçar, A.; Özer, M.B.; Taşcıoğlu, Y. Piezoelectric actuated insulin pump simulation model and controller design. In Proceedings of the 8th International Conference, ICAT'19, Sarajevo, Bosnia and Herzegovina, 26–30 August 2019; pp. 351–356.
28. Chandrasekaran, A.; Packirisamy, M. Improved efficiency of microdiffuser through geometry tuning for valveless micropumps. *J. Fluids Eng.* **2015**, *138*, 031101. [CrossRef]
29. Nguyen, A.V.; Huang, X. Miniature valveless pumps based on printed circuit board technique. *Sens. Actuators A Phys.* **2001**, *88*, 104–111. [CrossRef]
30. Gidde, R.R.; Pawar, P.M.; Dhamgaye, V.P. Fully coupled modeling and design of a piezoelectric actuation based valveless micropump for drug delivery application. *Microsyst. Technol.* **2019**, *26*, 633–645. [CrossRef]

31. Hariri, A.; Wang, L.Y. Observer-based state feedback for enhanced insulin control of type 'I' diabetic patients. *Open Biomed. Eng. J.* **2011**, *5*, 98–109. [CrossRef]
32. Swan, G.W. An optimal control model of diabetes mellitus. *Bull. Math. Biol.* **1982**, *44*, 793–808. [CrossRef]
33. Acikgoz, S.U.; Diwekar, U.M. Blood glucose regulation with stochastic optimal control for insulin-dependent diabetic patients. *Chem. Eng. Sci.* **2010**, *65*, 1227–1236. [CrossRef]
34. COMSOL: Multiphysics Software for Optimizing Designs. Available online: https://www.comsol.com/ (accessed on 1 June 2020).
35. Piezo Round Bimorph Actuator for Pumps 27 × 0.5mm. Available online: https://www.steminc.com/PZT/en/piezo-round-bimorph-actuator-for-pumps-27x05mm (accessed on 1 June 2020).
36. Schmandt, B.; Herwig, H. Diffuser and nozzle design optimization by entropy generation minimization. *Entropy* **2011**, *13*, 1380–1402. [CrossRef]
37. Ben Mansour, R.; Sahin, A.Z. Optimization of conical micro-diffusers and micro-nozzles considering entropy generation. *Arab. J. Sci. Eng.* **2012**, *38*, 3161–3170. [CrossRef]
38. Laxminarayan, S.; Reifman, J.; Steil, G.M. Use of a food and drug administration-approved type 1 Diabetes mellitus simulator to evaluate and optimize a proportional-integral-derivative controller. *J. Diabetes Sci. Technol.* **2012**, *6*, 1401–1412. [CrossRef]
39. Maeder, M.D.; Damjanovic, D.; Setter, N. Lead free piezoelectric materials. *J. Electroceram.* **2004**, *13*, 385–392. [CrossRef]
40. SPETEC—Syringe Pump Symax. Available online: https://www.spetec.de/en/products/laboratory-equipment/syringe-pumps/syringe-pump-symax (accessed on 1 June 2020).

applied sciences

MDPI

Article

Virtual Reality Exposure Therapy for Driving Phobia Disorder: System Design and Development

Amy Trappey [1,*], Charles V. Trappey [2], Chia-Ming Chang [3], Routine R.T. Kuo [1], Aislyn P.C. Lin [1] and C.H. Nieh [3,4]

1 Department of Industrial Engineering and Engineering Management, National Tsing Hua University, Hsinchu 300, Taiwan; s108034518@m108.nthu.edu.tw (R.R.T.K.); s105034013@m105.nthu.edu.tw (A.P.C.L.)
2 Department of Management Science, National Chiao Tung University, Hsinchu 300, Taiwan; trappey@faculty.nctu.edu.tw
3 Psychiatry Department, Chang Gung Memorial Hospital, Taipei 333, Taiwan; cmchang58@cgmh.org.tw (C.-M.C.); 408456055@gapp.fju.edu.tw (C.H.N.)
4 Department of Clinical Psychology, Fu Jen Catholic University, Taipei 242, Taiwan
* Correspondence: trappey@ie.nthu.edu.tw; Tel.: +886-3572-7686

Received: 25 June 2020; Accepted: 13 July 2020; Published: 15 July 2020

Abstract: Driving phobia is an anxiety disorder. People are greatly impaired in their daily lives when suffering from driving phobia disorders. The anxieties can be triggered under various conditions, such as driving over bridges, driving at high speeds, or driving in close proximity to large trucks. Traditional cognitive behavioral therapy (CBT) and exposure therapy are the most common approaches used in the treatment of psychological disorders, such as anxiety disorder (AD) and panic disorder (PD). This research focuses on virtual reality (VR)-based exposure therapy, called VRET, and describes the design and development of a system which uses alternating levels of fear-based driving scenarios that can be recorded and automatically adjusted to maximize exposure effectiveness without causing the subjects to panic. The proposed VRET integrates an advanced feedback database module for tracing and analyzing the system, along with the user's bio-data to show the valid data collection of the system and its effectiveness for future use in clinical trials. The research conducts a system's pre-test analysis using 31 subjects to demonstrate the effectiveness of the system. This research demonstrates the systematic development of the VRET for driving phobia disorder by depicting the system framework, key system modules, system integration, bio-database management, and pre-test data analysis to support our next research efforts in hospital-based clinical trials and for additional VRET development applications for clinical psychology.

Keywords: virtual reality exposure therapy; driving phobia; post-traumatic stress disorder; physiological signal

1. Introduction

Post-traumatic stress disorder (PTSD) is a general term for any mental health issue that is triggered by a traumatic event experienced or witnessed by the patient. Many types of assaults can result in PTSD, such as physical or mental abuse, sexual assault, and serious physical accidents. People that suffer from PTSD have problems with daily, societal, and work-related activities. The condition interferes with one's ability to deal with normal life tasks. In 1980, PTSD was officially recognized as a mental illness by the American Psychiatric Association after the analysis of soldiers injured and exposed to traumatic experiences during the Vietnam war [1].

Cognitive behavioral therapy (CBT) and exposure therapy (ET) are the most common approaches for treating PTSD, anxiety disorder (AD), and panic disorder (PD) [2]. The goal of therapies is to change patterns of thinking or behavior that cause mental disorders. CBT works by changing people's attitudes

and their behaviors by focusing on the thoughts, images, beliefs and attitudes. Because there is no invasive treatment or psychoactive drugs used while conducting CBT, it is generally recommended by medical institutions [3]. The challenges of CBT are that it requires patient cooperation, is time consuming, and is difficult to execute as a standard procedure.

An emerging treatment approach for PTSD takes advantage of immersive-based information technology to advance exposure therapy using virtual reality (VR) and more sophisticated physical measuring devices (called VR-based exposure therapy (VRET)). VRET allows patients to slowly expose themselves to different levels of traumatic stimuli using immersions of vision, sound and tactile feedback, which matches the principle of systematic desensitization (SD). SD is evaluated by researchers to be as effective as CBT [2,4]. Using VRET, patients interact and are exposed to a simulation of the phobic surroundings, but do not physically encounter the feared situations and the immersive condition can be immediately adjusted to reduce additional harm that can be caused by stress and panic attacks resulting from overexposure. The curative effects of VRET are more significant (and more realistic) then CBT [5]. There are some issues to be considered when designing VRET as a therapeutic treatment [6]. First, VRET is an evolving technology, psychiatrists and psychotherapists have to experiment with designs and configurations of therapy, develop base scenes, changing scenarios, and integrate complex monitoring equipment while demonstrating that the treatment is effective, reliable, and valid. The development costs and design thresholds of VRET are considerably more challenging than traditional CBTs. Further, researchers must consider the realism of the immersive environments. If the immersive environment is not realistic, the patients will lack exposure and the curative effect (or an effective meta-analytic effect size for clinical trials) will be compromised. If the immersive environment is too realistic, it could trigger severe phobic reactions during the experiments and endanger the subject's safety. Finally, some patients may not be familiar with VR hardware and software settings. Thus, severe dizziness during the experiment may hinder the VRET results. Thus, patients' physical conditions and their suitability for VRET need to be carefully investigated to ensure the effectiveness of VRET implementations and applications [6].

Section 2 presents a literature review of immersive applications in PTSD, including traditional ET, CBT, and VRET. Section 3 introduces the methodology framework and the approaches used in this research. Section 4 demonstrates the system architecture and the hardware and software components that are adopted and integrated to build the immersive environment. Section 5 performs statistical analysis to the pre-test data, using the correlation coefficients between system and bio-data, nonparametric testing for gender difference and anxiety group difference, and an ANOVA test for ET level effects. A Shewhart control chart was applied to monitor the subjects' emotional arousal. Section 6 summarizes the VRET systematic research, describes the research contributions, and highlights the next phase VRET research for controlled clinical trials.

In principle, this research focuses on VRET design and development using seven increasingly frightening driving scenario levels. The proposed VRET integrates with an advanced system and bio-database module for tracing and analyzing the system and user's bio-data. The research conducts the system's pre-test analysis to demonstrate the effectiveness of the system. The main objectives of this research are to present the systematic development of the VRET for driving phobia disorder, including the VRET system framework, key system modules, system design theory, bio-feedback database management, and pre-test data analysis. The research outcomes will support our next efforts in using VRET for hospital based clinical trials for driving phobia disorders, and potentially extending VRET development to other applications in clinical psychology.

2. Literature Review

In this section, the literature review focuses on the latest state of immersive technologies and applications in PTSD-related psychotherapies. Publications from the American Psychological Association (APA), the Institute of Electrical and Electronics Engineers (IEEE) Xplore, and the Web of Science (WoS) digital library are searched using keywords Cognitive Behavior Therapy, Post Traumatic

Stress Disorder, and Exposure Therapy. The results were further refined to include Virtual Reality Exposure Therapy and Driving Phobia. The two groups of literature are simply divided into VRET and traditional treatments. The traditional treatment types are further divided into CBT and ET.

CBT and ET are commonly used to treat PTSD, depression, anxiety, and panic disorders. CBT reduces cognitive anxiety by letting patients understand the causes of their reactions and how to manage and change reactions that may exasperate their mental condition. The efficacy of CBT on anxiety-related mental disorders, especially PTSD, has been confirmed by many studies [7–10].

Exposure therapy exposes patients to various levels of stimulating situations and continuously increases the intensity of the exposure to gradually induce a tolerance toward the exposure. Subjects are taught to self-analyze their reactions and change their behavioral response to better adapt to the changing conditions of exposure. Exposure therapy includes both imaginary and in vivo exposure. For imagined exposure, the therapist may ask the patient to imagine what they are afraid of. On the other hand, in vivo exposure allows patients to face the phobia directly. Some clinical trials have confirmed the effectiveness of exposure for treating PTSD. For example, Bryant et al. [11] divided 45 patients with PTSD into three groups—waiting list, exposure or counseling. The results showed that only 14% and 20% of the group members that received prolonged exposure and prolonged exposure plus anxiety management still suffered from symptoms of PTSD after treatment. Fifty-six percent of the supportive counseling group members were not affected by the PTSD treatment. The findings indicated that prolonged exposure may be a critical approach in the treatment of PTSD [11].

Aside from treating phobias, one of the successful applications of virtual reality technology is in the field of education. In one study, researchers have conducted a bibliometric study of the last twenty years from the Scopus database, and conclude that the use of virtual reality in education can improve the quality of the teaching and learning processes [12]. In Jesús López Belmonte's research, he asserted that digital technology has become a part most of people's lives and entered various fields of society. For example, he applies VR to education and reports that VR yields many benefits such as optimizing teaching and learning processes, timely access to new information, greater mobility, ubiquitous access, and adaptable to the uniqueness of each student [13].

At present, there are many studies on the applications of VRET for various kinds of phobias such as acrophobia, arachnophobia, and aviophobia [14]. In one study, a 50-year-old officer who suffered from PTSD caused by the Vietnam War underwent VRET. After 14 treatments of up to 90 min over seven weeks, his PTSD symptoms fell 34% under standard clinical measures. Self-assessment decreased by more than 45% [15]. Another study of flying phobia ET confirmed that VRET and traditional ET have no difference in statistical effect size. Seventy-five patients with fear of flying (FOF) were divided into three groups (25 people in each group): VRET, traditional ET and the waitlist (do nothing). After treatment, the results of VRET and traditional ET were almost equivalent while both groups were superior to those on the waitlist [16]. Another study used meta-analysis to integrate effects from 21 clinical studies with a total of 300 subjects. The analysis results (effect size) demonstrated that VRET effectively reduces anxiety [17]. Finally, our research studied the application of VRET in arachnophobia treatment, incorporating Arduino bio-sensors to collect real-time bio-data from subjects. Bio-data are integrated with the VRET system data and stored in SQL database for data mining and real-time VRET level adjustment is used to minimize over-exposer to the treatment [18].

Driving is an essential skill that facilitates independence and mobility of individuals in modern society and is often a requirement of employment. Being diagnosed with a driving phobia limits an individual's work options and creates issues associated with social interaction when mass transportation or transportation for hire is not available or unaffordable. According to emotional processing theory, successful exposure therapy leads to new and more neutral memory structures that overrule old memories that provoke and heighten anxiety [19]. In a VRET for driving phobia pilot study, 14 subjects with serious driving phobia were placed into a series of experimental conditions, including psychotherapeutic, medical examination, psychotherapy sessions, VRET sessions, and a final behavioral avoidance test (BAT) when driving in traffic. The therapy session for each subject required 10 days

to complete the experiment. After 6 to 12 weeks, follow-up tracking of the subjects was performed to access the subjects' driving performance and evaluate the effectiveness of the treatment for each subject. The follow-up tracking indicated that 13 out of the 14 patients maintained successful treatment results [20]. Another VRET experiment for driving phobia used eight females who were willing to try VRET but unwilling participants used in vivo exposure. The VRET exposure environment consisted of eight sessions which gradually exposed participants to increasingly uncomfortable exposure over 50-minute intervals. Factors, such as mean mood, anxiety, cognitive evaluation, quality of life, sense of presence, subjective discomfort, and heart rate were recorded during the experiment. The result showed that the sense of presence decreased as the session progressed while subjects' subjective discomfort scores and heart rate increased. After the experiment, subjects were determined to be more confident with their driving ability. Six out of eight subjects were willing to conduct in vivo exposure after VRET [21]. A VRET experiment for driving phobia related to fear of driving in tunnels was conducted. In the virtual reality environment, the car passes through a tunnel with lighting adjusted to resemble natural daylight on entry and exit, with increasing darkness and increasing lightness upon exit. The sound of traffic was also included to enhance the realism of the simulations [22]. The above driving phobia VRET studies provide a solid basis for continued research. The numbers of subjects in these studies are generally too small to draw a decisive conclusion or provide suggestions for future VRET refinement. Moreover, most of the literature evaluated their VRET system based on subjects' driving performance, and few focused on the subjects' biological senses and system recorded data analysis. Therefore, this pre-test experiment will examine the feasibility of using biological sensors and system-data collection and analyses to measure subjects' driving performance to ensure the safety and effectiveness of VRET toward phobia treatment. Further, to ensure the VRET is scientifically conducted, collecting real-time bio-data of patients is vital during the ET sessions. Matured bio-sensor solutions, such as the Arduino micro-controller, can transmit bio-data to a remote computer or cloud database using an XBee wireless network [23].

3. Methodology Applied in This Research

Figure 1 presents the research flow of this study for the driving phobia VRET design and development. The project formulation made at the beginning was to decide how to implement the research, perform risk assessment, and hypothesize expected results. Literature related to VRET, driving phobia, CBT, and PTSD were reviewed and referenced before designing the exposure treatment scenario. The virtual reality immersive environments were constructed to model different fear levels of scenarios. The constructed VRET prototype has been examined by psychologists and an iterative modification process was executed until the psychologists were confident that the system matched the needs of ethical and medically acceptable driving phobia treatments.

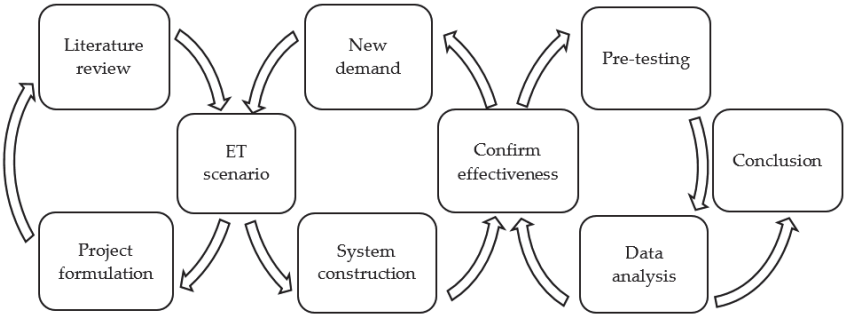

Figure 1. The research flow of the virtual reality-based exposure therapy (VRET) system design and development.

The VRET system is constructed using a seven-level exposure therapy design as shown in Figure 2. Since some patients are extremely afraid of car crashes, pedestrians and other driving vehicles do not appear in the immersive environment for the initial test runs. All of the simulation scenes follow a single route map. Subjects drive a specified distance to reach a destination before advancing to a higher level. Each level has its unique simulation environment, time, and treatment objectives. The details of each level are highlighted as follows.

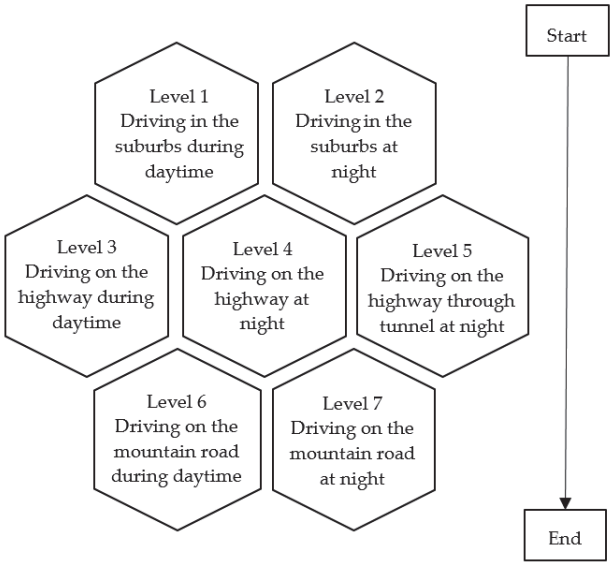

Figure 2. Scenario design level chart.

Level 1 Driving in the suburbs during the daytime, the speed limit is 40 km/h.
Level 2 Driving in the suburbs at night, the speed limit is 40 km/h.
Level 3 Driving on the highway during the daytime, the speed limit is 110 km/h, and the system will ask subjects to drive faster if the driving speed is less than 90 km/h.
Level 4 Driving on the highway at night, the speed limit is 110 km/h, and the system will ask subjects to drive faster if the driving speed is less than 90 km/h.
Level 5 Driving on the highway at night, the speed limit is 110 km/h, and the system will ask subjects to drive faster if the driving speed is less than 90 km/h. Subjects will be expected to traverse a tunnel.
Level 6 Driving on a mountain road during the daytime, the speed limit is 50 km/h.
Level 7 Driving on the mountain road at night, the speed limit is 50 km/h.

The VRET experiment flow is illustrated in Figure 3. The treatment begins with a detailed introduction about the experimental objective, method, procedure, expected risk, and relevant disclaimer information. A pre-test questionnaire is completed by the subject before the experiment to measure the subject's mental state. The questionnaire asks about the subject's behavior, thoughts, and emotions in regard to previous driving experiences. During the experiment, bio-data including heart rate, skin conductance, body temperature, respiration, and head movement are recorded in the computer database for statistical analysis. If virtual reality vertigo or other motion sickness symptoms occur to the subject during the VRET session, an emergency stop is triggered and the experiment is terminated. After the immersive treatment is finished, subjects are asked to complete a post-test feedback form.

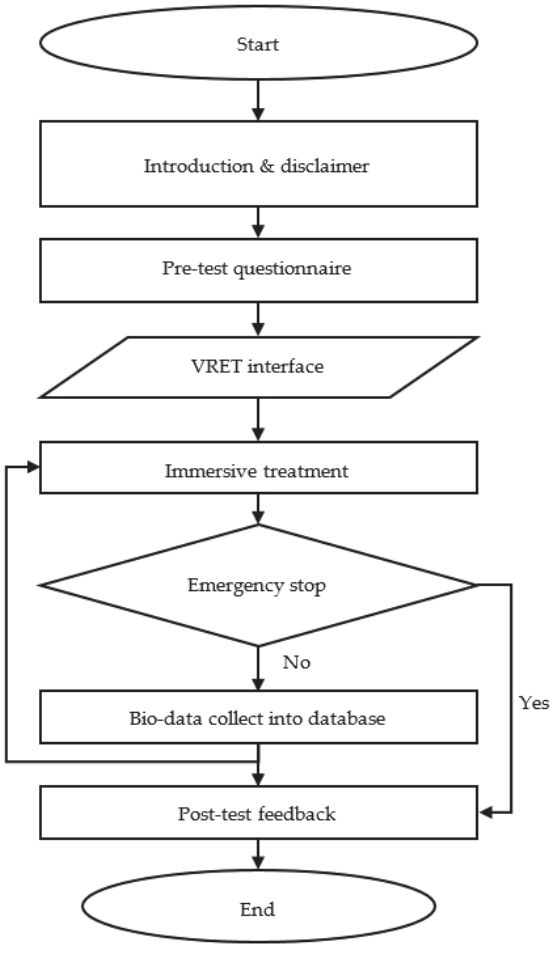

Figure 3. The driving phobia VRET experiment flow.

A total of thirty-one subjects including 14 males and 17 females at the university participated in the pre-test of the VRET prototype. The inclusion criteria are aged between 20 and 25 years old, possession of a valid driving license, and described a fear of at least one type of driving phobias such as driving on highways, mountain roads, or congested traffic.

4. System Architecture

The overview system architecture of this VRET research is presented in Figure 4. The VRET system (software) consists of four modules: the exposure therapy (ET) scenario module (7 scenario levels), the VR environment module, the data collection module, and the data analysis module. The VR–User interface (hardware) includes a VR headset, steering wheel, and bio-sensors. A database management system is developed to collect and integrate system and bio-data from the VRET system and the VR-User interface. The system's hardware, software, and database designs are described in the following paragraphs. For more technical details, please refer to [16].

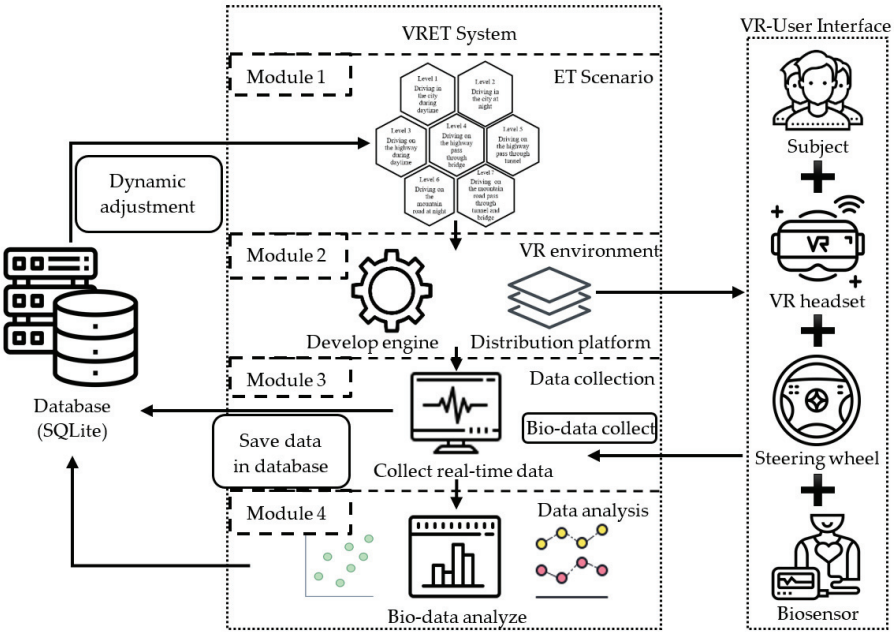

Figure 4. The system architecture for the driving phobia VRET prototype (refer to Figure 2 for Module 1 details).

4.1. Hardware

The hardware components used by the system include the VR headset (HTC, VIVE Pro, Taipei, Taiwan), the steering wheel (Guillemot Co., Thrustmeter T300 RS GT, Carentoir, France), and bio-sensors (Thought Technology Ltd., ProComp Infiniti, Montreal, Canada). The HTC VIVE Pro is a popular virtual reality immersive headset. The kit headset includes VR HMD, two base stations for movement tracking, and two motion controllers for virtual world interaction. The two base stations are able to connect the immersive environment with the subject's reactions to scene objects via motion controllers. The Thrustmeter T300 RS GT Edition is a high-end racing steering wheel equipped with a feedback mechanism, a specialized T3PA acceleration pedal that is integrated with steering wheel motion to provide realistic driving feedback to the subjects. The ProComp Infiniti is an eight-channel biofeedback system for real-time data acquisition that can be used with combinations of sensors including EEG, EKG, RMS EMG, skin conductance, heart rate, blood volume, pulse, respiration, temperature, force, and voltage.

4.2. Software

The software components adopted into the system include the development engine (Unity Technologies, Unity, San Francisco (HQ), CA, USA) and the distribution platform (Valve Corp., Steam, Bellevue, Washington, USA). Unity is a well-known real-time 3D development platform which enables users to develop both 2D and 3D games and models in Windows, iOS, Android, and over twenty types of systems. Microsoft C# is used as the programming language; users are allowed to control actions of virtual objects using specific C# scripts. Unity is compatible with other design software and gaming platforms that have external operating devices also compatible with Unity. Steam is one of the largest video game digital distribution service platforms in the world and also provides a virtual reality service called SteamVR to support the HTC VIVE virtual reality headset. Data collection and data management use SQLite (SQLite.org) as the database engine and BioGraph Infinite software to

record bio-data. The VRET database management system (DBMS)'s entity-relation diagram is shown in Figure 5.

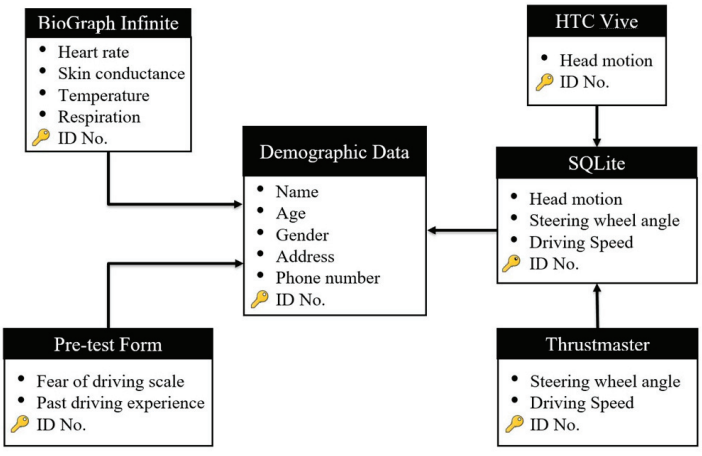

Figure 5. The entity-relation (ER) diagram for the VRET database.

4.3. Database

SQLite is a relational database management system (DBMS) contained in the C library. The reason for choosing SQLite over MySQL is because SQLite is a popular choice as an DBMS for client storage. SQLite is used to collect head motion, steering wheel rotation angle, and driving speed data in real time. These data are accessed from the database using the Python programming script. Th database storage model is shown in Figure 6. BioGraph Infinite is a software platform that is specifically used for ProComp Infiniti data access, allowing high end users to create their own screens, scripts and channel sets. The purpose of BioGraph Infinite is to collect heart rate, skin conductance, body temperature, and respiration rate data during ET experiments. The biological and system data are integrated for analysis.

Database Structure | Browse Data | Edit Pragmas | Execute SQL

Table: Car_Table

	Speed	X	Y	Z	DrivingWheel	Time	Level	SystemStartTime
	Filter	Filter	Filter	Filter	Filter	Filter	Filter	Filter
1	0.4380091	-1.472	0.706	-0.669	0	1588670841	2	1.8904374837...
2	0.6820499	-1.472	0.706	-0.669	0	1588670841	2	1.9701997041...
3	1.803597	-1.472	0.706	-0.669	0	1588670841	2	2.5554158687...
4	2.499635	-1.471	0.704	-0.669	0	1588670841	2	2.6618523597...
5	2.950378	-1.472	0.705	-0.668	0	1588670841	2	2.7415754795...
6	3.392918	-1.472	0.705	-0.669	0	1588670841	2	2.8164401054...
7	3.83314	-1.472	0.706	-0.669	0	1588670842	2	2.8997709751...
8	4.272413	-1.472	0.706	-0.669	0	1588670842	2	2.9741280078...
9	4.647296	-1.472	0.706	-0.669	0	1588670842	2	3.0429022312...
10	5.082554	-1.472	0.707	-0.669	0	1588670842	2	3.1084685325...
11	5.392045	-1.472	0.706	-0.669	0	1588670842	2	3.1676123142...
12	5.700471	-1.472	0.706	-0.668	0	1588670842	2	3.2321500778...
13	6.069105	-1.472	0.707	-0.669	0	1588670842	2	3.2917299270...
14	6.43635	-1.472	0.705	-0.668	0	1588670842	2	3.3538510799...
15	6.741084	-1.473	0.705	-0.669	0	1588670842	2	3.4180021286...

Figure 6. Example of VRET's system database storage.

5. Pre-Test and Pre-Test Data Analysis

In order to examine the effectiveness of the VRET system and to improve the VRET system to facilitate future clinical trials, this study recruited 31 subjects for pre-testing. Before the pre-test experiment, subjects were asked to fill out the "Self-rating fear of driving scale," for the purpose of measuring their degree of fear of driving. The rating scale was designed according to emerging measures offered by American Psychiatric Association [24]. During the pre-test experiment, the system data, bio-data, and subjects' suggestions for refinement of the VRET system were recorded. This study was approved by the Chang Gung Medical Foundation Institution Review Board (IRB), the institution's ethical commission, approval number 201901262B0.

5.1. Pre-Test Subjects' Demographic Data

This study recruited 14 males and 17 females at the university participated in the pre-test of the VRET prototype. Pre-testing subjects' demographic data including gender, height, weight, age, and the years of driving experience are presented in Table 1. 14 males with a mean height of 172.5 cm (SD = 5.21 cm) and a mean weight of 64.29 kg (SD = 7.61 kg), 17 males with a mean height of 160.43 cm (SD = 4.75 cm) and a mean weight of 52.71 kg (SD = 5.44 kg). All the subjects with a mean age of 22.39 years (SD = 0.95 year) and the mean duration of driving experience is 2.10 years (SD = 1.13 years).

Table 1. Pre-test subjects' demographic data.

Subject No.	Gender	Height (cm)	Weight (kg)	Age	Driving Experience (Years)
1	Female	164	52	23	4
2	Female	164	62	21	2
3	Male	173	57	24	3
4	Male	178	74	24	2
5	Male	160	48	22	1
6	Female	156	48	22	1
7	Male	174	75	22	2
8	Female	153	52	23	1
9	Female	152	47	22	1
10	Female	162	52	23	3
11	Male	167	69	22	3
12	Male	172	58	22	2
13	Female	164	49	22	1
14	Female	161	55	23	4
15	Female	167	49	22	2
16	Female	166	62	22	2
17	Female	158	50	22	1
18	Male	175	65	22	1
19	Male	170	65	22	2
20	Female	165	50	22	1
21	Male	171	60	22	3
22	Male	170	65	22	1
23	Female	162	53	22	3
24	Female	160	65	21	2
25	Female	164	52	22	1
26	Male	174	71	24	1
27	Male	177	71	24	2
28	Female	162	46	22	2
29	Male	172	65	22	3
30	Male	182	57	25	6
31	Female	162	52	21	2

5.2. Pre-Test Procedures

1. Explain the purpose and precautions of the experiment and ask subjects to sign the consent form.

2. Subjects filled out the "Self-rating fear of driving scale."
3. Subjects were equipped with bio-sensors for the purpose of detecting the real-time bio-data. Bio-sensors including heart rate, temperature, respiration, and skin conductance.
4. Conducting the pre-test VRET experiment and collect subjects' real-time bio- and system data.
5. After the pre-test experiment, subjects were asked to fill out the feedback form and provide some suggestions to the refinement of VRET system.

5.3. Pre-Test Data Analysis

The real-time VRET system data, shown in Figures 7 and 8, and the pre-test subject's bio-data, are shown in Figures 9 and 10. For the current prototype of VRET for driving phobia, the bio-data of each subject are monitored and analyzed for trends and correlations between bio-data and system data. The data spike abnormalities are monitored during the pre-testing experiment sessions. The goal is to improve the effectiveness of the therapy design of the VRET immersive system based on data analytic outcomes to avoid levels of driving conditions showing insignificant bio-effects or causing overly dramatic effects (i.e., lacking the feature of gradual systematic desensitization). The following discussion describes the statistical analysis results of the system's pre-test experiments with 31 subjects.

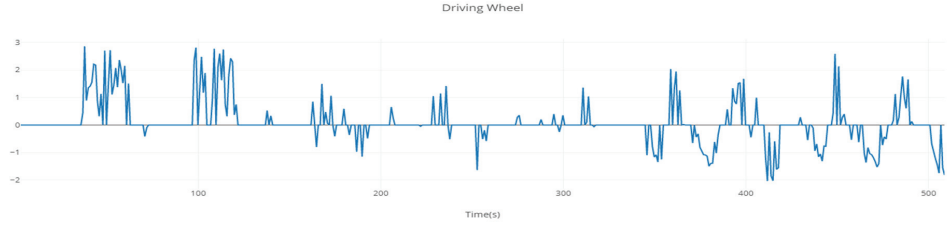

Figure 7. System data—Steering wheel rotation data tracking.

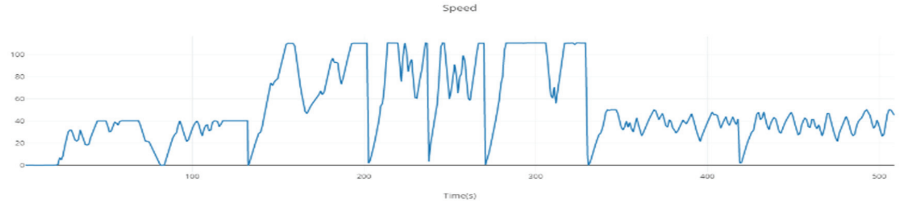

Figure 8. System data—Tracking driving speeds over time.

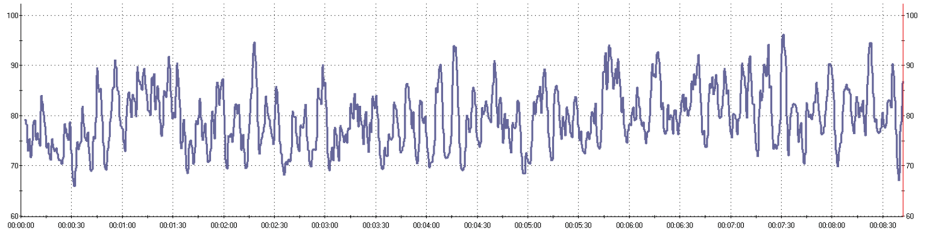

Figure 9. Bio-data—Tracking subject's heart rate during experiment session.

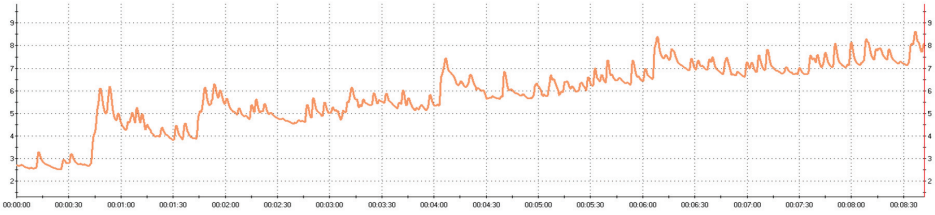

Figure 10. Bio-data—Subject's skin conductance during the experiment session.

The Pearson correlation coefficient has been applied to measure the strength of linear association between the VRET system data and the subject's bio-data. The result indicates that the correlations are relatively small with most coefficients falling between −0.3 and 0.3. Nonparametric test for gender differences compared the 14 males and 17 female subjects that participated in the pre-test experiment. The Mann–Whitney U test was used to test if there was a statistically significant difference between the overall satisfaction medians of the male and female groups. The null hypothesis is $\eta_{male} = \eta_{female}$, using a significance level of $\alpha = 0.05$, the p-values related to four kinds of bio-data are all higher than alpha value (0.05), so there is insufficient evidence to conclude a statistically significant difference between the overall satisfaction medians of the male and female groups.

The Mann–Whitney U test was also used to test if there is a statistically significant difference between the overall satisfaction medians of the high anxiety and low anxiety groups. Subjects were divided into two groups, high anxiety groups and low anxiety groups, according to the rating of "Self-rating fear of driving scale" filled out before the pre-test experiment. Eleven subjects were in the high anxiety group and 20 subjects were in the low anxiety group. The null hypothesis is $\eta_{high} = \eta_{low}$, using a significance level of $\alpha = 0.05$, three out of the four p-values related to bio-data (heart rate, respiration, and skin conductance) are lower than alpha value (0.05), so there is statistical evidence that there is a difference between the overall satisfaction medians of the two anxiety types. The VRET system does affect the subject's bio-data according to their degree of fear of driving.

One-way ANOVA tests comparing means of bio-data in seven scenarios are used to estimate the 95% confidence interval and determine whether the associated population means in different scenarios are significantly different. The results are presented in Figure 11a,c,e,g. Fisher's least significant difference method for multiple comparisons was applied to examine which means at different levels are different, as presented in Figure 11b,d,f,h.

The bio-feedback data of the one-way ANOVA interval plots, presented in Figure 11, indicate that pre-test subjects become increasingly anxious as the fear level of the scenarios increases (shown by heart rate, temperature, and skin conductivity trends). For detailed information from the ANOVA results, multiple comparisons analysis between different levels was also conducted, as higher fear levels tend to be assigned to the same groups and lower fear levels tend to be assigned to the same groups, a significant difference in the sample means between higher levels and lower levels was demonstrated. This trend supports the hypothesis that increases in the severity of pre-existing phobias increase the subject's bio-feedback responses.

An interesting observation is that the bio-feedback data in level 1 seems to be significantly higher than level 2 data as shown in heart rate and temperature plots and the Fisher's LSD method supports the same result. A possible cause of this phenomenon may be related to the experimental design where subjects never exposed to a VR environment may become more anxious during the initial ET session. As the experiment progresses, the subjects become acclimated to the VR environment so there is less tension and greater ease of use of the system. In order to prevent this problem from happening, a ten-minute static VR experience can be added to the experiment flow between pre-test questionnaire and VRET interface to stabilize the subject's bio-response before the experiment begins.

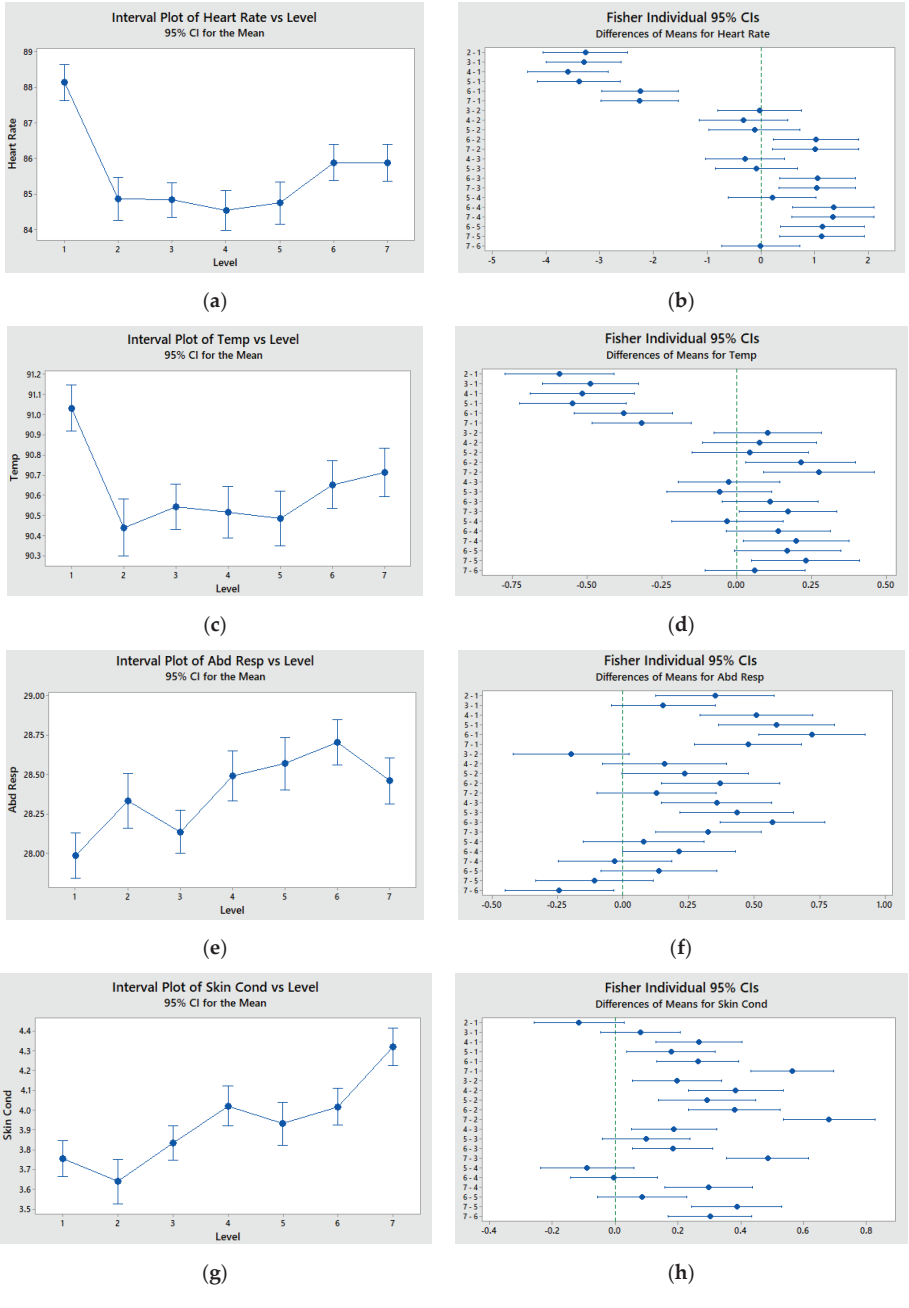

Figure 11. (**a**) One-way ANOVA interval plot of heart rate vs. level; (**b**) Fisher's least significant difference (LSD) method for multiple comparisons of heart rate vs. level; (**c**) One-way ANOVA interval plot of temperature vs. level; (**d**) Fisher's LSD method for multiple comparisons of temperature vs. level; (**e**) One-way ANOVA interval plot of respiration vs. level; (**f**) Fisher's LSD method for multiple comparisons of respiration vs. level; (**g**) One-way ANOVA interval plot of skin conductance vs. level; (**h**) Fisher's LSD method for multiple comparisons of skin conductance vs. level.

According to Dawson's research, if the amplitude of skin conductance is larger than 0.1 µs, then the skin conductance indicates a larger emotional response [25]. In this research, skin conductance data are converted into the form of amplitude data. A Shewhart control chart of amplitude data is presented in Figure 12. If four out of five data points exceed 0.1µs, it is marked in red, which means the subject has a larger emotional response at this point of time. Sixteen of the thirty-one subjects meet the above conditions and have data points marked in red. These data points frequently appeared for the 6th, 21st, 25th, and 32nd subjects.

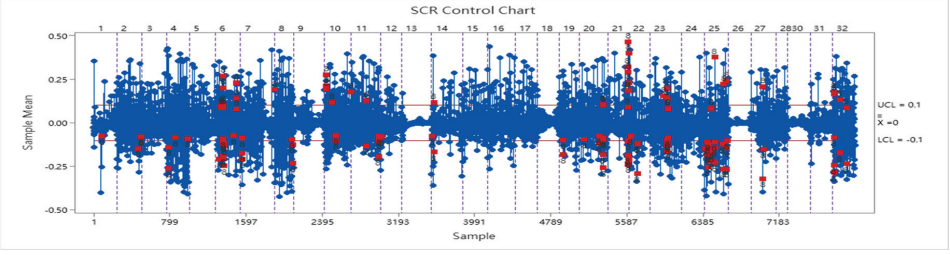

Figure 12. Shewhart control chart of skin conductance amplitude data.

The heart rate data are standardized according to individual data distribution and a Shewhart control chart of the standardized data is presented in Figure 13. If four out of five points exceed two standard deviations, the data points are marked in red indicating the subject has experienced a larger emotional response at this point of time. Twenty-one of the thirty-one subjects met the above condition with their heart rate data points marked in red.

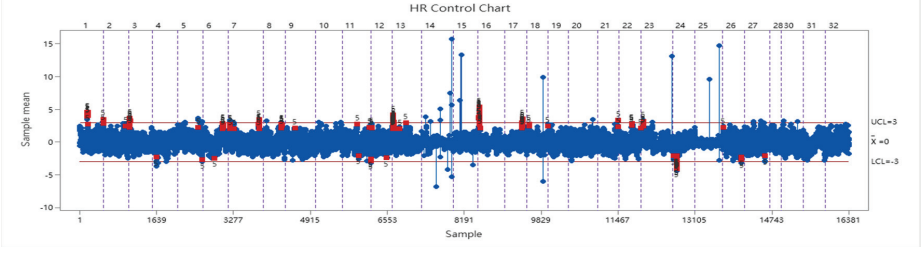

Figure 13. Shewhart control chart of standardized heart rate data.

5.4. Discussion of Pre-Test

The proposed VRET system has integrated system and bio-data collection for real-time data analytics compared to previous VRET research. In the Kaussner et al. VRET pilot study, anxiety and habituation during the VRET sessions were assessed using ratings on subjective units of a distress scale as well as the heart rate [20]. Costa et al. used subjective discomfort scores and heart rate to measure subjects' physiological response and sense of presence [21]. Additionally, in Claudio et al.'s fear of driving in tunnels research, questionnaires measured the outcome of the experiment and no real-time data was collected [22]. Most pervious VRET literature uses heart rate for real-time data tracking. Temperature, respiration, and skin conductance are for real-time data tracking in our VRET system. These preliminary design and development efforts are for the construction of a self-adaptive VRET system that will automatically adjust the levels of exposure according to real-time data tracking. The proposed future system will be tested for improvements to the immersive experience and to better ensure subjects' safety.

Compared to previous VRET research which only demonstrates the development of VRET without verification, this research has uniquely combined VRET design and development with the verification of its efficacy through pre-test. According to the results of Mann–Whitney U test, there is a significant difference between the overall satisfaction medians of high anxiety groups and low anxiety groups. Moreover, the results of ANOVA analysis show that bio-data and level are positively correlated except for Level 1. Therefore, through pre-test data analysis, VR is demonstrated to provide the subject with a sense of authenticity and can indeed cause anxiety similar to actual driving.

The problem of high level 1 bio-data is also emerging within pre-test data analysis. For this problem, follow-up studies may consider adding a ten minutes of VR experience before the experiment starts to assist the subjects to adapt to the VR environment and to improve the VRET system for official clinical trials.

6. Conclusions

The immersive technologies, most typically referred to as virtual reality (VR) and lately also to include augmented reality (AR) enabling technologies, are popularly researched and developed to improve healthcare and treatments for physical, psychological and social wellbeing with respect to different populations and their health issues (e.g., elderly, autism spectrum disorder, PTSD, phobia, etc.) [26,27]. For example, Lee et al. [24] have comprehensively reviewed VR and AR technologies developed for physical, psychological and social wellbeing of an elderly population. The review article discovers that plenty of R&D has been deployed for improving physical healthcare and treatments. Nonetheless, considering the rising psychological (mental and social) health issues, there are great needs to pursue immersive technologies and design immersive solutions for psychological therapies and treatments. The research presents the systematic design and development of virtual reality exposure therapy applied to fear of driving. Therapeutic treatments for this phobia remain as a major clinical challenge for psychiatrists, psychotherapists, and their patients. A VR headset, a high specification steering wheel, bio-sensors, and software are integrated to develop a realistic driving experience in an immersive environment for effective exposure therapy. The subjects are exposed to varying levels of fear inducing driving levels for treatment. Thirty subjects provided pre-test data for the system. The bio-feedback data and suggestions for improvement were derived from the experiments. Through pre-test data analysis, VR convincingly causes anxiety like actual driving. Furthermore, some systemic problems are discovered, so the follow-up research can improve the VRET system and improve the system design. Carefully crafted experimental design is required for collecting valid and reliable data for the VRET analytical models and system modification. The clinical psychiatrists' feedback is critical to improve the design before the VRET can be used for clinical trials.

In summary, this research has presented the VRET technical components, the system framework, key modules for implementation, and the experiment database design and development for the research. Specifically, the bio- and system-data analysis demonstrates the efficacy of the VRET for use in initial hospital-based clinical trials with continued improvement as the trails are analyzed. In the future, the research team hopes to extend the VRET treatments to other phobias, such as acrophobia, arachnophobia, and claustrophobia. The future research direction also includes the intelligent development of self-adaptive VRET systems incorporating progressive brain neurology and brain computer interface (BCI) technologies. When the degree of a subject's fears are detected through advanced BCI sensors, the self-adaptive VRET system will have sufficient knowledge and intelligence to automatically adjust the levels of exposure to ensure safe and effective gradual systematic desensitization.

Author Contributions: A.T.: Constructed the research framework and incorporated VR and IoT technologies for the system; C.V.T.: CBT and ET literature overview for anxiety disorders and panic disorders, interpretation of meta-analysis studies; C.-M.C.: PTSD, OCD, and PD theories and clinical ET design; R.R.T.K.: VRET system development and implementation, data analysis; A.P.C.L.: VR and VRET literature search, VRET prototype testing, data validation; C.H.N.: CBT and ET literature review and data validation. All authors have read and agreed on the published version of the manuscript.

Funding: This research is partially supported by the joint research grant of National Tsing Hua University and Chang Gong Memorial Hospital and the individual research grants of Ministry of Science and Technology, Taiwan (Grant numbers: MOST-108-2221-E-007-075-MY3 and MOST-108-2410-H-009-025-MY2).

Conflicts of Interest: The authors declare no conflict of interest.

References

1. American Psychiatric Association. *Diagnostic and Statistical Manual of Mental Disorders*; American Psychiatric Pub.: Washington, DC, USA, 2013.
2. Ougrin, D. Efficacy of exposure versus cognitive therapy in anxiety disorders: Systematic review and meta-analysis. *BMC Psychiatry* **2011**, *11*, 1–13.
3. Foa, E.B.; Rothbaum, B.O. *Treating the Trauma of Rape: Cognitive-Behavioral Therapy for PTSD*; Guilford Press: New York, NY, USA, 2001.
4. Wolpe, J. Psychotherapy by reciprocal inhibition. *Cond. Reflex* **1968**, *3*, 234–240. [PubMed]
5. Scozzari, S.; Gamberini, L. Virtual reality as a tool for cognitive behavioral therapy: A review. In *Advanced Computational Intelligence Paradigms in Healthcare 6. Virtual Reality in Psychotherapy, Rehabilitation, and Assessment*; Springer: Berlin/Heidelberg, Germany, 2011; pp. 63–108.
6. Meldrum, D.; Herdman, S.; Moloney, R.; Murray, D.; Duffy, D.; Malone, K.; French, H.; Hone, S.; Conroy, R.; McConn-Walsh, R. Effectiveness of conventional versus virtual reality based vestibular rehabilitation in the treatment of dizziness, gait and balance impairment in adults with unilateral peripheral vestibular loss: A randomised controlled trial. *BMC Ear Nose Throat Disord.* **2012**, *12*, 1–8. [CrossRef] [PubMed]
7. Matsuoka, Y.; Nishi, D.; Nakajima, S.; Yonemoto, N.; Noguchi, H.; Otomo, Y.; Kim, Y. Impact of psychiatric morbidity on quality of life after motor vehicle accident at 1-month follow up. *Psychiatry Clin. Neurosci.* **2009**, *63*, 235–237. [CrossRef] [PubMed]
8. Norris, F.H. Epidemiology of trauma: Frequency and impact of different potentially traumatic events on different demographic groups. *J. Consult. Clin. Psychol.* **1992**, *60*, 409. [CrossRef] [PubMed]
9. Hofmann, S.G.; Asnaani, A.; Vonk, I.J.; Sawyer, A.T.; Fang, A. The efficacy of cognitive behavioral therapy: A review of meta-analyses. *Cogn. Ther. Res.* **2012**, *36*, 427–440. [CrossRef] [PubMed]
10. Bisson, J.; Andrew, M. Psychological treatment of post-traumatic stress disorder (PTSD). *Cochrane Database Syst. Rev.* **2007**, *2007*, CD003388.
11. Bryant, R.A.; Sackville, T.; Dang, S.T.; Moulds, M.; Guthrie, R. Treating acute stress disorder: An evaluation of cognitive behavior therapy and supportive counseling techniques. *Am. J. Psychiatry* **1999**, *156*, 1780–1786. [PubMed]
12. Campos Soto, M.N.; Navas-Parejo, M.R.; Moreno Guerrero, A.J. Realidad virtual y motivación en el contexto educativo: Estudio bibliométrico de los últimos veinte años de Scopus. *ALTERIDAD Rev. Educ.* **2020**, *15*, 47–60. [CrossRef]
13. Belmonte, J.L.; Sánchez, S.P.; Cevallos, M.B.M.; Meneses, E.L. Competencia digital de futuros docentes para efectuar un proceso de enseñanza y aprendizaje mediante realidad virtual. *Edutec Rev. Electrón. Tecnol. Educ.* **2019**, 1–15. [CrossRef]
14. Gerardi, M.; Cukor, J.; Difede, J.; Rizzo, A.; Rothbaum, B.O. Virtual reality exposure therapy for post-traumatic stress disorder and other anxiety disorders. *Curr. Psychiatry Rep.* **2010**, *12*, 298–305. [CrossRef] [PubMed]
15. Rothbaum, B.O.; Hodges, L.; Alarcon, R.; Ready, D.; Shahar, F.; Graap, K.; Pair, J.; Hebert, P.; Gotz, D.; Wills, B. Virtual reality exposure therapy for PTSD Vietnam veterans: A case study. *J. Trauma. Stress* **1999**, *12*, 263–271. [CrossRef] [PubMed]
16. Rothbaum, B.O.; Anderson, P.; Zimand, E.; Hodges, L.; Lang, D.; Wilson, J. Virtual reality exposure therapy and standard (in vivo) exposure therapy in the treatment of fear of flying. *Behav. Ther.* **2006**, *37*, 80–90. [CrossRef] [PubMed]
17. Parsons, T.D.; Rizzo, A.A. Affective outcomes of virtual reality exposure therapy for anxiety and specific phobias: A meta-analysis. *J. Behav. Ther. Exp. Psychiatry* **2008**, *39*, 250–261. [CrossRef]
18. Trappey, A.J.; Trappey, C.V.; Chang, C.-M.; Govindarajan, U.H.; Shih, X.-Y.; Su, I.-A.; Gupta, N. Behavioral Therapy for Phobias Using Immersive Virtual Reality Technology. *J. Chin. Soc. Mech. Eng.* **2020**, *41*, 131–140.
19. Costa, R.T.D.; Carvalho, M.R.D.; Nardi, A.E. Virtual reality exposure therapy in the treatment of driving phobia. *Psicol. Teor. Pesqui.* **2010**, *26*, 131–137. [CrossRef]

20. Kaussner, Y.; Kuraszkiewicz, A.; Schoch, S.; Markel, P.; Hoffmann, S.; Baur-Streubel, R.; Kenntner-Mabiala, R.; Pauli, P. Treating patients with driving phobia by virtual reality exposure therapy–A pilot study. *PLoS ONE* **2020**, *15*, e0226937. [CrossRef] [PubMed]
21. Costa, R.T.D.; Carvalho, M.R.D.; Ribeiro, P.; Nardi, A.E. Virtual reality exposure therapy for fear of driving: Analysis of clinical characteristics, physiological response, and sense of presence. *Rev. Bras. Psiquiatr.* **2018**, *40*, 192–199. [CrossRef] [PubMed]
22. Claudio, A.P.; Carmo, M.B.; Gomes, I.L.; Esteves, F.; Gaspar, A. Sense of presence inside a feared (virtual) tunnel. In Proceedings of the 2015 10th Iberian Conference on Information Systems and Technologies (CISTI), Aveiro, Portugal, 30 July 2015; pp. 1–7.
23. Kioumars, A.H.; Tang, L. ATmega and XBee-based wireless sensing. In Proceedings of the 5th International Conference on Automation, Robotics and Applications, Wellington, New Zealand, 6–8 December 2011; pp. 351–356.
24. Craske, M.; Wittchen, U.; Bogels, S.; Stein, M.; Andrews, G.; Lebeu, R. *Severity Measure for Specific Phobia—Adult*; Lake St. Louis: American Psychiatric Association: Washington, DC, USA, 2013.
25. Dawson, M.E.; Schell, A.M.; Filion, D.L. The electrodermal system. In *Handbook of Psychophysiology*; Cacioppo, J.T., Tassinary, L.G., Berntson, G.G., Eds.; Cambridge University Press: Cambridge, UK, 2017. [CrossRef]
26. Liu, X.; Wu, Q.; Zhao, W.; Luo, X. Technology-facilitated diagnosis and treatment of individuals with autism spectrum disorder: An engineering perspective. *Appl. Sci.* **2017**, *7*, 1051. [CrossRef]
27. Lee, L.N.; Kim, M.J.; Hwang, W.J. Potential of augmented reality and virtual reality technologies to promote wellbeing in older adults. *Appl. Sci.* **2019**, *9*, 3556. [CrossRef]

applied sciences

MDPI

Article

Serious Game Platform with Haptic Feedback and EMG Monitoring for Upper Limb Rehabilitation and Smoothness Quantification on Spinal Cord Injury Patients

Álvaro Gutiérrez [1,*], Delia Sepúlveda-Muñoz [1], Ángel Gil-Agudo [2] and Ana de los Reyes Guzmán [2]

[1] Escuela Técnica Superior de Ingenieros de Telecomunicación, Universidad Politécnica de Madrid, Av. Complutense 30, 28040 Madrid, Spain; delia.sepulvedam@alumnos.upm.es

[2] Biomechanics and Technical Aids Unit, National Hospital for Paraplegics, Finca La Peraleda, 45071 Toledo, Spain; amgila@sescam.jccm.es (Á.G.-A.); adlos@sescam.jccm.es (A.d.l.R.G.)

* Correspondence: a.gutierrez@upm.es; Tel.: +34-91-06-72452

Received: 4 October 2019; Accepted: 24 January 2020; Published: 2 February 2020

Abstract: Cervical Spinal Cord injury (SCI) is a neurological disease that produces, as a consequence, impairments of the upper limb function. This paper illustrates a virtual reality platform based on three serious games for upper limb rehabilitation with electromyography monitoring, providing force feedback to the patient. In the rehabilitation process proposed, haptic feedback was provided to the patients to strength the arm muscles by means of the Novint Falcon device. This end-effector device was used to manipulate the serious games. During the therapy performance, the system recorded electromyography signals from the patient's arm muscles, which may be used to monitor muscle contraction. The work presented a virtual reality system developed for spinal cord-injured patients. Each virtual reality environment could be modified in strength and duration according to the patients' needs and was implemented for recording quantitative data about the motor performance. The platform was validated as a proof of concept in cervical spinal cord-injured patients. Results showed that this rehabilitation platform could be used for obtaining objective information in relation to motor control characteristics.

Keywords: upper limb rehabilitation; serious games; haptic feedback; electromyography sensors; virtual reality; smoothness

1. Introduction

Spinal Cord Injury (SCI) is one of the most important neurological diseases that produce deficiencies in the field of physical disability [1]. It is often a catastrophic condition requiring chronic care. Despite an enormous amount of research in SCI, the neurological prognosis for a patient with severe SCI remains dismal. Life expectancy after such an injury is markedly reduced due to complications proportional to the severity of injury or remaining neurological functions. Therefore, SCI is associated with a risk of developing secondary conditions that can be debilitating and even life-threatening, such as deep vein thrombosis, urinary tract infections, muscle spasms, osteoporosis, pressure ulcers, chronic pain, and respiratory complications [2]. Acute care, rehabilitation services and ongoing health maintenance are essential for the prevention and management of these conditions [3].

The worldwide incidence of SCI lies between 10 and 83 per million inhabitants per year [4]. In Spain, approximately 1000 new cases of SCI per year occur due to trauma, which is the main cause; half due to traffic accidents, the rest due to falls, blows, sport accidents or other injuries [5]. Most of these people have permanent damages. It is observed that people with SCI have difficulties

and limitations in mobility (96.9% of cases), in self-care (81.1% of cases) and in carrying out tasks of domestic life (84.3% of cases) [6]. This situation means that the majority of the population with SCI requires personal and technical support to carry out these activities. The treatment for SCI is often expensive: it can reach up to 55,000€ the first 60 days for a patient in acute phase, with an additional 10,000€ for the intensive care stay. Hence, the economic and societal impact is enormous, both to the immediate family and the society at large [7]. The inclusion of lower cost technologies is a key aspect for reducing the therapy cost. Therefore, there is a great need for new systems that improve the quality of life for SCI injured patients [8–10].

The impairment of the Upper Limb (UL) is one of the most common sequelae following neurological injuries [11]. The loss of arm and hand function is one of the most devastating consequences in tetraplegia [12]. One important aspect of this lost function is smoothness. Smoothness is a characteristic of a skilled and well-coordinated human movement [13] and it is an independent measure with respect to speed and distance [14]. When moving the hand between pairs of targets, people tend to generate roughly straight hand trajectories with a single-peaked, bell-shaped speed profile [15]. However, in presence of neurological pathologies, the UL movement is characterized by the lack of smoothness [16], the performance of more curved trajectories with directional changes and a higher peaks number in the speed profile. Smoothness has been used as a measure of motor performance in healthy people and neurological pathologies, mainly stroke patients [11,14,17,18], being the neurological injury with the highest incidence and prevalence in the population. This control motor characteristic has been quantified by means of different variables, extracted of the movement analysis as the peaks number in the speed profile, the ratio between the maximal and mean velocity and the jerk metric computed as the time derivative of acceleration [13,19]. As our expertise in this field, after the developmental work of kinematic indices applied to spinal cord injured patients, smoothness metric computed from the peaks number in the speed profile is discriminative between healthy and neurological patients [20,21].

Small progresses in arm and hand function may lead to increase autonomy in activities of daily living [22], improving independence and quality of life. For this reason, rehabilitation for the improvement in UL function after cervical SCI is a top priority in individuals with tetraplegia [23]. In rehabilitation, considerable amounts of practice are required to induce neuroplastic changes and functional recovery of neurological motor deficits [24]. SCI rehabilitation works through mechanisms of experience-dependent plasticity [25]. The process of plasticity consists of changes in the activation pattern, either of structure or function of neural connections. These changes involve the modification of the strength of existing connections or the creation of new neural connections. Although it is likely that some of the reorganization after central nervous system injuries take place in the cortex, plasticity changes may also occur in subcortical structures, such as the spinal cord [26]. Therefore, neuroplasticity is essential in the SCI rehabilitation process.

Nowadays, technology is typically involved in rehabilitation. It makes use of high cost devices, such as exoskeletons or robotic devices [27], or low cost devices, such as the Leap Motion, Kinect, or Novint Falcon, among others [28]. In this paper, we make use of the Novint Falcon device, a desktop haptic robot with 3 degrees of freedom (see Section 2). Several studies found in the literature have investigated the use of the Novint Falcon in healthy subjects: Scalona et al. analyzed the motor performance during six reaching movement sessions varying the force levels [29]. The subjects had to reach eight different objectives placed on a circumference (vertical and horizontal line and in each diagonal). Cappa et al. analyzed the response to different force feedback in healthy population with an educational purpose [28]. Palsbo et al. used the Novint Falcon to train fine movements in a group of healthy developing children and noted significant improvements in handwriting performance [30]. However, there is no evidence of research studies with the Novint Falcon in spinal cord injured patients. Nonetheless, some studies have been performed with the Novint Falcon to analyze the UL function in patients who have suffered stroke [31,32]. These studies have been conducted with a rehabilitation purpose. Chortis et al. evaluated the effects of repetitive arm movements with a group of eight post-stroke subjects by using the commercial virtual games included in Novint

Falcon [33]. These games were oriented to reach UL functional tasks, following the rehabilitative principles. The patient performance was compared between pre and post condition by using only clinical tests. Unfortunately, in those studies, smoothness was not analyzed.

Additionally, the use of technology in rehabilitation in combination with virtual reality (VR) environments has increased in the last years [34–37], mainly because the quantity of therapy that patients receive increases. VR has many advantages for intervention, such as enabling the grading of activities, obtaining precise performance measures, providing a safe and ecologically valid environment, and being enjoyable and motivating [24,38]. There is evidence about the acceleration in the rehabilitation process by the combination of these VR treatments with conventional rehabilitation [39]. Moreover, the use of VR environments can increase the intensity of the therapy through the adequate repetitions number [27]. VR reality games increase motivation in patients both in occupational and physical therapy [40]. Therefore, the health care sector is showing steadily increasing interest in serious games [41].

The work presented in this paper is centered in reaching the patient's assessment in an objective way by means of the smoothness movement characteristic. Therefore, the aim of the present paper, an extension of [42], is to develop three serious games based on UL functional tasks, manipulated by the Novint Falcon device, and to collect quantitative data about SCI patients for analyzing movement smoothness. Moreover, this research involves the novelty of applying force feedback to SCI patients while analyzing the movement smoothness. In addition, electromyographic signals are obtained, integrating a Myo Gesture armband into the platform, which could be useful in the future for analyzing impairments in the muscles activation pattern.

The rest of the paper is organized as follows: Section 2 describes the methodology in relation to the integration of a commercial haptic device (Novint Falcon) and a commercial electromyography (EMG) sensor (Myo Gesture armband) into a virtual reality platform; the development of the serious games and the validation proof. Section 3 presents the results of the implemented proof of concept. Section 4 includes the discussion and Section 5 concludes the paper.

2. Materials and Methods

2.1. UL Rehabilitation Platform

The platform was composed of a PC, including the serious games developed in Unity3D, and two hardware devices: Novint Falcon for providing force feedback and manipulating the serious games; and Myo Gesture Arm Band for providing information about muscle contraction (see Figure 1).

Figure 1. Scheduled illustration of the upper limb rehabilitation platform: Myo Gesture armband (left object in image) and Novint Falcon device (right object in image).

2.1.1. Novint Falcon

The Novint Falcon (see Figure 1, right) is a desktop haptic robot device with 3 degrees of freedom (DOF). It provides haptic feedback where the users feel virtual objects as they virtually touch them [43]. The device consists of three motorized arms attached to an interchangeable end-effector providing kinesthetic feedback. It uses a USB 2.0 port, has a capacity of 9 N of force, and provides a $10 \times 10 \times 10$ cm^3 working space. The device has a refresh rate up to 1000 times per second [44].

In this paper, the Novint Falcon was selected because of its low cost, at least one order of magnitude, compared to similar devices, such as the Delta.3 [45] or Omega-3 [46], and because it can generate

more force feedback than other low cost haptic devices [28]. It was used as an end-effector robotic device for upper limb rehabilitation. However, the Novint Falcon comes with a standard ball grip which is difficult to use by patients with SCI, as a fine pinch is necessary to perform the grasp [47]. The grip selected for SCI patients was of a cylinder shape for a better hand-grasp. This was a novelty in comparison to previous studies and it was designed and printed on a 3D printer.

In previous studies, tests were performed with an EMG recording system located in the main arm muscles [48]. The tests showed that using the Novint Falcon to give force feedback activates the Anterior Deltoid muscle, which flexes and medially rotates the arm, and the Extensor Carpi Ulnaris muscle, which extends and adducts the hand at the wrist joint. This was demonstrated by applying different degrees of haptic feedback in an exercise where participants would press down on a vibrating cube [48]. Therefore, the tests concluded that, by using the Novint Falcon, the shoulder and the forearm are activated.

2.1.2. Myo Gesture Arm Band

The Myo Gesture armband (see Figure 1, left) is a wearable gesture and motion control device working with EMG sensors to measure electrical pulses in the arm [49]. While muscles expand and contract, the armband sends signals wirelessly to other devices. It uses a Bluetooth 4.0 low energy connection, it has a proprietary muscle activity EMG sensor, a 9-axis inertial measurement unit (IMU), a rechargeable lithium-ion battery with one full day use out of single charge and haptic feedback which provides short, medium or long vibrations.

Deeping into the sensors, the device has 8 EMG sensors and an IMU, containing a three-axis gyroscope, a three-axis accelerometer and a three-axis magnetometer. Thanks to this 9-axis IMU, Myo Gesture armband senses the motion, orientation and rotation of the forearm, used to recognize hand and wrist movements.

In this paper, the device was used for obtaining a correct EMG monitoring during the performance of the rehabilitation games. By using this armband, the muscle contraction and the arm kinematics were stored for a posterior data analysis. Because of the Myo Gesture armband design, the 8 EMG sensors are located equally distributed in the perimeter of the forearm. The EMG data was streamed at 200 Hz by Bluetooth communication to the PC.

Moreover, the rehabilitation platform implemented provided the opportunity to visualize in real time the data obtained from the EMG sensors. This functionality allowed to measure the muscle strength that the patient performs during each game.

2.1.3. Communication Protocol

The communication between the virtual environment and the devices were implemented via sockets. The communication frequency between these devices was very important. Because the user needed to perceive continuity in the images, the frequency of 30 Hz was selected for the graphics. However, for haptic stability without oscillations a sampling rate greater than 500 Hz was mandatory. In this paper, the frequency selected was around 650 Hz.

2.2. Serious Games Development

The first step to create the rehabilitation platform was to implement the virtual end-effector. A software created the socket between the Unity 3D platform and the Novint Falcon device, enabling the bidirectional transmission and reception of information.

To study the movement of the virtual object, it was necessary to establish a relationship between the Cartesian coordinates of the end of the haptic device and the coordinates of the virtual object. This module updated every frame in the scene with the position of the end-effector. The axes reference of the Novint Falcon and the games are shown in Figure 2, where the x and y axes are horizontal and vertical movements on the screen respectively, and the z axis comes out of the screen.

(a) **(b)**

Figure 2. (**a**) Novint Falcon and (**b**) serious games reference axes.

Then, the serious games have been implemented with a therapeutic sense. To create a complete platform, different menus focused on the patients were developed. The configuration of the games attributes was essential to fit the games according to the needs of each patient in relation to the functional capabilities. Within each serious game proposed, patients had to reach the number of objectives selected by the therapist. To achieve this goal, the time of execution was restricted. If the patient did not achieve the objectives in the available time, the game would finish. To help patients in developing this task, the movement made with the end-effector was visualized in the virtual environment.

A summary of the main characteristics analyzed in each game is shown in Table 1. The behavior and characteristics of each serious game are explained in subsequent sections. These features were measured in terms of movement smoothness. Moreover, each serious game included elements of visual feedback, recommended to boost the rehabilitation. Therefore, each serious game sought to check if it was able to positively modify neural mechanisms and improve motor performance by tuning the control structure of a patient. This effect should be analyzed in a future work, where a clinical validation should be carried on. This effect has been mostly analyzed in stroke patients [50] but these feedback sources can be extended to patients who have suffered other neurological diseases. Nevertheless, more studies focused exclusively on SCI upper limb impairments and their recovery are needed to elucidate if there are any difference in the residual motor control after an SCI compared to post-stroke patients.

Table 1. Summary with the main characteristics of each game.

Game	Exercise Type	Force Type	Therapeutic Objective
Following the path	Path guidance	Hooke's law	Accuracy
Picking bananas	Resistive	Viscosity	Accuracy, Strength
Collecting stars	Resistive	Hooke's law	Accuracy, Strength

2.2.1. Following the Path

The end-effector in the scene was represented by a pencil which emulates a path drawn by the patient. In this game, there was not a selection of the number of the objectives. The path was the same in all configurations. Users had to travel inside the path without going out of the edges and when they got out of it, an opposed force was exerted. When the user completed a segment, it changed its color to a darker one (see Figure 3a) until the user completed all segments or the time was exhausted.

This game was implemented in 2D (x and y axes) because the depth of the scene could cause trajectory disturbance in patients. The range of motion was of 5 cm in x axis and of 7.5 cm in y axis. The path of the trajectory had a width of 0.5 cm.

Therapeutic Objective

This rehabilitation game was based on a path guidance exercise. The therapeutic objective was to improve the precision and smoothness in the UL movement made by the patient and to recover fine

motor control. This training modality using robot-mediated therapy was a combination of assistive and active exercise. When the patient was moving the end-effector inside the path, the active mode was working and the patient felt no force. However, when the patient went out the path, the assistive modality started to push the patient's hand inside. Therefore, the haptic robot assisted by providing force feedback opposing to the movement of the patient.

In this training, the trajectory performed by the patient acquires relevant importance. For this reason, the trajectory made by the patient was collected, so the movement smoothness could be analyzed.

The force feedback ($\boldsymbol{F}_V$) was implemented by using Hooke's law (see Equation (1)).

$$\boldsymbol{F}_V\,(kT) = -k_V\,\Delta\boldsymbol{X}(kT), \tag{1}$$

where T was the sampling time, kT a specific instant in the discrete domain ($k \in [0,1,2,\ldots]$), $\Delta\boldsymbol{X}(kT)$ the distance to the edge of the path, and k_V the stiffness or elasticity simulated in the edge of the path. The force was implemented in the edges of the path, so patients felt these edges like walls that they should not cross.

(**a**) (**b**)

Figure 3. (**a**) Serious game "Following the path"; (**b**) Serious game "Picking bananas".

2.2.2. Picking Bananas

The end-effector was a basket which must collect different bananas that were located in different trees (see Figure 3b). The patient moved into the environment with the basket and when a banana fell from the tree, he had to get it with the basket before it touched the floor.

The therapist selected the number of bananas in the scene and the time for the duration of the task. Then, the game selected the frequency of falling and it randomized the falls for every session. The game notified the user when one banana was going to fall by changing its color and producing a sound. If the banana fell into the basket, the score increased. If it did not fall into it, it simply disappeared. When all the bananas fell, the game ended and the final result screen was visualized.

The force feedback provided by the haptic device was proportional to the number of bananas inside the basket, as a concept of weight and friction. Depending on the user, a high number of bananas could be tiring. Therefore, users could empty the basket in the left corner of the screen when they passed by.

The trees were disposed in the floor using a distance of 6 cm. With this distribution, users had enough space to move the end-effector in the total range of motion offered by the haptic device.

Therapeutic Objective

The rehabilitation exercise implemented in this serious game was resistive, so the robot opposed to the movement that the patient performed. In this kind of exercises, the number of repetitions should be small to avoid fatigue. A rest between exercises should be sufficient for recovery, and the resistance should be modulated to increase it as the patient ability grows.

The force feedback implemented was a viscosity resistance. This force was proportional to the velocity and opposed to the end-effector movement (see Equation (2)). This force ($\boldsymbol{F_V}$) should increase according to the number of objectives collected.

$$\boldsymbol{F_V}(kT) = -b_V\dot{\boldsymbol{X}}(kT), \tag{2}$$

where T was the sampling time, kT a specific instant in the discrete domain ($k \in [0,1,2, \dots]$), $\dot{\boldsymbol{X}}(kT)$ the velocity of the end-effector and b_V a constant referred to the viscosity. In this exercise, an isotonic muscle contraction was produced. This muscle contraction implied the shortening and lengthening of muscle fibers. Depending on the amount of force working against an individual's body, one of two kinds of isotonic contractions took place: concentric and eccentric contractions. Concentric contractions occur when muscles shorten while its tension is greater than the force opposing it. On the other hand, eccentric contractions occur when muscles extends in length [51].

2.2.3. Collecting Stars

The virtual visualization of the end-effector was a rocket and the objectives were stars which must be eliminated (see Figure 4). To destroy the stars, the patient moved the rocket to the star position. The game finished when the total number of objectives were achieved or the time was up. The stars had different sizes: the bigger ones were easier to catch than the others.

Figure 4. Collecting stars interface; one star has been collected.

A star was eliminated when the rocket collided with it. Once the collision was done, the star disappeared from the scene, the score was incremented and a sound was produced. After collecting a star, the user had to come back to the center of the screen before performing other destruction. To achieve this behavior, the collision detection module was disabled during this period.

This game was designed in 2D, because it focused on following a straight trajectory, rejecting the depth of the scene. Therefore, the allowed movements were in the y and x axes, but not in z axis.

The center of the stars was disposed in a circumference with a radius of 4.5 cm, centered in x and y equal to zero. Consequently, the range of motion of the haptic device was fully covered, allowing a range of motion of −5 cm to 5 cm in both axes.

Therapeutic Objective

The exercise implemented in this game was resistive. The robot provided force opposing the movement. Thus, its goal was to obtain the strengthening of the UL muscles. In addition, with this game the linearity of the movement could be checked. Patients with UL lesion usually tried to compensate movements performing curved trajectories when they tried to catch an objective which was in a straight direction.

In this case, there was a zone without force in the middle of the game circle, but when the patient was close to the targets, the force applied increased. The force began to act only in a radius of 2.5 cm from the objective. The force applied followed the Hooke's law (see Equation (1)). Therefore, the force scaled linearly with respect to the distance when the end-effector was entering into the force area.

As in the picking bananas game, the muscle contraction was isotonic, because the force depended on the movement and the position. A shortening and lengthening of the muscle fibers occurred during the game performance.

2.3. Participants

A total of 8 people participated in the study divided into two groups: a group of healthy people (n = 4) and a group of cervical SCI patients (n = 4). All patients fulfilled the following inclusion criteria: age 16 to 65 years, at least 6 months from the injury onset, and cervical injury of the metameric levels between C1 (first cervical vertebra) and C7 (7th cervical vertebra), neurologically classified according to the American Spinal Injury Association (ASIA) scale into grades C or D [52]. Patients who presented any vertebral deformity, joint constraint, surgery on any of the UL, balance disorders, dysmetria due to associated neurologic disorders, visual acuity defects, cognitive deficit, or head injury associated with the SCI were excluded. Background data of patients are provided in Table 2. The healthy subjects were chosen according to reach two groups of similar demographic characteristics (3 males of 19, 21 and 23 years old and a female of 44). The guidelines of the declaration of Helsinki were followed in every case. Informed consent was obtained from all individual participants included in the study, which was approved by the Local Ethics Committee, Toledo, Spain.

Table 2. Spinal Cord Injury (SCI) patients' characteristics.

Patient	Age	Sex	Injury Level	ASIA
1	19	M	C4	C
2	18	M	C4	C
3	45	F	C5	D
4	20	M	C6	C

2.4. Experimental Setup

The study was performed during two days, with two sessions per day. Therefore, the study was formed by data obtained from four different sessions. In all sessions, participants performed the test before starting with the serious games. This methodology was used to obtain clear results. In this way, participants had a previous knowledge of the games and the results obtained did not show the variability of the learning process.

The three games were performed in all sessions, always in the same order and with the same characteristics to avoid including variability into the study. First, the "Picking bananas" game was performed for 2 min and 15 objectives were selected. Second, the "Collecting stars" game was performed for a maximum of 2 min and 16 objectives were selected. Finally, the "Following the path" game was also performed for a maximum of 2 min. The maximum force selected in all games was at a value of 4.5 N, half of the maximum available force at the Novint Falcon. This parameter selection was chosen because in all tests participants showed skills to perform the task with this configuration.

All participants were right handed. The end-effector of the Novint Falcon was held with the right hand and the Myo Gesture armband placed in the same arm, specifically in the forearm, with the electrodes located on the flexor and extensor wrist muscles. The tasks were performed in the frontal plane of the patients (see Figure 5).

Figure 5. Example of a healthy trial with the Novint Falcon held on the right hand and the Myo Gesture armband on the right forearm.

2.5. Data Processing

In this study, the UL motor performance of each participant was measured in terms of movement smoothness, computing the peaks number from the velocity profile during the task execution proposed by the serious games.

A processing script was developed by using the software MATLAB (MathWorks®). The speed profile was obtained from the position data obtained by the haptic robot. These data were stored into text files during the performance of each serious game. The trajectories were analyzed in 2D.

The statistical non-parametric U Mann-Whitney test was applied to analyze the possible differences between both populations (healthy and patients groups) with a significance level of 5%. The results were expressed as mean and standard deviation for the following variables: mean and peak speed (m/s), number of peaks on the trajectory, and duration of the task.

3. Results

The results in relation to the motor performance in each variable within the serious games are shown in Tables 3 and 4.

Table 3. Results about duration, as well as peak and mean velocity in each serious game for both experimental groups (a, statistical differences $p < 0.05$).

Following the Path	Healthy Group (n = 4)	SCI Patients (n = 4)
Duration (s)	**28.55 (7.91)** [a]	**49.52 (13.33)** [a]
Peak velocity x (m/s)	0.255 (0.121)	0.406 (0.133)
Peak velocity y (m/s)	0.556 (0.203)	0.270 (0.125)
Mean velocity x (m/s)	0.063 (0.008)	0.058 (0.015)
Mean velocity y (m/s)	0.070 (0.018)	0.058 (0.020)
Picking bananas		
Duration (s)	120.00 (0)	120.00 (0)
Peak velocity x (m/s)	1.600 (0.441)	1.752 (0.591)
Peak velocity y (m/s)	0.799 (0.813)	0.818 (0.902)
Mean velocity x (m/s)	**0.060 (0.013)** [a]	**0.141 (0.065)** [a]
Mean velocity y (m/s)	**0.047 (0.013)** [a]	**0.091 (0.022)** [a]
Collecting stars		
Duration (s)	34.66 (7.91)	41.78 (15.83)
Peak velocity x (m/s)	1.232 (0.223)	0.878 (0.231)
Peak velocity y (m/s)	1.317 (0.387)	0.898 (0.145)
Mean velocity x (m/s)	0.160 (0.082)	0.140 (0.056)
Mean velocity y (m/s)	0.158 (0.054)	0.137 (0.054)

Table 4. Peaks number in each serious game for both experimental groups (a, statistical differences $p < 0.05$).

Peaks Number	Healthy Group (n = 4)	SCI Patients (n = 4)
Following the path	51.12 (11.53) [a]	81.32 (22.93) [a]
Picking bananas	154.75 (12.63)	164.72 (17.22)
Collecting stars	54.48 (10.25)	67.42 (24.58)

3.1. Following the Path

The time spent in the performance of the task was significantly different: healthy people spent on average 28.55 s and SCI patients 49.52 s. This indicates that patients needed to perform the movement slowly for avoiding going out of the edges. During the task execution, a counter quantified the number of times that a participant went out of the path. The analysis shows that healthy subjects went out of the path an average of 2.75 times and SCI patients 13.75 times. This fact increases the corrections number of the hand due to the force feedback applied. So, the number of peaks in the speed profile is statistically different between both groups.

3.2. Picking Bananas

In this serious game, all the participants spent 2 min. The average of the speed profile is slightly higher in SCI patients than in healthy subjects. This is because SCI patients made quick movements trying to catch the objectives.

The number of peaks obtained in the analysis shows that SCI patients perform more accelerations and decelerations in the speed profile. However, the number of peaks was very high in both groups, not showing statistical differences. Nonetheless, by observing the speed profile we observe that the speed profile of SCI group is more abrupt than the healthy participants. An example of average speed profile on axis x during the execution of the Picking bananas game for one healthy and one SCI participant is shown in Figure 6. This profile shows a maximum speed peak of 1.3 m/s for the healthy participant and 1.9 m/s for the SCI one. Two peaks higher than 0.5 m/s can be observed in the healthy subject, while this number rises up to fourteen for the SCI participant within the same time frame. Similar results are observed in all axes for all games and participants. However, a larger clinical study should be carried on to better analyze those differences and obtain statistical differences.

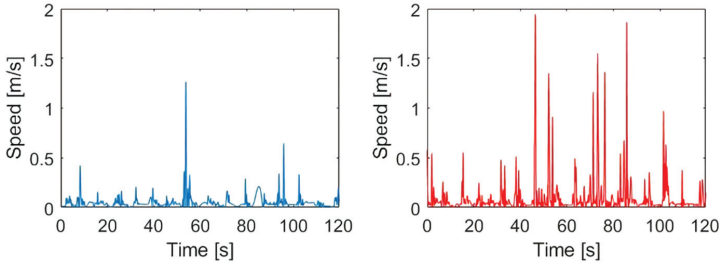

Figure 6. Example of a Healthy (blue) and SCI (red) participant speed profile of *x* axis measured from the end-effector of Novint Falcon device in the Picking bananas game.

3.3. Collecting Stars

During the execution of this serious game, SCI patients spent more time for reaching the 16 objectives (41.78 s) than healthy subjects (34.66 s). The duration of the exercise could affect the smoothness of the movement. This was because carrying out the task more slowly produced segmentation of the movement and more peaks appeared in the speed profile. In addition, SCI patients performed longer trajectories with a higher number of peaks than the healthy subjects (see Figure 7 for

an example). This longer trajectories were due to the difficulty of accurately reaching the objectives, both the starts and the center position. For the examples shown in Figure 7, it can be observed how the healthy performed more accurately trajectories both on the center and the start positions. It can also be observed that just one approximation, or two at maximum in some points, was performed to reach every star. On the contrary, the SCI participant performed multiple passes through the same point. Some stars, especially shown at the left-bottom part of the image, needed more than five approximations to be reached. Moreover, the lines accumulation on the center of the image is clearly stronger in the SCI patient plot.

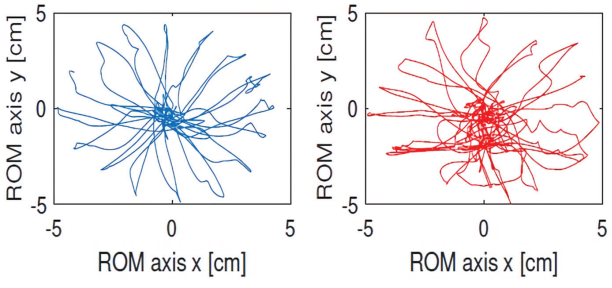

Figure 7. Example of a Healthy (blue) and SCI (red) participant range of motion (ROM) measured from the end-effector of Novint Falcon device in the Collecting stars game.

3.4. Electromyography Recording

An example of the activation pattern in flexors and extensors muscles measured from the Myo Gesture armband placed on the forearm of a healthy subject and an SCI patient during the execution of the serious games is shown in Figure 8. These data were analyzed taking into account the potential values obtained from the Myo Gesture armband. The EMG data provided by the Myo Gesture armband was unitless, 8 bit value. Hence, it provided a potential range between 0 and 255. To represent the muscle contraction, the value of the data collected from the sensor placed in the muscles of interest had been calculated. In all trials, SCI patients showed a stronger activation than healthy people. However, for all users, the muscle contraction was low, obtaining an average of 38.13 in "Following the path" game, 39.64 in "Picking bananas" games, and, finally, 53.35 in "Collecting stars".

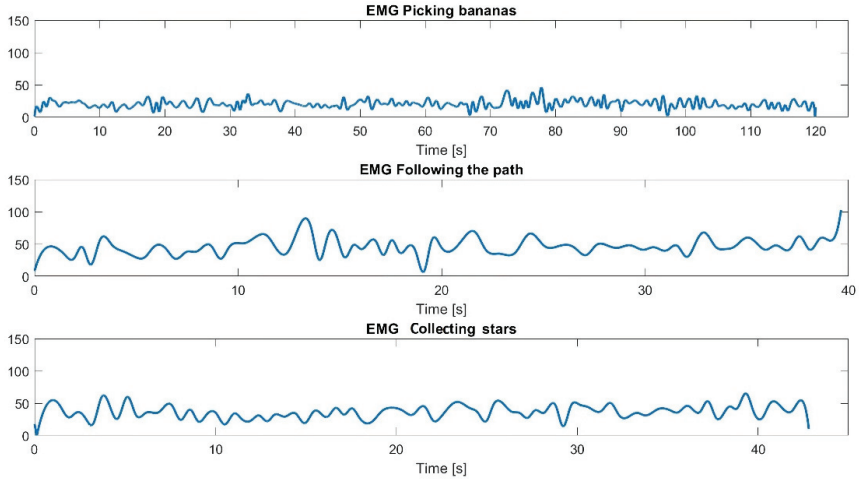

(a)

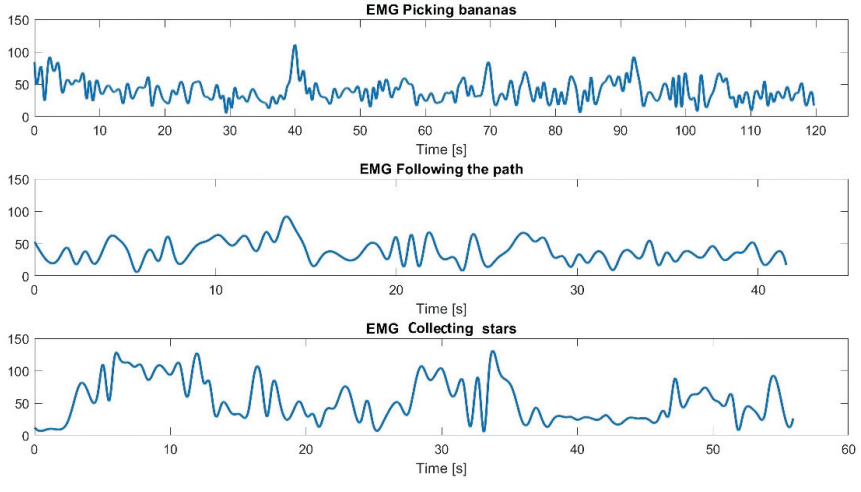

(b)

Figure 8. Activation pattern in the flexors and extensors muscles from Novint Falcon device placed on the forearm for the three serious games for (**a**) a healthy subject and (**b**) an SCI patient. The information provided by the Myo Gesture armband is unitless, with a potential value in the range of [0,255]. EMG = electromyography.

4. Discussion

In the present study, all virtual environments developed focus on reaching UL functional tasks. For the performance, they require a combination of analytical movements in each involved joint. The force feedback delivered by means of Novint Falcon provides sensitive information to the patient that modifies the kinematic patterns performed and, as a consequence, the kinematic variables measured.

An important contribution in this research with respect to previous studies is the integration of the Novint Falcon device and the Myo Gesture armband into a unique platform, obtaining EMG signals from flexors and extensors muscles of the wrist joint. The monitoring of EMG signals could be useful in the future for analyzing impairments in the muscles activation pattern during the serious games performance. The EMG values obtained are low, far from the maximum value provided by the Myo Gesture armband. This effect occurs because the load of the therapy proposed is also moderate. Therefore, the muscle activity that patients need to overcome the force feedback is moderate. It can be appreciated that, in the "Collecting star" game, where the force feedback applied is higher, the muscle contraction is also higher. To represent the muscle contraction, the value of the data collected has been calculated. For that reason, it is necessary to validate this EMG signal with those activation patterns measured from a clinical EMG system. In previous studies, differences in EMG patterns between healthy subjects and patients with cervical SCI have been reported to match with the differences in kinematic results [53]. Therefore, the EMG signal is essential for monitoring the muscle contraction during the games performance. In a posterior analysis, these data could be used to check the changes in the patterns of motor activity during the rehabilitation process. The data provided by the EMG could also be useful for controlling the appearance of peripheral fatigue [54]. Moreover, its supervision is important to avoid damaging the patient's muscle with an overload of work.

In relation to the content of the games, the "Collecting stars" game has been developed similar to those proposed by Scalona et al., where they provide 8 objectives to reach with different levels of force feedback [29]. In our proposal, the game involves 16 objectives around the circumference: four in the vertical and horizontal line, and the other 12 in the diagonal lines. The other two serious games were oriented to complete functional tasks, like the commercial games included in Novint Falcon and used by Chortis et al. [33]: one of them, the "Picking bananas" game, to pick up and carry objects; and the other one, the "Following the path" game, to follow a hand trajectory.

Nonetheless, the lack of movement smoothness has already been demonstrated in presence of neurological pathologies [16]. It is measured at the distal segment and shows as a consequence longer hand trajectories with a higher number of directional changes. This characteristic provides objective quantitative information of UL motor function and control. The ideal condition when moving the hand between pairs of targets is to generate roughly straight hand trajectories with a single-peaked, bell-shaped speed profile [15]. This behavior was proved to be independent of the part of the work-space in which the movement was performed. Moreover, the results obtained were strong indicators that movement planning takes place in terms of UL distal segment, by means of hand trajectories rather than joint rotations [55,56]. Nevertheless, smoothness metric has shown to be discriminative between healthy and neurological patients when smoothness is computed from the peaks number in the speed profile [20,21]. Therefore, in this paper, smoothness has been measured by computing the peaks number within the speed profile. Results from the proof of concept show that this behavior was maintained, and a higher peaks number was obtained in SCI patients than in healthy people for the three serious games. However, statistical differences were only obtained in the "Following the path" game.

5. Conclusions

The use of new technologies in the rehabilitation field has increased in the last years. Robot aided and VR rehabilitation provide higher motivational environments to the patient, facilitate the performance of the necessary movement repetitions for inducing the UL motor learning and increase the amount of therapy that patients receive. However, these technologies are expensive, and a need for low-cost devices exists. This work takes advantage of low-cost VR systems and robotic haptic devices to enhance involvement and engagement of patients to provide a congruent multisensory afferent feedback during motor exercises and benefit from the flexibility of virtual scenarios.

The low cost platform developed in the present work enables the UL rehabilitation with haptic feedback and EMG monitoring for SCI patients. First of all, three serious games have been designed

and implemented to compute within them the smoothness movement. The design and implementation of each serious game required the definition of a unique interface and physical models related to haptic feedback. In all of them, the movement smoothness has been reported lower in patients than in healthy people, showing an inverse relation with the peaks number obtained. As a conclusion, the three serious games proposed are suitable for measuring movement smoothness, but the most suitable game for discriminating between healthy and SCI patients is the "Following the path" game. This is because, in this game, the order to reach the different nodes has been imposed, being always the same and allowing an identical comparison between participants. Nonetheless, these assumptions should be confirmed with a large clinical validation.

A proof of concept to check the functionality of the platform with SCI patients was made. Results obtained in terms of movement smoothness show differences in the movement patterns. Some benefits drawn from this research are exposed as follows:

- All the devices of the platform are low-cost and easily adaptable for different people, with a short time spent in preparation for the serious games performance.
- The configuration options used in this research allow to create different virtual scenarios, in order to personalize each patient rehabilitation.
- The final design generates a good haptic response and reliable monitoring of the muscle contractions.

Author Contributions: Conceptualization, Á.G., D.S.-M. and A.d.l.R.G.; methodology, Á.G., D.S.-M., A.d.l.R.G.; software, D.S.-M.; validation, D.S.-M., A.d.l.R.G., and Á.G.-A.; formal analysis, A.d.l.R.G., Á.G.; investigation, D.S.-M., A.d.l.R.G.; resources, Á.G. and Á.G.-A.; data curation, D.S.-M. and A.d.l.R.G.; writing—original draft preparation, Á.G., D.S.-M. and A.d.l.R.G.; writing—review and editing, Á.G., A.d.l.R.G. and Á.G.-A.; visualization, Á.G., A.d.l.R.G.; supervision, Á.G., A.d.l.R.G.; project administration, Á.G.-A. and A.d.l.R.G.; funding acquisition, Á.G. and A.d.l.R.G. All authors have read and agreed to the published version of the manuscript.

Funding: This research has been funded by grant from the Spanish Ministry of Economy and Competitivity and co-funded from FEDER, National Plan for Scientific and Technological Research and Innovation. Project RehabHand (Plataforma de bajo coste para rehabilitación del miembro superior basado en Realidad Virtual, ref. DPI2016-77167-R).

Acknowledgments: This work was supported by the National Hospital for Paraplegics in Toledo (Spain) and the Universidad Politécnica de Madrid (Spain). The authors acknowledge the collaboration of the participants in this study.

Conflicts of Interest: The authors declare no conflict of interest.

References

1. Chen, Y.; Tang, Y.; Vogel, L.C.; Devivo, M.J. Causes of spinal cord injury. *Top. Spinal Cord Inj. Rehabil.* **2013**, *1*, 1–8. [CrossRef]
2. World Health Organization. Spinal Cord Injury. Available online: http://www.who.int/news-room/fact-sheets/detail/spinal-cord-injury (accessed on 1 August 2019).
3. Humphreys, J.S. Key considerations in delivering appropriate and accessible health care for rural and remote populations: Discussant overview. *Aust. J. Rural Health* **2009**, *17*, 34–38. [CrossRef]
4. Wyndaele, M.; Wyndaele, J.J. Incidence, prevalence and epidemiology of spinal cord injury: What learns a worldwide literature survey? *Spinal Cord* **2006**, *44*, 523–529. [CrossRef] [PubMed]
5. DeVivo, M.; Biering-Sorensen, F.; Charlifue, S.; Noonan, V.; Post, M.; Stripling, T.; Wing, P. International Spinal Cord Injury Core Data Set. *Spinal Cord* **2006**, *44*, 535–540. [CrossRef] [PubMed]
6. Pérez, K.; Novoa, A.M.; Santamariña-Rubio, E.; Narvaez, Y.; Arrufat, V.; Borrell, C.; Cabeza, E.; Cirera, E.; Ferrando, J.; García-Altes, A.; et al. Incidence trends of traumatic spinal cord injury and traumatic brain injury in Spain. *Accid. Anal. Prev.* **2012**, *46*, 37–44. [CrossRef] [PubMed]
7. Goel, S.; Modi, H.; Dave, B.; Patel, P. Socio-Economic Impact of Cervical Spinal Cord Injury Operated in Patients with Lower Income Group. *Glob. Spine J.* **2016**, *6*, 264. [CrossRef]
8. Kemal, N.; Levent, Y.; Volkan, S.; Abdulkadir, A.; Kadriye, O. Rehabilitation of spinal cord injuries. *World J. Orthop.* **2015**, *6*, 8–16.
9. Oldrige, N.B. Outcomes Measurement: Health-Related Quality of Life. *Assist. Technol.* **1996**, *8*, 82–93. [CrossRef]

10. Steel, E.J. Content analysis to locate assistive technology in Queensland's motor injury insurance rehabilitation legislation and guidelines. *Assist. Technol.* **2018**, *13*, 1–5. [CrossRef]
11. Murphy, M.A.; Sunnerhagen, K.S.; Johnels, B.; Willen, C. Three-dimensional kinematic motion analysis of a daily activity drinking from a glass: A pilot study. *J. Neuroeng. Rehabil.* **2006**, *3*, 18. [CrossRef]
12. Lu, X.; M Zoghi, C.R.; Galea, M.P. Effects of training on upper limb function after cervical spinal cord injury: A systematic review. *Clin. Rehabil.* **2015**, *29*, 3–13. [CrossRef]
13. Rohrer, B.; Fasoli, S.; Krebs, H.I.; Hughes, R.; Volpe, B.; Frontera, W.R.; Hogan, N. Movement smoothness changes during stroke recovery. *J. Neurosci.* **2002**, *22*, 8297–8304. [CrossRef]
14. Bartolo, M.; De Nunzio, A.M.; Sebastiano, F.; Spicciato, F.; Tortola, P.; Nilsson, J.; Pierelli, F. Arm weight support training improves functional motor outcome and movement smoothness after stroke. *Funct. Neurol.* **2014**, *29*, 15. [CrossRef]
15. Morasso, P. Spatial control of arm movements. *Exp. Brain Res.* **1981**, *42*, 223–227. [CrossRef]
16. Krebs, H.I.; Aisen, M.L.; Volpe, B.T.; Hogan, N. Quantization of continuous arm movements in humans with brain injury. *Proc. Natl. Acad. Sci. USA* **1999**, *96*, 4645–4649. [CrossRef]
17. Platz, T.; Denzler, P.; Kaden, B.; Mauritz, K.-H. Motor learning after recovery from hemiparesis. *Neuropsychologia* **1994**, *32*, 1209–1223. [CrossRef]
18. Kahn, L.E.; Zygman, M.L.; Rymer, W.Z.; Reinkensmeyer, D.J. Robot-assisted reaching exercise promotes arm movement recovery in chronic hemiparetic stroke: A randomized controlled pilot study. *J. Neuroeng. Rehabil.* **2006**, *3*, 12. [CrossRef]
19. Casadio, M.; Pressman, A.; Fishbach, A.; Danziger, Z.; Acosta, S.; Chen, D.; Tseng, H.-Y.; Mussa-Ivaldi, F.A. Functional reorganization of upper-body movement after spinal cord injury. *Exp. Brain Res.* **2010**, *207*, 233–247. [CrossRef]
20. De los Reyes-Guzmán, A.; Dimbwadyo-Terrer, I.; Pérez-Nombela, S.; Monasterio-Huelin, F.; Torricelli, D.; Pons, J.L.; Gil-Agudo, A. Novel kinematic indices for quantifying upper limb ability and dexterity after cervical spinal cord injury. *Med. Biol. Eng. Comput.* **2017**, *55*, 833–844. [CrossRef]
21. De los Reyes-Guzman, A.; Dimbwadyo-Terrer, I.; Pérez-Nombela, S.; Monasterio-Huelin, F.; Torricelli, D.; Pons, J.L.; Gil-Agudo, A. Novel kinematic indices for quantifying movement agility and smoothness after cervical Spinal Cord Injury. *NeuroRehabilitation* **2016**, *38*, 199–209. [CrossRef]
22. Hoffman, H.G.; Patterson, D.R.; Carrougher, G. Use of Virtual Reality for Adjunctive Treatment of Adult Burn Pain During Physical Therapy: A Controlled Study. *Clin. J. Pain* **2000**, *16*, 244–250. [CrossRef] [PubMed]
23. Kalsi-Ryan, S.; Curt, A.; Verrier, M.C.; Fehlings, M.G. Development of the Graded Redefined Assessment of Strength, Sensibility and Prehension (GRASSP): Reviewing measurement specific to the upper limb in tetraplegia. *J. Neurosurg. Spine* **2012**, *17*, 65–76. [CrossRef] [PubMed]
24. Lohse, K.R.; Hilderman, C.G.E.; Cheung, K.L.; Tatla, S.; Van Der Loos, H.F.M. Virtual reality therapy for adults poststroke: A systematic review and meta-analysis exploring virtual environments and commercial games in therapy. *PLoS ONE* **2014**, *3*, e93318.
25. Ding, Y.; Kastin, A.J.; Pan, W. Neural plasticity after spinal cord injury. *Curr. Pharm. Des.* **2005**, *11*, 41–50. [CrossRef] [PubMed]
26. Kaas, J.H. *International Encyclopedia of the Social & Behavioral Sciences*; Elsevier: Amsterdam, The Netherlands, 2001.
27. Yozbatiran, N.; Francisco, G.E. Robot-assisted Therapy for the Upper Limb after Cervical Spinal Cord Injury. *Phys. Med. Rehabil. Clin.* **2019**, *30*, 367–384. [CrossRef]
28. Cappa, P.; Clerico, A.; Nov, O.; Porfiri, M. Can Force Feedback and Science Learning Enhance the Effectiveness of Neuro-Rehabilitation? An Experimental Study on Using a Low-Cost 3D Joystick and a Virtual Visit to a Zoo. *PLoS ONE* **2013**, *8*, e83945. [CrossRef]
29. Scalona, E.; Hayes, D.; del Prete, Z.; Palermo, E.; Rossi, S. Perturbed Point-to-Point Reaching Tasks in a 3D Environment Using a Portable Haptic Device. *Electronics* **2019**, *8*, 32. [CrossRef]
30. Palsbo, S.E.; Marr, D.; Streng, T.; Bay, B.K.; Norblad, A.W. Towards a modified consumer haptic device for robotic-assisted fine-motor repetitive motion training. *Disabil. Rehabil. Assist. Technol.* **2011**, *6*, 546–551. [CrossRef]
31. Andaluz, V.H.; Salazar, P.J.; Silva, S.M.; Escudero, V.M.; Bustamante, D.C. Rehabilitation of upper limb with force feedback. In Proceedings of the 2016 IEEE International Conference on Automatica (ICA-ACCA), Curico, Chile, 19–21 October 2016; pp. 1–6.

32. Yeh, S.C.; Lee, S.H.; Chan, R.C.; Wu, Y.; Zheng, L.R.; Flynn, S. The efficacy of a haptic-enhanced virtual reality system for precision grasp acquisition in stroke rehabilitation. *J. Healthc. Eng.* **2017**, *2017*, 9840273. [CrossRef]
33. Chortis, A.; Standen, P.J.; Walker, M. Virtual reality system for upper extremity rehabilitation of chronic stroke patients living in the community. In Proceedings of the 7th ICDVRAT with ArtAbilitation, Maia, Portugal, 8–11 September 2008; pp. 221–228.
34. Alcover, E.A.; Jaume-i-Capó, A.; Moya-Alcover, B. PROGame: A process framework for serious game development for motor rehabilitation therapy. *PLoS ONE* **2018**, *13*, e0197383.
35. Pirovano, M.; Surer, E.; Mainetti, R.; Lanzi, P.L.; Borghese, N.A. Exergaming and rehabilitation: A methodology for the design of effective and safe therapeutic exergames. *Entertain. Comput.* **2016**, *14*, 55–65. [CrossRef]
36. Dimbwadyo-Terrer, I.; Trincado-Alonso, F.; los Reyes-Guzmán, A.D.; López-Monteagudo, P.; Polonio-López, B.; Gil-Agudo, A. Activities of daily living assessment in spinal cord injury using the virtual reality system toyra: Functional and kinematic correlations. *Virtual Real.* **2016**, *20*, 17–26. [CrossRef]
37. Eckert, M.; Gómez-Martinho, I.; Meneses, J.; Martínez, J.F. New approaches to exciting exergame-experiences for people with motor function impairments. *Sensors* **2017**, *17*, 354. [CrossRef] [PubMed]
38. Bart, O.; Agam, T.; Weiss, P.L.; Kizony, R. Using videocapture virtual reality for children with acquired brain injury. *Disabil. Rehabil.* **2011**, *33*, 1579–1586. [CrossRef]
39. Dimbwadyo-Terrer, I.; Gil-Agudo, A.; Segura-Fragoso, A.; de los Reyes-Guzman, A.; Trincado-Alonso, F.; Piazza, S.; Polonio-López, B. Effectiveness of the virtual reality system toyra on upper limb function in people with tetraplegia: A pilot randomized clinical trial. *Biomed. Res. Int.* **2016**, *2016*, 6397828. [CrossRef]
40. Omelina, L.; Jansen, B.; Bonnechère, B.; Van Sint Jan, S.; Cornelis, J. Serious games for physical rehabilitation: Designing highly configurable and adaptable games. In Proceedings of the International Conference on Disability, Virtual Reality and Associated Technologies, Laval, France, 10–12 September 2012; The University of Reading: Reading, UK, 2012; pp. 195–202.
41. Graafland, M.; Dankbaar, M.; Mert, A.; Lagro, J.; Wit-Zuurendonk, L.D.; Schuit, S.; Schaafstal, A.; Schijven, M. How to systematically assess serious games applied to health care. *JMIR Serious Games* **2014**, *2*, e11. [CrossRef]
42. Sepúlveda-Muñoz, D.; de los Reyes Guzmán, A.; Gil-Agudo, A.; Gutiérrez, A. Design and implementation of a Virtual Reality platform for Upper Limb rehabilitation. In Proceedings of the XXXVI Congreso Anual de la Sociedad Española de Ingeniería Biomèdica, Ciudad Real, Spain, 21–23 November 2018; Ediciones Visilab: Ciudad Real, Spain, 2018; pp. 203–206.
43. Virtual Reality Society. The Novint Falcon Haptic System—Virtual Reality Society. 2019. Available online: http://www.vrs.org.uk/virtual-reality-gear/haptic/novint-falcon.html (accessed on 1 August 2019).
44. Novint Falcon. Wide Variety of Games. 2019. Available online: http://www.robotshop.com/media/files/PDF/datasheet-nf1-s01.pdf (accessed on 1 August 2019).
45. Delta.3. Force Dimension. 2019. Available online: https://www.forcedimension.com/downloads/specs/specsheet-delta.3.pdf (accessed on 3 December 2019).
46. Omega.3. Force Dimension. 2019. Available online: https://www.forcedimension.com/downloads/specs/specsheet-omega.3.pdf (accessed on 3 December 2019).
47. Curtin, M. An Analysis of Tetraplegic Hand Grips. *Br. J. Occup. Ther.* **1999**, *62*, 444–450. [CrossRef]
48. Nagaraj, S.B.; Constantinescu, D. Effect of Haptic Force Feedback on Upper Limb. In Proceedings of the Second International Conference on Emerging Trends in Engineering & Technology, Nagpur, India, 16–18 December 2009; pp. 55–58.
49. ThalmicLabs. Myo Gesture Armband Product Specs—Welcome to Myo Support. 2019. Available online: http://support.getmyo.com/hc/en-us/articles/202648103-Myo-armband-product-specs (accessed on 1 August 2019).
50. Urra, O.; Casals, A.; Jané, R. The impact of visual feedback on the motor control of the upper-limb. In Proceedings of the 2015 37th Annual International Conference of the IEEE Engineering in Medicine and Biology Society (EMBC), Milan, Italy, 25–29 August 2015; pp. 3945–3948.
51. Muscle Physiology. Muscle Physiology—Types of Contractions. 2006. Available online: http://muscle.ucsd.edu/musintro/contractions.shtml (accessed on 1 August 2019).
52. Kirsblum, S.C.; Burns, S.P.; Biering-Sorensen, F.; Donovan, W.; Graves, D.E.; Jha, A. International standards for neurological classification of spinal cord injury (revised 2011). *J. Spinal Cord Med.* **2011**, *34*, 535–546. [CrossRef]

53. De los Reyes-Guzmán, A.; López-Dolado, E.; Lozano-Berrio, V.; Pérez-Nombela, S.; Torricelli, D.; Pons, J.L.; Gil-Agudo, A. Upper Limb Electromyographic Analysis Synchronized with Kinematics in Cervical Spinal Cord Injured Patients during the Activity of Daily Living of Drinking. *JSM Phys. Med. Rehabil.* **2017**, *1*, 1004.
54. Cifrek, M.; Medved, V.; Tonkovic´, S.; Ostojic´, S. Surface EMG based muscle fatigue evaluation in biomechanics. *Clin. Biomech.* **2009**, *24*, 327–340. [CrossRef]
55. Flash, T.; Hogan, N. The coordination of arm movements: An experimentally confirmed mathematical model. *J. Neurosci.* **1985**, *5*, 1688–1703. [CrossRef] [PubMed]
56. Krebs, H.I.; Ferraro, M.; Buerger, S.P.; Newbery, M.J.; Makiyama, A.; Sandmann, M.; Lynch, D.; Volpe, B.T.; Hogan, N. Rehabilitation robotics: Pilot trial of a spatial extension for MIT-Manus. *J. Neuroeng. Rehabil.* **2004**, *1*, 5. [CrossRef] [PubMed]

applied sciences

MDPI

Article

Improving the Efficiency of Robot-Mediated Rehabilitation by Using a New Organizational Model: An Observational Feasibility Study in an Italian Rehabilitation Center

Irene Aprile [1], Cristiano Pecchioli [1], Simona Loreti [1], Arianna Cruciani [1], Luca Padua [2,3] and Marco Germanotta [4,*]

1 IRCCS Fondazione Don Carlo Gnocchi, 20121 Milan, Italy; iaprile@dongnocchi.it (I.A.); cpecchioli@dongnocchi.it (C.P.); sim.lor@tiscali.it (S.L.); ariannacrux@gmail.com (A.C.)
2 Department of Geriatrics, Neurosciences and Orthopaedics, Università Cattolica del Sacro Cuore, 00168 Rome, Italy; luca.padua@unicatt.it
3 Fondazione Policlinico Universitario Agostino Gemelli IRCSS, 00168 Rome, Italy
4 IRCCS Fondazione Don Carlo Gnocchi, 50143 Florence, Italy
* Correspondence: mgermanotta@dongnocchi.it; Tel.: +39-06-3308-6448

Received: 28 October 2019; Accepted: 4 December 2019; Published: 8 December 2019

Featured Application: By using new organizational models, robotic rehabilitation can be sustainable; therefore, it is possible to provide high technological upper limb treatment to a high number of patients.

Abstract: Robotic rehabilitation is a promising way to restore upper limb function, but new organizational models are crucial in order to improve its sustainability. We aimed to analyze the feasibility of a robot-Assisted REhabilitation Area (robotAREA) equipped with four devices, using a new organizational model in which one physiotherapist supervises up to four patients. In 33 days, 60 patients were treated in the robotAREA. Two hundred fifty-five rehabilitation sessions were analyzed, each including two, three, or four patients supervised by one physiotherapist (the R2, R3, and R4 group, respectively). For each session, the duration of (a) setup, (b) training, (c) supervision, (d) session closure, and participant satisfaction were measured. For each patient, upper limb impairment, disability, mobility, and comorbidity were recorded. The time of training in the R4 group was lower by only 2 and 3 min compared to the R2 and R3 groups, respectively, while the supervision significantly changed between the R2, R3, and R4 groups. No differences were observed in satisfaction. Moreover, according to the logistic regression analysis, when the mean disability of the group is moderate, four patients can be supervised by one physiotherapist. These results suggest that the proposed model is feasible, and the mean disability of the group could influence the proper physiotherapist/patient ratio.

Keywords: rehabilitation; robotics; technological devices; upper limb impairment; organizational model

1. Introduction

Upper limb impairment is defined by the International Classification of Functioning, Disability and Health model [1] as (1) impairments of body function, such as a significant deviation or loss in neuromusculoskeletal and movement-related function related to joint mobility, muscle power, muscle tone, and/or involuntary movements, or (2) impairment of body structures, such as a significant deviation in structure of the nervous system or structures related to movement.

Robot-mediated therapy after upper limb impairment, because of neurological or orthopedic diseases, is emerging in the rehabilitation field. A recent Cochrane review highlighted a potential benefit of the electromechanical and robot-assisted upper limb training in stroke patients [2]. In addition, robotic therapy can increase the efficiency of therapy, and therefore the accessibility to treatment [3]. In fact, in an era of increasing focus on healthcare resource utilization, a considerable interest is devoted toward reducing costs while preserving a high-quality level. From this perspective, economic evaluations of rehabilitation interventions using cost-effectiveness and/or cost-utility analysis are needed [4]. However, few studies have been conducted on the real costs of robotic and technological rehabilitation when compared to traditional rehabilitation. Wagner et al. [5] found that the costs of an additional upper limb treatment (robotic or conventional) in stroke patients can be recuperated because of lower general healthcare costs. Moreover, a recent systematic review, including five studies, found that robotic therapy produces a better economic outcome when compared to conventional therapy [6].

In addition, Masiero et al. [7] suggested that the availability of a room equipped with more than one device can further increase the sustainability of the treatment, addressing an essential need of under-resourced healthcare systems [8]. In fact, although robotic devices are expensive, new organizational models where one physiotherapist supervises more than one patient could optimize the human resources. Some authors [9–11] suggested that this approach can be as effective as traditional therapy for stroke patients, presenting a more cost- and labor-efficient option. However, to the best of our knowledge, there have been no previous studies that analyzed either the rehabilitation dose provided to the patients or patient's satisfaction when different physiotherapist/patient ratios have been used. Moreover, the clinical characteristics of patients that could influence the proper physiotherapist/patient ratio remain uninvestigated.

In April 2016, to implement the robotic rehabilitation in a sustainable way, a set of four technological and robotic devices for the upper limb was identified, and a robotic rehabilitation area was built and equipped with the set [12]. This allowed experimenting with a new organizational model where more than one patient is supervised by one physiotherapist, in order to increase the efficiency of the robotic treatment.

Then, to critically evaluate the feasibility of this model, a study based on data related to the use of these devices in clinical practice was carried out.

Specifically, the aim of this study was twofold: (1) to verify the feasibility, in terms of rehabilitation dose (as measured by the time of training) and patient satisfaction (as measured by the Visual Analogue Scale for Satisfaction), of a new organizational model in which one physiotherapist supervises up to four patients using a set of four robotic-technological devices; and (2) to identify the optimal number of patients that can be supervised by one physiotherapist, in accordance to the patients' upper limb impairment (measured by the Motricity Index), disability (measured by the Barthel Index), mobility (measured by the Deambulation Index), and comorbidity (measured by the Cumulative Illness Rating Scale).

2. Materials and Methods

2.1. Study Design

An observational feasibility study examining the daily activity of the robot-Assisted REhabilitation Area (robotAREA) of a rehabilitation center in Italy.

2.2. Ethics

The study was carried out in compliance with the Helsinki Declaration. All the patients (both inpatients and outpatients) provided signed written informed consent to use collected data for clinical research purposes at the admission in the rehabilitation center. This study was approved by the Ethics and Experimental Research Committee of the "IRCCS Fondazione Don Carlo Gnocchi" (Prot. N.8/2016CE_FDG/FC/SA) on 6 April 2016.

2.3. Setting

The study was conducted over a period of 33 days (from February to March 2017). The RobotAREA is equipped with a set of four devices, three robots (MOTORE, Humanware, Italy, and Amadeo and Diego, Tyromotion, Austria), and one sensor-based device (Pablo, Tyromotion, Austria) [12]. MOTORE is a robotic device that allows passive, active, and active-assistive planar movements of the shoulder and elbow joints; Amadeo is a robotic device that allows passive, active, and active-assistive flexion and extension finger movements (also separately for each finger); Diego is a robotic device that allows three-dimensional, unimanual, and bimanual movements of the shoulder joint, both in sitting and in standing, with gravity compensation; Pablo is a sensor-based device that requires patients to perform unassisted three-dimensional movements of the shoulder, elbow, and wrist joints, both unimanual and bimanual, both when sitting and standing. All physiotherapists who worked in the RobotAREA had an expertise in robotic rehabilitation and used these devices for more than one year. Figure 1 shows the distribution of the device stations inside the robotic-technological area.

Figure 1. Distribution of the devices in the robot-Assisted REhabilitation Area (robotAREA). Beginning by the door, clockwise: Diego; Amadeo; Pablo; MOTORE.

2.4. Participants

Inclusion criteria: both inpatients and outpatients admitted to our rehabilitation facility with an upper limb impairment due to neurologic or orthopedic disorders. We excluded patients with a contraindication to robotic therapy, which was identified as: (1) inability to understand the physiotherapist's instructions and device exercises; (2) fixed contraction deformity/excessive spasticity; (3) any psychiatric disorder or severe cognitive disturbance that could reduce treatment compliance; and/or (4) severe visual impairment.

2.5. Robotic Rehabilitation Treatment

Each RS lasted 45 min, and the training frequency was 3 or 5 times/week, depending on the rehabilitation setting (outpatients or inpatients, respectively). During the treatment, both the distal and the proximal segments of the patients' upper arm were treated by means of the robotic and sensor-based devices. Motor and cognitive tasks were performed during the treatment, while visual and auditory feedback was provided to help the patients. During each session, the physical therapist uses one system for each patient to minimize the time required to move the patients from one system

to another. The rehabilitation program starts with the robotic device for the shoulder and elbow joints, followed by the robotic device for the hand, the sensor-based device for the shoulder, elbow, and wrist and, finally, the robotic system for the shoulder. The adopted protocol followed the general indications, which were laid out in a flow chart, in order to ensure the homogeneity of treatment; however, for each patient, the physiotherapist selected the device and adapted the exercises to his/her residual abilities. More details on the rehabilitation protocol were previously reported [13]. During the rehabilitation session (RS), one physiotherapist supervised more patients at once with a physiotherapist/patient ratio of 1/2 (R2), 1/3 (R3), or 1/4 (R4). The number of patients treated in each RS was chosen by the physician depending on the upper limb impairment, disability, mobility, and comorbidity of the entire group, based on the experience done with a wide multicenter study [13].

2.6. Data Collection

A trained researcher monitored the patients during each robotic-technological rehabilitation session (RS). The data collected during each session for each patient was called "observation". During the study, for each patient, several observations were performed, according to the individual rehabilitation program. In order to limit bias due to researcher's presence, neither physiotherapists nor patients knew when data collection would take place.

To investigate whether and in which patients this new organizational model was applicable, we compared the different rehabilitation settings (R2, R3, and R4) in terms of the rehabilitation dose and clinical characteristics of the patients. For each session, the number of patients supervised by one physiotherapist was recorded, together with the clinical status of the patients, using validated clinical scales administered by trained operators. Specifically, we evaluated disability (according to the Barthel Index, BI [14]), upper limb impairment (using the Motricity Index, MI [15]), mobility (according to the Deambulation Index, DI [16]), comorbidities and severity (described according to the Cumulative Illness Rating Scale-Comorbidity Index, CIRS-CI, and the Cumulative Illness Rating Scale-Severity Index, CIRS-SI [17–19]). Complete demographic and clinical details were collected at the first observation for each patient.

Moreover, to evaluate the feasibility of the model, the following measures were recorded: (a) tSetup (minutes): time spent for the correct patient placement and for planning of the session exercises; (b) tTraining (minutes): time spent by patient to perform the training; (c) tSupervision (minutes): time spent by the physiotherapist in the individual interaction with the patient; and (d) tClosure (minutes): time spent by the physiotherapist to close the exercise session and remove the patient from the device. These measures were obtained in a subsample of observations. In addition, the Visual Analogue Scale for Satisfaction [20], a self-assessment scale ranging from 0 (no satisfaction) to 10 (extreme satisfaction), was used to measure patients' satisfaction. The exact question was "Are you satisfied with your rehabilitation session?"

2.7. Statistical Analysis

To evaluate the feasibility of the model, data obtained from the three groups were compared by using one-way ANOVA tests, followed by post-hoc analysis with Bonferroni correction, or Kruskal–Wallis tests, followed by post-hoc analysis, using Dunn's procedure with a Bonferroni correction, as appropriated.

To evaluate the impact of disability, upper limb impairment, mobility, and comorbidity on the number of patients in each group, for each session, the mean data of the group were computed and compared between groups (univariate analysis) using Kruskal–Wallis tests, followed by post-hoc analysis, using Dunn's procedure with a Bonferroni correction. Then, to identify the best physiotherapist/patient ratio, a multivariate logistic analysis was performed, considering the variables identified in the univariate analysis as covariates. Finally, a receiver operating characteristics ROC analysis was used to identify a possible cutoff.

For all statistical tests, the significance level was set to 0.05. Statistical analysis was performed using SPSS (IBM Corp. Released 2017. IBM SPSS Statistics for Windows, Version 25.0. Armonk, NY, USA: IBM Corp.).

3. Results

In a period of 33 days, 60 patients were observed in our rehabilitation department. Table 1 shows the demographic and clinical characteristics of the analyzed sample. Spinal disorders included spinal cord injury after trauma or surgery on the column for neoplasia/lumbar spinal stenosis or spinal disc herniation; orthopedic disease included patients with shoulder prosthesis, upper limb fractures/surgery, and polytrauma. Upper limb impairment, disability, mobility, and comorbidities are reported in Table 2. During the study, each patient performed a variable number of rehabilitation sessions depending on the hospitalization stay and frequency of treatment per week. No serious adverse events were observed, and the robotic therapy was well accepted by all patients, without changes in the initial plan. None of the patients declined to participate in the study, since it did not interfere with their rehabilitation plan.

Table 1. Demographic and clinical characteristics of the observed sample.

Age (Years)	**64 ± 16 (Range: 19–91)**	
Sex	Male	27 (45.0%)
	Female	33 (55.0%)
Setting	Outpatient	11 (18.3%)
	Inpatient	49 (81.7%)
Diagnosis	Stroke	41 (68.3%)
	Multiple sclerosis	3 (5.0%)
	Charcot Marie Tooth	1 (1.7%)
	Guillain Barrè syndrome	1 (1.7%)
	Motoneuron disease	1 (1.7%)
	Parkinson disease	1 (1.7%)
	Spinal disorder	7 (11.7%)
	Orthopedic disease/trauma	5 (8.3%)

Table 2. Disability, upper limb impairment, mobility, and comorbidities of the sample.

Variable	Mean ± SD	Range
Barthel Index	57.7 ± 23.1	(14–97)
Motricity Index	57.5 ± 23.2	(1–93)
Deambulation Index	2.9 ± 2.2	(0–7)
CIRS-SI	1.0 ± 0.4	(0.3–2)
CIRS-CI	1.9 ± 1.0	(0–6)

SD: standard deviation; CIRS-CI: Cumulative Illness Rating Scale-Comorbidity Index; CIRS-SI: Cumulative Illness Rating Scale-Severity Index.

The total observations (data collected at each session for each patient) were 782, with a mean of 24 observations/day (range: 17–31) and a mean of 13 observations/patient (range: 1–50) (see also the supporting document: Supplementary Table S1). Two hundred fifty-five rehabilitation sessions were recorded with a ratio of physiotherapist/patient as follows: 45 sessions (17.7%) with a ratio of 1/2 (R2); 148 sessions (58.0%) with a ratio of 1/3 (R3), and 62 sessions (24.3%) with a ratio of 1/4 (R4). The mean value of the physiotherapist/patient ratio was 1/3.1.

3.1. Feasibility of the Model

Data related to the rehabilitation dose, supervision, and patients' satisfaction were recorded in a subsample of 329 observations (supporting document: Supplementary Table S1) and reported in

Table 3. As expected, the tTraining was significantly different between groups ($p = 0.007$); post-hoc analysis showed that it was significantly lower in the R4 group, when compared with both R2 (mean difference: 3.2 min) and R3 groups (mean difference: 2.3 min). Instead, no differences in tTraining were found between R2 and R3 groups. The tSupervision was significantly different between all groups ($p < 0.001$), as confirmed also by post-hoc analysis. With respect to patient satisfaction, no significant differences were observed between groups ($p = 0.39$).

Table 3. Feasibility measurements: rehabilitation dose (tTraining) and supervision time (tSupervision) during a 45-min rehabilitation session, and patients' satisfaction in the whole sample and the three groups, separately, together with the statistical analysis. Data were obtained from 329 observations.

	Whole Group	R2	R3	R4	*p*	Post-Hoc Analysis		
	Mean ± SD	Mean ± SD	Mean ± SD	Mean ± SD		R2 vs. R3	R2 vs. R4	R3 vs. R4
tTraining (min)	31.3 ± 6.4	32.8 ± 5.0	31.9 ± 6.0	29.6 ± 7.2	**0.007**	>0.99	**0.04**	**0.01**
tSupervision (min)	9.7 ± 2.3	11.0 ± 3.2	9.7 ± 2.0	8.9 ± 2.1	**<0.001**	**0.005**	**<0.001**	**0.007**
VAS for satisfaction	8 ± 1	8 ± 2	8 ± 1	8 ± 1	0.39	–	–	–

R2, R3 and R4 indicate groups with 2, 3 or 4 patients supervised by one physiotherapist, respectively. Values in bold indicate statistical significance ($p < 0.05$). SD: standard deviation; VAS: Visual analogue scale.

In addition, we found that the mean time needed for the setup (tSetup) was 3.3 ± 1.3 min, while the mean time needed for the session closure (tClosure) was 1.4 ± 0.5 min.

3.2. Impact of Disability, Upper Limb Impairment, Mobility, and Comorbidity on the Model

A comparison of upper limb impairment, disability, mobility, and comorbidity mean score between the three groups was made and reported in Table 4. The results showed significant differences only in BI, DI, and CIRS-SI between the groups R2 versus R4, and R3 versus R4. Considering the lack of statistical significance between the R2 and R3 groups, a further analysis was made combining the R2 and R3 groups (R2 + R3 group). The logistic regression model was carried out on the three statistically significant variables obtained from the univariate analysis. We found that the model was statistically significant, $\chi2(3) = 36.096$, $p < 0.001$. As shown in Table 5, among the three predictor variables, only the BI was statistically significant. To obtain a reference value for the only significant variable (BI) in the logistic regression model, an ROC analysis was carried out. According to the Youden index, the obtained cut-off value was equal to 57.

Table 4. Disability, mobility, and comorbidity variables for the three groups, separately. Data were obtained from 782 observations.

	R2	R3	R4	*p*	Post-Hoc Analysis		
	Mean ± SD	Mean ± SD	Mean ± SD		R2 vs. R3	R2 vs. R4	R3 vs. R4
BI	49.0 ± 10	53.0 ± 12.6	63.0 ± 14.3	**<0.001**	0.24	**<0.001**	**<0.001**
MI	59.5 ± 14.7	57.2 ± 11.8	57.9 ± 8.8	0.42	-	-	-
DI	2.1 ± 1.2	2.4 ± 1.4	3.3 ± 1.4	**<0.001**	0.98	**<0.001**	**<0.001**
CIRS-SI	1.1 ± 0.3	1.0 ± 0.2	0.9 ± 0.2	**<0.001**	0.26	**<0.001**	**<0.001**
CIRS-CI	2.1 ± 0.8	2.0 ± 0.6	1.8 ± 0.4	0.06	-	-	-

Values in bold indicate statistical significance ($p < 0.05$). R2, R3 and R4 indicate groups with two, three, or four patients supervised by one physiotherapist, respectively. SD: standard deviation; BI: Barthel Index; MI: Motricity Index; DI: Deambulation Index; CIRS-CI: Cumulative Illness Rating Scale-Comorbidity Index; CIRS-SI: Cumulative Illness Rating Scale-Severity Index.

Table 5. Logistic regression model for the identification of the best physiotherapist/patient ratio (R2/R3 versus R4), considering the mean disability, mobility, and comorbidity of the group (identified in the univariate analysis). Data were obtained from 255 rehabilitation sessions (782 observations).

	β	Standard Error	*p*	Exp (β)	95% Confidence Interval for Exp (β)	
				Relative Risk	Lower Bound	Upper Bound
BI	0.099259	0.039318	**0.01**	1.1044	1.0224	1.1928
DI	−0.52213	0.37	0.16	0.5933	0.2873	1.2252
CIRS-SI	−1.41553	0.75418	0.06	0.2428	0.0554	1.0647

Values in bold indicate statistical significance ($p < 0.05$). BI: Barthel Index; DI: Deambulation Index; CIRS-SI: Cumulative Illness Rating Scale-Severity Index.

4. Discussion

Robotic tools are emerging in the rehabilitation field, showing promising expectations for an intensive and personalized treatment. Nonetheless, these devices are expensive. Therefore, it is necessary to find the best organizational models to increase the number of patients who may have access to the technological rehabilitation, optimizing human resources. In this perspective, it is crucial to know if and how patient's disability, mobility, or comorbidity can influence an organizational model where a new, non-traditional ratio of physiotherapist/patient would be adopted.

This study shows the feasibility, in terms of rehabilitation dose and patient's satisfaction, of an organizational model with one physiotherapist supervising more than one patient, using a set of four devices for a comprehensive upper limb rehabilitation. In a 45-min rehabilitation session, regardless of the physiotherapist/patient ratio, each patient performed about 30 min of training with an individual physiotherapist supervision of about 10 min. As expected, the time of training was significantly lower in the R4 group but with a gap of only 2 and 3 min compared to the R2 and R3 groups, respectively. Regarding the difference in the training time recorded between the R2/R3 and R4 groups, an increase of about 3 min of the rehabilitation session of the R4 group can be used to overcome this small gap.

Therefore, our results showed that the physiotherapists in this study were able to supervise up to four patients, without a reduction of the treatment dose provided to the patient. This is a crucial point: in fact, several studies report an intensity–effect relation between the amount of therapy that individuals receive and the motor recovery [21,22]; additionally, no ceiling effect for the intensity of the therapy has been observed [23–25]. Note that patient satisfaction was very high (8/10) without significant differences between groups, so patients were very satisfied even if treated together with one, two, or three other patients at the same time. Regarding the clinical characteristics of the patients, our data did not show differences when two or three patients were supervised by one physiotherapist. On the contrary, though as expected, the group in which four patients were supervised by one physiotherapist (R4) had a lower disability and comorbidity and higher mobility than the R2 and R3 groups. A remarkable result is that upper limb impairment did not influence the organizational model proposed, since the MI not significantly different between the groups (R2, R3, and R4). The multivariate analysis showed that only the BI can predict significantly the treatment group, meaning that the maximum number of patients supervised by one physiotherapist can be dependent on their level of autonomy. Therefore, the BI seems to be the most important variable that could influence the physiotherapist/patient ratio. Based on our results, a ratio of 1/4 could be used if the mean value BI of the group of patients is higher than 57. Note that patients with BI values lower than 60 are considered patients with a severe disability [14]. Our results showed a similar cut-off of disability, even if calculated as the mean of the group (BI mean score of group <57).

The analysis of both clinical data and feasibility measures suggests that patients with a severe disability (BI mean score of the group <57) can be equally treated in groups of two or three patients, providing that they had the same dose. Instead, when a moderate disability is present, up to four patients can be supervised by one physiotherapist. This study also confirms the possibility of optimizing resources allocation. In fact, in our rehabilitation planning, a mean of 24 patients were treated each

day with a mean value of physiotherapist/patient ratio of 1/3.1, which means eight rehabilitation sessions/day. In a traditional rehabilitation model (with a physiotherapist/patient ratio of 1/1) to treat 24 patients/day, obviously 24 rehabilitation sessions/day are needed. As highlighted in the proposed organizational model, it is possible to reduce the number of rehabilitation sessions/day (needed to treat the same number of patients) by about 1/3, with better human resources allocation.

Moreover, it is worthy to note that we have specifically chosen a set of devices with a limited time required to start the rehabilitation session, as highlighted by the reported tSetup, and therefore, these have a limited impact on the provided rehabilitation dose. On the contrary, more complex devices, as exoskeletons, require a longer time to fit the robot for individual patients, and it is one of the main barriers to efficient use [26]. As in our approach, two studies on the same topic [8,9] used both robotic and non-robotic devices, supporting the idea that this approach can be effective and sustainable.

Anyway, robotic rehabilitation is not merely a matter of increasing the amount and intensity of therapy [27]. It provides extrinsic biofeedback that makes the patient aware of his movements and consequently allows him to modify his movement patterns, thus fostering his participation in the rehabilitation exercise [28–30]. Furthermore, it seems that the impact of technological rehabilitation on functional outcome could be optimized by offering more chances to the nervous system to experience "real" activity-related sensorimotor input during the training of upper limb movement [31].

From this knowledge and from our experience, it is very important to underline that physiotherapists have to perform an adequate training to acquire expertise with regard to these devices. With a correct use of them, the workload of the physiotherapists can be alleviated, their work time can be optimized, and they can focused toward personalizing rehabilitation treatments, according to each patient's residual abilities and progress in order to optimize functional recovery [27].

The organizational model herein discussed shows the feasibility of providing a comprehensive and a high technological level upper limb treatment that would be accessible to a high number of patients at once, while preserving an adequate training time and physiotherapist supervision. Finally, thanks to the sustainability in terms of optimizing human resources, this model can be applied to the usual care of the clinical practice considering the advantages that the robotic devices can provide (for example, to objectively measure the improvement during the therapy) [32,33].

Limitations of the Study

This study was conducted in a highly specialized rehabilitation center where all physiotherapists had an expertise in robotic rehabilitation and used these devices for more than one year. Therefore, this could limit the extension of our results to different rehabilitation units with lower levels of expertise. However, we believe that this limitation does not severely impact on the application of the results, since a high level of expertise is required to efficiently use these devices. Moreover, this study was not aimed to evaluate the validity and the reliability of the used outcome measures. Finally, this study did not compare the effect of different physiotherapist/patient ratios on the outcome of the rehabilitation process. These aspects should be addressed in future studies.

5. Conclusions

In conclusion, this study showed the feasibility, in terms of rehabilitation dose and patients' satisfaction, of a new organizational model, where a group of patients supervised by one physiotherapist is treated with a set of robotic and sensor-based devices. Moreover, it highlighted that the mean disability of the group, as measured by the Barthel Index, could influence the proper physiotherapist/patient ratio. Future studies should be addressed to analyze the impact of this new model on the rehabilitation outcomes.

Supplementary Materials: The following are available online at http://www.mdpi.com/2076-3417/9/24/5357/s1.

Author Contributions: Conceptualization, I.A. and M.G.; methodology, I.A., M.G.; formal analysis, M.G.; investigation, C.P. and A.C.; data curation, C.P. and M.G.; writing—original draft preparation, I.A., S.L. and M.G.; writing—review and editing, I.A. and M.G.; supervision, I.A. and L.P.

Funding: This research received no external funding.

Acknowledgments: The authors would like to thank Enrica Di Sipio for her help in making figures, Manuel Triolo for the support given from a linguistic standpoint and Claudia Loreti for administrative and technical support.

Conflicts of Interest: The authors declare no conflict of interest.

References

1. World Health Organization. *International Classification of Functioning, Disability and Health: ICF*; World Health Organization: Geneva, Switzerland, 2001.
2. Mehrholz, J.; Pohl, M.; Platz, T.; Kugler, J.; Elsner, B. Electromechanical and robot-assisted arm training for improving activities of daily living, arm function, and arm muscle strength after stroke. *Cochrane Database Syst. Rev.* **2015**. [CrossRef]
3. Laut, J.; Porfiri, M.; Raghavan, P. The Present and Future of Robotic Technology in Rehabilitation. *Curr. Phys. Med. Rehabil. Rep.* **2016**, *4*, 312–319. [CrossRef]
4. Hayward, K.S.; Kramer, S.F.; Thijs, V.; Ratcliffe, J.; Ward, N.S.; Churilov, L.; Jolliffe, L.; Corbett, D.; Cloud, G.; Kaffenberger, T.; et al. A systematic review protocol of timing, efficacy and cost effectiveness of upper limb therapy for motor recovery post-stroke. *Syst. Rev.* **2019**, *8*, 187. [CrossRef] [PubMed]
5. Wagner, T.H.; Lo, A.C.; Peduzzi, P.; Bravata, D.M.; Huang, G.D.; Krebs, H.I.; Ringer, R.J.; Federman, D.G.; Richards, L.G.; Haselkorn, J.K.; et al. An economic analysis of robot-assisted therapy for long-term upper-limb impairment after stroke. *Stroke* **2011**, *42*, 2630–2632. [CrossRef] [PubMed]
6. Lo, K.; Stephenson, M.; Lockwood, C. The economic cost of robotic rehabilitation for adult stroke patients: A systematic review. *JBI Database Syst. Rev. Implement. Rep.* **2019**, *17*, 520–547. [CrossRef] [PubMed]
7. Masiero, S.; Poli, P.; Armani, M.; Ferlini, G.; Rizzello, R.; Rosati, G. Robotic upper limb rehabilitation after acute stroke by NeReBot: Evaluation of treatment costs. *Biomed Res. Int.* **2014**, *2014*. [CrossRef]
8. Atashzar, S.F.; Shahbazi, M.; Tavakoli, M.; Patel, R.V. A Computational-Model-Based Study of Supervised Haptics-Enabled Therapist-in-the-Loop Training for Upper-Limb Poststroke Robotic Rehabilitation. *IEEE/ASME Trans. Mechatron.* **2018**, *23*, 563–574. [CrossRef]
9. Buschfort, R.; Brocke, J.; Heß, A.; Werner, C.; Waldner, A.; Hesse, S. The arm studio to intensify the upper limb rehabilitation after stroke: Concept, acceptance, utilization and preliminary clinical results. *J. Rehabil. Med.* **2010**, *42*, 310–314. [CrossRef] [PubMed]
10. Hesse, S.; Heß, A.; Werner, C.C.; Kabbert, N.; Buschfort, R. Effect on arm function and cost of robot-assisted group therapy in subacute patients with stroke and a moderately to severely affected arm: A randomized controlled trial. *Clin. Rehabil.* **2014**, *28*, 637–647. [CrossRef]
11. Bustamante Valles, K.; Montes, S.; de Madrigal, M.J.; Burciaga, A.; Martínez, M.E.; Johnson, M.J. Technology-assisted stroke rehabilitation in Mexico: A pilot randomized trial comparing traditional therapy to circuit training in a Robot/technology-assisted therapy gym. *J. Neuroeng. Rehabil.* **2016**, *13*, 83. [CrossRef]
12. Aprile, I.; Cruciani, A.; Germanotta, M.; Gower, V.; Pecchioli, C.; Cattaneo, D.; Vannetti, F.; Padua, L.; Gramatica, F. Upper Limb Robotics in Rehabilitation: An Approach to Select the Devices, Based on Rehabilitation Aims, and Their Evaluation in a Feasibility Study. *Appl. Sci.* **2019**, *9*, 3920. [CrossRef]
13. Aprile, I.; Germanotta, M.; Cruciani, A.; Loreti, S.; Pecchioli, C.; Cecchi, F.; Montesano, A.; Galeri, S.; Diverio, M.; Falsini, C.; et al. Upper Limb Robotic Rehabilitation after Stroke: A Multicenter, Randomized Clinical Trial. *J. Neurol. Phys. Ther.* **2019**, in press. [CrossRef]
14. Shah, S.; Vanclay, F.; Cooper, B. Improving the sensitivity of the Barthel Index for stroke rehabilitation. *J. Clin. Epidemiol.* **1989**, *42*, 703–709. [CrossRef]
15. Demeurisse, G.; Demol, O.; Robaye, E. Motor evaluation in vascular hemiplegia. *Eur. Neurol.* **1980**, *19*, 382–389. [CrossRef] [PubMed]
16. Korner-Bitensky, N.; Mayo, N.; Cabot, R.; Becker, R.; Coopersmith, H. Motor and functional recovery after stroke: Accuracy of physical therapists' predictions. *Arch. Phys. Med. Rehabil.* **1989**, *70*, 95–99. [PubMed]
17. Miller, M.D.; Paradis, C.F.; Houck, P.R.; Mazumdar, S.; Stack, J.A.; Rifai, A.H.; Mulsant, B.; Reynolds, C.F. Rating chronic medical illness burden in geropsychiatric practice and research: Application of the Cumulative Illness Rating Scale. *Psychiatry Res.* **1992**, *41*, 237–248. [CrossRef]

18. Conwell, Y.; Forbes, N.T.; Cox, C.; Caine, E.D. Validation of a measure of physical illness burden at autopsy: The Cumulative Illness Rating Scale. *J. Am. Geriatr. Soc.* **1993**, *41*, 38–41. [CrossRef]
19. Salvi, F.; Miller, M.D.; Grilli, A.; Giorgi, R.; Towers, A.L.; Morichi, V.; Spazzafumo, L.; Mancinelli, L.; Espinosa, E.; Rappelli, A.; et al. A manual of guidelines to score the modified cumulative illness rating scale and its validation in acute hospitalized elderly patients. *J. Am. Geriatr. Soc.* **2008**, *56*, 1926–1931. [CrossRef]
20. Brokelman, R.B.G.; Haverkamp, D.; van Loon, C.; Hol, A.; van Kampen, A.; Veth, R. The validation of the visual analogue scale for patient satisfaction after total hip arthroplasty. *Eur. Orthop. Traumatol.* **2012**, *3*, 101–105. [CrossRef]
21. Kwakkel, G.; van Peppen, R.; Wagenaar, R.C.; Wood Dauphinee, S.; Richards, C.; Ashburn, A.; Miller, K.; Lincoln, N.; Partridge, C.; Wellwood, I.; et al. Effects of augmented exercise therapy time after stroke: A meta-analysis. *Stroke* **2004**, *35*, 2529–2539. [CrossRef]
22. Byl, N.N.; Pitsch, E.A.; Abrams, G.M. Functional outcomes can vary by dose: Learning-based sensorimotor training for patients stable poststroke. *Neurorehabil. Neural Repair* **2008**, *22*, 494–504. [CrossRef] [PubMed]
23. Langhorne, P.; Wagenaar, R.; Partridge, C. Physiotherapy after stroke: More is better? *Physiother. Res. Int.* **1996**, *1*, 75–88. [CrossRef] [PubMed]
24. Kwakkel, G. Impact of intensity of practice after stroke: Issues for consideration. *Disabil. Rehabil.* **2006**, *28*, 823–830. [CrossRef] [PubMed]
25. Huang, H.-C.; Chung, K.-C.; Lai, D.-C.; Sung, S.-F. The impact of timing and dose of rehabilitation delivery on functional recovery of stroke patients. *J. Chin. Med. Assoc.* **2009**, *72*, 257–264. [CrossRef]
26. Swank, C.; Sikka, S.; Driver, S.; Bennett, M.; Callender, L. Feasibility of integrating robotic exoskeleton gait training in inpatient rehabilitation. *Disabil. Rehabil. Assist. Technol.* **2019**. [CrossRef]
27. Poli, P.; Morone, G.; Rosati, G.; Masiero, S. Robotic Technologies and Rehabilitation: New Tools for Stroke Patients' Therapy. *Biomed Res. Int.* **2013**, *2013*. [CrossRef]
28. van Vliet, P.M.; Wulf, G. Extrinsic feedback for motor learning after stroke: What is the evidence? *Disabil. Rehabil.* **2006**, *28*, 831–840. [CrossRef]
29. Masiero, S.; Poli, P.; Rosati, G.; Zanotto, D.; Iosa, M.; Paolucci, S.; Morone, G. The value of robotic systems in stroke rehabilitation. *Expert Rev. Med. Devices* **2014**. [CrossRef]
30. Gassert, R.; Dietz, V. Rehabilitation robots for the treatment of sensorimotor deficits: A neurophysiological perspective. *J. Neuroeng. Rehabil.* **2018**, *15*, 46. [CrossRef]
31. Nudo, R.J. Functional and structural plasticity in motor cortex: Implications for stroke recovery. *Phys. Med. Rehabil. Clin. N. Am.* **2003**, *14*, S57–S76. [CrossRef]
32. Germanotta, M.; Vasco, G.; Petrarca, M.; Rossi, S.; Carniel, S.; Bertini, E.; Cappa, P.; Castelli, E. Robotic and clinical evaluation of upper limb motor performance in patients with Friedreich's Ataxia: An observational study. *J. Neuroeng. Rehabil.* **2015**, *12*, 41. [CrossRef] [PubMed]
33. Germanotta, M.; Cruciani, A.; Pecchioli, C.; Loreti, S.; Spedicato, A.; Meotti, M.; Mosca, R.; Speranza, G.; Cecchi, F.; Giannarelli, G.; et al. Reliability, validity and discriminant ability of the instrumental indices provided by a novel planar robotic device for upper limb rehabilitation. *J. Neuroeng. Rehabil.* **2018**, *15*, 39. [CrossRef] [PubMed]

MDPI
St. Alban-Anlage 66
4052 Basel
Switzerland
Tel. +41 61 683 77 34
Fax +41 61 302 89 18
www.mdpi.com

Applied Sciences Editorial Office
E-mail: applsci@mdpi.com
www.mdpi.com/journal/applsci

MDPI
St. Alban-Anlage 66
4052 Basel
Switzerland

Tel: +41 61 683 77 34
Fax: +41 61 302 89 18

www.mdpi.com

ISBN 978-3-0365-2312-5